Microscope-mode Imaging Mass Spectrometry with the PImMS Camera

A thesis submitted for the degree of Doctor of Philosophy

Physical and Theoretical Chemistry

Edward Halford

Jesus College, University of Oxford

January 11, 2016

Microscope-mode Imaging Mass Spectrometry with the PImMS Camera

Edward Halford, Jesus College

A thesis submitted for the degree of Doctor of Philosophy

Trinity Term, 2015

Abstract

Until recently, the use of microscope-mode imaging mass spectrometry (MSI) was restricted by the available technology. Fast cameras were limited to acquiring a single image relating to a set m/z range which had to be predefined before the experiment was started. Now, new developments in camera technology have produced time-stamping cameras that can record the arrival time of ions at a detector, without the need to define an exposure time. This allows the images relating to different species with a range of m/z to be acquired simultaneously. One of these cameras is the Pixel Imaging Mass Spectrometry (PImMS) camera, which has the added advantage that each pixel within the sensor has four memory registers. This means that up to four events can be observed, by each pixel, within a single time-of-flight cycle.

Here, the application of the PImMS camera to microscope-mode MSI is presented. Initial experiments are conducted using a converted conventional velocity-map imaging instrument. Simulations are presented in order to predict the performance of the ion optics when used for spatial imaging, and the result of these simulations is then compared to those obtained experimentally, using a commercially available charge-coupled device (CCD) camera and a photomultiplier tube (PMT). These spatial resolutions along with simultaneously obtained mass resolutions are then compared to those obtained using a PImMS1 camera.

Further experiments are presented in which the PImMS1 camera is used in conjunction with a modified commercially available mass spectrometer, the LT2 Plus (produced by Scientific Analysis Instruments Ltd — SAI). This instrument is designed to obtain isotopic resolution for $m/z < 1000$, whilst also maintaining a spatial resolution better than $50\,\mu$m. These specifications are obtained using the PImMS1 camera, and it is shown that images of multiple chemical species can be obtained simultaneously.

A new data analysis method is developed, which attempts to model the shape of PImMS data event clusters. Although the application of this method cannot be fully realised with data obtained with a PImMS1 camera, a modified version is successfully applied to PImMS1 data and produces both an improvement in the time precision of the camera, as well as a more efficient use of the available data.

Finally, various designs for a primary ion beam are presented that could be used in place of the standard laser desorption system. The ion beam is designed for use with an MSI instrument, ablating sample from a large area of sample, and with a short pulse length for time-of-flight analysis. A final design is presented that can produce beam pulse that can be focussed down to form a pulse length of 5 ns, across a target of 2.5 mm.

As a collection, the works detailed in this thesis present the development of a stigmatic ion microscope that uses the PImMS camera, from a proof-of-concept to a viable analytical instrument.

Acknowledgements

I would first like to thank my supervisor, Mark Brouard. He has supported me throughout, not only my postgraduate study, but my undergraduate studies as well. He has always given me enough freedom and encouragement to explore ideas, whilst simultaneously being available to give advice and guidance whenever necessary. It is his influence on the Brouard group that has made the past years so enjoyable and rewarding.

I also would like to thank everyone at SAI who made me feel so welcome on my trips to Manchester. In particular, I owe so much to Steve Thompson and Mark Mills, who taught me a great deal about mass spectrometry during some very intense "technical discussions".

None of the work in this thesis would have been possible without the work of the PImMS collaboration. Jaya John John, and Jason Lee have both put an incredible amount of work and effort into the project, and were always more than happy to help with anything PImMS related.

Working in the basement has been made so much more enjoyable thanks to the companionship that exists between the members of the Brouard group. A surprisingly large amount of work and progress has been made over tea, coffee, and beer. Ben Winter's enthusiasm for experimental work was truly inspiring, and I was very lucky to have worked alongside him on the "spatial imaging rig". A special mention also has to go to Bethan Nichols whom I have worked with at Oxford for eight years, and who has always been a great friend.

I have been fortunate enough to have met many wonderful people during my years at Oxford, and have gained so much from all of them. The Oxford University Rifle Club has been a wonderful distraction from work, teaching me the philosophy of the Vs & 3s.

My family, especially my parents, have been hugely supportive throughout my student life. I truly appreciate their attempts at finding this work interesting.

Finally, I would like to thank Hannah Wills. From the shared trauma of late night gun running, to putting all this science into (an historical) perspective, she has made the years of my DPhil so much more enjoyable.

Contents

Chapter 1

Introduction

Mass spectrometry (MS) was first performed, over a hundred years ago, by J. J. Thomson [1]. It now forms the basis for a multitude of analytical techniques and procedures ranging from the analysis of everyday species such as food or soil samples [2–4], to security applications such as explosives detection or forensic analysis [5–8], and research applications such as pharmacology and reaction dynamics [9–14].

Imaging mass spectrometry (MSI[1]) is a more specialised field that combines the analytical strengths of mass spectrometry with the spatial resolution of optical microscopy. The result is a chemically resolved map of the surface of a sample. This map can then either be analysed to show the mass spectrum for a specific area, or the image corresponding to species within a specific range of mass to charge ratio values. These data are therefore more enlightening than that produced by either of the techniques on their own. These techniques have been used widely for tissue imaging where knowing the location of certain proteins is of use [15, 16], and especially in the mapping of pharmaceuticals in tissues [11, 17]. The images produced can range from detailed analysis at cellular lengths all the way up to whole-body rodent sections [18, 19]. Alternatively, they can also be used for other applications such as to connect fingerprints (and therefore an identity) to the handling of specific substances [20, 21].

In this chapter some of the concepts of mass spectrometry will be presented, focussing

[1]The acronym MSI is preferred to the more obvious IMS in order to avoid confusion with ion mobility spectrometry.

on those that are most relevant to MSI. First there will be an introduction to techniques used in time-of-flight mass analysis, especially for analysis in MSI. This will be followed by an explanation of some of the common detector technologies, and specifically those capable of acquiring spatially resolved images. After this there will be a discussion of the various methods of sample ionisation. Lastly, the work building up to this thesis will be discussed along with an outline of this document.

1.1 Mass Analysis

In the original work by Thomson, the mass of a species was obtained from the magnitude of the deflection, d, of the ionised particle by a magnetic field,

$$d = \frac{z}{mv}A, \tag{1.1}$$

where z is the charge number of the particle, m is its mass number, v its velocity, and A is some constant that is dependent on the strength of the magentic field. It follows from this equation that rather than the mass of the particle, it is the particles mass-to-charge ratio (m/z) that is measured. This is a common theme in MS, and although many applications and publications refer to the mass of a species being measured it is important to note that it is in fact the m/z of the species that is obtained.

There is a wide variety of technologies available that enable the m/z of a species to be determined [22]. The work in this thesis solely uses a technique known as time-of-flight mass spectrometry which will be discussed in detail in the following section.

1.1.1 Time-of-Flight Analysers

Time-of-flight mass spectrometry (TOFMS), in its simplest form, is a four stage process [23]. First, a sample of ions is produced at a defined time, t_0, and position, (x_0, y_0), either by some direct ionisation process or otherwise. Second, the ions are accelerated from their original position, for example by a static electric field, E, and in the process they gain

some kinetic energy, qV, where q is the charge of each ion (and is a multiple, z, of the elementary charge, e), and V is the kinetic energy of each ion (in electronvolts). The ions will then reach a final velocity, v_f, that will be described by,

$$v_\mathrm{f} = \sqrt{\frac{2zeV}{m}}. \tag{1.2}$$

In the third step, the ions traverse a field-free flight tube of length, L, and as their velocities are dependent on their m/z, they separate out along the TOF axis. Finally, the ions arrive at the detection assembly of the instrument and their arrival times, t_TOF, are recorded. From equation (1.2) it would be expected that these arrival times should follow:

$$t_\mathrm{TOF} = \frac{L}{\sqrt{2eV}} \cdot \sqrt{\frac{m}{z}}. \tag{1.3}$$

From this it is simple to see that species with a higher m/z will arrive later than those with a low m/z. More specifically, the arrival time is equivalent to the square root of the m/z of a species multiplied by a factor that is entirely dependent on the design and operation of the mass spectrometer. Equation (1.3) can be rearranged to find the dependence of m/z on t_TOF,

$$m/z = \frac{2eVt^2}{L^2}, \tag{1.4}$$

which can be used to convert a TOF spectrum into a mass spectrum. There is no theoretical limit to the range of masses that can be analysed using such a TOFMS system, but each of the four stages in the TOFMS process does come with its practical limitations due to the instrumentation and ionisation processes.

These limitations result in an uncertainty in the arrival time of ions even though they have an identical m/z: rather than each peak appearing at an exact point in the mass spectrum, the peak has some definite width. This uncertainty is quantified, when analysing a mass spectrum, as the mass resolution, $m/\Delta m_{50\%}$. Here m is the centre (or weighted average) of the peak, and $\Delta m_{50\%}$ is the width of the peak — specifically it is the full width at half the maximum (FWHM) of the peak. The qualifying subscript, 50%, is used

to explicitly specify that the width of the peak is being taken as the FWHM although this is generally accepted so that the simpler nomenclature, $m/\Delta m$ will suffice, and this simpler form will be used in the remainder of this thesis. The resolution obtained for a peak in a spectrum is only valid for that given peak (as is clear from the equation) so it is also necessary to qualify a resolution with the m/z (or species) to which it applies.

An approximation to the mass resolution of a spectrum can also be obtained directly from the TOF spectrum. The relationship between the mass resolution and "time resolution" is found by first differentiating equation (1.4),

$$\frac{1}{z}\frac{dm}{dt} = \frac{2eV}{L^2}2t. \tag{1.5}$$

With the approximation that the gradient of the slope defined by this equation does not change with a small deviation (such as that of the width of a peak in the TOF spectrum) from the average value of the peak, then the equation can be written with the peak widths, Δm and Δt,

$$\frac{1}{z}\frac{\Delta m}{\Delta t} \approx \frac{2eV}{L^2}2t. \tag{1.6}$$

The final result is then found by the division of equation (1.4) by equation (1.6):

$$\frac{m}{\Delta m} \approx \frac{t}{2\Delta t}. \tag{1.7}$$

There are many factors that reduce the achievable mass resolution by increasing the uncertainty in ion arrival times. The ion production step requires a precise control over the time that the ionisation occurs. Ionisation techniques will be discussed later in this chapter, but for the analysis of surface samples this is mostly limited to the use of either a laser beam or a beam of primary ions [24–26]. The lasers that are used for these experiments typically have a pulse width of several nanoseconds which instantly adds to the uncertainty in the arrival time of a given species [27]. However, it is important to note that depending on the ionisation mechanism, the spread in the time of production of ions may not match directly to the laser pulse width [28].

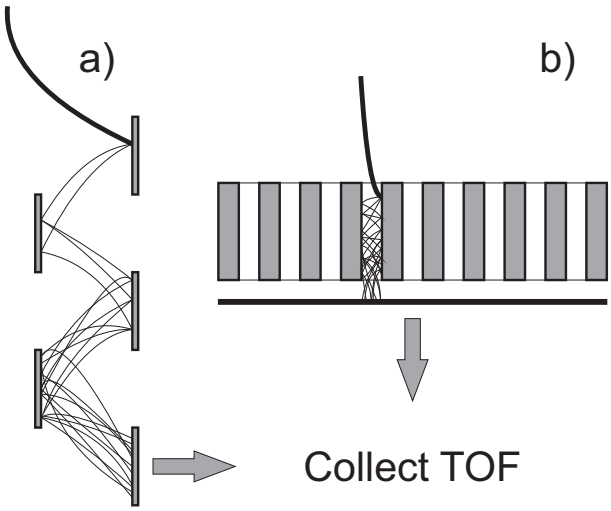

Figure 1.1: *A cartoon representation comparing two different designs of electron multiplier: a) a discrete dynode design; and b) a transmissive microchannel plate (MCP). Both of these designs can either be directly read out using an oscilloscope or the signal can be converted into light using a scintillating screen.*

One of the largest factors contributing to a reduced mass resolution is the spread of initial ion velocities. The derivation above assumes that all ions have no initial kinetic energy which would not be the case. If the acceleration occurs in a uniform field, the total final velocity would be found as the square root of the sum of the squares of the initial velocity, v_i, and the velocity gained from the accelerating field (which was calculated above in equation (1.2)):

$$v_\mathrm{tot} = \sqrt{v_\mathrm{i}^2 + v_\mathrm{f}^2}. \tag{1.8}$$

By increasing the accelerating voltage, the value of v_f will increase, which in turn decreases (relatively) the contribution of v_i to v_tot. The contribution of the initial spread of ion velocities to the resolving power of a TOFMS instrument will be reduced by increasing the accelerating voltage. Although the peak width is decreased, the arrival time of ions will also be decreased so that the same TOF spectrum will be compressed into a much smaller time range. At this point, the precision of the ion detection assembly can become the limiting factor for the instrument's resolving power.

There are a number of different methods for the detection of ions, but they all depend on the principle of amplification of the signal before recording the output [29]. The amplification step is usually achieved through the use of an electron multiplier (or dynode).

Figure 1.1 shows two different designs that result in an amplified electron signal from a single incident ion. Figure 1.1 a) shows a discrete dynode design where an ion impacts on the first "conversion" dynode which emits secondary electrons. These electrons are accelerated towards a further dynode, which is biased towards a more positive voltage, and the electrons from this dynode are then accelerated towards the next, and so on creating a cascade of electron emissions resulting in a signal gain on the order of 10^6. The second design, shown in figure 1.1 b) shows a microchannel plate (MCP). The electrode is created with an array of channels which, when impacted by an ion, emit further electrons. The electron cascade continues through the channel, controlled by a voltage gradient held across the plate, finally resulting in a cloud of electrons exiting at the other end. The resulting electronic signal can then either be directly recorded by reading the current from the final electrode (or a Faraday cup), or it can be converted into light by a scintillating material.

1.2 Imaging Mass Spectrometry

MSI can be performed in two distinct and complementary ways [30]: the microprobe method, shown in figure 1.2 a); and the microscope method, shown in figure 1.2 b). The microprobe method uses the ionising beam to resolve the sample spatially. The beam is focussed down to a spot that defines a small "pixel" on the surface which is then sampled, and a mass spectrum for that position is collected. The position of the beam on the sample is then moved, and the mass spectrum for this next pixel is collected. This process is continued across the area of interest on the sample, with the size of the movement of the beam (as well as the beam spot diameter) defining the spatial resolution of the image. The mass resolution is therefore decoupled from the imaging mechanism as the analyte ions extracted from each spot can be sent to any mass analyser.

Conversely, the microscope method for MSI uses a defocussed ionising beam that ablates analyte from a large area of the sample. The ions produced must then be mass analysed whilst maintaining their spatial resolution [31–34]. This is achieved by using a

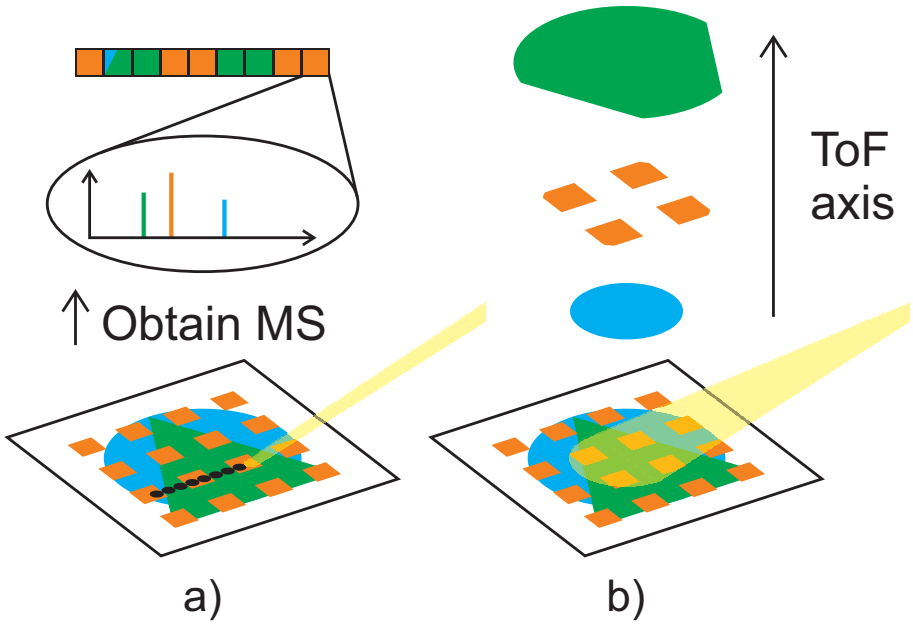

Figure 1.2: *A cartoon comparing the a) microprobe, and b) microscope modes of imaging mass spectrometry. In the microprobe method the ionising beam is focussed down to a small spot which then defines the spatial resolution of the data. A full mass spectrum is acquired for each of these spots (or pixels). In the microscope mode a large portion of the sample is ionised simultaneously and the information on where these ions were produced is conserved whilst they are accelerated towards the detector.*

technique known as "ion imaging".

1.2.1 Ion Imaging

Ion imaging is analogous to optical microscopy in that the trajectories of ions are manipulated by electric fields much like light is focussed using lenses [35, 36]. The spatial distribution of ions on a sample is considered the object. The ions are accelerated and focussed through an assembly of ion lenses which have a certain focal distance, and so the ions form an image on the detector [37]. Just as with optical lens assemblies, depending on the number of ion optic elements, the resultant image may be inverted.

Figure 1.3 illustrates an ion optic assembly focussing ion trajectories from two different locations into an inverted and magnified image. The focussing is achieved independently of the initial ion velocities (represented by the direction of the arrows). The spatial mapping of the ions is therefore decoupled from the method of ionisation as it is not the ionising beam that now defines the resolution; instead, the quality of the focussing done by the

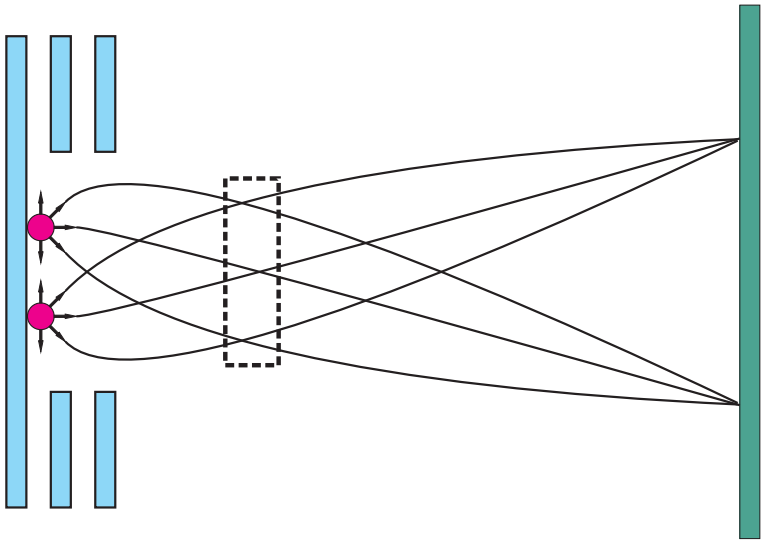

Figure 1.3: *A cartoon representation of ion trajectories from two different positions coming to a spatial focus. The trajectories are comprised of ions with different velocities which are mapped within the region marked by the dashed box. The image is both inverted and magnified.*

ion optics defines the quality of the mapping.

The dashed box in figure 1.3 marks out the region across which ions with the same velocity are focussed to the same distance from the TOF axis. This region is known as the velocity-mapping focal plane (analogous to the back-focal plane in optical microscopy). Here, ions with a high transverse velocity are mapped further from the TOF axis than those with a low transverse velocity component. Overlapping this region with the ion detector it is possible to obtain images of the velocity distribution of ions which can be used to map the dynamics of reactions and collisions of gaseous species [38, 39].

Similarly, by the appropriate placement of a contrast aperture at the back focal plane of the ion optics, a range of ion trajectories may be selected. This allows for either only ions with a low transverse velocity to be permitted, or even for dark-field ion microscopy [40].

1.2.2 Increased Mass Resolution in Microscope Mode

Although the spatial resolution of the instrument is decoupled from the ionising beam spot size, the methods available to increase the mass resolution of an obtained spectrum are more restricted. This is because the ion trajectories need to be controlled in order to

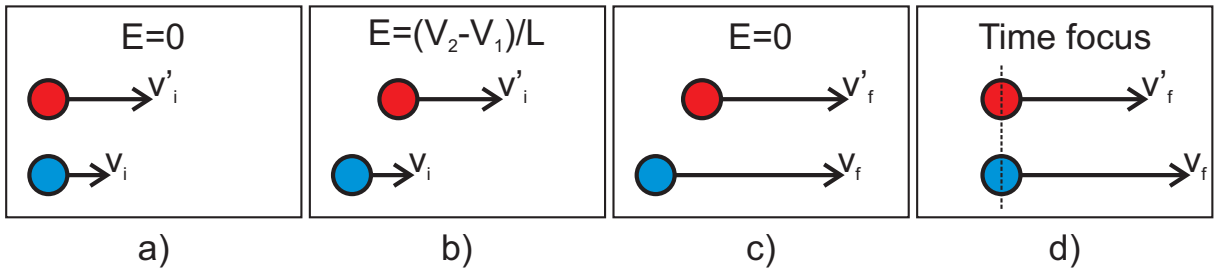

Figure 1.4: *Four panels showing the steps involved in the delayed extraction pulsing regime. This technique is used to compensate for the spread in the initial velocities of ions produced in a TOFMS source.*

retain the spatial resolution. Nonetheless, it is possible to improve the resolving power of a microscope imaging instrument with only a modest reduction in the spatial resolution.

Delayed Extraction

Delayed extraction (DE) is a technique that compensates for the difference in the initial velocities of ions in TOFMS [41–43]. Figure 1.4 shows the process of the technique. In panel a), there is no extraction field. The two ions shown in this panel have different initial velocities where $v_i' > v_i$. In panel b) the faster ion has covered more ground than the slower one, and so has traversed further through the extraction region of the ion optics. It is at this point that the extraction field is applied. As the faster ion has traversed further through the extraction region it is subjected to less of an increase in velocity. In panel c) the ion that was initially slower has gained such kinetic energy that it is now faster than the other ion. The two ions are now in the field free drift tube, and as they reach the detector the ion that has originally been slower catches up with the other ion forming a time focus, as shown in panel d).

This technique can be used in conjunction with microscope mode MSI. However, as the cloud of ions expands during the field-free period before the extraction field is employed, spatial resolution is lost. Not only do the ions spread out along the TOF axis but they also drift laterally obfuscating their original position. Furthermore, the time focussing is mass dependent: only a specific m/z range is fully time focussed, ions outside of this range are only partially focussed. By changing the delay time, the range can be moved

to higher masses by increasing the delay time, but with microscope MSI there is a limit to how long the delay time can be before the lateral spread of ions completely blurs the obtainable spatial resolution.

Post Extraction Differential Acceleration

The lateral spread of ions experienced with the delayed extraction of higher mass species limits the use of the technique for microscope MSI. This can be overcome by using a modified version of the delay pulsing technique: post extraction differential acceleration (PEDA) [44]. With this technique, the ions are immediately extracted after they have been ionised. The ions pass out of the extraction region and into the next part of the ion optic assembly. In this second region, the strength of the electric field is increased. This leads to a similar disparity in the transfer of electric potential energy to the kinetic energy of the ions as with the DE technique: those ions that had a larger initial velocity will have travelled further through this section of the ion optics, so that when the field is increased they gain less kinetic energy. In much the same way as with DE, the ions form a time focus which can then be made to coincide with the detector.

As the ions are immediately extracted, they do not suffer from spatial blurring due to their lateral motion; however, there is still a dependence on the mass of the ions being focussed. The range of ions that are time focussed is less with PEDA than with DE; however, the technique can be extended without the same repercussions. A velocity correction to the PEDA technique (VCPEDA) has been shown and allows the retuning of the mass range of the PEDA technique without any loss in the spatial or mass resolutions [45]. This technique is presented and explained thoroughly in the DPhil thesis of Benjamin Winter [46].

1.2.3 Non-linear Imaging Geometries

Although the simplest method of maintaining the spatial resolution of an image is using a linear TOF geometry, it is also possible to maintain a stigmatic image through various non-linear ion optic components. A reflectron is a mirror which acts to reverse the direction of

motion (or at least one component of the motion) of charged particles [47, 48]. It consists of a potential wall that is set so that no ion should be able to fully scale it. Ions with a higher kinetic energy will penetrate further into the potential and in doing so will take a longer time to turn about. If the reflectron is designed correctly, the extra time that the faster ion spends within the ion mirror should compensate exactly for the extra time that the slower ion takes to traverse the field free regions (those between the extraction optics and the reflectron, and the detector and the reflectron).

Such a design has been shown to successfully conserve a velocity-mapped image through a reflectron [49–51]. Designs for the use of reflectrons in stigmatic imaging have also been filed [52, 53]; but, despite the resurgence of MSI, there is little current research into their use. As with the electrode voltage pulsing regimes for linear TOFMS, it would be expected that the use of a reflectron will impose a limit on the mass range of a microscope MSI instrument.

Another system used to increase the mass resolving power for non-linear TOFMS is the use of sector analysers. Sector analysers use either magnetic or electric fields to control the trajectories of ions according to their momentum or kinetic energy respectively [54]. These sectors can be used to transfer an ion image, and have been used in conjunction to that effect in one of the earliest commercial ion microscopes: the CAMECA IMS-3f [55].

Electrostatic analysers (ESAs) are currently favoured for research applications of the microscope method of MSI. Ron Heeren (FOM-AMOLF [56]) has used a triple focussing time-of-flight (TRIFT) instrument for numerous applications [57–59]. The TRIFT is composed of three consecutive 90° ESAs which turn the ion trajectories by a total of 270°. This system allows for an impressive spatial resolution of 4 μm [18].

The MULTUM II is another system using ESAs to transfer a stigmatic ion image [60–62]. It is comprised of four ESAs which each turn an incoming ion beam by 157.1°. The sectors are arranged so that ions travel in a "figure of eight" pattern. This trajectory can therefore be cycled, theoretically giving a limitless flight tube length, although in practice the spatial resolution obtained with the instrument reduces with repeated cycles [61].

1.3 Detector Technology

Stigmatic ion microscopy also increases the burden on the detector technology used as the detection assembly must be spatially sensitive. A chevron stack of MCPs is used, where two plates are mounted consecutively so that the pores in each align, and the bias angle of these pores is offset between them. The amplified signal produced by this assembly can then be obtained either by a device within the vacuum (such as a delay line detector — DLD), or the signal can be transferred *ex vacuo* using a scintillating screen and a camera.

A DLD consists of a length of electrical conductor wire attached at each end to a signal time recorder such as a time-to-digital converter (TDC). Incident charge, such as a cloud of electrons produced by an MCP, propagates along the conducting wire in both directions and the time of arrival of this signal at each end of the wire is noted. The difference in the signal times between the two ends of the wire can then be used to calculate at what point along the line the charge originated [63–66]. By contorting the conducting wire into a serpentine pattern the DLD can be made to cover a two dimensional area and this can be made to match the output of an MCP stack.

Such a simple DLD can only resolve a single ion event at a given time. A hexanode DLD has been developed to overcome this and allow for much higher count rates, although they are still limited so that ions arriving within approximately 10 ns of one another, and within 1 mm on the detector cannot be resolved [67]. These DLDs have been used in various applications of ion microscopy with observed spatial resolutions of only a few microns [68–70]. The timing resolution of these detectors is incredibly fast at around a few hundred picoseconds [68].

By positioning a scintillating screen behind the MCP stack the electron cloud can be converted into light which can then be collected by a camera. In this implementation the screen will be positively biased from the output face of the MCP stack so that emitted electrons are accelerated towards it. Different materials will scintilate at different wavelengths, and with different response times [71]; although, there is a general trend for brighter (more efficient) screens to have a slower response.

There are many cameras (mostly consisting of a charge coupled device — CCD) that

can be used to record the image illuminated on such a scintillating screen with the main criterion being that the overall detection system needs to have sufficient precision to distinguish between consecutive peaks in the TOF spectrum. This is usually achieved by gating one of either the MCP stack or the exposure time of the camera itself. If the MCP is gated then it is the gain voltages applied across one of the plates that is adjusted. With a reduced gain, no image is seen, but when the gain is reapplied, the image appears. The speed at which this can be done is dependent on the switching technology, but it is possible to pulse MCPs faster than 10 ns [72]. The intensified CCD cameras that are used with MCP-scintillator detectors also have an inbuilt MCP (which acts as the intensifier). These can therefore also be gated to a similar precision of a few nanoseconds.

These solutions only allow a single image to be acquired for each duty cycle of an experiment. With the microscope method MSI many different ions will be produced that correspond to different species with different m/z. A single frame camera has to be set to a specific m/z range. There are some framing cameras that can record multiple images for a single experimental cycle, but these still have to be preprogrammed and the number of frames is still limited [73–75].

1.3.1 Pixel Cameras

Whereas DLDs are limited in the number of particles that can be detected simultaneously, and framing cameras need to be preprogrammed and can only record a small number of images, there is a new generation of cameras that can be used to acquire ion images for many different m/z at high count rates. Two of these cameras, both of which are based on complementary metal-oxide-silicon (CMOS) technology, are the Timepix sensor, and the PImMS sensor [76–78]. Both of these sensors have levels of logic built into each pixel which allow them to function independently of their neighbours. These are time-stamping sensors that record the time that an event occurs so that at the end of the acquisition cycle time codes and positions can be read out and stored. As each pixel has inbuilt logic, there is no need to define an exposure time as each pixel will record the time of an event relative to some external sync trigger; and as the pixels run independently of one another

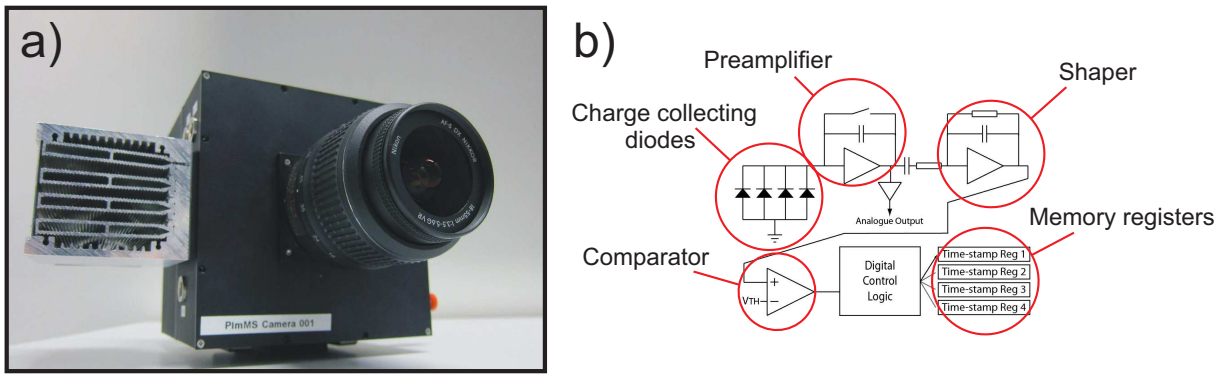

Figure 1.5: *a) the PImMS camera, and b) an overview of the pixel logic contained within each pixel of the PImMS sensor.*

they can record events that occur at different times allowing multiple peaks in a TOF spectrum to be simultaneously recorded.

The Timepix sensor is an implementation of the Medipix sensor designed for use with TOFMS and mounted inside a vacuum chamber directly behind the MCP stack. It has been used in conjunction with numerous experiments including a velocity-map instrument [79], a TRIFT ion microscope [80–84], and neutron detection [85]. It has also been used with commercial quadrupole mass spectrometers to improve the efficiency and resolution, and similarly with a linear MALDI TOFMS instrument as a diagnostic tool [86–88].

The Timepix sensor currently has a timing precision of 10 ns, and is usually employed in an array of four chips giving a pixel count of 512×512. The sensor can currently record the time of a single event in each pixel, but there is a new generation of the Timepix sensor currently in development: Timepix3 [89]. This new version of the sensor has an improved timing precision of 1.6 ns. The sensor can also be continuously read so that there is no need to wait until the end of the acquisition cycle before transferring pixel event data.

The PImMS sensor is, in many ways, similar to the Timepix sensor; although, it also has some crucial differences. The most marked difference is that the PImMS sensor is used as a camera (shown in figure 1.5 a)) and so is designed for use at atmosphere outside of the vacuum chamber; whereas the Timepix sensor is (currently) used in-vacuum to directly detect electrons. The PImMS camera therefore requires a scintillating screen to be used to convert the electron cloud, produced by the MCP stack, into light. The PImMS sensor

uses the INMAPS production technique to increase the density of logic that can be located within each $70\,\mu$m $\times 70\,\mu$m pixel [90, 91]. Figure 1.5 b) details an overview of this logic. Light is collected in four photodiodes, which are equally spaced within the pixel, and is converted to a signal. This signal is then amplified before entering a shaper which converts the integrated increase in charge into two different pulses. The comparator then compares these pulses against two reference threshold levels in order to ascertain whether an event has been acquired. When an event has been triggered the time of that event is stored in one of four 12-bit memory registers.

The multiple memory registers allow for multiple time codes to be stored before the sensor needs to transfer the data. The 12-bit time code gives a dynamic range of 4095. The camera can currently be run at a maximum of 80 MHz which corresponds to a timing precision of 12.5 ns and a total acquisition time of $51\,\mu$s [92, 93]. Once an event has been recorded, there is a deadtime within the pixel of several hundred nanoseconds whilst the pixel resets. During this time no further events will be recorded within that pixel but all the remaining pixels will still function normally. There are also methods available to compensate for the loss of signal due to this dead time [94, 95].

1.4 Ionisation Methods

The method of ionisation within a mass spectrometer largely impacts the quality of the resulting spectrum, affecting the kinetic spread of any successfully ablated ions, as well as the level of charge and degree of fragmentation that they undergo. Further, the chosen technique can also limit the type of sample that can analysed, restricting whether the sample must be gaseous or solid, or stable in a vacuum.

The earliest technique was that of electron ionisation (EI), also referred to as electron impact ionisation [96–98]. This technique requires a volatile sample that can be introduced into a vacuum chamber which will contain some sort of filament from which a discharge of electrons is produced. The electrons are accelerated towards an anode, colliding with the sample gas, causing the ionisation. Resultant analyte ions, produced by EI, are subject

to extensive fragmentation which leads to far more cluttered spectra.

For a stigmatic imaging instrument, such gas-phase ionisation techniques are not applicable. The desire to analyse a spatially resolved surface sample rules out the use of EI and other techniques, such as chemical ionisation (CI) [99, 100], and field ionisation (FI) [101], that require a gaseous sample. Field desorption (FD) is an extension of FI applicable to surface samples [102]; although, the technique requires a specific surface in order to generate the high electrostatic fields needed for the desorption and ionisation.

Perhaps the simplest surface ionisation technique employs direct irradiation with a laser. The technique evolved from spectroscopic methods, turning into a spectrometric one enabling the elemental analysis of metals [103], and in turn organic compounds [104, 105].

1.4.1 Matrix Assisted LDI

Laser desorption is an attractive technique for surface analysis as the probing beam can be easily adapted (in terms of size, and fluence) to suit a given application. However, the wavelength of the laser must be matched to produce ions for any given sample [106, 107], except for with the use of infrared (IR) LDI which can ablate a range of molecules but also induces fragmentation [108].

In the work by Karas, studying the dependence of LDI on wavelength, it was noted that the threshold irradiance needed to observe alanine was reduced in the presence of tryptophan to a value one tenth that needed for alanine alone [106]. It was suggested that although the alanine did not efficiently absorb the laser irradiation, the tryptophan did, and so resulted in the ablation of both species at the lower fluence. This phenomenon, termed "matrix assisted" LDI (MALDI), was soon shown to be applicable to further non-absorbing compounds and also to large species (10 kDa) [109, 110].

With the MALDI mechanism, a matrix and laser system are chosen so that the absorption spectrum of the former coincides with the output wavelength of the latter [111, 112]. There is then no longer a requirement for the ionisation system to be adjusted for a different choice of analyte. Furthermore, as it is the matrix, rather than the analyte, that absorbs the incident light there is very little analyte fragmentation: the matrix acts as a

shield.

Although MALDI is often heralded as a "universal" ionisation technique there are still many factors that need to be kept in mind once a matrix / laser pair has been chosen. The laser fluence, beam spot size, and the laser pulse length all impact on the quality of an obtained spectrum [113–116]. Furthermore, there is still a search for yet more species that can be used as matrices that might be more robust to different applications [117,118].

The underlying ionisation mechanism is still a topic of debate. Initially, the mechanism was assumed to involve some level of energy pooling through which matrix molecules could be ionised before next transferring a proton to the analyte [119–124]. More recently, a new model has been proposed: the so-called "lucky survivor" model [125, 126].

The lucky survivor model assumes that analyte ions are formed within the solid solution of the matrix on the surface of the sample, before the desorption step has occurred. The laser then causes clusters of molecules to be ablated, some of which will encase these pre-ionised analyte molecules. Throughout the plume expansion, the matrix molecules evaporate from the cluster, leaving only the ionised analyte.

Although these models attempt to explain the desorption and ionisation steps of the MALDI process, a thorough study into the dynamics of the process has not been undertaken. A number of smaller studies have been attempted that measure the supersonic expansion of the MALDI plume [127], and the speed or angular distribution of the analyte ions [128–131]. These studies do give contradictory results so there is still a great need for a more in-depth study into the plume dynamics that could then be used to validate or disprove some of the current models.

1.4.2 Secondary Ion Mass Spectrometry

Another, popular, ionisation technique used with surface samples is secondary ion mass spectrometry (SIMS) [132]. Here a primary beam of ions is directed at the surface of the sample with a kinetic energy of several thousand eV. This energy is transferred to the sample through a "cascade" of collisions resulting, initially, from the primary ion and the molecules within the surface, and then subsequently, between these recoiling molecules

and further stationary particles in their vicinity. Any molecule near the surface of the sample that is transferred sufficient energy to overcome its binding energy with the bulk is then ejected [133].

SIMS analysis can be performed in two different manners. "Static" SIMS uses a low-current primary ion beam in order to limit the damage dealt to the sample [134]. This results in the emission of neutrals and ions preferentially from the top layer of the sample. Conversely, "dynamic" SIMS uses high beam currents to drill down through a sample.

There are many different species that are used in the primary ion beam for SIMS [26]. These include smaller ions such as Cs^+, Ga^+, and Ar^+ [135–137], as well as larger molecules and clusters such as ${Au_n}^+$, and ${C_{60}}^+$ [138,139]. These different species interact in different ways with the target sample [140]. The smaller ions are more penetrating, leaving a cylindrical trail of particles with imparted momentum. The larger molecules and clusters fall apart on contact with the surface of the sample imparting their energy to the species at this level leading to a more efficient transfer of momentum to particles which can then escape the surface.

1.5 Outline of This Thesis

The work in this thesis succeeds that presented in the DPhil thesis of Wei Hao Yuen who began the investigation into converting a conventional velocity-map imaging instrument for spatial imaging [74, 141]. This work also introduced some of the first experimentally obtained spectra using the PImMS1 camera [78, 141, 142].

The work that will be presented outlines the development of a stigmatic imaging microscope that uses the PImMS1 camera for multi-mass imaging, and was conducted in parallel with further, complementary, developments in ion imaging and detector technologies that are presented in the DPhil thesis of Benjamin Winter [46].

In the next chapter there will be an overview of some of the experimental methodologies and the instrumentation used to obtain mass resolved ion images. This will be followed by an overview of the simulation techniques that are used to facilitate the development of this

instrumentation. There will then be two chapters featuring the bulk of the experimental data that features in this thesis. The first of these chapters will present a characterisation of a modified velocity-map imaging instrument alongside simulations, and will show some of the first multi-mass MSI experiments conducted that use the PImMS1 camera. The second of these experimental chapters will focus on the development of an instrument using the PImMS1 camera that can achieve higher resolutions than the simple VMI instrument. There will then be a chapter that discusses a model for the fitting of event clusters within a PImMS data set and shows the advantages that might be gained by applying this model. Finally, there will be a chapter which presents designs for a possible primary ion source for the development of a SIMS ion microscope.

Chapter 2

Experimental Methods

The requirements necessary for microscope-mode MSI are quite different to those of both conventional MS instruments, and ion imaging experiments. A compromise has to be found between these two instruments that offers both an acceptable mass and spatial resolution, across a wide mass range.

In this chapter the experimental methods and considerations applied in the testing of the PImMS1 camera with microscope-mode MSI will be described. First, two converted instruments: a velocity-mapped ion imaging instrument, and a commercial mass spectrometer, will be detailed. Their similarities and differences will be discussed specifically in relation to their operation. There will also be a description of the sample preparation methods employed to create the test patterns that are used to evaluate the systems.

There was also a further instrument designed specifically for the analysis of surface samples. This instrument was optimised to be used with the velocity-corrected post extraction differential acceleration technique outlined in the previous chapter, and is described in detail in the thesis of Benjamin Winter [46].

2.1 Modifications to the VMI Experiment

The first imaging mass spectrometer developed in the Brouard group laboratory was adapted from a velocity-map ion imaging instrument [143]. This instrument was built in-house for experiments with conventional framing cameras, and was further used with

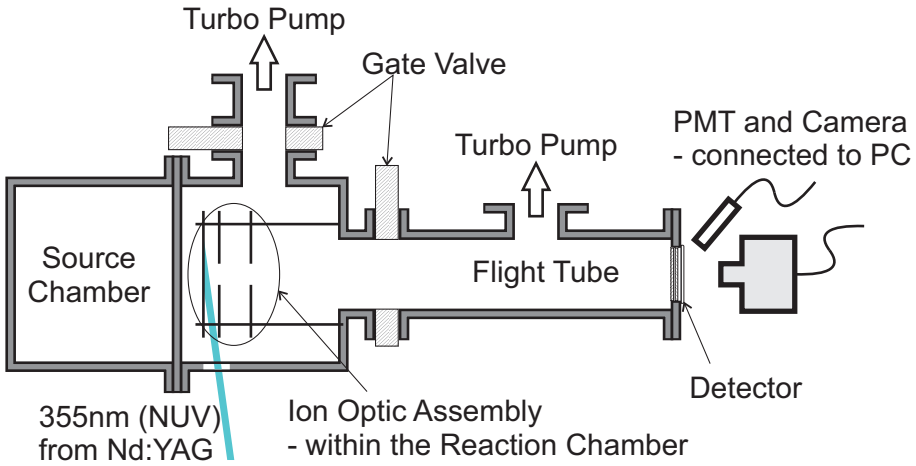

Figure 2.1: *A schematic of the modified imaging instrument. The path of the laser, the ion optics, the flight tube, and the ion detection system are all detailed. The schematic is not to scale.*

the DALSA camera (a fast-framing CCD camera capable of storing multiple ion images within an inbuilt shift register) [73]. The instrument was modified so that, with only minor changes, it could be switched between either analysing surface samples or investigating the reactions of gas phase species [74, 144]. It is formed of four distinct parts: the source chamber, the reaction chamber (housing the ion optics), a flight tube, and a detector. As the source chamber is solely used to introduce a collimated molecular beam into the ion optics, it is not needed for the analysis of surface samples, so this whole section can be separated by a blank vacuum flange. This also has the advantage of greatly reducing the time taken to pump the instrument down to vacuum from atmosphere. The ion optics are mounted on four threaded stainless-steel rods which screw into the flange separating the flight tube and the reaction chamber (see figure 2.1). The ion optics can be exchanged to suit different experiments. In general, for surface analysis, the first electrode is a solid stainless-steel plate, in contrast to its former design used in molecular beam experiments, which has an aperture at its centre through which the molecular beam passes before it intersects the laser beam.

2.1.1 The Laser

When the instrument is converted for surface analysis, a sample is mounted in the first electrode, which is then irradiated with the 355 nm (third harmonic) of an Nd:YAG laser (Continuum Powerlite 8010). The laser fires at a repetition rate of 10 Hz, limiting the full experimental repetition rate, and the temporal width of the pulse is between 3–7 ns. The laser beam is asymmetrically defocused such that the vertical divergence of the beam was greater than the horizontal divergence. As can be seen in figure 2.1, the laser beam enters the vacuum chamber through a fused silica window and approaches the sample plate at a low angle of incidence ($\approx 10^\circ$ from the surface). This angle has the effect of spreading the laser profile horizontally across the surface so that, when combined with the vertical divergence from the cylindrical lens, the beam is spread across the whole of the surface of the sample. The laser power is controlled by varying the delay between the external triggers for the laser flash lamps and the Q-switch, up to a maximum pulse energy of 350 mJ. The laser power is then further attenuated by passing the beam through two 50% beam splitters. This attenuation is necessary, as the shot-to-shot variation in the laser pulse energy is smallest when the laser is used at it highest power; however, this power is far too high for most applications, so the attenuation allows the laser to be run at its most stable, whilst still producing a practical output power. For a sample diameter of 5 mm the theoretical maximum fluence is approximately 100 mJ/cm^2; although, in practice a fluence closer to 45 mJ/cm^2 is used.

2.1.2 The Ion Optics

For both surface samples, and for molecular beam experiments, the ion optic assembly consists of three electrode plates. As already described, for surface analysis the first plate (commonly referred to as the "repeller") is made of stainless steel. It was manufactured 93 mm in diameter and had to be 2 mm thick so that a 25 mm × 25 mm recess could be created to a depth of 1.1 mm. This recess was added so that a surface sample, mounted on an indium tin oxide (ITO) coated glass slide, could be inserted into the plate. The ITO coating on the slide allows a voltage to be applied to the surface. To ensure that a

connection is made between the steel plate and the slide, a short single strand of conducting wire is attached across the both of them, secured by Kapton tape.

The second and third electrode plates (commonly referred to as the "extractor" and "grounded" plates respectively) are identical to one another, also being made of stainless steel. They too have a diameter of 93 mm, but are only 1 mm thick, and both have an aperture at their centres, 20 mm in diameter. The electrodes are separated from one another using ceramic (Makor) spacers which fit on the threaded mounting rods. The distance between the extractor and the repeller is 14 mm, and the distance between the grounded plate and the extractor is 21 mm. The ion optics are situated in the reaction chamber, which is also made of stainless steel and is pumped by a turbomolecular pump (Pfeiffer, Vacuum TMH-521P), which is in turn backed by a rotary pump (Leybold, Trivac D40V). The chamber pressure is monitored with a hot-filament ion gauge (T-100K, Duniway Stockroom Corp.) and is operated at a pressure of approximately 1×10^{-7} mbar.

The flight tube is separated from the reaction chamber by a mechanical gate valve, allowing the two sections to be isolated from one another, so that the flight tube (and detector) can remain under vacuum whilst adjustments are made to the reaction chamber. The flight tube is pumped by a separate turbomolecular pump (Pfeiffer, Vacuum TMU 071P [145]), which is backed by the same rotary pump as that on the reaction chamber. An active inverted magnetron ion gauge (AIM, Edwards [146]) is used to monitor the pressure in the flight tube, which is of a similar order to that in the reaction chamber. The full flight path of the ions from the sample surface in the ion optic assembly to the detector at the end of the flight tube is 615 mm.

2.1.3 The Detector

The detector assembly consists of a chevron pair of microchannel plates (MCPs) and a scintillating screen (Photonis — formerly Burle [147, 148]). The MCPs are imaging grade, referring to the quality control over the pores, and have an active diameter of 75 mm. Each channel (or pore) is 25 μm across, with a pitch of 32 μm, and a bias angle of 8°. The open area ratio of the MCPs is therefore 45%. The input face of the output MCP has a gold

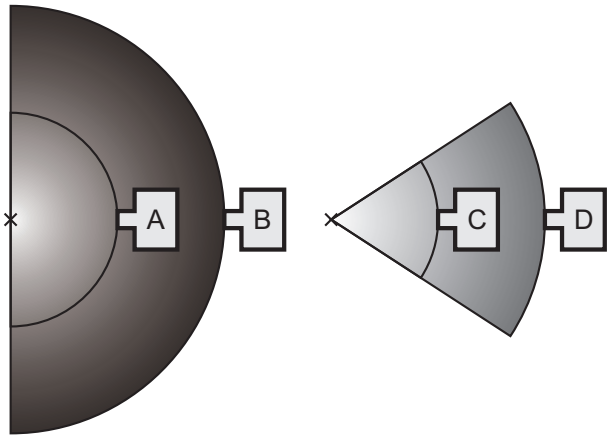

Figure 2.2: *A cartoon, two dimensional, representation of the difference between a camera viewing a point light source, or one that is collimated. The schematic on the left supposes that photons are released in all directions over a full 2π hemispherical surface, whereas that on the right is of a directed photon release comparable to what might happen with a fibre optic bundle.*

coating which allows a voltage to be applied quickly so that the detector may be pulsed on or off. There is a gap of 1 mm between the two MCPs, and they are aligned so that the channels between them match, increasing the obtainable gain. Each individual MCP can withstand a potential difference between its back and front face of 1.25 kV. The two middle faces (that is the output face of the input MCP, and the input face of the output MCP) are generally held at a voltage which is half that of the output face of the output MCP; however, the voltage applied to each face is controlled separately so this does not have to be the case.

The scintillating screen is a P47 phosphor (Y_2SiO_5:Ce) coated onto a fibre optic bundle, which is mounted 3 mm behind the output MCP. A voltage is applied to the screen which can be as high as 5 kV relative to the output face of the output MCP. The fibre optic bundle directs light along the normal from the surface, rather than allowing the light from a scintillation event to spread out in a full 2π hemispherical distribution. This is an important distinction to make (see figure 2.2). The physical size of the camera lens is constant (the cross sectional area, a) but depending on the distance of the camera from the source, d, the fraction of emitted light that is captured by the camera will change. For

an unfocussed 2π hemispherical distribution the fraction of light captured will be,

$$\frac{a}{2\pi d^2}, \tag{2.1}$$

whereas if the light has some directionality (for example, the photons produced may have a restricted maximum angle of emittance from the normal, θ), the fraction captured will be higher:

$$\frac{a}{2\pi\left[1-\cos\left(2\theta\right)\right]d^2}. \tag{2.2}$$

This is a simplification of the case where a fibre optic bundle is used. An optical fibre has an upper limit to the emission (and acceptance) angle known as the critical angle. This restricts the angles over which light can be emitted (known as a numerical aperture, NA). The result of this is a dramatic increase in the intensity of light observable by the camera. This is especially important when using an unintensified camera (such as the PImMS1 camera), the performance of which is dependent on incident light levels.

2.1.4 The Cameras

The light emitted from the scintillating screen is converted into a signal by using a photo-multiplier tube (PMT), giving time resolved intensity information, and a camera, giving positional information.

Two different cameras can be used: a conventional intensified CCD camera (Photonic Science), and the PImMS1 camera. The CCD camera converts incident light into a charge collected in each pixel, giving a map of the intensity. By gating the intensifier, the resulting image can be restricted to give only the positional information of a single ion species. The intensifier can be gated down to a width of a few hundred nanoseconds. The camera itself has a resolution of 768×576 pixels. It is fixed in a frame that is attached to three threaded stainless-steel rods, which are screwed into the vacuum flange of the detector housing and has to be positioned between 150 mm to 200 mm from the screen in order to focus on the whole of the detector screen. The camera is shrouded in a curtain to cut out all ambient light, which both gives a greater contrast between the flashes on the detector screen, and

also reduced the wear and damage to the intensifier which occurs at ambient light levels.

The PImMS1 camera has a relatively lower resolution of 72×72 pixels, although each pixel also records the timing information of an observed event. An internal clock counts the time passed after the camera is initially triggered. This clock currently has a base frequency of 80 MHz corresponding to a time precision of 12.5 ns. Each pixel has four 12-bit memory registers which can hold the time-stamp of observed events. This gives a maximum value of 4095, which means that at a time precision of 12.5 ns, the camera can record a time-of-flight spectrum for just over 51 μs. The PImMS1 camera is mounted on a table behind the instrument. It has a cooling unit which maintains the sensor's temperature at 25°C and a supply of dry nitrogen gas is constantly flushed through the camera box to avoid condensation. A c-mount camera lens (Navitar DO-5095) is used to maximise the light collection. The lens has to be positioned over 600 mm from the detector and a smaller area of the scintillating screen is focussed on. As with the CCD camera, a curtain is used to reduce the ambient light, although this is only done to increase the contrast as the PImMS1 camera does not have an intensifier tube.

The PMT can be used in conjunction with both of the previously described cameras. It is necessary in conjunction with the CCD camera to give time-of-flight information, and is useful with the PImMS1 camera, as it gives a second spectrum for comparison. The PMT is enclosed in a light-tight box with a liquid light guide (LLG) attached at one end. As with the cameras, the PMT must be shielded from ambient light when in use.

The data from both of the cameras, and the PMT, are collected on a computer, and then analysed. The data obtained with the CCD camera are analysed on the fly: each frame, that is each ion image resulting from one experimental duty cycle, has a threshold applied, and can then be centroided. These processed frames are then summed together to give a final output.

The data obtained using the PImMS1 camera are saved directly to disk. Only events where a pixel has gone over a specified threshold are saved, and these are formatted as: pixel x-coordinate, pixel y-coordinate, time-of-flight, duty cycle number, and register in which the time-stamp was stored. These data can then be further analysed at a later date

using a number of different post-processing methods which will be outlined in chapter 6.

Finally, the data obtained using the PMT are simply averaged over a number of duty cycles and saved as a comma separated list. These data are primarily used to calibrate the timing of the CCD camera intensifier gate, and as a comparison for the time-of-flight spectra obtained using the PImMS1 camera.

2.2 Modifications to the LT2 Plus

The LT2 Plus is a model of linear, time-of-flight, mass spectrometers, designed to be used for the analysis of MALDI MS samples. It is produced by Scientific Analysis Instruments Limited (SAI [149]). An automated sample exchange system allows the sample plate to be swapped without having to bring the entire instrument up to atmosphere. The sample plates are a standard 96 well design, allowing for multiple samples to be loaded simultaneously. "Thrust tubes" (three-phase electric motors, wound around a magnetic rod) are used to adjust the position of the sample plate, and these are controlled by an optical encoder system. A computer interface is used to select each well and display the collected mass spectra.

Being a commercial product, the LT2 Plus is designed to be simple to use; however, this also means that control over some of the parameters is hidden. Controls over detector voltages, for example, are altered by adjusting a small potentiometer control on the rear of the instrument, on one of many DAC (digital-to-analogue converter) boards. To this end, in order to have full control over all of the various experimental parameters, the coverings of the instrument had to be removed (see figure 2.3).

The entire instrument can fit on a table top, with a footprint of $52\,\text{cm} \times 83\,\text{cm}$. The height of the instrument is 130 cm, which is predominantly determined by the field-free time-of-flight tube ($\approx$1 m long). A single turbomolecular pump backed by a diaphragm pump achieves a chamber pressure of $10^{-7} - 10^{-6}$ mbar. In order to avoid breaking the vacuum whenever a sample is exchanged, the sample block can be retracted from the ion optics and a seal is formed around the sample plate. This small exchange region can then

Figure 2.3: *Images showing the LT2 Plus with its commercial covering (left), and after it has been stripped down.*

be brought to atmospheric pressure and the sample replaced. The exchange region is then evacuated to a rough vacuum by the diaphragm (backing) pump before the seal is broken and the pressure is left to equilibrate. The sample can then be positioned back within the ion optics. The whole process can take as little as five minutes.

The LT2 Plus uses a small N_2 laser (SRS NL100), which is coupled into a 1.5 m long optical fibre with a core diameter of 200 μm (Schaefter + Kirchoff [150]), and subsequently is coupled to the vacuum chamber via a focussing lens. The laser can operate at a repetition rate of 20 Hz producing light at 337 nm with a pulse width of $<$ 3.5 ns (FWHM) and an average power of 3.4 mW. The actual power incident on the sample will differ from that produced by the laser as there are losses due to the imperfect coupling of light into, and out of, the fibre. At the interface of the vacuum chamber, the light is coupled into a lens assembly built into the main body of the chamber, which focusses the light from the fibre onto the sample, passing through one of four symmetrically positioned holes within the extractor electrode of the ion optics. On the sample, the laser forms a spot with a diameter of roughly 200 μm.

As described above, the sample stage translates in order to choose different samples on the sample plate. The movement of the stage is controlled by piezoelectric motors which allow for high precision adjustments. A "webcam" gives a live video of the sample which is positioned at the centre of the instrument (directly on the time-of-flight axis): this is the sample that will be most effectively focussed onto the ion detector. This "webcam" image is obtained by focussing the camera with a lens and mirror assembly through another one of the four symmetrically positioned holes surrounding the main aperture in the extractor electrode of the ion optics. A small LED is used to illuminate the sample.

The ion optic assembly itself consists of five electrodes which form an extraction region followed by a pseudo-Einzel lens: it is only referred to as a pseudo-Einzel lens here, as the fields either side are not equal, so the lens itself is asymmetric (due to its environment) despite the symmetric voltages applied to it. A delayed extraction pulsing regime is used to increase the obtainable mass resolution (specified as > 2500 FWHM) over the 1 m flight tube. The synchronisation of the electrode pulsing with the firing time of the laser beam is achieved by the internal electronics of the LT2 Plus. A delay is set via the computer software, which is communicated to the DAC board in the LT2 Plus. A beam splitter directs a small portion of the beam to a photodiode, which is monitored by a DAC board and the pulse delay is triggered from that signal.

At the end of the flight tube there is an electron multiplier (ETP), which provides a fast readout mechanism that amplifies incident ion signal with a precision of approximately 2 ns. The electron multiplier is only capable of registering timing information, not spatial information. The signal is acquired by an analogue-to-digital converter board housed within the LT2 Plus frame, which then transfers the information to a computer via a USB interface.

In order to use the LT2 Plus for microscope-mode MSI, a number of modifications were necessary to the hardware. These consisted of adjustments to: the laser focussing; the ion optic pulsing regime and voltages; the detector; and therefore, the data acquisition and analysis.

2.2.1 The Laser

Microscope-mode MSI has unique requirements on the laser power and profile in order to achieve the best results. For MALDI microprobe-mode MSI, the fluence of the laser on the surface needs to be held constant, just above the threshold level necessary to produce ion signal. The profile of the beam is also important, in as much as hot-spots in the profile will cause a reduced mass resolution, as they induce a wider velocity distribution in the nascent ions [151]. The spatial resolution in microprobe-mode analysis is directly coupled to the size of the laser beam spot: a smaller spot gives a more precise location for the acquired mass spectrum. Conversely, with microscope-mode analysis, the spatial resolution is decoupled from the spot size and instead, is solely dependent on the resolution of the ion optics; however, the quality, and quantitative reliability of a microscope-mode acquisition are both dependent on the uniformity of the beam profile.

Initial ion images obtained using the LT2 Plus were dominated by ring structures. Figure 2.4 a) shows an ion image, for which the laser fluence is only over threshold at the very extremes of its profile. The sample that was analysed consisted of a grid pattern (repeating squares) of a dye that had been applied to a sample plate. As only a ring of the sample is well illuminated, it is difficult to ascertain whether the ion optics are successfully spatially focussing the analyte ions. The accompanying line profile shows that ion intensity from the centre of the spot almost reaches zero intensity. It was confirmed that the observed structure arose due to the laser profile by adjusting the configuration of the optical fibre, and by fine tuning the coupling of the laser into the fibre. This led to an improvement in the profile of the spot as shown in figure 2.4 b). However the intensity at the centre of the image shown is still much lower than that at its extremes.

In order to further assess the quality of the beam, a power meter was used to measure the pulse energy emitted from the fibre optic, and the CCD sensor from a "webcam" was used to measure the profile of the beam. The CCD sensor and printed circuit board (PCB) were extracted from the protective casing and the lens was removed, leaving the sensor exposed. By aligning the fibre with the sensor, it was possible to record single frames using the proprietary camera software. This approach was far more reproducible than any

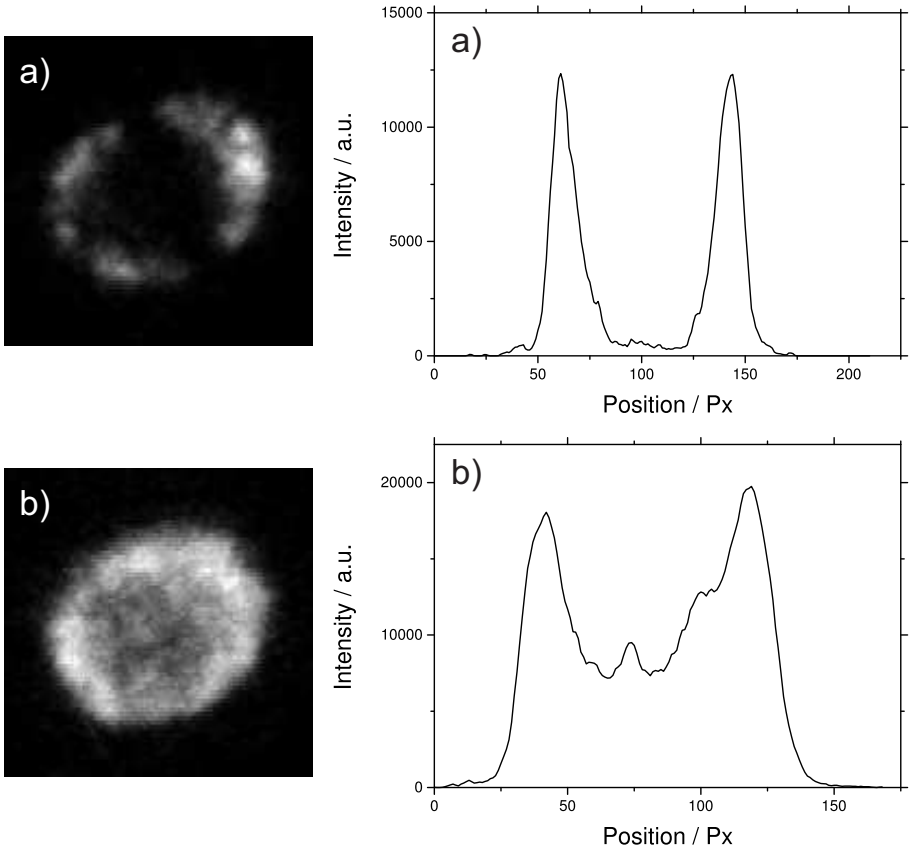

Figure 2.4: *Ion images of the Crystal Violet parent ion (nominal mass 372 Da) obtained from a square gridded sample of laser dye applied to a glass slide. The images show the ring structure observed due to the inhomogeneity of the laser profile. Each ion image is accompanied by a plot of a line profile taken across the image. Image a) was the original observation and image b) was obtained after changing the coupling of the laser into the optical fibre.*

attempts to optimise the laser profile using an ion image as it removes the sample quality from the problem.

Figure 2.5 shows a comparison between the beam profiles as measured by the modified "webcam". Figure 2.5 a) shows an acquired image of the beam profile before any optimisation, alongside a line profile taken from the image. Although the centre of the profile is the most intense, there is still high intensity at the edge of the spot. This implies that there is a large amount of light being transported through the cladding of the fibre, as opposed to the core. This will also have an impact on the laser power transmitted.

The fibre optic launcher, the optic which couples the laser from free space into a fibre optic cable, is attached directly to the NL100 laser. The assembly has very little control

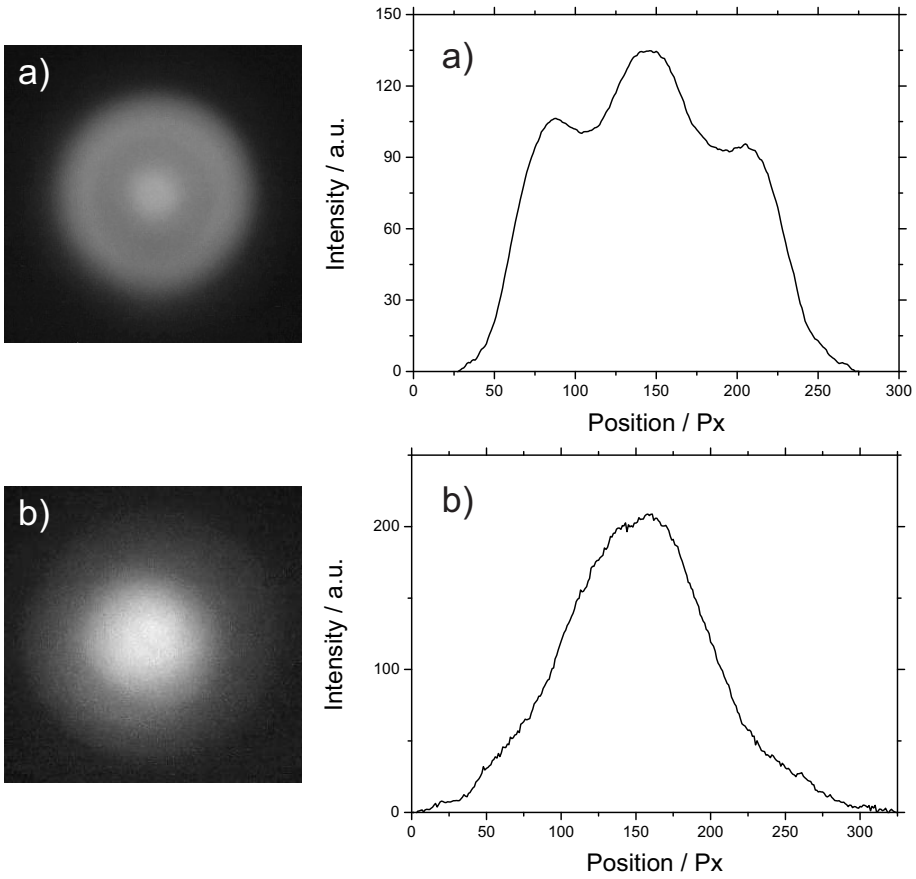

Figure 2.5: *Images of the laser beam profile before (a) and after (b) optimisation. The images were taken using the CCD sensor from a "webcam", and are accompanied by line profile plots.*

over the transverse position of the launcher relative to the beam, as by design the laser beam and the launcher should be aligned. However, there is control over the focussing optics of the launcher as, depending on the diameter of the beam, and the length of the optical fibre, the focussing will need to be adjusted. Figure 2.5 b) shows the profile obtained once the coupling of the laser with the fibre optic had been fully optimised. The profile shown here has the single peak that is expected, implying that there is very little transmission of light through the fibre cladding.

Figure 2.6 shows a comparison between the measured power output from the optical fibre as a function of the power set on the laser. The laser power is set through software included with the LT2 Plus, and can be set to a value between 0 and 340; although, this is not expected to be linearly proportional to the laser power (which has a maximum rating of 3.4 mW). The blue points in figure 2.6 are those measurements taken before the

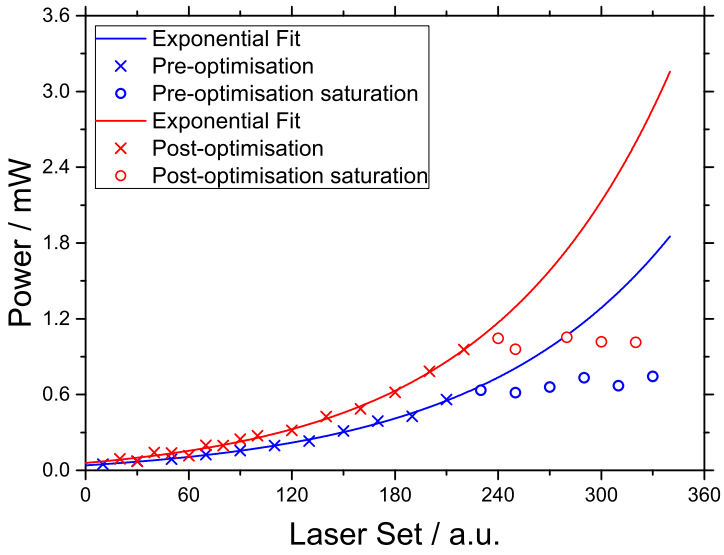

Figure 2.6: *A plot of the measured laser power emitted from the optical fibre as a function of the set laser power (an arbitrary integer between 0 and 340). Data in blue was obtained before the optimisation process, whereas data in red was obtained after optimisation. The crosses and circles are experimental measurements: the crosses are considered to be the points before the optical fibre is saturated; the circles are considered to be those points after saturation. The lines are exponential fits to the data obtained before saturation.*

coupling optimisation, and the blue line is an exponential fit through the first 11 points (which were determined to be those measurements representing the optical fibre before saturation). Similarly the red points are those taken after the optimisation and the red line is an exponential fit through the first 15 points which were determined to be pre-saturation.

It can be seen from the figure that after the optimisation the recorded power levels were ≈50% higher than before. However, even after the optimisation, the laser power still saturates the fibre (albeit at a higher level). An exponential extrapolation can be made from the data in the early part of the graph, before the fibre saturates (the crosses representing the regime before saturation). This extrapolation shows that the optimised fibre coupling does lead to the maximum power of 3.4 mW, however this value is not realised due to fibre saturation.

2.2.2 The Ion Optics

The LT2 Plus employs a delayed extraction pulsing regime. This is not ideal for a microscope-mode MSI instrument, as during the delay, before the extraction, there is no electric field, so any ablated ions are free to expand from their origin point on the sample. When the extraction optics are finally switched on, there is already a degree of uncertainty in the position of the analyte ions that is therefore impossible to recover through ion optical focussing. This implies an upper limit in the length of the delay before ion extraction. Longer delays preferentially time focus ions with higher m/z so the upper limit in the length of the delay is really an upper limit in the mass range.

Under normal conditions, the LT2 Plus would operate with an acceleration voltage of 20 kV. This high accelerating voltage is ideal as it reduces (in a relative sense) the "chromatic" blurring from the ion velocity spread, which would otherwise reduce the mass resolution. At these high accelerating voltages, the difference in arrival time between two ions of different mass will be very short (on the order of nanoseconds), which is not compatible with a time-stamping camera with a precision > 10 ns. In order to estimate the voltages needed to spatially focus the analyte ions, whilst still retaining a high mass resolution, it is necessary to simulate the ion optic assembly. Simulation methods will be described in chapter 3, and the experimentally observed resolutions will be presented in chapter 5.

2.2.3 The Detector

The electron multiplier supplied with the LT2 Plus is capable of high resolution time-of-flight measurements ($\approx$2 ns FWHM) and has an active area of 10 mm $\times$ 25 mm, but does not record any spatial information. Rather than the micro-scale array of transmissive pores in an MCP, TOF-MS electron multipliers, in general, consist of either a single macro-scale funnel or a succession of reflective dynodes. In the former case, a potential gradient is applied from one end of the funnel to the other, encouraging the creation of secondary electron emission and amplifying the charge. With reflective dynodes, each consecutive surface is held at an ever increasing voltage, attracting emitted secondary electrons. At

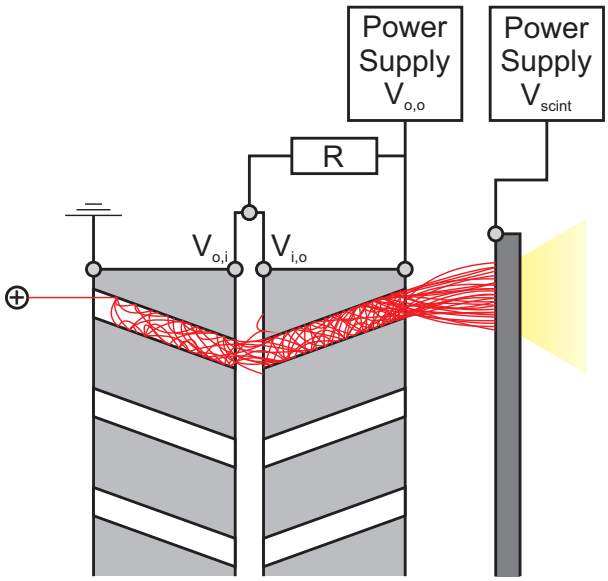

Figure 2.7: *A cartoon of the detector assembly featuring the MCP chevron stack and the scintillating screen. An incident ion (represented by the +) initiates an electron cascade (represented by the red lines). Electron excitation causes the scintillating screen to emit photons. The power supply attached to the output face of the output MCP is divided down to supply the output face of the input MCP and the input face of the output MCP.*

the end of the funnel, or dynode chain, there will be a final electrode or Faraday cup which can measure the incident current.

In order to amplify the current without losing the spatial information of the ions incident on the detector, MCPs must be used. The electron multiplier in the LT2 Plus was replaced with a 25 mm double-stack MCP (Photonis). The MCPs are fixed with a 1 mm gap between them, and are arranged in a chevron formation where their pores are aligned to maximise the transmission of electrons between them. The pores have a pitch of 12 μm, a diameter of 10 μm, and a bias angle of 5°. A potential gradient must be applied across the MCPs to produce a current, and each individual plate is rated up to a maximum potential difference of 1 kV. As shown in figure 2.7, a single power supply is used to apply both the potential for the output face of the output MCP, as well as the potential that is applied to the output face of the input MCP, and the input face of the output MCP. A resistor chain divides the supply voltage such that the potential applied to the two middle faces is half of that applied to the output face. The front face of the first MCP is held at earth ground. This means that a maximum voltage of 2 kV can be

safely applied to the MCP stack.

In order for this detector to be used with a CCD camera, or the PImMS1 camera, the electrons produced must be converted into photons. This can be achieved using any of a number of different scintillating materials (see chapter 1). For the work presented in this thesis, two different scintillating materials were used with the LT2 Plus detector: originally a plastic scintillating material with a short (≈2.5 ns) response time was used (BC-408, Saint-Gobain Crystals); this was then later replaced by an organic scintillating material with an equally short response time (E404 [46]). Both of these materials have emission spectra that cross from the ultraviolet into the blue end of the visible range with the output of BC-408 peaking at 425 nm and E404 peaking at 412 nm.

The housing for the detector used with the LT2 Plus was manufactured by SAI and was designed such that the scintillating screen could be exchanged with relative ease. The screen was mounted with a 3 mm gap from the back of the MCP stack and can withstand a potential difference across that gap of 5 kV. Unlike the detector used on the converted VMI instrument (section 2.1.3), there is no fibre optic bundle to focus the light emitted from the scintillating screen; instead, the screen is contained fully within the vacuum and any camera that is used must focus through a window at the screen itself.

2.2.4 The Cameras

As with the VMI instrument, a CCD camera and the PImMS1 camera were alternately used with the LT2 Plus. Both of these were used alongside the PMT (as in section 2.1.4). Using a 10 mm spacer for the c-mount camera lens, the field of view of the PImMS1 camera can be reduced to perfectly match the 25 mm detector screen. The minimum focal length of the camera is also reduced from 600 mm to 250 mm. This increases the intensity of light collected as well as making mounting the camera much easier.

The PMT (1P28, RCA) can be interfaced with the same analogue-to-digital converter (ADC) board that originally was connected to the electron multiplier. This also allows the LT2 Plus software to incorporate the PMT signal, which is necessary when using the automated scripts to find signal and record data.

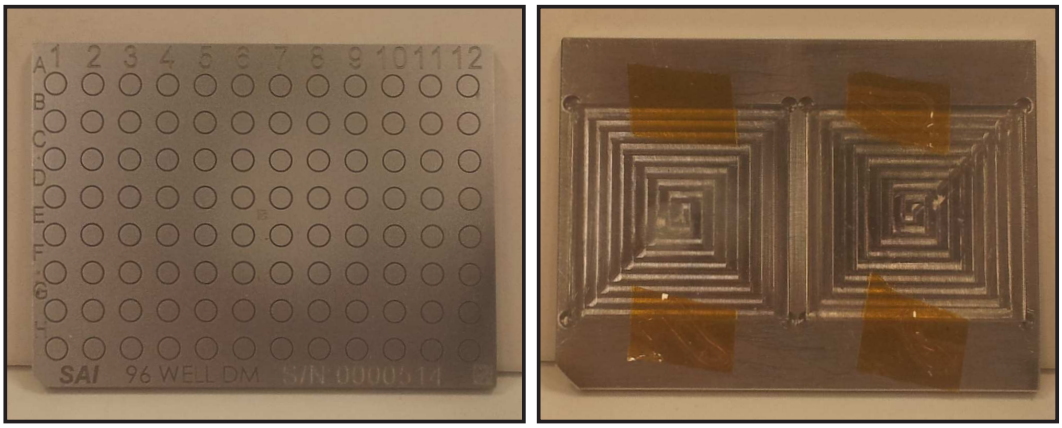

Figure 2.8: *A photo of the conventional 96 well sample plate used with the LT2 Plus (left) and the sample plate built in-house to hold two ITO coated glass slides (right). The glass slides are held in place with Kapton tape, and a small piece of wire is used to make a connection between the stainless-steel holder and the ITO coating of the slides.*

2.3 Sample Preparation

In the course of designing and testing a mass spectrometry instrument, it is necessary to prepare samples of known compounds that can be analysed in order to test what resolutions can be achieved. In imaging mass spectrometry, these samples also need to have some spatial definition.

All the samples used for the work presented in this thesis were applied to indium tin oxide (ITO) coated glass slides. The slides are 25 mm × 25 mm and 1.1 mm thick. The ITO coating (on one side) gives the slide a conducting layer, so that a voltage can be applied. This is necessary so that the electric field around the sample retains its homogeneity. The slides are inserted into the repeller plates of whichever instrument they are to be analysed in. In the case of the LT2 Plus, an adapted version of the 96 well sample plate was manufactured in-house, which can hold two glass slides (see figure 2.8). Kapton tape is used to hold the slides in place, and a small piece of conductive wire is used to make an electrical connection between the stainless-steel sample holder and the ITO coating of the glass slides.

A number of different chemical species were used to test the capabilities of microscope-mode MSI. Organic dyes (e.g. Crystal Violet, Auramine O, Exalite 398, etc.) were used for the majority of the experiments, as they produce samples that are very robust, lasting

for, in some cases, days before they have to be replaced. This robustness is necessary when attempting to optimise some parameter of an instrument, a task which can take hours. The dyes chosen were all susceptible to simple laser desorption, as opposed to needing a matrix to facilitate the ionisation process, which made the testing procedure more reproducible as it removed any interaction from the matrix solution from the quality of the results.

As both instruments were being designed as MALDI sample analysers, it was also necessary, after optimisation with the organic dyes, to perform tests with a MALDI sample. For this process a range of polyethylene glycol (PEG) compounds were used. These polymers give a predictable and regular succession of mass peaks, which make them ideal for calibrating mass spectrometers. They can be used in a matrix solution which, in the case of the work presented in this thesis, is often α-cyano-hydroxycinnaminic acid (CHCA). The drawback of these samples is that they do not hold a spatial pattern well and these samples do not last as long under laser irradiation. PEG itself is a liquid, and even in the solid solution of a MALDI matrix there is a significant amount of flow which blurs the lines of any attempted pattern.

A combination of the dye samples used for optimisation and testing of the spatial resolution, and the PEG samples used for a more thorough testing of the mass resolution with the MALDI process over a wider mass range allowed for a thorough understanding of how each instrument performs. For the experiments described in this thesis, a number of different methods were used to apply each sample to the ITO coated glass slides. The most common methods were the dried droplet technique, printing using a customised inkjet printer, and electrospray deposition.

2.3.1 The Dried Droplet Method

The simplest method of applying an analyte to a glass slide is by the dried droplet method. The analyte (and, if used, the matrix) is dissolved in some solvent and mixed. This solution is then transferred directly to the sample plate using, for example, a dropping pipette. The droplet is then left as the solvent evaporates. Depending on the conditions, matrix crystals

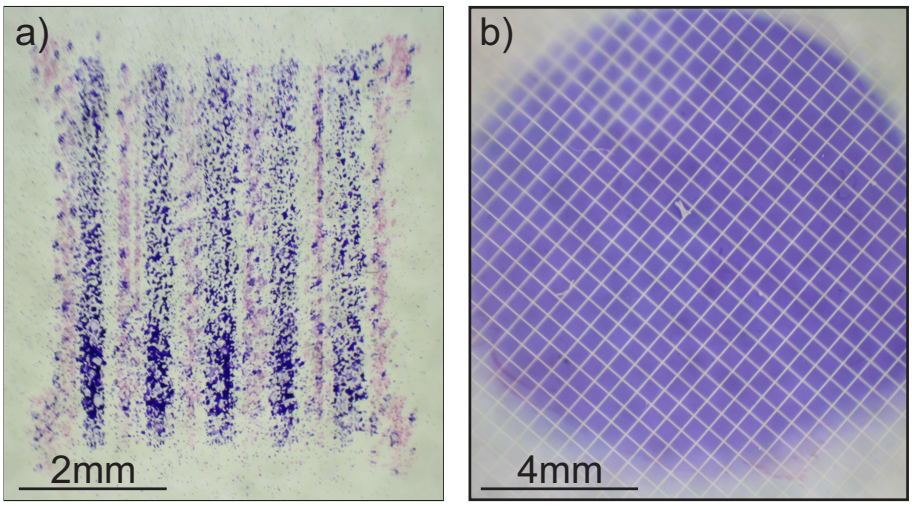

Figure 2.9: *A photographic comparison of samples created for testing the spatial performance of the MSI instruments. The samples were created using a) printing using an inkjet printer , and b) electrospray deposition.*

will form in varying sizes. The sample coverage should be relatively homogeneous at the centre of the spot; although, the edge of the droplet often shows a higher concentration of solute. Obviously this technique is not compatible with any spatial patterning; but is nonetheless, a very useful first step in instrument testing due to the simplicity and speed of the preparation process.

2.3.2 Using Inkjet Printers

As the work in this thesis will be testing imaging mass spectrometry, it is also necessary to have spatially defined samples. Figure 2.9 shows a photographic comparison between two samples created by different techniques.

Figure 2.9 a) was produced by an inkjet printer. Two different inkjet printers were used to produce samples for the MSI testing: a Canon Pixma IP 4950; and an Epson Stylus R320. By designing a test pattern of colours that consist of only a single printer ink (cyan, magenta, yellow, or black for the Canon printer; the Epson printer also has a light cyan, and light magenta), it is possible to print multiple solutions onto an ITO coated glass slide at different positions. The solutions are injected into empty replacement ink cartridges, which are then loaded into the printer.

Both printers have a CD printing facility, which is used by adding a CD holder which automatically feeds through the printer. A glass slide can be inserted into a CD by cutting out a 25 mm × 25 mm square. The CD has to be fixed into the holder, so that the position of the glass slide, relative to the holder, is known. This was achieved by drilling a pair of matching holes in both the CD, and the holder, so that the CD can be reproducibly positioned in a specific orientation.

In figure 2.9 a), two different dyes have been sprayed in alternating stripes using the Epson printer. It can be seen that this technique is not perfect as there is some overlap of colour between the stripes, but the separation is enough to be used for MSI. The stripes are also not perfectly homogeneous as the printing process effectively spots the solution onto the glass slide. This effect can be reduced by repeated applications (the sample shown in the figure was printed in ten layers), but with this there is the risk that if the sample is not loaded correctly the pattern will be ruined.

The stripes in figure 2.9 a) were each printed with a width of 400 μm. It is possible to print patterns with a resolution of down to 200 μm with printer inks, but with the organic dyes favoured for these experiments, the resolution is closer to the separation shown in the figure [152].

2.3.3 Electrospray Deposition

Figure 2.9 b) was produced using an electrosprayer which was built in-house [46]. The electrosprayer consists of a sample holder, beneath a suspended needle with a flat tip, through which the analyte solution is pushed. The solution flow is controlled using an automatic syringe pump (KDS Legato 100 [153]). The solution is pushed to the end of the needle tip, where it forms a hemispherical interface due to surface tension [154]. A positive voltage is then applied to the needle (up to a maximum of 5 kV), which polarises the solution so that an excess of positively charged species are found at the surface of the solution obtruding from the needle. The electric field which forms between the high voltage needle and the grounded sample plate below distorts the hemisphere into a Taylor cone. Charged droplets of the solution are then emitted from the apex of the Taylor cone

and are attracted towards the sample plate, creating a reproducible circular pattern.

The electrosprayer can be controlled by adjusting the voltage applied to the needle and by adjusting the height of the needle from the sample plate. This changes the strength and shape of the electric field formed between the needle and sample, which results in a change in the size of the spot produced. The voltage applied to the needle needs to be high enough to polarise the solution sufficiently, but also must be set correctly to form a stable Taylor cone. The sprayer can be effectively turned off by increasing the needle voltage above this ideal level, at which point the Taylor cone reduces in size to the point where it is almost fully retracted back within the needle. This can be extremely useful when a sample has been sprayed, as it reduces the likelihood of large drips of solution falling from the needle as the sample is removed.

In order to produce a spatial distribution of analyte a stencil must be used. The sample shown in figure 2.9 b) was produced using a nickel grid with a pitch of 500 μm and a wire width of 67 μm (Goodfellow NI008720 [155]). A drop of acetone can be used to fix the grid flush against the slide, and after spraying, once the solution has dried, the grid must be carefully removed rather than dragged in order to avoid damaging the sample. The sample thickness can be controlled by adjusting the spraying time. This process is hard to reproduce for multiple analyte samples, as if too much solvent is deposited onto the original pattern it can redissolve the analyte and blur the image, but with a low enough flow rate it is possible to create samples with multiple analytes with different spatial distributions. The optimum distance between the needle and the sample surface was found to be 17.5 mm.

2.4 Centroiding

When considering the acquisition of an ion image in a simulation, an ion reaching a detector is recorded accurately and precisely, but an ion reaching a detector in an experiment is subject to a three step conversion process: first, the ion is converted to a shower of electrons by the MCPs; next, this electron footprint is converted into light by a scintillator; and

finally, the light is converted back into an electronic signal by a camera or PMT. This process doubtless contributes to the form of the acquired image, most noticeably as the electron cloud produced by the MCPs will spread out transversely before reaching the scintillating layer. This means that each ion event will be converted into a spot source on the detector which, in turn, will illuminate a cluster of the camera's pixels. The intensity observed for each ion is therefore different, so an ion counting technique needs to be used in order to properly verify the true number of ions present in an image [156]. The image blurring from the detector can be reduced, to some extent, by centroiding the image acquired for each shot before summing it into the total output.

2.4.1 CCD Camera

The process of centroiding is divided into three parts: each image must have a threshold applied so that signal can be distinguished from the background noise; the next step is to group those pixels that have been found to contain signal into clusters representing individual ion events; each of these ion events can then be reduced down to a single value which should best describe the position of the original ion. This process results in a large reduction in the quantity of data and can reduce the "smoothness" of ion images, so it is usually necessary to acquire much larger data sets.

Applying a threshold to an image is relatively trivial as, especially when using an intensified CCD camera, the intensity of an event resulting from the millions of electrons produced by the MCP stack is much higher than that observed for background noise. The CCD camera outputs an 8-bit image; therefore, each pixel can have a value from 0 to 255. A lower bound threshold can be applied, e.g. 17, so that pixels with greater intensity than this are retained and any pixels with a lower value are reduced to zero intensity.

In order to identify which pixels belong to specific ion events, the Labview IMAQ "Find Circles" function was used [157]. This function accepts an image as its input and returns the coordinate (position of centre, and radius) of any features in that image that are circular. This method can distinguish between overlapping events and by applying a threshold to the minimum radius of the event, further background noise can be eliminated

from the image. The final coordinate of the ion event is simply taken as the centre of the circle and this value is then added to the summed image with each ion event being given equal intensity.

For a CCD camera, this process is done on-the-fly, i.e. continuously during the acquisition. This means that the original "raw" data set cannot be recovered.

2.4.2 PImMS1 Camera

Centroiding of data obtained with the PImMS1 camera is rather different. The data collected do not have an analogue dimension: there is no intensity for each event. However, each event is collected and resolved in time as well as by its position on the sensor. The challenge with centroiding a PImMS data set is to decide which events correspond to a single ion arriving at the detector. This list of events is referred to as a cluster. As with the data from the CCD camera, events in a cluster will occur in adjacent pixels (either defined as the four closest neighbours within 1 Px (where Px is the pitch of the pixels on the sensor), or the eight closest neighbours within $\sqrt{2}$ Px). However, the proximity of these events in time is less clear-cut. In order to search for events in neighbouring pixels there must be some restriction on the number of time-bins to search through. Anecdotal observations of these clusters imply that a gap of several time bins may occur between spatially adjacent pixel events, and that the earliest time bins of a cluster are almost always found at its centre.

The PImMS data is recorded so that each event has its pixel position (x, y) and its time bin (τ) recorded. The criteria for pixels belonging to a single cluster is defined spatially where both Δx and Δy may take a value of -1, 0, or 1. This is the aforementioned "eight-connectivity", as it encompasses all eight nearest neighbours to a given pixel. The temporal displacement is less simple to define, but must be restricted such that $\Delta\tau \leq \Delta\tau_{\mathrm{MAX}}$. It is the definition of $\Delta\tau_{\mathrm{MAX}}$ that makes the temporal displacement more complex.

In order to investigate a suitable value for $\Delta\tau_{\mathrm{MAX}}$, data taken with the PImMS1 camera was analysed, and figure 2.10 shows plots obtained from this data. The data were taken from a section of a time-of-flight spectrum covering the mass of only a single species,

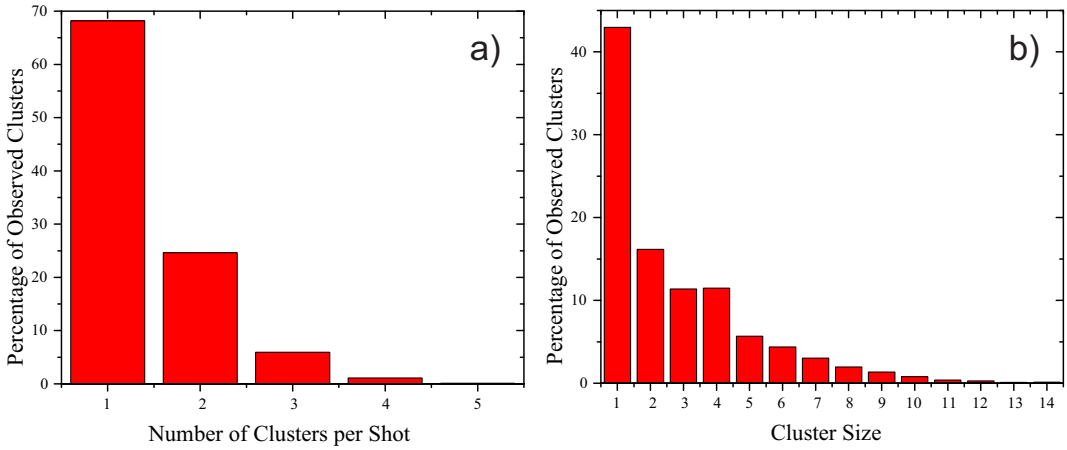

Figure 2.10: *Two frequency plots pertaining to data, obtained with the PImMS1 camera, that was used to define the centroiding algorithm used for future PImMS1 data sets. Plot a) shows the number of clusters observed for each laser shot, whilst plot b) shows the sizes of these clusters (i.e. the number of pixels).*

covering a range of only 50 time bins. The experiment was purposely conducted at a very low count rate, so that ion clusters could be assumed to be completely separate. At this low count regime, $\Delta\tau_{\mathrm{MAX}}$ was set to 50 so that any spatially adjacent pixel events would be included in a given cluster.

With these criteria for cluster detection, the number of clusters observed per shot was, indeed, found to be very low, as is shown in figure 2.10 a). The size of these clusters, N, was also found to vary: although over 40% of clusters were found to include just a single pixel, many clusters contained between two and eight pixels, with cluster sizes as large as twelve being observed.

Each of these clusters was then further analysed to measure their temporal spread. The full spread in time of a cluster from the first time code, τ_0, to the last, τ_{N}, was measured and figure 2.11 a) shows the resulting frequency plot. The distribution is seen to peak at around five time bins; however, there is also a significant fraction of clusters with wider time spreads up to a maximum of eleven time bins.

This observation, $(\tau_N - \tau_0)_{\mathrm{MAX}} \approx 11$, gives a method for identifying clusters by testing all of the events within eight-connectivity that occur within eleven time bins of the earliest observed event [158, 159]. However, it is also possible to use the difference in time code for sequential events within a cluster. Here the sequential time bin displacement must be

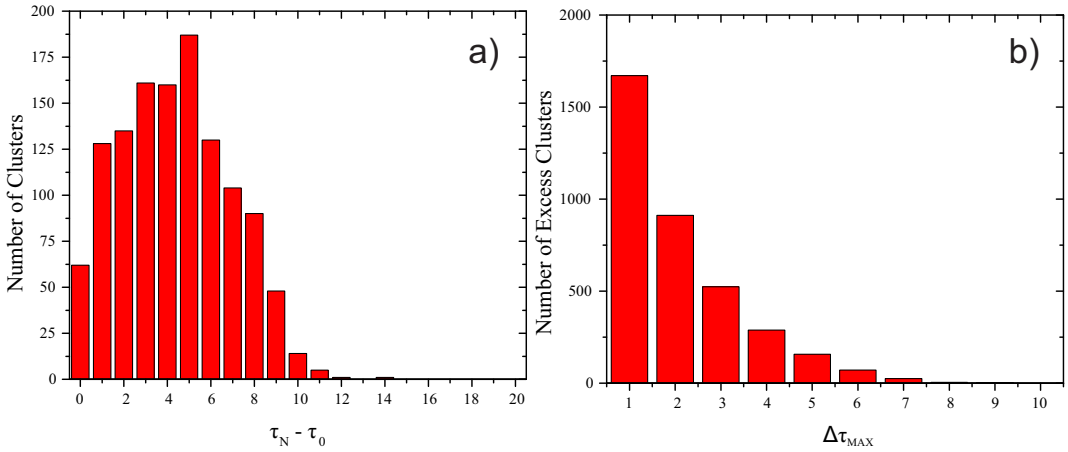

Figure 2.11: *Two plots showing spread of time codes observed in the PImMS1 data set. Plot a) shows the full distribution of the full time spreads from the first event observed in a cluster to the last. Plot b) shows the excess number of clusters observed when centroiding a data set as a function of* $\Delta\tau_{\mathrm{MAX}}$ *with the recursive search.*

used in a recursive algorithm that searches for neighbours to the first event and, if any are found, then searches for further neighbours to them (and so on).

Both of these methods have merit. By only looking at the full time spread of a cluster the search window is limited, whereas with a recursive search there is no upper limit to how far an event must be from the first time code. Conversely, with the recursive search, two clusters that overlap spatially will still be distinguishable, as the algorithm expects new events displaced from the centre of the cluster to arrive later in time.

In order to test the cluster searching algorithm, the data were analysed multiple times, using the method of recursively searching for events belonging to each cluster, but with a different value for $\Delta\tau_{\mathrm{MAX}}$ each time. The number of clusters was then counted and compared. It was observed that as $\Delta\tau_{\mathrm{MAX}}$ increased, the number of clusters observed was reduced. This is because, for small values of $\Delta\tau_{\mathrm{MAX}}$, events are incorrectly excluded from a cluster and so are identified as belonging to an extra cluster in their own right. Figure 2.11 b) shows a plot of the number of excess clusters observed as a function of $\Delta\tau_{\mathrm{MAX}}$. It can be seen that after $\Delta\tau_{\mathrm{MAX}} = 7$ there is no longer an excess of clusters identified.

Although both methods for cluster identification appear to be valid, the recursive method has the advantage that distinctions can be made between adjacent clusters, and

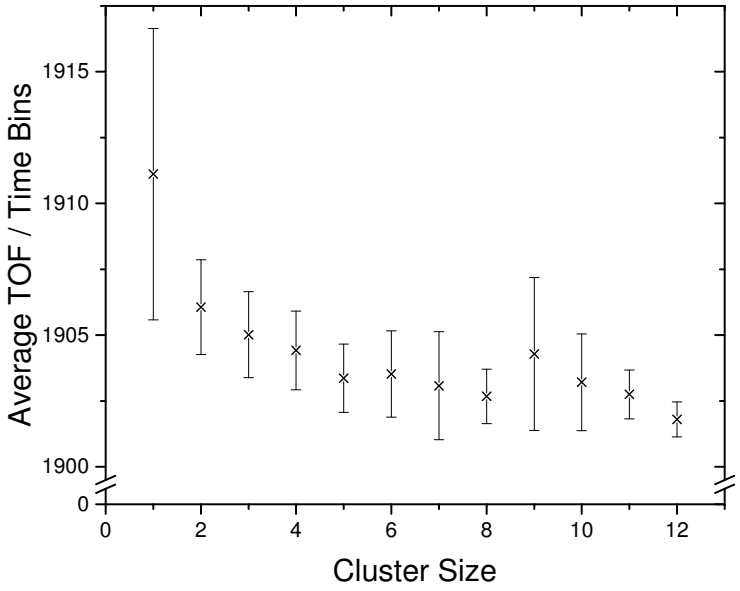

Figure 2.12: *A plot of the average time code observed in the spectrum of data separated out depending on the size of the observed clusters. The error bars represent the standard deviation of the data.*

that even if there is an occasional large cluster with many events, the algorithm will continue to search for neighbours. For these reasons, all references to the centroiding of PImMS1 data in this thesis refer to the use of the recursive analysis with the parameter $\Delta\tau_{\mathrm{MAX}} = 7$.

Once a cluster of pixels has been identified, the act of reducing this list to a single coordinate is very simple. As an event cannot be recorded before it has occurred, it can be assumed that the earliest observed time code in the list is the most accurate, and so it is this time code that is set for the cluster. Spatially, a centre-of-mass is taken for all the events where each event is given an equal weighting. The result of the centre-of-mass is then binned back to the original pixel map. If the value of the centre-of-mass falls directly between two pixels, then the cluster is pseudo-randomly assigned to one of the pixels. There are more advanced and complex methods for assigning the spatial centroid of a cluster, but these are not used in the work presented in this thesis [79, 160, 161][1].

[1]Discussion of these more advance spatial centroids for PImMS data sets can be found in the works of Craig Slater [158, 159]

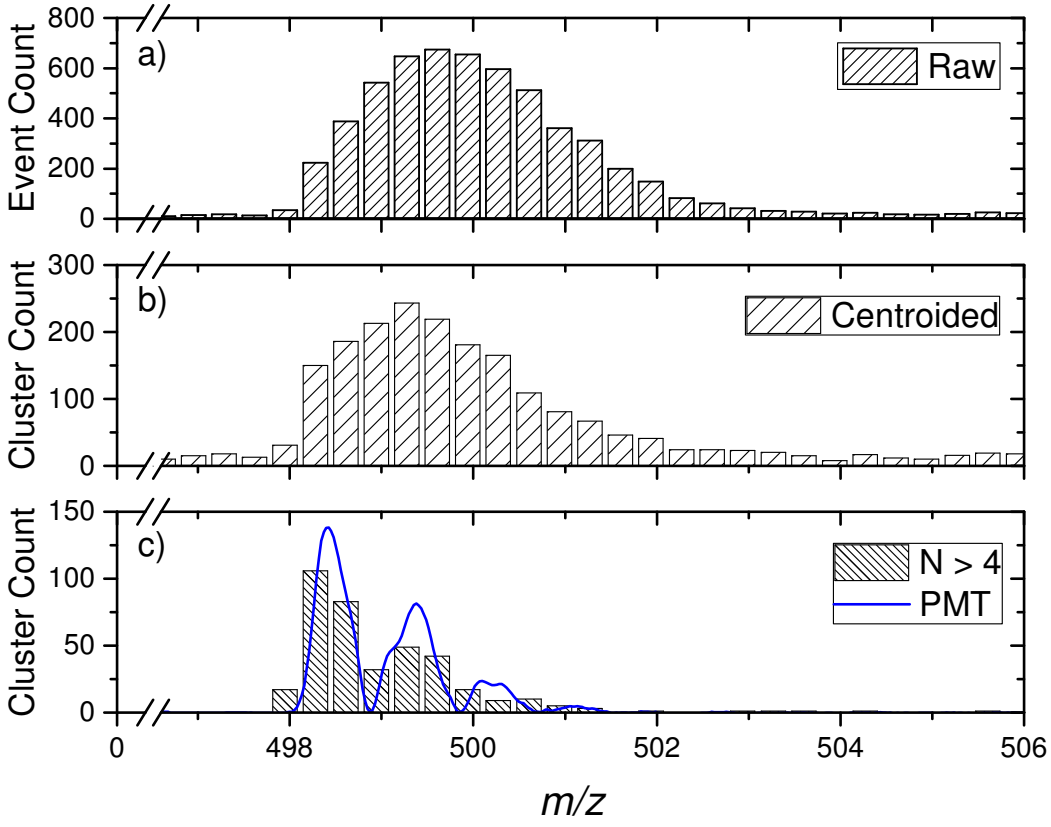

Figure 2.13: *Plots displaying the progression of PImMS1 data as it is centroided from a) the raw data set. Clusters are identified using the recursive searching method and each cluster of events is reduced to its earliest observed time code resulting in b). Finally, the smaller clusters are discarded (here only clusters of five pixels or more are kept) and this spectrum in c) is compared with the spectrum obtained with a PMT.*

Applying these criteria, and with $\Delta\tau_{\mathrm{MAX}} = 7$, the PImMS1 data were again analysed. Figure 2.12 shows the average time code observed for each cluster, as a function of the size of that cluster. There is a general trend observed for smaller clusters to be observed at later times than larger clusters. At the largest cluster sizes (nine to twelve pixels), the number of observed clusters is very low and the trend becomes less regular.

As was stated earlier, an event cannot be observed before it has occurred. This implies that the average time observed for the largest clusters is more accurate than the time observed for smaller clusters (although this does assume that all of the clusters result from ion events from the same species). In order to take advantage of this, these smaller, less reliable, clusters can be discarded.

Figure 2.13 shows a different data set taken with the PImMS1 camera under the same conditions as the data used previously. Figure 2.13 a) shows the mass spectrum that is obtained from the "raw" data set, and shows an evident slow rise with a long tail. Figure 2.13 b) shows the result of centroiding on the PImMS data set. Rather than event counts, this plot shows the cluster counts from the data. This plot includes all of the identified clusters. Finally, figure 2.13 c) shows a comparison between a mass spectrum obtained from the centroided PImMS1 data where only clusters of five pixels or more are included. There are now multiple peaks present in the spectrum. This can be compared to the spectrum obtained with a PMT (shown in blue), which confirms that this peak structure is real. As would be expected, the count of events and clusters is reduced in applying this algorithm, but the three graphs show how information can be extracted from a previously featureless peak.

2.5 Summary

In this chapter the instrumentation and techniques used for the studies in this thesis have been presented. Two instruments have been described which have been modified and converted so that they can produce mass-resolved microscope-mode images with either a conventional CCD camera or the PImMS1 camera (or indeed any other light sensitive camera). Three methods for producing samples, with which to test the resolutions of these instruments, were also described.

In the following chapters, the methods for predicting the resolutions of these instruments will be discussed and methods for analysing the data produced by them will be presented. Experimental data obtained using these methods will later be presented and then some improvements to the instrumentation will be discussed.

Chapter 3

Simulation Methods

Before undertaking laboratory work, the performance of the instruments was simulated. As the ion optics have to focus ions both spatially and temporally (i.e. position and mass) any adjustments to the assembly's parameters will affect both of these resolutions. It is important to understand the interplay between these specifications in order to design an instrument that is able to reach the resolutions required by whatever application may be in mind. The final specifications will be a compromise (there is no trivial solution to a high resolution, all-round mass imaging spectrometer), and the situation is complicated further if one tries to take other specifications (such as mass range, sensitivity, and analysis time) into account.

In this chapter some of the techniques used for modelling and predicting the performance of ion optics will be presented and discussed. There will first be an overview of the first order analytical models that can describe charged particle trajectories. This will be followed by an in-depth look at the more sophisticated particle trajectory simulation program, SIMION [162].

3.1 Modelling Ion Optics

A simple analytical model can be formed to describe the motion of charged particles within an electric field using Newton's laws of motion. The assumptions in this model limit its use as a direct comparison to experiment; however, these first order approximations do

describe the general trends that can be expected from an ion optic assembly, and allow for a more intuitive understanding of how the ion lenses work than the more accurate "black box" trajectory simulation programs. An understanding of the underlying theory, coupled with the use of more advanced simulation software give a rounded view of an experiment as a whole.

3.1.1 Transfer Matrices

The transfer matrix treatment of charged particle trajectory calculations reduces the influence of an ion optic element to that of an operator acting on a vector which represents the current state of that particle. The derivation is based on that by Liebl [163], and a more rigorous treatment can be found in appendix 9.

A particle, p, is defined by its progress along the TOF axis (which here is the x axis) relative to each ion optic element, n, and at each of these elements it has two values: its orthogonal displacement from the major axis, $r_{p,n}$, and its direction relative to the parallel of that major axis, $r'_{p,n}$, where

$$r' = \frac{\Delta r}{\Delta x}. \tag{3.1}$$

The simplest "element" in an ion optic is a drift space, or field free region. Simply, a drift space will only change the translational displacement of a particle, and this is done according to the length of the space, L_n, and the direction of the motion of the particle:

$$\begin{pmatrix} r \\ r' \end{pmatrix}_{p,n} = \begin{pmatrix} 1 & L_n \\ 0 & 1 \end{pmatrix} \begin{pmatrix} r \\ r' \end{pmatrix}_{p,n-1}. \tag{3.2}$$

The field formed between two plates with differing voltages will be a uniform field. A particle entering this field at a potential, V_{n-1}, having already been accelerated from some higher potential, V_0, will be further accelerated to the next electrode if it is held at an even lower voltage, V_n. The trajectory of a particle can also be described by a transfer matrix,

the derivation of which can be found in appendix 9, culminating in equation (9.26):

$$\begin{pmatrix} r \\ r' \end{pmatrix}_{p,n} = \begin{pmatrix} 1 & \frac{2L_n}{\sqrt{\frac{V_0-V_n}{V_0-V_{n-1}}}+1} \\ 0 & \sqrt{\frac{V_0-V_{n-1}}{V_0-V_n}} \end{pmatrix} \begin{pmatrix} r \\ r' \end{pmatrix}_{p,n-1} . \tag{3.3}$$

In practice, there will be a deviation from a perfectly uniform field close to any plate that has an aperture through which higher strength fields can penetrate; however, the perturbation to a particle's trajectory can be compensated for, approximately, by adding a further transfer matrix which represents the lensing effect of the aperture,

$$\begin{pmatrix} r \\ r' \end{pmatrix}_{p,n} = \begin{pmatrix} 1 & 0 \\ -\frac{1}{f_n} & 1 \end{pmatrix} \begin{pmatrix} r \\ r' \end{pmatrix}_{p,n-1} = \begin{pmatrix} 1 & 0 \\ -\frac{E_{n+1}-E_n}{4(V_0-V_n)} & 1 \end{pmatrix} \begin{pmatrix} r \\ r' \end{pmatrix}_{p,n-1} , \tag{3.4}$$

where f is the focal length of the lens, E_n and E_{n+1} are the electric fields before the aperture and after it respectively, and $V_0 - V_n$ is the approximate particle energy at the aperture, in electronvolts [35, 36].

The previous approximations took advantage of the fact that the accelerating voltages experienced by the particle are much greater than the particle initial kinetic energy so that the trajectory of the particle is closely parallel to the major axis (the so called paraxial approximation). This approximation is not valid for the initial extraction region as, in spatial imaging, particles will be emitted at a variety of angles. This means that a more explicit definition is necessary for the initial extraction vector (this is also derived in appendix 9, equation (9.27)),

$$\begin{pmatrix} r \\ r' \end{pmatrix}_{p,1} = \begin{pmatrix} r_{p,i} + \sin(\alpha_{p,i}) 2L_1 \sqrt{\frac{V_{p,i}}{V_0-V_1}} \\ \sin(\alpha_{p,i}) \sqrt{\frac{V_i}{V_0-V_1}} \end{pmatrix} , \tag{3.5}$$

where $r_{p,i}$ is the initial radial position of the particle on the repeller plate, $\alpha_{p,i}$ is the initial angle between the direction of motion of the particle with the major axis of the assembly, and V_i is the initial particle kinetic energy in electronvolts.

For a three electrode assembly (shown in figure 3.1) there is an initial extraction, E_1,

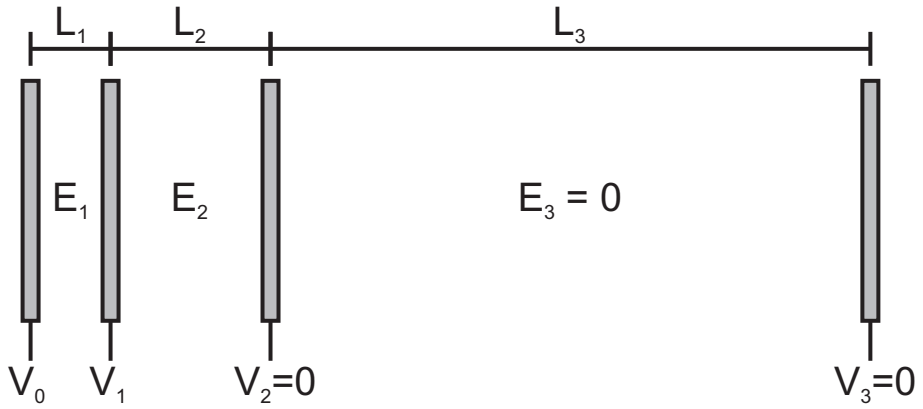

Figure 3.1: *A cartoon of the simple three electrode ion optic assembly. The potentials, V_n, and element lengths, L_n, are annotated along with the resulting electric fields, E_n.*

followed by a lens, V_1, then a uniform acceleration field, E_2, before a final lens, V_2. This whole assembly is then described by the multiplication of the appropriate matrices,

$$\begin{pmatrix} r \\ r' \end{pmatrix}_{p,3} = M_{\text{Drift}} M_{\text{Lens2}} M_{2,1} M_{\text{Lens1}} M_{\text{Extr}} \tag{3.6}$$

$$= \begin{pmatrix} 1 & L_3 \\ 0 & 1 \end{pmatrix} \begin{pmatrix} 1 & 0 \\ -\frac{E_3-E_2}{4(V_0-V_2)} & 1 \end{pmatrix} \begin{pmatrix} 1 & \frac{2L_2}{\sqrt{\frac{V_0-V_2}{V_0-V_1}}+1} \\ 0 & \sqrt{\frac{V_0-V_1}{V_0-V_2}} \end{pmatrix}$$

$$\times \begin{pmatrix} 1 & 0 \\ -\frac{E_2-E_1}{4(V_0-V_1)} & 1 \end{pmatrix} \begin{pmatrix} r_{p,i} + \sin(\alpha_{p,i}) 2L_1 \sqrt{\frac{V_{p,i}}{V_0-V_1}} \\ \sin(\alpha_{p,i}) \sqrt{\frac{V_i}{V_0-V_1}} \end{pmatrix} \tag{3.7}$$

Figure 3.2 shows nine trajectories corresponding to three different point sources (forming the "object") situated on the TOF axis, at 1 mm from the axis, and at 2 mm from the TOF axis. Each trace represents a particle, all of which are assumed to have an initial kinetic energy of 0.65 eV, and a slope of r' =0, -1, or 1 respectively. The trajectories are traced through the ion optics which are based on those in the converted velocity mapping instrument (L_1 = 15 mm, L_2 = 22 mm, L_3 = 546 mm; V_0 = 2000 V, V_1 = 1760 V) and are then focussed onto a detector creating an image. The image is magnified $\times$ 15 and is inverted. The inset to the figure shows the trajectories expanded around the ion optics. The back-focal plane is marked in the figure: in ion imaging this is also referred to as the velocity-mapping plane as it is the position along the TOF axis at which particles with the

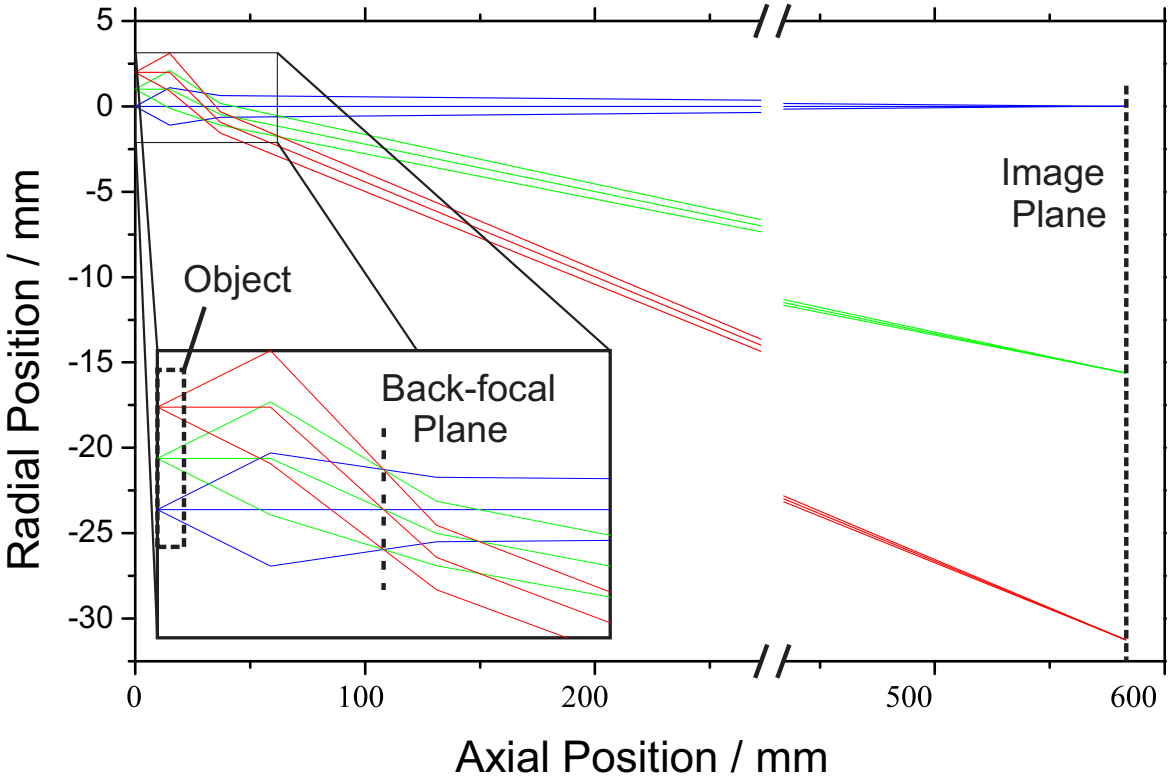

Figure 3.2: *Three traces of trajectories calculated using equation* (3.7)*. The object, back-focal plane and image plane are marked accordingly.*

same velocity are focussed to the same point in space, irrespective of their initial position.

The focussing can be altered by adjust the ratio of the two fields, E_1 and E_2. In practice the acceleration potential of the ion optics is set, and the last electrode is held at ground so the ratio of the fields is controlled solely by adjusting the potential applied to the extractor electrode.

3.1.2 Accounting for Aberrations

The trajectories shown in figure 3.2 are an ideal case. Taking, for example, the equation for the lensing effect of any aperture (equation (3.4)), the focal length, f_n, is equated to a ratio of the difference between the fields either side of the aperture, $E_{n+1} - E_n$, and a multiple of the particle energy at the aperture, $V_0 - V_n$. One of the approximations made to obtain this equation was that the accelerating potential was large enough that any initial kinetic energy gained from the ablation process could be considered negligible (this approximation was also made when deriving the other equations). However, if the kinetic

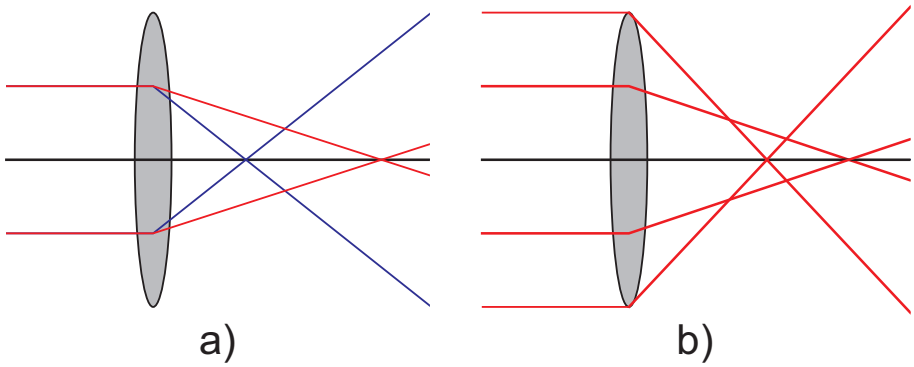

Figure 3.3: *A cartoon depiction of a) chromatic aberrations observed in the difference in focal lengths for particles with higher (red) or lower (blue) kinetic energy, and b) spherical aberrations observed in the difference in focal lengths for trajectories passing at different distances from the major axis of the lens.*

energy spread is large enough, the effect of the lens will be observably reduced for those particles that have a higher initial energy. This is referred to as a chromatic aberration as it is directly analogous with the chromatic aberrations observed in optical microscopy when those rays of different colours are focussed at different lengths. Figure 3.3 a) shows a cartoon depiction of chromatic aberrations where the trajectories in red represent a particles with higher energy which are therefore converged to a lesser degree (resulting in a longer focal length) than those particles with lower energy, represented in blue.

Figure 3.3 b) shows another common aberration, namely: spherical aberrations. Here the degree of lensing is no longer independent of the radial displacement of the particle from the major axis. The consequence of this is that the quality of the focussing of an image is related to the ratio between the size of the object (sample diameter) and the diameter of the apertures in the lens electrodes. If the size of the aperture in an electrode is significantly greater than the distribution of radial displacements of the particles at that aperture then the spherical aberrations will be negligible.

3.2 Particle Trajectory Simulations: SIMION

The SIMION software package is a particle trajectory simulator and electric field calculator. The user can input the geometries and applied voltages of an ion optic assembly, and specify the properties of particles within that assembly. The simulation will then run and

the resulting particle trajectories can be recorded. In practice, it is only ever the position of a particle as it reaches the area representing the detector, and the time at which this occurs, that are needed in order to model the system: these being the only results that would be obtainable in the laboratory.

SIMION uses the same premise to calculate trajectories as is used in the transfer matrix treatment of charged particle optics: the classical equations of motion are applied to an object as it traverses a potential field. However, rather than simplifying the problem down to give an analytical solution, an iterative approach is taken to calculating the electric field. This has the advantage of giving a far more accurate simulation of an ion optic assembly; crucially, higher order aberrations (such as those discussed in section 3.1.2) can be estimated. The method is still not perfect though. The accuracy of the simulation is dependent on the precision of the calculated electric field and the trajectory itself. Higher precision simulations are both processor and memory intensive.

3.2.1 Solving Laplace's Equation

The form of an electrostatic field, E, can be deduced from the potential field, V. Laplace's equation states that the divergence of the gradient of such a field is equal to zero:

$$\nabla^2 V = 0, \tag{3.8}$$

or

$$\frac{\partial^2 V}{\partial x^2} + \frac{\partial^2 V}{\partial y^2} + \frac{\partial^2 V}{\partial z^2} = 0. \tag{3.9}$$

This equation limits the viable options for a solution to those with no minima or maxima as the potential at any point is equivalent to the average of the potential over a spherical surface centred at that point. Combining this property with the boundary conditions of the potential at the surface of the system gives all the information needed to calculate the field. These boundary conditions come in two types: Dirichlet boundaries have a defined potential, and Neumann boundaries have a defined derivative (e.g., that at the edge of the simulation $\frac{dV}{dn'} = 0$).

An ion optic is constructed by defining each electrode as a collection of voxels which are each considered a known Dirichlet boundary condition. Thanks to the superposition principle each electrode can be considered in turn and the complete field can later be calculated as a weighted linear combination. This is especially convenient when adjusting the voltage of one electrode relative to the rest during the particle flight time (this is often done when simulating pulsed extraction techniques). Neumann boundaries are used at the extremes of the simulation volume and to define planes of symmetry allowing for fewer grid points to be used.

As the solutions to each of the fields relating to the electrodes are not likely to be analytically elegant, an iterative solution is found using a finite difference technique. Once the boundary conditions are set each voxel is considered in turn, setting its potential to an average of its neighbours. This process is then repeated with each successive iteration resulting in a numerical solution for the field that is closer than the previous. At some success criterion the process is stopped (in SIMION this criterion is that no voxel has changed in value by more than 0.005 V in a single iteration).

Once the field has been obtained, particles can be introduced to the system and their trajectories calculated. The Runge-Kutta method of numerical integration is used to calculate the position and velocity of each ion in discrete steps. The time-step for the calculation can be varied such that more complicated regions of the field are traversed with a higher precision than simpler regions (e.g., the field free flight tube). It is at each time steps that the electric field is re-evaluated so that a time variance can be applied to the field.

3.2.2 Defining Particles

However accurate the estimation of the electrostatic potential field may be, the simulation results will be meaningless unless combined with a realistic definition for the ablated ions. As discussed in chapter 1, the MALDI process is not well understood and so does not offer us a definitive model from which to calculate the initial conditions expected from a MALDI sample. There is, however, some literature that details experimentally obtained

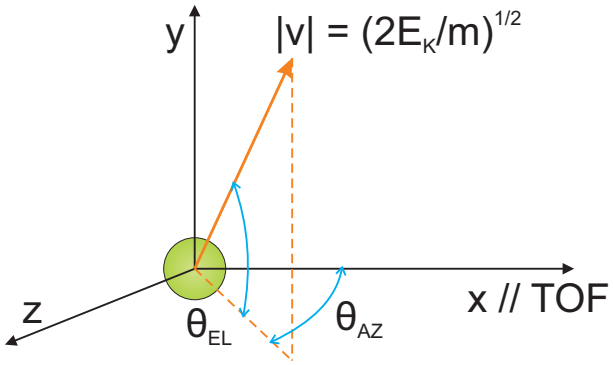

Figure 3.4: *A depiction of the coordinate system used in SIMION. The major axis (time-of-flight axis) is the x-axis. The initial velocity of the particle, v, is defined by the initial kinetic energy, E_{E}, and the direction of motion which is separated into azimuth, θ_{AZ}, and elevation, θ_{EL}, components.*

velocity distributions for various species.

Ions are defined by a set of variables which are: mass, charge, initial position, initial speed, initial direction of motion, and "time of birth". The effect of the depth of the sample (spread in the x, or time-of-flight axis), speed distribution, and directional distribution on the resolutions of SIMION simulations has been investigate and unsurprisingly can have a large impact on the results of a simulation [152]. This means that it is important to set these initial ion conditions correctly if any estimation of the absolute resolutions is desired.

A curiosity of the MALDI process is that the speed distribution observed for different species seems to be independent of mass: for a given laser ablation, the analyte molecules will be produced with the same average speed. According to Beavis and Chait this average speed is close to $750\,\mathrm{ms}^{-1}$ distributed with a full width at half the maximum (FWHM) $\approx 150\,\mathrm{ms}^{-1}$ [128]. However, there are a number of different articles which all report different average velocities. The same is true of the angular distribution of the velocities of ablated ions is not so neatly confined. Zhang and Chait showed that for a number of molecules with different masses a $\cos^n(\theta)$ distribution could be used to describe the distribution where n was dependent on the ion mass. It was suggested that higher mass ions tended towards higher values of n (giving a more forward focussed distribution) but there was no thorough investigation into this relationship. Values as high as $n = 28$ were measured by

Zhang and Chait and there was a general trend of forward peaking [129].

The x-position spread of the sample and the "time-of-birth" distribution of the ions are both considered to be negligible. The topography of a sample will undoubtedly impact the obtainable resolution as the focussing condition needed at different positions will vary (see the variable L_1 in equation 3.7). A sample with high peaks and low troughs will effectively have a range of starting positions from which ions can be ablated but samples produced using the electrospray device described in chapter 2 are created with very little variance in thickness (as little as 50 nm). Similarly, although the ionising laser can have a temporal width as large as 10 ns, the actual ionisation time of molecules in the MALDI process has been shown to have a much reduced variance. It has been proposed that this is due to certain energy pooling mechanisms that occur during the plume expansion, resulting in the actual ionisation event occurring only when there is a high concentration of multiple excited state molecules: a criterion that is only satisfied at the absolute peak of the laser intensity [28].

There are a number of different data formats that can be used to define particles for SIMION simulations. The most flexible of these is the *.ion format in which the definitions of each individual ion can be explicitly set. It is trivial to create codes to generate these files to conform to any desired distribution. SIMION also has some internal particle distribution generators which can be used with *.fly2 files. These files state the parameters of the distribution and SIMION generates a pseudo-random list of ions accordingly. There is no option for a $\cos^n(\theta)$ distribution of angles, but a Gaussian function can be used to approximate this.

Due to the lack of consensus on what ion definitions should be used, a set of parameters were chosen that would give a cautious estimate [130,131]. An average velocity of 500 ms^{-1}, with a full width at half the maximum of 500 ms^{-1} was chosen, along with an angular spread of 60° (FWHM). These parameters are likely to be an overestimate of the true velocity spreads observed in the instrument, but will therefore give a lower limit for the measure of the spatial and mass resolutions.

3.2.3 Defining Ion Optics

The potential arrays that describe the ion optic assembly (and the rest of the instrument) are defined using a space of voxels. The precision of the electric field calculated in SIMION is set by the size (set in millimetres) of each grid unit. Smaller grid units will give a higher resolution but will require more computer memory to be stored and will slow each trajectory calculation.

Symmetry in the ion optics can be exploited to reduce the number of grid points needed to define an ion optic assembly. A majority of the linear, time-of-flight instruments described in this thesis are cylindrically symmetric about the time-of-flight axis. This greatly reduces the number of points needed to define the electric field as only a single (x, y) plane of potentials needs to be defined and the two faces of the plane are then defined as Neumann boundaries.

Once the electrodes have been defined (and then refined) individual voltages can be applied to each. As stated earlier, the superposition principle means that, at each time step, voltages can be changed and the whole field can then be recalculated with relative ease and speed. The time precision of the simulation is great enough that a pulsed electrode should be observed as a slope rather than a step function. Simply, a voltage switch and an electrode form a resistor-capacitor circuit which will have a time constant, $\tau = RC$, such that the voltage on the plate is given by

$$V(t) = V(0) + V_{\mathrm{d}} \exp\left[-\frac{t - t_{\mathrm{s}}}{RC}\right], \tag{3.10}$$

where $V(0)$ is the voltage on the plate before the switch, V_{d} is the potential difference between the baseline voltage before the switch and the target voltage after the switch, t_{s} is the time at which the switch is triggered, R is the internal resistance within the switching electronics, and C is the capacitance of the electrode.

Further additions can be made in an attempt to more fully simulate the ion optics; for example, a voltage ripple can be applied to each of the ion optics to model the instability of power supplies. At some point a line must be drawn, and if such exhaustive measures

are to be applied, an understanding of the other limitations of the simulation should be kept in mind.

3.2.4 Interpreting Simulation Results

Once the ion optics have been modelled and the particle trajectories have been calculated, the results of the simulation have to be interpreted. The most useful data to extract from the simulation are the final positions of the ions on the detector, and the times at which each ion arrives. From this information spatial and mass resolutions can be calculated. If the initial position of the particles are defined as originating from a progression of discrete point sources then the resulting positions on the detector should be separated into a progression of spots also. The distance between each spot allows the magnification of the image at that position, M_i, to be calculated and the spatial resolution of each point source can be determined from the spatial spread of the ions. Here the standard deviation of the ion positions, σ_y and σ_z (the spread parallel to the detector face), are used to calculate the FWHM,

$$\Delta R_{50\%,i} = 2\sqrt{2\ln(2)}\sqrt{\sigma_y^2 + \sigma_z^2} \approx 2.354\sigma. \tag{3.11}$$

Here it is assumed that $\sigma_y = \sigma_z = \sigma$ which should be the case in a cylindrically symmetric simulation. This resolution can then be used, along with the calculated magnification, to calculate the resolution at the sample surface,

$$\Delta r_{50\%,i} = \frac{\Delta R_{50\%,i}}{M_i}. \tag{3.12}$$

Although taking the FWHM of the image produced by a point source is simple enough *in silico*, in practice the production of a sample that acts as such a source is more troublesome. Samples used in experiment to ascertain the spatial resolution obtainable with an instrument are composed of a repeating pattern with well defined pitch. A common measure for the spatial resolution of images of these samples is to take the distance covered from 20% to 80% of the maximum intensity of an edge of a feature [164].

As has been shown in equation (3.11), the FWHM of a peak described by a Gaus-

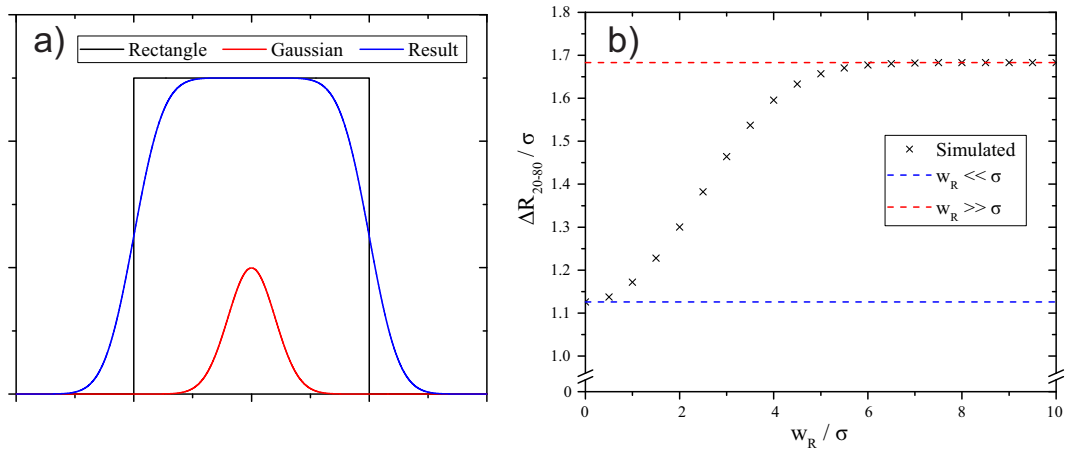

Figure 3.5: *Results from the numerical convolution of a Gaussian function and a rectangle function. Figure a) shows a plot of the rectangle function (in black), the normalised Gaussian function (in red), and the result of the convolution (in blue). In this plot the width of the rectangle is ten times the σ of the Gaussian. Figure b) shows the variation of the rising edge (from 20–80%) of the result of the convolution as a function of the width of the rectangle function (relative to the Gaussian width). Rising (from 20–80%) of a pure Gaussian function is shown in blue, and the upper limit to the observed trend is shown in red.*

sian distribution is related to the standard deviation of that distribution by a factor of $2\sqrt{2\ln(2)} \approx 2.354$. The rising edge of such a distribution, from 20–80% its maximum value, is related to the standard deviation by a factor of $\sqrt{2\ln\left(\frac{1}{0.2}\right)} - \sqrt{2\ln\left(\frac{1}{0.8}\right)} \approx 1.126$. As, in practice, a sample will not be comprised of discrete point sources, but rather a feature with a size much larger than the spatial resolution of the ion optics. The rising edge of such a feature will be a product of the underlying shape convolved with the Gaussian response function.

Figure 3.5 shows the results of a numerical convolution of a Gaussian function and a rectangle function. Figure 3.5 a) is a plot of a rectangle function (in black), a normalised Gaussian function (in red), and the result of the convolution of the former two functions (in blue). The width of the rectangle function is 10σ, where σ is the Gaussian width. The result follows the form of the rectangle function but with a blurring at each extremity. By measuring the rising edge of the this result, from 20–80%, for various different widths of the rectangle function, whilst keeping the Gaussian width constant, the plot in figure 3.5 b) is obtained.

Figure 3.5 b) shows the variation in the rising edge (from 20–80%), measured on the

result of the convolution of a rectangle function with a Gaussian function, with respect to the width of the rectangle function. The plot starts at the value for the rising edge of a pure Gaussian function ($\Delta R_{20-80} \approx 1.126\sigma$ – shown in blue), and rises as the width of the rectangle function is increased. The variation reaches an asymptote at $\Delta R_{20-80} \approx 1.683\sigma$ (marked in red).

Using the value for the rising edge of a feature from 20–80%, assuming that the feature is at least an order of magnitude wider than the resolution of the image, then in order to compare with experiment, the simulated resolution should be found by:

$$\Delta R_{20-80,i} \approx 1.683\sigma, \tag{3.13}$$

$$\approx 0.715\Delta R_{50\%,i}. \tag{3.14}$$

Both the magnification and the spatial resolution at the sample are dependent on their displacement from the time-of-flight axis. This means that it can be helpful to consider the standard deviation of these values over all of the point sources as well as the average. A high standard deviation implies that there is some distortion or aberration in the focussing property of the lens system; for example, a pincushion distortion in an image means that the magnification of that image increases with increasing displacement from the centre. There is likewise Petzval field curvature, which means that any imaging system that uses a curved medium (e.g., a glass lens or an electric field) to transfer the image of a flat surface cannot focus that image onto a plane. Instead the image is focussed across a concave surface: a consequence of the spherical aberrations observed in finite width lenses.

The mass resolution of a system is defined as

$$m/\Delta m \approx \frac{t}{2\Delta t}, \tag{3.15}$$

where t is the average arrival time of the ion packet, and Δt is the full width of the arrival time distribution at half of its maximum value. The approximation for obtaining the mass resolution directly from the TOF spectrum is used so that each and every simulation does not have to be calibrated (see the derivation in chapter 1). This resolution is also, by

definition, only valid for a given mass (or mass to charge ratio) and should be referenced accordingly.

As outlined in chapter 2, the detector used experimentally has a response time, and the PImMS1 camera further results in digital time-binned data. Equation (3.15) assumes that the mass resolution can be calculated from the distribution of arrival times, $g(t)$, but in an experiment with a detector that exhibits some response time, $h(t)$, the observed distribution will then be the result of the convolution integral of the two distributions,

$$f(t) = (g * h)(t) = \int_0^t g(\tau)h(t-\tau)d\tau. \tag{3.16}$$

If we assume that both $g(t)$ and $h(t)$ are close to Gaussian-like functions with standard deviations, σ_g and σ_h, respectively then the convolution of the two functions will be a further Gaussian function where

$$\sigma_f = \sqrt{\sigma_g^2 + \sigma_h^2}. \tag{3.17}$$

As well as being a convenient choice of functional form, it is also a good approximation that both the distribution of ion arrival times due to the ion optics and the detector response can be described by Gaussian functions. This means that $\Delta t_{50\%}$ can be defined explicitly:

$$\Delta t_{50\%} = 2\sqrt{2\ln(2)}\sigma_{\text{tot}}, \tag{3.18}$$

where

$$\sigma_{\text{tot}} = \sqrt{\sigma_{\text{ion}}^2 + \sigma_{\text{det}}^2}. \tag{3.19}$$

Here σ_{ion} is the standard deviation of the ion arrival time distribution, and σ_{det} is the standard deviation of the detector response.

It is important to bear this limitation in mind when interpreting simulation results as it is possible to invest large amounts of effort into reducing the value of σ_{ion} without

realising that σ_{tot} has already reached its limit,

$$\lim_{\sigma_{\text{ion}} \to 0} (\sigma_{\text{tot}}) = \sigma_{\text{det}}. \tag{3.20}$$

3.3 Summary

In this chapter, a selection of tools and methods has been presented that allow the prediction of the spatial and mass resolutions obtainable with a given MS instrument. The simplest, approximate, treatments of a system were presented that give insight into the mechanism behind the design of ion optics, and explains how a system *should* work. However, this model is not sufficient as it cannot give a quantitative measure of all of the various sources of aberrations that arise. For a more rigorous investigation into the performance of MS instrumentation a higher level trajectory simulation program is needed, for which SIMION 8.1 is used; and a brief explanation of how this program works was also presented.

With SIMION, a quantitative analysis of the an ion optic assembly can be obtained. The final challenge being the precise modelling of the assembly itself, as well as the definition of the ions that are to traverse it. The ion optic assembly can be relatively well modelled, but it is the ion definitions that hold back a fully complete simulation. Nonetheless, SIMION is a powerful tool that can accurately predict the relative behaviour of an ion optic, as well as the expected resolutions to within an order of magnitude, at the very least.

Finally within this chapter, some methods for the analysis of the results of SIMION simulations were presented. The proper analysis of these results is just as crucial as the setting up of the simulation in order for them to be properly understood. This is most relevant in understanding the role of the detection assembly in an instrument which is not modelled in SIMION.

With these tools, understanding the behaviour of ion optics is made far simper. This leads to the subject of the next chapter, in which both simulation and experimental re-

sults will be presented detailing the conversion of a conventional velocity-map imaging instrument, with the goal of purposing the instrument for use with the PImMS camera.

Chapter 4

Multi-Mass Imaging with the PImMS1 Camera

The motivation for using the PImMS1 camera with microscope-mode imaging mass spectrometry instrumentation comes from the camera's ability to acquire multiple ion images within the same duty cycle of an experiment — so called multi-mass imaging. This allows data to be obtained at a much higher rate as both the spatial and the chemical information of a sample are collected simultaneously. The disadvantage of this is that both the spatial and m/z resolutions are then defined by the quality of the ion optic assembly, as is the accessible m/z range. Any microscope-mode instrument designed will necessarily have to settle at some level of compromise between those three specifications on order to realise the benefit of the increased throughput.

In order to study the capability of the PImMS1 camera to perform multi-mass imaging a study was conducted involving the simultaneous acquisition of spatially resolved images of two species with different and distinct locations on a surface. The aim of this experiment was to ascertain the benefits and limitations of using the PImMS1 camera for such an application paving the way for more advanced instrument design.

In this chapter a study of the multi-mass imaging capability of the PImMS1 camera will be presented. First, results of the simulation of the instrument in question will be presented; these will next be compared to results obtained with a conventional CCD

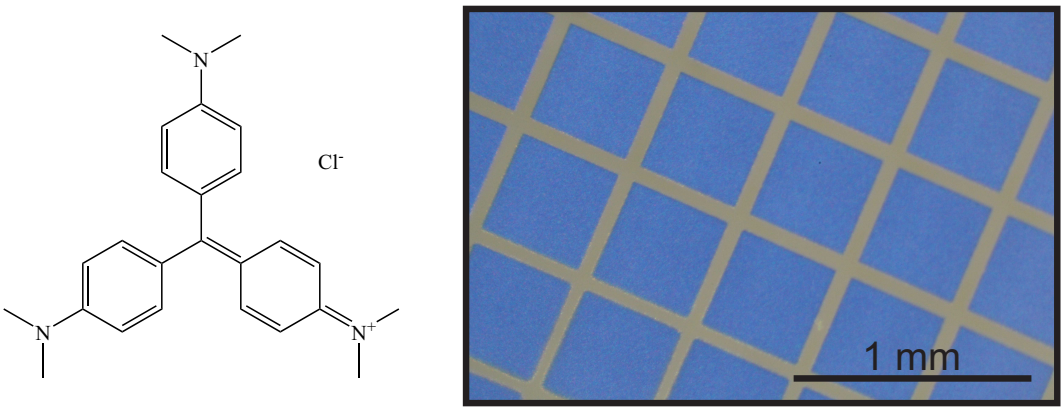

Figure 4.1: *The structure of the Crystal Violet molecule. The positively charged ion that is ablated under laser irradiation has a mass of 372 Da. The image on the right was obtained using an optical microscope and shows a well-produced grid pattern of Crystal Violet on an ITO coated glass slide.*

camera and PMT; then the tests involving the PImMS1 camera will be presented before; finally, the PImMS1 camera is tested, in direct comparison with a CCD camera and PMT, in the acquisition of multi-mass imaging data.

4.1 Simulation Results

Before testing the capability of an instrument to simultaneously produce resolved m/z and spatial information, it is useful to test the ability of that instrument to resolve both separately. This allows the general resolution trends to be understood and predicted when attempting to focus both at once.

These tests were first conducted using the converted velocity-map imaging instrumentation described in chapter 2. Crystal Violet (the structure of which is shown in figure 4.1) was chosen as the sample analyte for the initial tests. This molecule is easily ionised with simple laser ablation (as opposed to requiring a matrix to facilitate the process) which reduced errors in the reproducibility of experiments, which could otherwise have occurred during the sample preparation. It also persists on the sample surface so that a single sample will suffice for a days testing whereas more delicate samples can be exhausted after less than an hour of laser irradiation. Further still, it is relatively easy to handle, facilitating the production of well-defined samples that, thanks to their vivid colour, can be

easily analysed by optical microscopy (an example sample is shown in figure 4.1). Crystal Violet is ablated to form a singly charged ion ($C_{25}H_{30}N_3^+$) with a nominal mass of 372 Da. SIMION simulations (as described in chapter 3) were conducted in an effort to predict the expected trends in both the m/z resolution and spatial resolution as a function of the voltage ratios applied across the ion optic assembly.

Simulations were conducted using four ion source spots which were positioned at the sample plate of the instrument in a sequence along the y-axis. These spots were separated by 1 mm starting at the origin ($y = 0$, $z = 0$) and finishing at ($y = 3$ mm, $z = 0$). These four spots were chosen so that the image they would create would fit on the detector, which was modelled as with a diameter of 75 mm, as long as the magnification factor of the system was less than 12.5. The velocity distribution of the ions was set to that described in chapter 3, and the ions were defined with the nominal mass of Crystal Violet (372 Da). The ion optics were modelled on those in the converted velocity-map ion imaging instrument, as described in chapter 2, with the full length of the flight tube set to 615 mm.

Figure 4.2 shows a selection of the resolutions obtained from the simulations. The two plots in the top row, figures 4.2 a) and b), show spatial resolutions (defined as 20–80% of the rising edge of a feature — see equation (3.14)), whilst those in the bottom row, figures 4.2 c) and d), show m/z resolutions. The ion optic assembly was made up of a simple three electrode lens, and the last of these was held at ground in order to maintain a field-free drift length. In an arrangement such as this, the first electrode (the repeller) defines the total acceleration voltage of the ion optics (i.e. the total amount of potential energy transferred to each ion), and the second electrode (the extractor) defines the ratio of the strengths of the two electric fields generated by the ion optics (i.e. adjusts the focussing of the system). The two plots on the left, figures 4.2 a) and c), show data obtained with an acceleration of voltage of 4 kV, whilst the two on the right, figures 4.2 b) and d), show data obtained with an acceleration voltage of 10 kV. All of the graphs show the variation of resolution as a function of the voltage applied to the extractor electrode. Each plot consists of five different sets of data. The first four are illustrated with open markers and represent the resolutions for each of the four individual ion origin points used

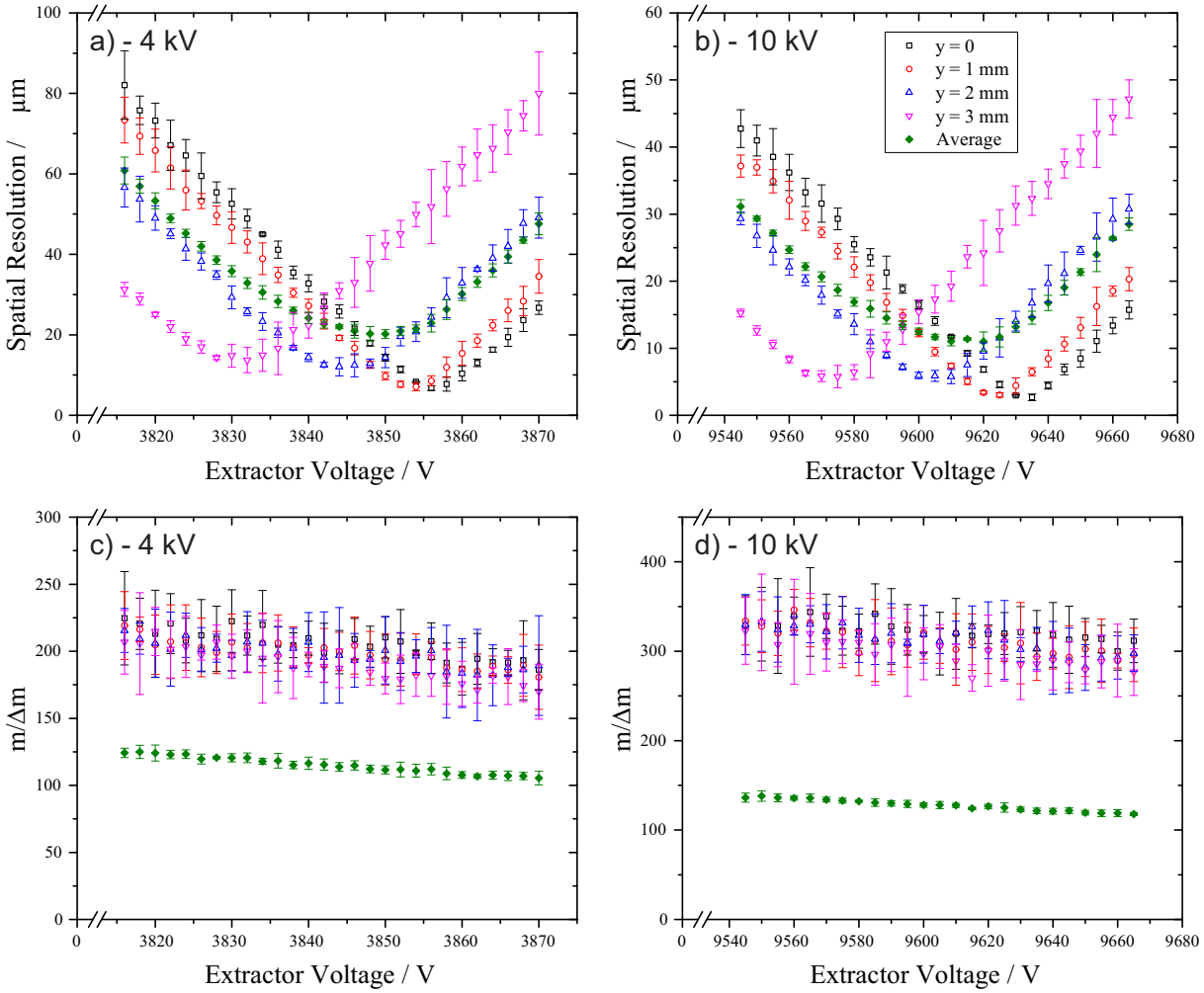

Figure 4.2: *Plots of the simulated spatial resolutions (top row), and m/z resolutions (bottom row) for both 4 kV (left column) and 10 kV (right column) acceleration voltages. The plots show how the respective resolutions were found to vary as a function of the extraction voltage applied to the ion optic assembly. The trends in resolution are shown both separately for each simulated ion source spot, as well as amalgamated into an average value. The key included in the top right plot is applicable to all four graphs.*

in the simulation. The fifth data set is illustrated by a filled marker and represents the resolutions obtained over the simulation as a whole (i.e. the aggregation of all four spots). For each data point, the simulation was run a number of times, and the resolutions were obtained for each of these runs. The data shown in the graphs is an average over all of these runs and the error bars shown are the standard deviation of each individual run from the average — i.e. the degree to which the simulation has converged. Whereas the average value for the spatial resolution is a simple average of the resolutions for each spot, the aggregate mass resolution is obtained by re-analysing the data set as a whole.

Figure 4.2 a) shows the variation of the spatial resolution, obtained with an acceleration voltage of 4 kV, as a function of the voltage applied to the extractor. It can be seen that each individual source position has a different optimal resolution: the extractor voltage required for the optimal spatial focussing of a point source positioned on the time of flight axis was found to be 3856 V whilst the voltages needed for optimal focussing of a point source one, two, or three millimetres displaced from the axis were found to be 3854 V, 3844 V, 3832 V respectively. Not only does each position need a different extraction voltage to achieve optimal focussing but there is also a difference in the optimal resolution obtainable from each position. The on-axis position can be focussed with a resolution of 6.8 μm whilst the off-axis positions can only be focussed to resolutions of 7.1 μm, 12.0 μm, and 13.7 μm respectively. These results are not unexpected as was explained in chapter 3: the discrepancy in the extractor voltage needed is the manifestation of Petzval field curvature whereby a planar sample is focussed onto a concave surface; whilst the worsening spatial resolution with deviation of the source from the time-of-flight axis is a spherical aberration arising from the ion optic design. Choosing the optimal averaged spatial resolution is not trivial: the lowest averaged resolution is 20.2 μm and is obtained at 3850 V but it should not be ignored that the difference in the resolutions of the four positions is smallest at 3842 V. At these voltages the ion image is magnified by a factor of 10.2 from the sample onto the detector.

The overall form of figure 4.2 b) is very similar to the previous figure. Here the acceleration voltage has been increased to 10 kV, and consequently the spatial resolutions obtained are improved compared to those obtained at the lower voltage; although, the image magnification is maintained at 10.2. This is because the electric fields that focus the particles are now stronger relative to the kinetic energy spread of those particles: the chromatic aberrations arising from the ionisation process are reduced. The best average spatial resolution is now 11.0 μm, and is obtained with an extractor voltage of 9620 V. This is the same voltage ratio as at 4 kV.

The two plots shown in figures 4.2 c) and d) depict the variation of the m/z resolution as a function of the voltage applied to the extractor electrode of the ion optic assembly

with an acceleration voltage of 4 kV and 10 kV respectively. Both graphs have the same features; namely, that the m/z resolution decreases with increasing voltage applied to the extractor electrode but that the decrease is small over the range shown. In both cases it is, in fact, possible to obtain much higher m/z resolutions than those shown. This can be achieved by applying a lower voltage to the extractor electrode but by doing this there will no longer be any discernible spatial focussing, and so the instrument could no longer be considered an imaging mass spectrometer. Both plots also show that the m/z resolution obtained for any individual ion source position is much higher than the m/z resolution obtained when taking all source positions together. This implies that the focussing ability of the instrument is not much dependent on the ion source position but that, instead, a deviation from the time-of-flight axis results in an increase in the total flight time so that ions from each of the source positions arrive at the detector in discrete packets with those positioned on-axis arriving first. As the m/z resolutions do not vary by much when compared to the spatial resolutions it is sensible to focus the instrument using the spatial resolution as the sole criterion. It is then found that $m/\Delta m = 112$ with a 4 kV accelerating voltage, and that $m/\Delta m = 127$ with a 10 kV accelerating voltage.

The plots above give an indication of the resolutions obtainable with the modified velocity-map imaging instrument. They indicate that, as the spatial resolution is far more sensitive to a change in the focussing of the instrument, the instrument should be spatially focussed preferentially to focussing in the m/z domain, and that there should be only minor aberrations in the images obtained. This leads to the conclusion that the conversion of a velocity-map imaging instrument is more than capable of providing the necessary resolving powers to test the multi-mass imaging capability of the PImMS1 camera.

4.2 Comparison of Experiment with Simulation

Experimental data were obtained, complementary to the SIMION simulations outlined in the previous section, using the methods outlined in chapter 2. The velocity-map imaging instrument was modified to accept the ITO-coated glass slides and the high resolution

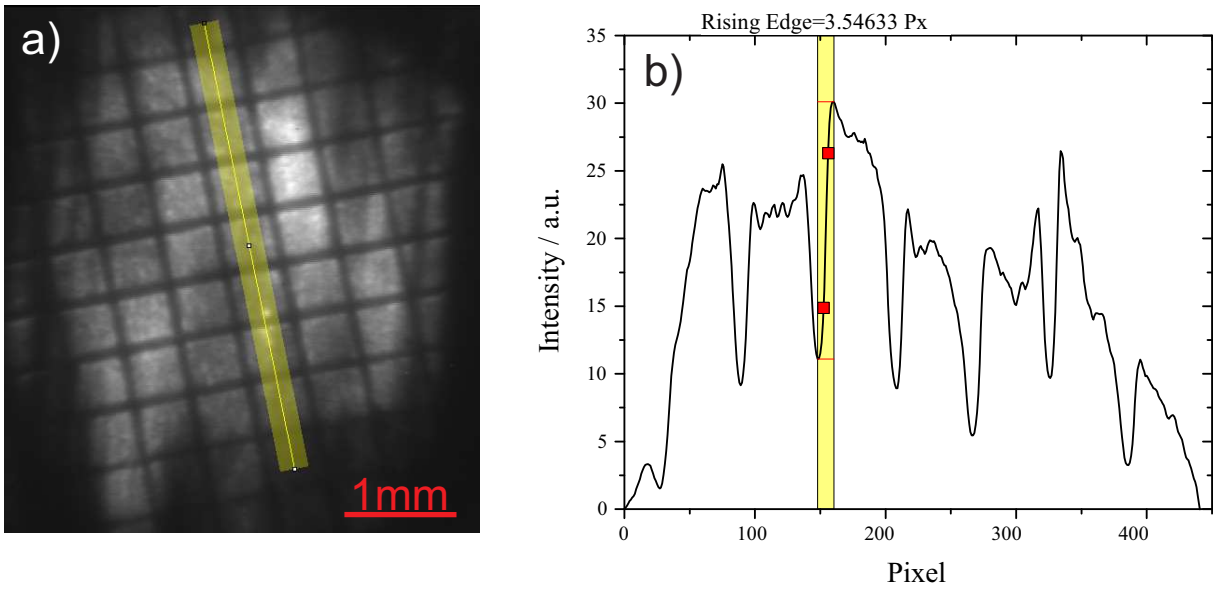

Figure 4.3: *An ion image of Crystal Violet (nominal mass 372 Da), distributed in a grid pattern, alongside a plot of a line profile taken across the image. The line profile includes an example of the spatial resolution analysis method: measuring the rising edge of a feature. The image was obtained at an acceleration voltage of 4 kV.*

CCD camera was mounted onto the detector, along with a PMT, focussing at the P47 scintillating screen.

A saturated solution of Crystal Violet in 50% ethanol was sprayed onto the ITO-coated glass slides using the electrospray deposition equipment detailed in section 2.3. The solution was sprayed through a Nickel mesh with a 75% transmission, a wire thickness of 67 μm, and a wire pitch of 500 μm (Goodfellows NI008720), producing a grid pattern as was shown in figure 4.1). After spraying, the grid was carefully removed in order to avoid damaging the structure of the sample.

4.2.1 Spatial Resolutions

Images were obtained using the CCD camera, and time-of-flight spectra were obtained using the PMT. The laser power was adjusted so that there was a steady signal observed with the camera. Due to the relative indifference of the mass resolution on the voltage ratios, the focussing of the instrument was adjusted to give the best image resolution. With the acceleration voltage set, the voltage applied to the extractor electrode was changed, and the CCD camera signal was monitored. Once the optimum voltages had been found

the gate for the camera image intensifier was shifted to overlap with the most intense peak in the time-of-flight spectrum, and ion images were summed over a number of laser shots (from 1000 to 10,000). These were then saved on a PC along with the relevant time-of-flight spectra from an oscilloscope. Figure 4.3 a) shows an ion image of the Crystal Violet grid pattern obtained with an acceleration voltage of 4 kV, summed over 2000 laser shots. The grid pattern is clearly visible indicating a spatial resolution better than the Nickel mesh wire diameter of 67 μm. The intensity across the image appears to be uniform indicating that both the application of the sample onto the glass slide, and the intensity of the laser profile were uniform.

In order to obtain a more quantitative measure of the spatial resolution of the sample several line profiles were taken perpendicular to the repeating pattern (e.g. the yellow stripe across the image in figure 4.3 a)). A plot of one of the profiles is shown in figure 4.3 b). The line profile plot is shown as a function of the CCD camera pixels but this can be converted to reflect the distance on the sample as the pitch of the repeating pattern is known: the sample has a pitch of 500 μm which can be compared to the pitch of the minima in the profile, in this case 59.4 Px, resulting in a ratio of 8.42 μm/Px.

The common method, within the field of microscope-mode ion imaging, for calculating the spatial resolution of an image, is to use the distance of the rising or falling edge of a feature from 20% to 80% of its intensity [58, 61, 67, 83, 164]. Figure 4.3 b) illustrates this measurement for the rising edge of one of the peaks in the line profile taken from the accompanying image. The measured value of 3.55 Px corresponds to a spatial resolution of 29.9 μm. This evaluation can then be repeated for each edge and an average value can then be obtained. Using this methodology the spatial resolution of the image shown in figure 4.3 a) was found to be 35.4 μm with a standard deviation of 10.6 μm. This is a worse resolution than that expected from the simulations presented in the previous section which predicted a resolution of 20.2 μm. The simulated spatial resolution was obtained with an extractor voltage of 3850 V whereas the experimental image was obtained with an extractor voltage of 3914 V.

There is no trend across the image indicative of the spherical aberrations observed

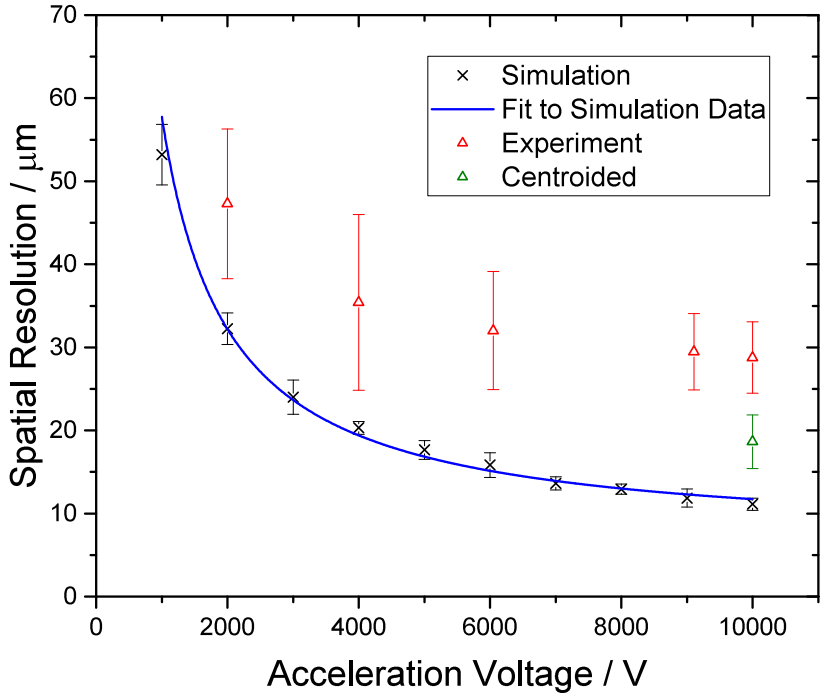

Figure 4.4: *A plot comparing the spatial resolutions obtained in both experiment and simulation as a function of the acceleration voltage. The blue line is a fit to the simulation data marked as black crosses. The experimental data are shown as red triangles with error bars representing one standard deviation from the mean value, and a datum for the spatial resolution after centroiding is marked by the green triangle.*

in the SIMION simulations. The variation across the sample, expressed as the standard deviation of the resolution measurements above, would likely obscure such a small feature if it were to be present. This variation across the sample likely arises from inconsistencies in either, or both of, the sample surface layer, or the laser profile.

In order to further assess the quality of the simulation as a model for the instrument further ion images were obtained of similar Crystal Violet grids. Each of these images was then analysed as before to produce the plot shown in figure 4.4 which shows the variation of spatial resolution as a function of the acceleration voltage applied to the ion optics. The red triangles represent the experimental data with error bars of one standard deviation from the mean value. The black crosses are the spatial resolutions predicted by the SIMION simulations and these points are fit by the blue line which goes with the inverse of the acceleration voltage. The form of this fitting function was chosen as it describes

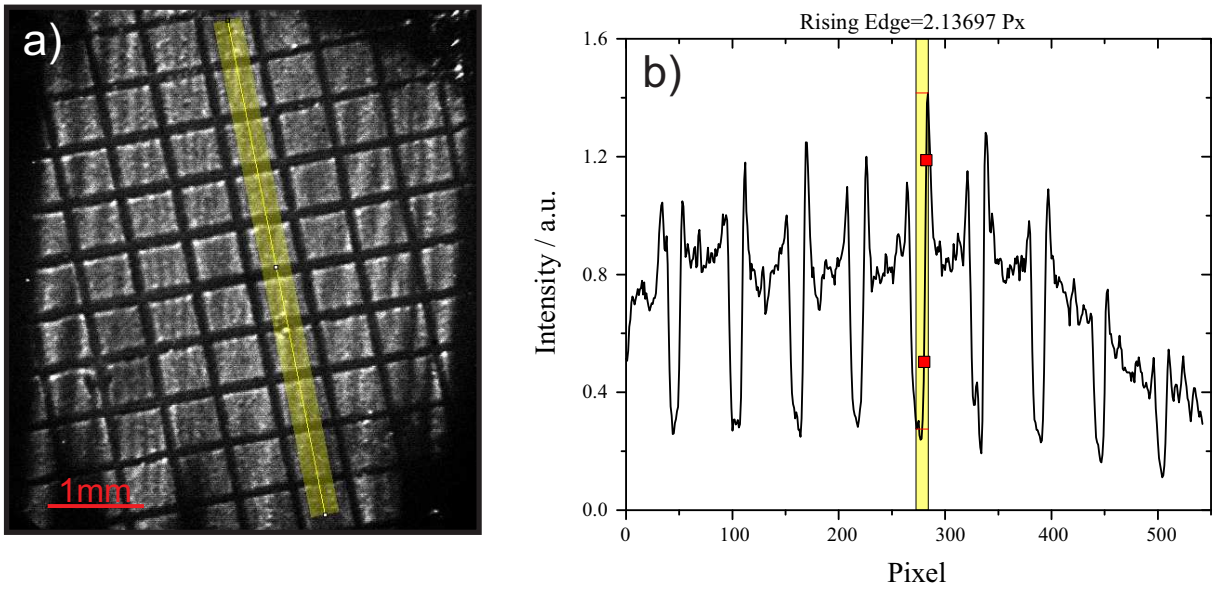

Figure 4.5: *A centroided ion image of Crystal Violet, distributed in a grid pattern, alongside a plot of a line profile taken across the image. The image was obtained over 10,000 laser shots with the image for each shot being centroided and then added to a summed image. The image was obtained at an acceleration voltage of 10 kV. This image along with a similar analysis method is also presented in the DPhil thesis of Benjamin Winter [46].*

the reduction in the contribution to the spatial resolution of chromatic aberrations [163].

It can be seen that the agreement between experiment and simulation is closer at lower acceleration voltages, and that the two trends diverge further as the voltage is increased. Whilst the simulated spatial resolution continues to follow the inverse trend up to an acceleration voltage of 10 kV, the experimental resolution plateaus at a value of roughly 30 μm. Again, it is the contribution from the detector which is limiting the achievable resolution of the experiment, whereas this is not taken into account for the resolutions obtained by simulation.

A further image was acquired, this time with on-the-fly image centroiding (as described in chapter 2). The image was obtained over 10,000 laser shots as the process of centroiding the image results in a reduction in the signal level. The image was acquired from the same sample of Crystal Violet used in the previous experiments, and with the same 10 kV acceleration voltage.

The resultant centroided ion image is presented in figure 4.5 a). A threshold level of 17 was applied so that all pixels with a value of 16 or lower were reduced to zero. This was

found to almost entirely eliminate the background signal in each individual image[1].

The spatial resolution of the centroided image shown in figure 4.5 a) was calculated using the same method as with the previous images. A sample line profile taken from the image is shown in figure 4.5 b), and the features presented are clearly sharper than that shown earlier in figure 4.3 b). The image pitch is, this time, found to be 57.4 Px which corresponds to a ratio of 8.71 μm/Px. This, in turn, leads to a spatial resolution of 20.1μm with a standard deviation from this mean of 4.01μm. This is much closer to the simulated spatial resolution, obtained with an acceleration voltage of 10 kV, of 11.1μm; however, it does not compensate completely for the discrepancy implying that the blurring of the image from the detector is not completely eradicated by the centroiding process.

The spatial resolutions, obtained by experiment, have here been shown to follow the trends predicted in the SIMION simulations. The absolute magnitude of the resolution predicted by resolution is of the same order as was predicted by the simulation but as that resolution is improved discrepancies do appear as the experimental detector becomes the limiting factor. This disparity can be overcome, at least to some extent, by certain analysis techniques such as centroiding.

4.2.2 Mass Resolutions

The mass resolutions predicted by simulation do not vary considerably with the voltage applied to the extractor electrode. Over a wider range of ratios it is possible for the mass resolution to be much improved but this completely sacrifices any spatial resolving power. For such a simple, linear, time-of-flight instrument, without the aid of more advanced pulsing techniques, there is little that can be done to avoid this.

To more completely characterise the instrument, the mass resolving power was also tested. Figure 4.6 shows a simulated frequency plot of the arrival times of ions in SIMION. The simulation was slightly altered from the original parameters to better predict the true shape of a time-of-flight peak in the mass spectrometer. Rather than producing ions at

[1]This image along with a similar analysis method is also presented in the DPhil thesis of Benjamin Winter. There, this final resolution is compared with further, impressive, improvements in the focussing of the ion optics using a novel pulsing technique [46].

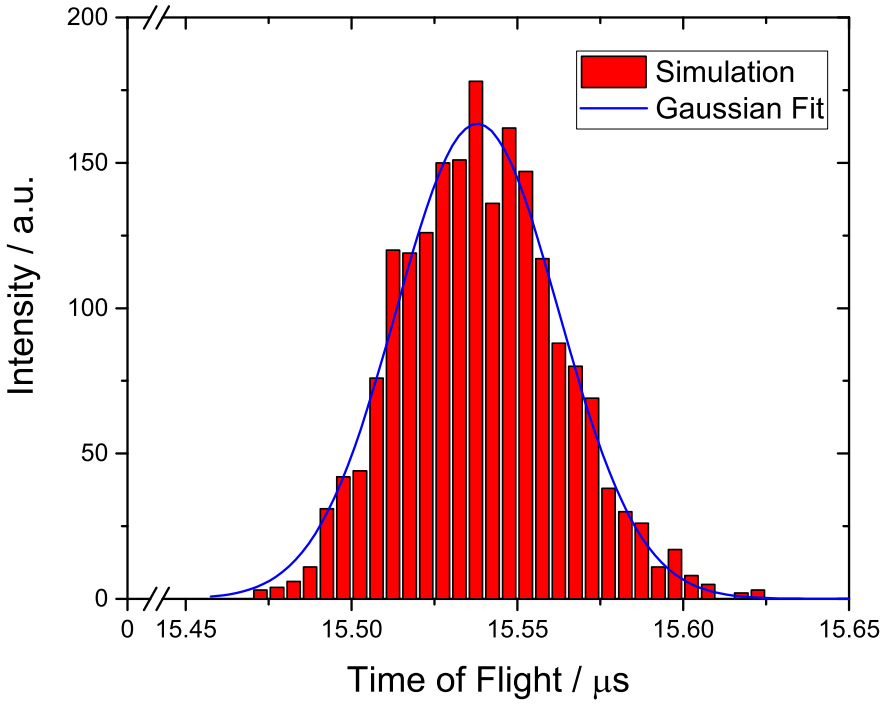

Figure 4.6: *A simulated time-of-flight peak with a Gaussian distribution fit. The ions were generated with the same velocity distributions as in previous simulations but with positions distributed evenly across the repeller plate within a circle with a radius of 3 mm.*

four discrete points on the repeller plate, ions are created according to a uniform random distribution within a circle on the face of the repeller plate, centred on the time-of-flight axis and having a radius of 3 mm. This simulation gives no information on the spatial resolving power of the instrument but creates a more continuous distribution. It can be seen that the Gaussian distribution in figure 4.6 fits closely to the distribution of the simulated arrival times. From this it can be expected that a time-of-flight peak obtained by experiment should also have considerable Gaussian character.

Figure 4.7 shows a plot of the time-of-flight spectrum, obtained with the PMT, of the Crystal Violet sample[2]. The spectrum was acquired under the same conditions as the image shown in figure 4.5 at an acceleration voltage of 10 kV. A number of peaks are evident in the spectrum with the most intense peak being that of the Crystal Violet parent

[2]These time-of-flight data are also presented in the DPhil thesis of Benjamin Winter although the subsequent analysis methodology differs [46].

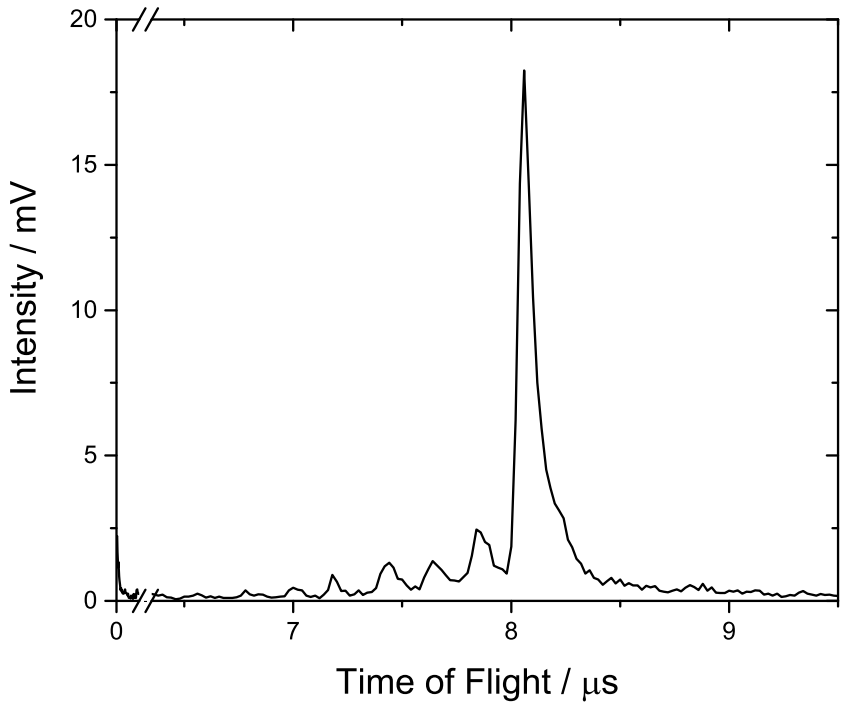

Figure 4.7: *A plot of the TOF spectrum of a sample of Crystal Violet, at an acceleration voltage of 10 kV, obtained with a PMT directed at the P47 scintillating screen. These TOF data are also presented in the DPhil thesis of Benjamin Winter [46].*

ion. The preceding smaller peaks observed with shorter times-of-flight likely arise from the substitution, in various combinations, of the six methyl groups by protons from the solvent (demethylation) [165].

The peaks in the spectrum do not appear to strictly follow a Gaussian distribution, but as with the spatial resolution measurements presented earlier, this is not entirely surprising. Again, the detector has an inherent response function which is convoluted with the true ion signal to give the observed signal. For time-of-flight measurements, it is the decay time of the scintillating screen, here a P47 phosphor coating applied to a fibre optic bundle, that is most likely to be the limiting factor (see the discussion of detector time-of-flight convolutions in section 3.2.4). Literature values for the decay time of the phosphor vary with values such as 80 ns, 114 ns, or 168 ns being just a sample [71, 166, 167]. What is more, these three example decay times were chosen from those articles which explicitly define the measure of the decay time (in all three of these cases it is defined as the time

for the intensity to fall from 100% to 10%); many other articles are less explicit with their definitions. These decay times can be compared to the width of the simulated ion peak shown in figure 4.6 which is approximately 60 ns.

To compensate for this long exponential tail, a program was designed to fit the discrete convolution of a Gaussian distribution and an exponential decay to the experimental data. The program uses a Nelder-Mead simplex fitting algorithm to optimise the parameters of the Gaussian distribution for a given exponential decay constant [168].

The equations used to define this distribution are,

$$f(t) = g(t) * r(t), \tag{4.1}$$

$$g(t) = A.\exp\left[-\frac{1}{2}\left(\frac{t - t_{\mathrm{Av}}}{w}\right)^2\right], \tag{4.2}$$

$$h(t) = \begin{cases} 0 & \text{if } t < 0 \\ N.\exp\left[\frac{-k.\ln(10)}{\tau_{1/10}}.t\right] & \text{if } t \geq 0 \end{cases}, \tag{4.3}$$

where the convolution, $f(t)$, is used as the trial fit to be applied to the observed signal, $g(t)$ is the true signal (here our trial Gaussian distribution), and $r(t)$ is the response function (here the exponential decay). The form of $r(t)$ assumes that, as the rise time of the P47 scintillator has been measure as being over an order of magnitude shorter than the decay time, it can be assumed to be negligible. The Gaussian amplitude, A, average value, t_{Av}, and the Gaussian width, w, are the variable used in the fitting procedure; whilst N is the amplitude of the exponential decay, which has a set decay time from 100% to 10%, $\tau_{1/10}$. The discrete convolution is obtained by applying the response function to the true signal at every point across a discrete time-line so that,

$$f[t] = \sum_{i=t_{\min}}^{t_{\max}} g[i]r[t-i], \tag{4.4}$$

where $t_{\min}$ and $t_{\max}$ represent the extremities of the data set. As the response function is an exponential decay, $r[t-i]$ will only be non-zero whilst $t > i$, so the equation can be

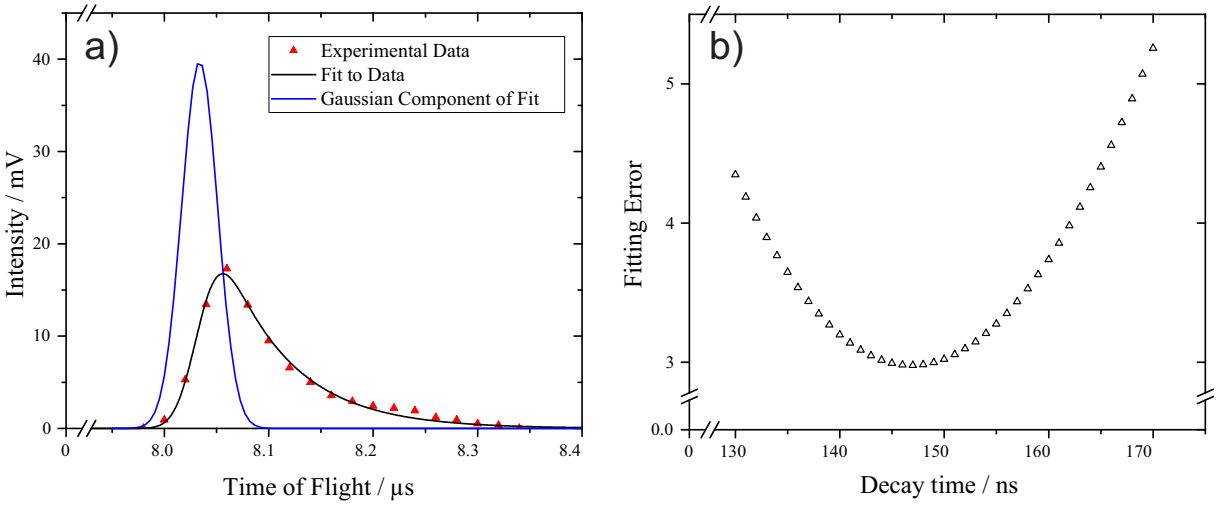

Figure 4.8: *A plot of the most intense peak from the time-of-flight spectrum shown in figure 4.7 fit with the discrete convolution of a Gaussian distribution and an exponential decay, and a plot of the fitting error obtained for different exponential decay constants. In a) the experimental data are represented by the red squares, the fit is represented by the black line, and the Gaussian component of the fit is represented by the blue line; whereas, in b) the open black triangles represent the fitting error (sum of square deviations) as a function of the decay time from 100% to 10% in nanoseconds.*

simplified to,

$$f[t] = \sum_{i=t_{\min}}^{t} g[i]r[t-i]. \tag{4.5}$$

The result of the discrete convolution is then compared to the experimental data and a least squares fitting error is calculated. This is the metric used in the Nelder-Mead algorithm to search for the optimum parameters of the Gaussian distribution. This methodology for fitting is not fool-proof, as it is possible for the fitting algorithm to become trapped in a local minimum rather than the true global minimum. By leaving the exponential decay time, $\tau_{1/10}$, out of the fitting process (as here the process is repeated for different fixed values of the decay time) a plot of the optimum fitness as a function of decay time is obtained. If this graph is free from discontinuities it can be assumed that there is no contest between adjacent local minima increasing the confidence of the fit.

With this fitting process, the fit with the least error can, tentatively, be considered to give both the time-of-flight resolution due to the ion optic assembly, and an estimate of the decay time of the scintillating screen. The values produced from such a fitting method should be read with caution: there is no guarantee that the time-of-flight peak arises from

a single species so the application of a single Gaussian distribution is assumptive.

Figure 4.8 a) shows the result of the discrete convolution fitting algorithm when applied to the most intense peak isolated from the time-of-flight spectrum in figure 4.7. Figure 4.8 b) shows the fitting error obtained with different values for the exponential decay constant. The decay constant represents the time taken for the intensity to fall from 100% the maximum value to 10%. The smallest fitting error indicates the closest fit, and is found with an exponential decay constant of 148 ns. The fit in figure 4.8 a) was obtained using this optimum value. The blue peak represents the Gaussian component of the fit with an average value of 8.03 μs and a full-width-at-half-maximum of 40.4 ns. Using the approximation, $m/\Delta m \approx t/2\Delta t$, a m/z resolving power of approximately 100 is found for the ion optic assembly (compared with 120 found by simulation). In contrast the full width at half maximum of the raw peak is found to be roughly 83 ns leading to a resolving power of 48.

The mass resolutions, obtained by experiment, have here been shown to be limited by the detector technology; and specifically, the decay time of the P47 phosphor screen. It has been shown that it is possible to account for this and so to calculate a resolving power for the ion optic assembly. This analysis cannot lead to the resolution of overlapping peaks; it only offers to "de-convolute" the decay of the phosphor screen from a Gaussian-like time-of-flight signal. Despite this, these "de-convoluted" m/z resolutions show a reasonable agreement with simulation, and they are more than sufficient to allow for an analysis of a multi-mass imaging sample.

4.3 Experiments with the PImMS1 Camera

In the previous section an experiment was presented that demonstrates the use of conventional technologies, a CCD camera and a PMT, being used with the modified velocity-mapping instrument. In this section a direct comparison will be presented between a mass spectrum obtained with the PImMS1 camera and one obtained simultaneously with a PMT. The data presented in this section were acquired using the same velocity-mapping

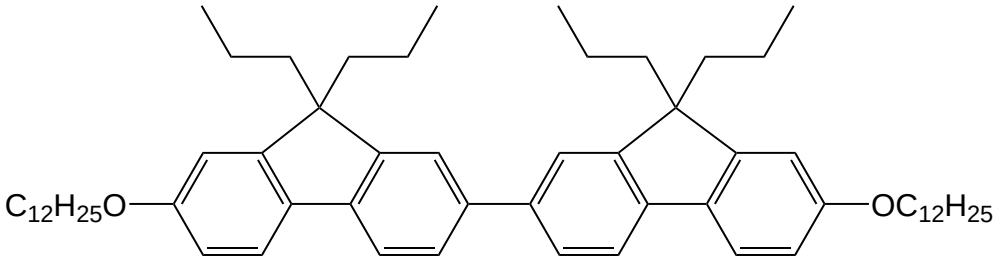

Figure 4.9: *The structure of the E398 molecule. The molecule has a nominal mass of 867 Da.*

instrument but with an improved mass resolution obtained using the PEDA pulsing technique[3].

For this experiment, a new sample was prepared using the Exalite dye, E398. The structure of this molecule is shown in figure 4.9. This chemical has a mass of 867 Da and also benefits from all of the advantages enjoyed when using Crystal Violet as a sample: that a solution of the species can be easily applied to a sample plate, and that the signal obtained under laser irradiation is strong and persistent. A saturated solution of the dye in 50% Methanol was sprayed onto an ITO coated glass slide through a Nickel mesh, in the same manner as before, leaving a grid pattern of squares.

The PMT was placed alongside the PImMS1 camera so that it could provide a direct comparison with any spectra obtained. The camera was mounted at a distance of 23 cm from the scintillating screen of the detector. In order to focus the camera at this distance a 10 mm spacer was inserted between the c-mount lens and the camera body. This also reduced the field-of-view of the camera to have a diameter of approximately 25 mm. The camera cycle was set at a rate of 80 MHz which corresponds to a timing precision of 12.5 ns.

Data were obtained with an acceleration voltage of approximately 8.5 kV over a total of 20,000 laser shots. Complementary PMT data were taken at the same time in shorter exposures of 100 laser shots. Figure 4.10 shows the comparison of the mass spectrum

[3]The simulation and optimisation of the instrument undertaken to obtain these improved mass resolutions are beyond the scope of this work but are presented in the DPhil thesis of Benjamin Winter [46].

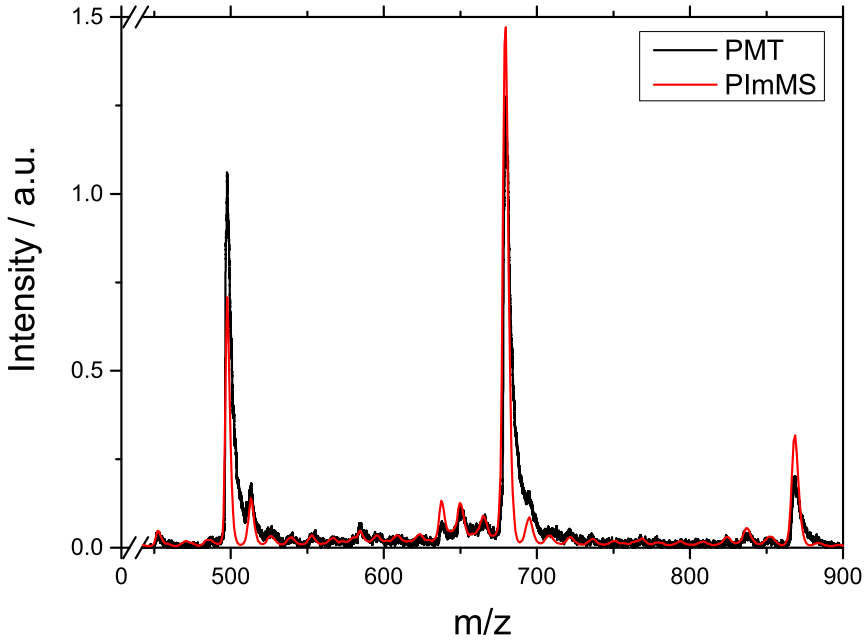

Figure 4.10: *A mass spectrum of E398 obtained both with a PMT (black line), and with the PImMS1 camera (red line). The three most intense peaks represent the parent ion and two fragment ions.*

acquired with the PImMS1 camera with that obtained with the PMT. The intensities of the two spectra have been artificially adjusted in order to make them more comparable. The disparity between the relative peak heights in the two spectra is likely due to changes in the sample composition affected after the continuous irradiation.

The spectra were analysed separately and can be seen to closely agree in terms of the existence of peaks and their positions. The peak observed with the highest mass was identified as the parent ion peak ($m/z = 867$). The two most intense peaks, observed at lower masses than that of the parent ion, were identified as products of fragmentations where either or both of the ether links had been cleaved (leaving $m/z = 682$ or 497 respectively). This identification is corroborated, in both cases, by the presence of small shoulder peaks that appear close to each of these intense peaks with m/z values 16 units higher than that observed for the intense peaks themselves. These likely arise from cleavage across the other side of the ether link.

From a qualitative inspection of the two spectra, there is some indication that the

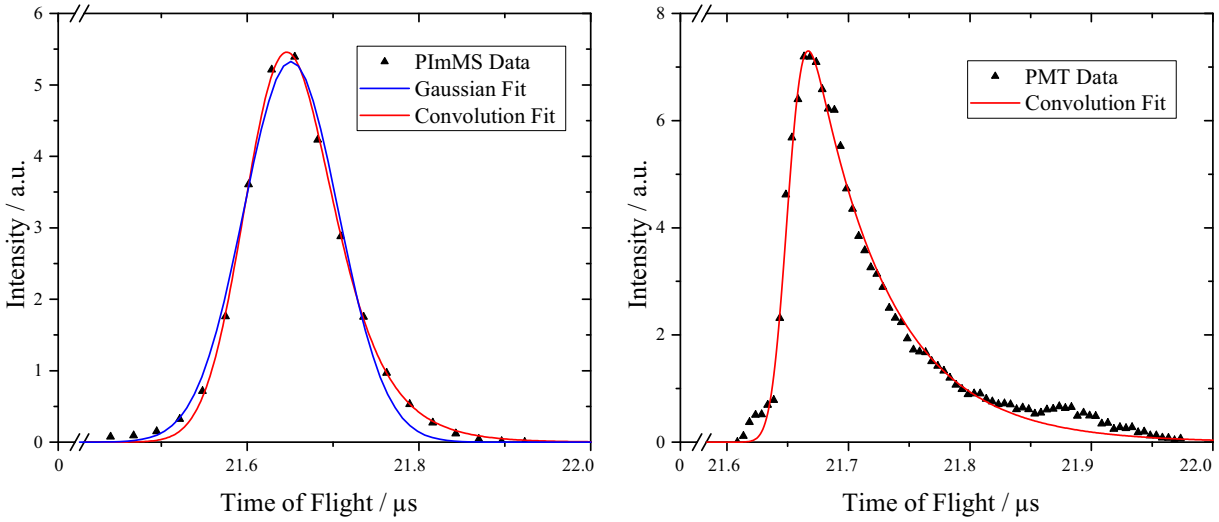

Figure 4.11: *Two graphs comparing the fitting of time-of-flight peaks from a) a PImMS1 data set, and b) a PMT data set. The experimental PImMS1 data in a), marked by the black triangles, is fit by both a Gaussian distribution, in blue, and the discrete convolution of a Gaussian distribution and an exponential decay, marked in red. The experimental PMT data in b), also marked by black triangles, is only fit by the discrete convolution, in red.*

falling edges of peaks in the PMT data have a longer tail than those observed in the PImMS1 data set. As an event is triggered in the PImMS1 camera after a certain threshold level of charge has been gained it follows that the PImMS1 camera would be less sensitive to the exponential decay of the P47 scintillation.

Figure 4.11 a) shows a comparison of two fitting methods applied to the most intense peak observed in the mass spectrum of the data obtained with the PImMS1 camera. The solid black triangles represent the experimentally obtained PImMS1 data points; the blue line represents the optimal fit of a Gaussian distribution to these data; and the red line represents a fit obtained using the same discrete convolution as described in the previous section. As before the convolution fitting was performed with various values for the exponential decay constant. The fit with the least error was obtained with an exponential decay time (measured from 100% to 10%) of 48 ns. With this decay time, the Gaussian component of the convolution fit is found to have a peak width of 46.1 ns. This gives an approximate mass resolving power of 206. When fitting with the Gaussian distribution alone, a width of 60.7 ns is obtained which corresponds to a mass resolving power of 156.

Figure 4.11 b) shows the equivalent peak obtained with the PMT fit with the convolution fitting program. The experimental data are represented by the black triangles, and a fit, using the convolution fitting program, is presented as the red line. Here, the optimum decay constant (from 100% to 10%) is found to be 143 ns corresponding to a mass resolving power of 375.

It can be seen that, as with the PMT data, the PImMS1 peak can be better fit using the convolution of a Gaussian distribution and an exponential decay rather than the Gaussian distribution alone. This, obviously, also leads to an improved mass resolution when using the discrete convolution fit, as some of the width of the peak is absorbed into the decay. Although this phenomenon can be rationalised by the PImMS1 camera's sensitivity to the tail end of the phosphor screen decay, caution should be exercised when assuming that this is the case. The higher resolving power obtained with the PMT compared to the PImMS1 camera, is expected and is due to the difference in the response times of the two different technologies. The PMT has a response time of 2-5 ns whereas the PImMS1 camera has a timing precision of 12.5 ns.

The detector used in this was the same as that used in the previous section so the observed decay constants should be the same; however, the PImMS camera triggers an event from the rising edge of a peak so the peak shape obtained with the PImMS1 camera would be expected to exhibit much less character derived from the exponential decay of the phosphor screen with only a 48 ns decay observed compared with the 143 ns decay observed with the PMT in the same experiment. This value can be compared with the previous decay constant found with the PMT in the previous section, 148 ns. It is encouraging that the decay constants found with the PMT are in such close agreement across the two experiments, as these values should only depend on the detector decay time.

Figure 4.12 a) shows the ion image of the grid pattern of E398, obtained with the PImMS1 camera. It can immediately be seen that the field-of-view is much reduced compared to that observed with the CCD camera in the previous section. The image also has a lower spatial resolution, as some of the squares are hard to resolve by eye. The accompanying profile plot shown in figure 4.12 b) shows the analysis of this profile from

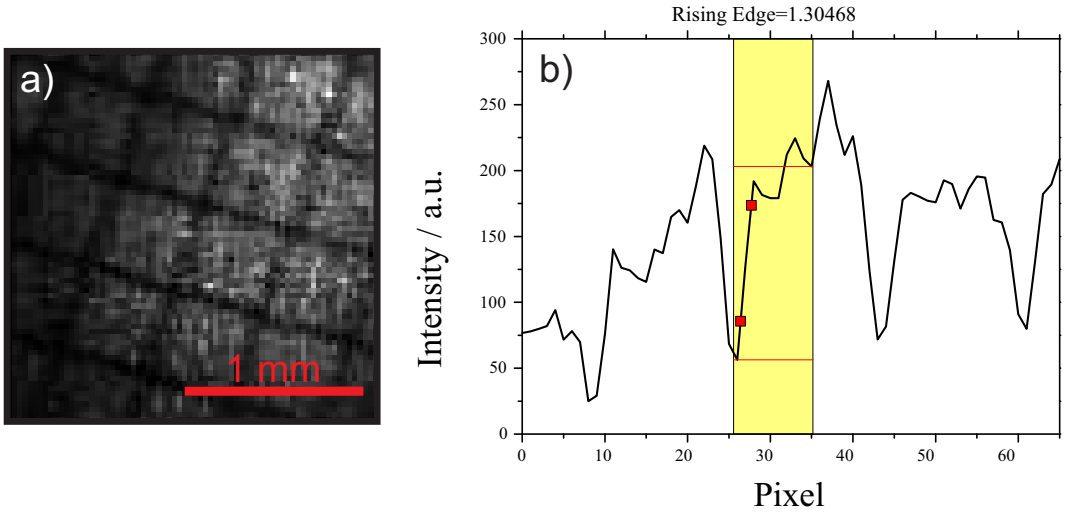

Figure 4.12: *An ion image of E398 in a grid pattern, obtained using the PImMS1 camera, alongside a plot of a line profile taken from the image. The data were obtained with an acceleration voltage of 8.5 kV.*

which a spatial resolution of 46.7 μm is obtained. This confirms that the resolution is worse than that obtained with the CCD camera which was found to be approximately 30 μm. The PImMS1 sensor is only made up of 72×72 pixels which, when compared to the CCD camera's 768×576 pixels, is relatively few. Despite the difference in field-of-view observed in the two separate experiments, for the image acquired with the CCD camera each pixel corresponds to approximately 8.5 μm at the sample surface, whereas for the image acquired with the PImMS1 camera each pixel corresponds to over 28 μm at the sample surface. This drastic difference in pixel resolution explains the differences between the observed images.

In this section, the PImMS1 camera has been tested in conjunction with a converted velocity-map imaging instrument. It has been found that the pixel resolution limits the achievable spatial resolution, although this can be reduced by adjusting the field-of-view. The timing precision of the camera is also not as good as a standalone PMT, but the limiting factor for the m/z resolution of the instrument is the phosphor screen. However, the strength of the PImMS1 camera lies in the flexibility and quality of the data it produces. However, this strength will only present itself when analysing samples with spatially separated chemical species.

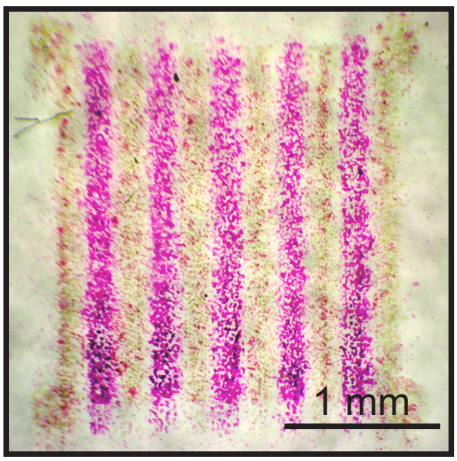

Figure 4.13: *An optical microscope image of the sample prepared for the multi-mass imaging experiments. Alternating stripes of Auramine O (yellow/orange) and Rhodamine 590 (pink) were applied to an ITO coated glass slide using an inkjet printer. The surface was printed ten times to increase the density of sample within each stripe.*

4.4 Multi-Mass Imaging

The experiments presented so far in this chapter have showcased the development of a microscope-mode imaging mass spectrometer, converted from a conventional velocity-mapping ion imaging instrument. These developments have culminated in the addition of the PImMS1 camera, creating an instrument that should be capable of multi-mass imaging where the location and mass of analytes on a surface are simultaneously acquired. In order to fully test this capability a different type of sample must be prepared.

Figure 4.13 shows an optical microscope image of an ITO coated glass slide onto which alternating stripes of Auramine O (nominal mass 268 Da), and Rhodamine 590 (nominal mass 443 Da) have been applied. The sample was produced using an inkjet printer as described in section 2.3.2. Each stripe has a width of roughly 400 μm so that the whole sample covers just less than the 5 mm$\times$5 mm field-of-view that can be imaged by the CCD camera. The sample was printed in a total of ten coatings in order to give a thick, and relatively consistent, coating. It can be seen from the optical image that there is very little cross contamination of the two different dyes between adjacent stripes.

This sample was inserted into the repeller plate of the converted velocity-mapping ion image instrument and the same conditions were applied as were used in section 4.2.1, i.e

static electric fields were used, and the total acceleration voltage applied to the ion optics was set to 2 kV. The instrument was set up so that the CCD camera and the PImMS1 camera could be exchanged with relative ease. The focussing distances of the cameras were adjusted, as much as was possible, so that the entirety of the phosphor screen could be seen by both. The PMT was also aligned so that a time-of-flight spectrum could be obtained to accompany the CCD camera images and to assist in the positioning of the CCD camera intensifier gate. The PImMS1 camera cycle rate was adjusted to 40 MHz corresponding to a timing precision of 25 ns.

4.4.1 Results with the CCD Camera

The experiment was conducted with the CCD camera mounted behind the detector. A number of images were obtained with the intensifier gate positioned at different points along the time-of-flight. This gate position was monitored against the time-of-flight spectrum, obtained with the PMT, using an oscilloscope. Each image was summed over roughly 500 laser shots whilst the accompanying time-of-flight spectra were averaged over a shorter period of 100 laser shots.

Initially the gate for the CCD camera intensifier was set to such a large width that it encompassed all of the major peaks that were assumed to relate to both the Auramine O and the Rhodamine 590. The mass spectrum, obtained with the PMT, and presented in figure 4.14 a), shows the major peaks that were selected by the intensifier gate alongside the acquired ion image in figure 4.14 b).

A large number of peaks are observed in the mass spectrum. It is a simple assumption to make that those peaks with a mass greater than the parent mass of Auramine O (268 Da) must arise from fragments of the Rhodamine 590[4]. The peak progression observed in the Auramine O peaks is likely due to sequential removal of methyl groups. The Rhodamine 590 parent ion is not observed in the mass spectrum but instead a peak is observed at $m/z = 398$ due to the cleavage of an ester link in the parent ion.

The ion image shown in figure 4.14 b) already shows some distinction between the

[4]This assumes that the Auramine O does not form clusters in solution.

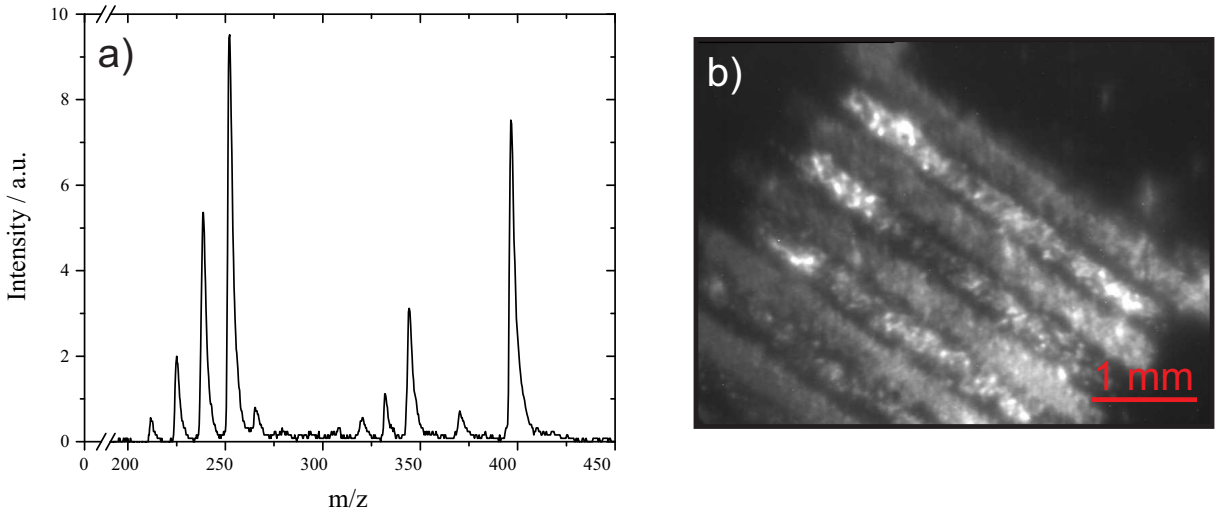

Figure 4.14: *The mass spectrum (obtained with a PMT) and accompanying ion image of the Auramine O and Rhodamine 590 striped sample, obtained with an acceleration voltage of 2 kV. The mass spectrum shows two fragmentation patterns, that on the left corresponding to the less massive Auramine O, and that on the right corresponding to Rhodamine 590. The ion image was acquired with a large enough gate width applied to the CCD camera intensifier that the ion image corresponds to the position of both the Auramine O and the Rhodamine 590.*

alternating stripes of the different dyes. The concentration of each dye appears to be stronger at the centre of the stripe than at the edge leading to an observable separation of the dyes. There is also a signal level difference between the two species; although, it is not possible to tell whether this is due to differences in the concentrations of the species on the sample surface or differences in their ablation rates or, of course, a combination of both factors.

As before the mass spectrum acquired with the PMT has the characteristic tail observed due to the phosphor screen decay constant. Figure 4.15 shows fits to the two most intense peaks in the mass spectrum, obtained using the convolution fitting program. The experimental data are represented by the filled red triangles; the fit obtained from the convolution procedure is marked as a black line; and the Gaussian component of this fit is marked by the blue line.

Figure 4.15 a) shows the fit obtained from the convolution program to the data corresponding to the most intense peak in the mass spectrum of the Auramine O. The decay constant, according to the fitting program, was found to be 166 ns which is roughly 20 ns

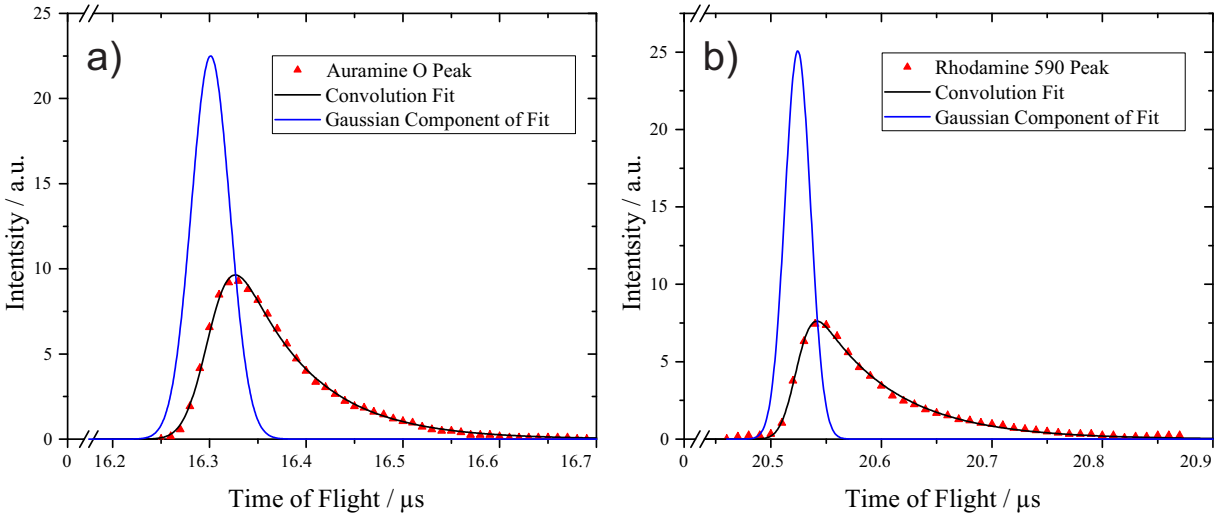

Figure 4.15: *Results of the convolution fitting program applied to the two most intense peaks observed in the mass spectrum shown in figure 4.14 a). The first fit corresponds to the most intense Auramine O peak (a), and the second fit corresponds to the most intense Rhodamine 590 peak (b).*

longer than was found when using the CCD camera in the previous sections. The Gaussian component of this fit was found to have a full width at half the maximum of 46.9 ns which results in a mass resolution of $m/\Delta m = 191$.

Figure 4.15 b) shows the same fitting methodology applied to the most intense peak in the mass spectrum of the Rhodamine 590. Here the decay constant is found to be 159 ns which is a close match to the other peak from this same spectrum. This implies that there must have been a small difference in either or both of the voltages applied to the detector assembly, or to the PMT itself which result in changing the decay time of the P47 phosphor. The Gaussian component of the fit was found to have a full width at half the maximum of 27.3 ns which corresponds to a higher mass resolution of $m/\Delta m = 350$.

Once the overall image and mass spectrum had been obtained the CCD intensifier gate position was reduced and moved so that it only overlapped with either the peak arising from the Auramine O or the peaks arising from the Rhodamine 590. This allowed separate images to be obtained corresponding to the Auramine O and Rhodamine 590 locations.

Figure 4.16 a) shows the ion image relevant to the Auramine O mass peaks. The image was acquired with a camera intensifier gate that overlapped only with those peaks with a m/z less than 270. The contrast in the image confirms that all of these peaks belong to

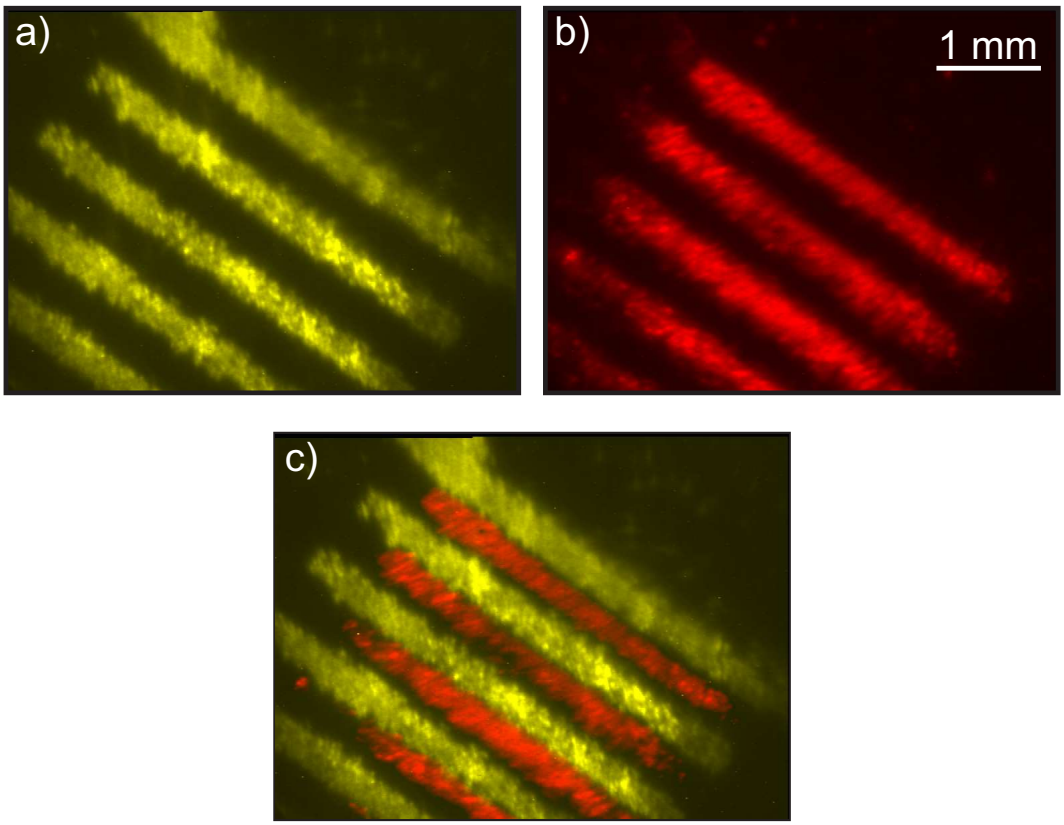

Figure 4.16: *Ion images of the Auramine O and Rhodamine 590 surface sample, obtained with the CCD camera. Figures a) and b) were acquired with the camera intensifier gate set to correspond to the mass peaks of Auramine O (approximately 200 Da to 280 Da — shown in yellow), and Rhodamine 590 (approximately 300 Da to 425 Da — show in red) respectively. Figure c) shows an overlay of the two previous images with their respective colour coding maintained.*

the Auramine O molecule as they are strictly localised within one set of the stripes. As with the ion images of square presented earlier in this chapter, a spatial resolution can be obtained for the image. By using the pitch of the stripes (800 μm) a pixel ratio can be found of approximately 7.00 μm/Px. By taking the rising edge of the stripes, from 20% to 80% of their maximum intensity, a spatial resolution of 110 μm is found.

Figure 4.16 b) shows the ion image relevant to the Rhodamine 590 mass peaks. The camera intensifier gate was adjusted to encompass all of those peaks observed with a m/z greater than 290. As before with the Auramine O image, there is little signal from between the stripes observed. For this image the pixel ratio was found to be approximately 7.21 μm/Px. This value is very slightly different when compared with that found for the Auramine O ion image due to the difference in the magnification of the ion image by the

ion optics. The spatial resolution of the image is found to be slightly worse too, with a value of 134 μm being obtained.

The two images can be superimposed on one another to produce the composite ion image shown in figure 4.16 c). This image is analogous to the one presented earlier in figure 4.14 b) except that here the two image has been colour-coded to identify the separate contributions from the two dye species. This image also confirms that the yellow stripes are, indeed, the Auramine O sample as they can be compared to the optical microscope image shown in figure 4.13 where the Auramine O stripes can be seen to surround the Rhodamine 590 ones.

The resolution obtained from the image in figure 4.16 have much worse resolution that that found previously when analysing the Crystal Violet samples. This is predominantly down to the method of sample preparation. A comparison between the two samples was shown in chapter 2 in figure 2.9 in which it can be seen that the electrospray deposition method results in a far more precise layer of sample than that produced by the inkjet printer. The resultant spatial resolutions obtained from figure 4.16 therefore include a contribution from the sample preparation as well as the instrument focussing itself.

In total, three ion images and a PMT spectrum were acquired in order to resolve to show the alternating positions of the two different dye molecules, and the origin of the mass peaks and ion images was confirmed.

4.4.2 Results with the PImMS1 Camera

Using the same sample as in the previous section, the multi-mass imaging experiment was repeated, this time replacing the CCD camera and PMT with a PImMS1 camera. No gating of the camera is required so a simple trigger was used to synchronise the PImMS1 camera acquisition with the experimental duty cycle. The internal sensor threshold levels were adjusted to reduce the number of events observed due to thermal noise. Data was then acquired over a total of 8,000 laser shots. Unlike with the CCD camera, the data are stored as separate events and so various analysis techniques can be applied at any point in the future without the need for further experiments.

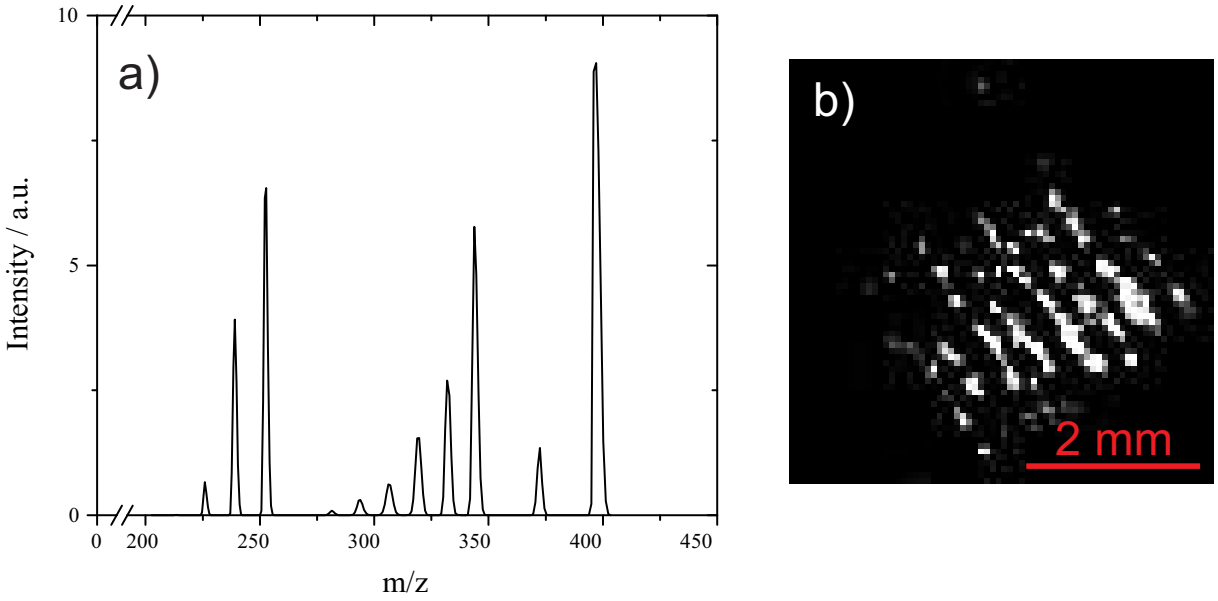

Figure 4.17: *The mass spectrum, and accompanying ion image of the Auramine O and Rhodamine 590 sample, obtained at an acceleration voltage of 2 kV, using the PImMS1 camera. As with those data obtained with the PMT, the mass spectrum in figure a) shows two fragmentation patterns with the one at lower mass corresponding to the Auramine O, and the other corresponding to Rhodamine 590. The ion image was generated from data covering the full range of the mass spectrum.*

Figure 4.17 shows the mass spectrum and total ion image extracted from the PImMS1 data set after centroiding[5]. The mass spectrum, in figure 4.17 a), shows the major peaks corresponding to the Auramine O and Rhodamine 590 dyes, summed over all shots and all of the pixels in the sensor. Likewise, the ion image, shown in figure 4.17 b), is extracted from all of those data that were obtained and so corresponds to $200 < m/z < 450$. These images are therefore directly comparable to the overview plots obtained with the CCD camera and the PMT presented in figure 4.14.

When comparing the PImMS1 data with those obtained with the CCD and PMT, there are a few differences of note. As the images were obtained sequentially the sample has been unequally ablated so that the ratio between Auramine O and Rhodamine 590 peaks in the mass spectrum are different: there is now a lower concentration of the Auramine O. There is also a difference in the illumination of the sample leading to a decrease in the intensity of the ion image observed in the top left hand corner of figure 4.17 b). This could either be due to the consumption of the surface sample or due to the laser profile

[5]The centroiding mentioned here is described in chapter 2.

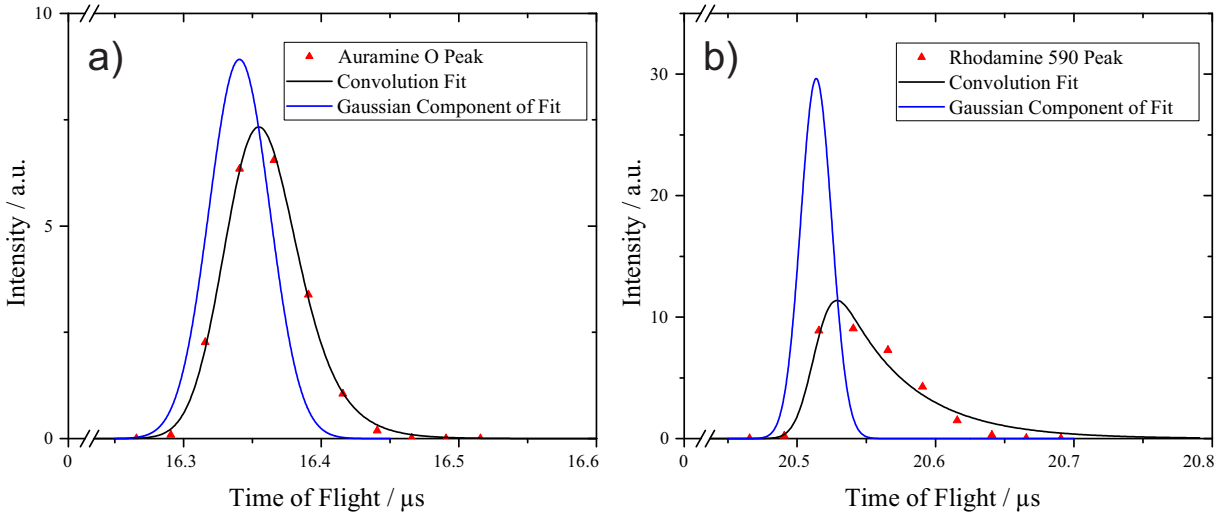

Figure 4.18: *Two plots showing the result of applying the convolution fitting method to two of the most intense peaks observed in the mass spectrum, obtained with the PImMS camera, shown in figure 4.17 a). The experimental data are marked by the filled red triangles; the fit to this peak is represented by the black line; and the Gaussian component of the fit is shown as the blue line.*

and position having changed.

Despite these differences, the overall form of both the mass spectrum and the ion image presented in figure 4.18 closely agrees with that obtained with the CCD and PMT. The same fragmentation patterns are observed in the mass spectrum, although the least intense peaks corresponding to Auramine O are no longer observed much above the baseline noise. That being said, it is also worthy of note that there is a reduced level of noise in the PImMS1 mass spectrum. This is because any noise observed on the phosphor screen does not have sufficient intensity to trigger an event in a pixel. This acts a form of pre-threshold for the data set comparable to that employed with the CCD camera. The ion image also still has the same alternating striped pattern that was observed previously with the CCD camera.

As was found in section 4.3, the time-of-flight data obtained with the PImMS1 camera still exhibits character due to the exponential decay of the phosphor screen; although, this character is much reduced compared to that observed with the time-of-flight data obtained with the PMT.

As a comparison with the analysis, presented in figure 4.15, of the data obtained with

the PMT, the equivalent two intense peaks, obtained with the PImMS1 camera, were subjected to the same fitting program. The result of this analysis is presented in figure 4.18. The experimentally obtained data points are marked by the filled red triangles; the result of the convolution fit is represented by the black line; and the Gaussian component of the fit procedure is represented by the blue line. The first plot, figure 4.18 a), shows the result of the convolution fitting program applied to the most intense peak arising from Auramine O. The decay constant obtained from this fit is found to be 47 ns which is in good agreement with the value found previously. The Gaussian component of the fit has a full width at half the maximum of 51.9 ns which is slightly wider than that value found for the corresponding peak with the PMT (46.9 ns). This, in turn, means that the mass resolution obtained for this peak is lower than before at a value of $m/\Delta m = 173$.

The analysis of the most intense Rhodamine 590 peak, presented in figure 4.18 b), shows a less good fit to the experimental data than that for the Auramine O peak. The decay constant obtained from this fit is found to be 111 ns which is a much longer decay constant than has been previously observed with this data analysis method on PImMS1 data sets. The Gaussian contribution to the fit was found to have a full width at half maximum of 23.6 μs which very close to the observed peak width obtained with the PMT. In turn, this leads to a similar mass resolution of $m/\Delta m = 356$. Due to the difference in the response characteristics of the PMT and the PImMS1 camera, it would not be expected that these two technologies should give similar resolutions so the coincidence is suspicious. Taking a closer look at the experimental data in figure 4.18 b), it can be seen that the rising edge of the peak is lost and instead the peak has a plateau which cannot be fit easily by the Gaussian-exponential convolution. This would appear to be an artefact of the binned data that the PImMS1 camera produces: if a feature, such as the rising edge of a peak, happens to fall completely within a single time bin in the PImMS1 camera, there will be very little information available to reconstruct this feature. That is to say that the coarseness of the binning obfuscates some of the subtleties of the feature.

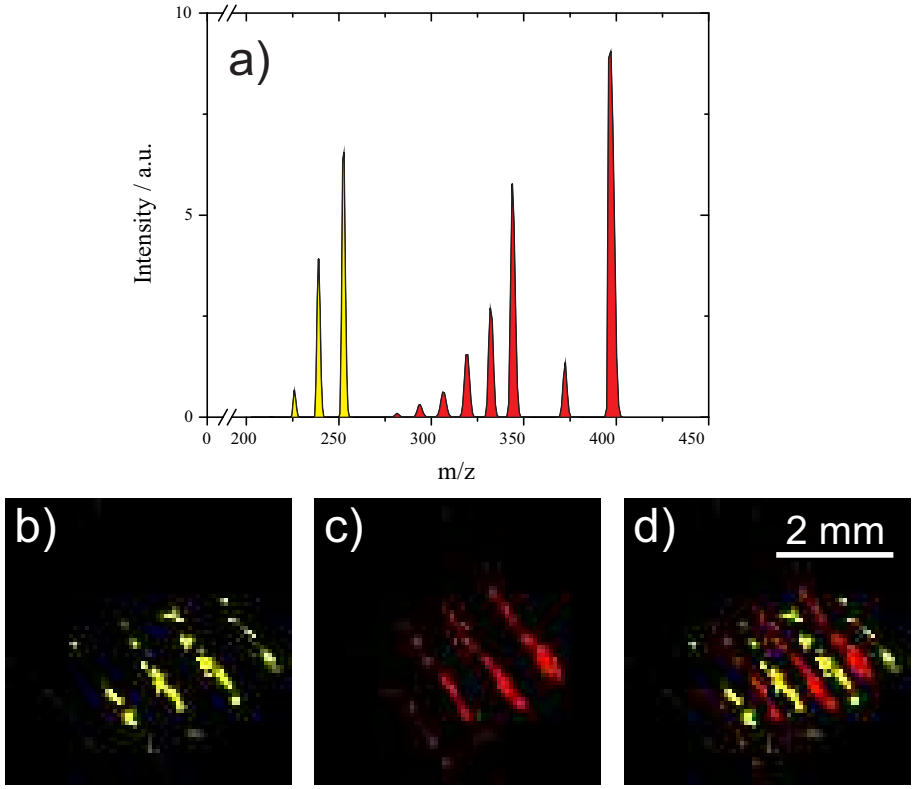

Figure 4.19: *The mass spectrum and accompanying ion images obtained from the further analysis of the PImMS1 data set. The ion images have been generated from a subset of the full data with figure b) corresponding only to those mass peaks marked in yellow; and figure c) corresponding only to those mass peaks marked in red. Figure d) is a composite of the two previous images with their original colour coding maintained.*

Exploring the PImMS Data

At this point, with the data obtained with the CCD camera and the PMT, it would now be necessary to return to the experiment and obtain more data in order to generate further ion images: e.g., one corresponding to the location of the Auramine O, and another for the location of the Rhodamine 590. With the PImMS1 data set, this information is already contained within the data file. The overview plots presented in figure 4.17 were obtained by analysing the data set in its entirety, but it is also possible to filter out that data which might be of interest.

Figure 4.19 shows the mass spectrum obtained with the PImMS1 camera along with three ion images which were generated using different subsets of the full PImMS1 data set. The mass spectrum in figure 4.19 a) has been colour coded so that the peaks arising from the Auramine O molecule are highlighted in yellow, and those arising from the Rhodamine

590 molecule are highlighted in red. The first ion image, shown in figure 4.19 b)was generated using only events within the data set that occupy time bins corresponding to m/z values between 210 and 260. The image shows the Auramine O stripes and can plainly be seen to be of a lower resolution than that obtained with the CCD camera. Quantitatively this is sensible as the pixel ratio for this first PImMS1 image is found to be 65.3μm/Px. Due to the coarseness of the camera pixels, it is not possible to take a measure of the edge of a feature. Instead, a best estimate at the resolution might be found by taking the full width at half maximum of the feature. By this method an approximation to the resolution is found to be 132 μm.

Figure 4.19 c) was generated using those events taken from the data set that occupied time bins corresponding to m/z values between 265 and 410, and shows the stripes of the Rhodamine 590. The pixel ratio of this image is found to be 68.4 μm/Px, similar to that of the Auramine O image save for the difference in the magnification afforded by the ion optics. Again, the coarseness of the resolution means that it is not possible to take a measure of the edge of a feature but the same method for approximating the resolution can be used, and results in a resolution of 158 μm. As with the CCD camera the image corresponding to the Rhodamine 590 mass peaks is found to have a better resolution than that corresponding to the Auramine O mass peaks.

The final image, shown in figure 4.19 d), is a composite of the previous two images. It emphasises the alternating pattern of the Auramine O, and Rhodamine 590 stripes. Although the resolutions are not comparable to those obtained with the CCD camera, it is this filtering of the data set that addresses the goal of the experiment: it shows how the PImMS1 camera can be used to obtain, in one experimental run, the same data that a framing camera has to acquire over a number of runs. The data shown in figure 4.19 has been filtered in such a way that it is analogous to using a framing camera, but this is not the only option for analysing the data.

Just as the PImMS1 data set may produce images that pertain to a given mass range, it is equally capable of producing mass spectra that correspond to a given spatial region. Figure 4.20 shows the mass spectra of two different regions selected from the ion

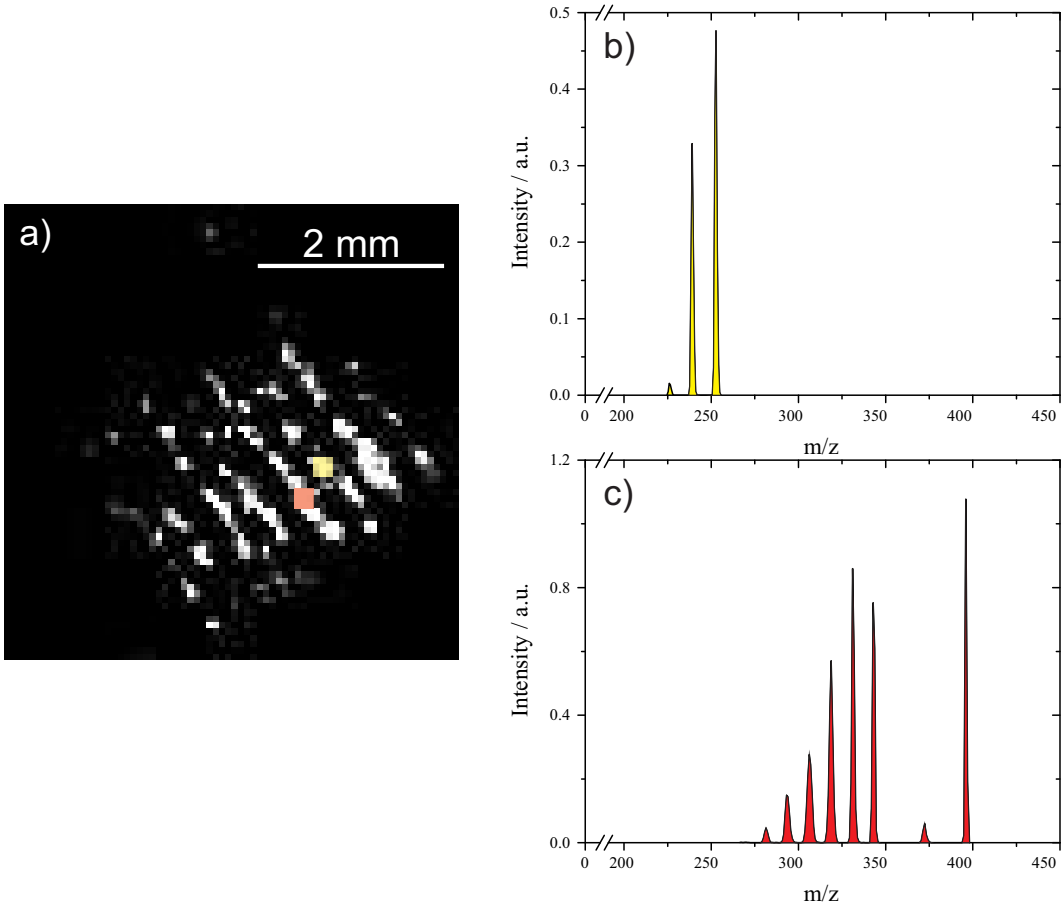

Figure 4.20: *An ion image with accompanying mass spectra obtained from the further analysis of the PImMS1 data set. The mass spectra have been generated by selecting out data, from the full range, which only correspond to a small region of the full ion image. The regions have been marked, and colour coded, on the ion image with the yellow range leading to the mass spectrum in figure b), and the red region leading to the mass spectrum in figure c).*

image. The two corresponding regions have been highlighted with corresponding colours in figure 4.20 a).

The spectrum presented in figure 4.20 b) corresponds to the nine-pixel area of the ion image (marked in yellow) which only overlaps with one of the stripes that has been attributed to the Auramine O sample. This identification is again corroborated by this mass spectrum which only shows the mass peaks of the Auramine O molecule.

The spectrum presented in figure 4.20 c) corresponds to the nine-pixel area of the ion image (marked in red) that only overlaps with one of the stripes that has been attributed to the Rhodamine 590 sample. Again, this mass spectrum only shows the mass peaks of the Rhodamine 590 molecule.

Both of the mass spectra presented in figure 4.20 appear to have a more well resolved peak structure than that obtained when including data from all of the pixels. This would tally with the simulation results presented in section 4.1: the mass resolutions obtained from these simulations were higher for each individual point than for the full simulation. Here, by taking a section of the image, mass spectra from more specific locations have been generated which appear to have a better resolution than the spectrum obtained from across the image as a whole.

By subjecting these new spectra to an identical analysis as that performed for figure 4.18 a revised measure of the decay time and mass resolution is possible. By this, the decay time found from the Auramine O peak is 40 ns which is still in close agreement with all of the decay times observed with the PImMS1 camera so far. The full width at half maximum of this peak is now found to be 39.3 ns which is indeed less than the 51.9 ns found previously. This peak width produces a mass resolution of $m/\Delta m = 229$ which is better even than the resolution obtained with the PMT (173).

The corresponding analysis of the Rhodamine 590 peak is again anomalous. The peak is only formed of three time bins giving insufficient statistics to obtain a reliable fit. Instead, the convolution fit is almost entirely defined by the Gaussian distribution with the fitting error reducing continuously towards zero decay time. The resulting Gaussian fit has a full width at half maximum of 25.2 ns which corresponds to a mass resolution of $m/\Delta m = 373$, which is only slightly greater than that observed with the PMT; although, as the fitting was erroneous, the comparison is not fair.

In this section it has been shown that, in a single experiment with the PImMS1 camera, data are obtained that can be separated in such a way that would require multiple experimental runs with a conventional CCD camera. Whereas, with the CCD camera, data are lost or ignored by the selective gating of the camera, the PImMS1 camera acquires the data in full which can then be analysed at the leisure of the operator. As has been discussed, each pixel in the PImMS1 camera can store up to four time stamps, relating to separate events, in each duty cycle of an experiment. Depending on the number of mass peaks which overlap in space, and the ion intensity of these peaks, the burden on the later

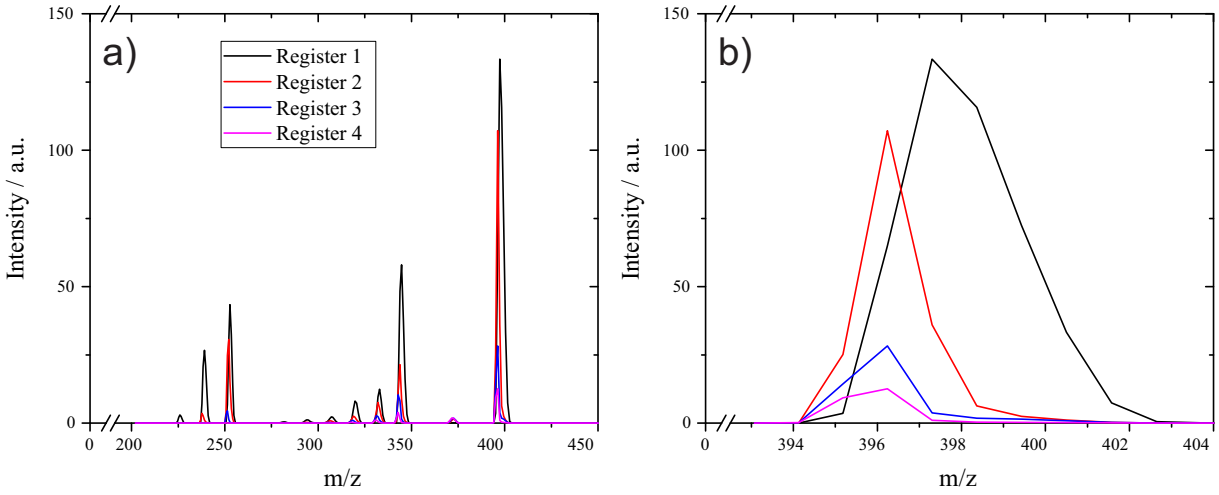

Figure 4.21: *A plot of the, register separated, mass spectrum of the Auramine O and Rhodamine 590 sample, obtained with the PImMS1 camera. The mass spectrum arising from only taking those data found in the first memory register of each pixel is plotted in black, whilst the further spectra corresponding to the data found in the second, third, and fourth registers are plotted in red, blue, and pink respectively. Figure b) shows, in more detail, the final, most intense, peak. The colour coding is the same for figure b) as that used in figure a).*

memory registers will vary.

Figure 4.21 a) shows the mass spectrum obtained by integrating across all of the pixels. The mass spectrum has been separated into the contributions stored in the different memory registers with the first register spectrum marked by the black line and the contributions from the second, third, and fourth registers marked by the red, blue, and pink lines respectively.

It can be seen that the contributions to the mass spectrum from the later registers increases for higher masses, as these peaks arrive later in the time-of-flight. As the Auramine O and Rhodamine 590 samples are spatially separated the use of later registers for the later, Rhodamine 590, peaks should not be influenced by the presence of the earlier Auramine O peaks.

Figure 4.21 b) shows an enlarged portion of the full, register separated, mass spectrum. It is focussed around the last, and most intense, mass peak of the Rhodamine 590, and so contains the greatest contribution of events found in later memory registers. The colour coding of the contributions from the different registers is consistent with the that in figure 4.21 a).

It can plainly be seen that the greatest contribution to this peak is from the first register, and that the contribution reduces further for each successive register. It is also apparent that the different contributions have different shapes, with the peaks for the later registers being less than that for the first register. There is also an offset in the centre of the four different peaks. These features will be studied in further detail later, in chapter 6.

As the relative register occupation will be dependent on the spatial image, it is sensible to conduct any further analysis across a smaller subsection of the sensor. Figure 4.22 uses the same pixel region selections as are marked out in figure 4.20 a) giving one region purely consisting of Auramine O, and another, more intense region, purely consisting of Rhodamine 590. In all four of the plots in figure 4.22 contributions from the first, second, third, and fourth registers are plotted in black, red, blue, and pink respectively.

Figure 4.22 a) shows the register separated mass spectrum obtained from the nine-pixel region covering one of the Auramine O stripes. The three Auramine O peaks can be clearly seen and it is immediately evident that the first two peaks (least massive) are mainly composed of data taken from the first memory register. Figure 4.22 c) shows the ratios of how much each register contributes to the three peaks in figure 4.22 a). This plot confirms that the first peak is, indeed, completely composed of events found in the first registers of the nine-pixels. For the second peak there is a small contribution from events held in the second memory register. The third peak has almost as much contribution from the second register as the first and there is a further small contribution from the third register. This is the ideal scenario for the PImMS1 camera: it is operating in a regime where, without the ability to fill multiple registers in every pixel, data would be lost.

Figure 4.22 b) shows the register separated mass spectrum obtained from the nine-pixel region covering one of the Rhodamine 590 stripes. There are a number of mass peaks in this region, and it is immediately clear that later registers are used heavily. The corresponding register occupancy ratio plot is shown in figure 4.22 d). The contribution from the first register can clearly be seen to reduce, as the peak mass increases, up until the last peak where the first register contributes the least. The contribution from the second register grows as the first register is filled, until it reaches a maximum at the fifth peak, after this

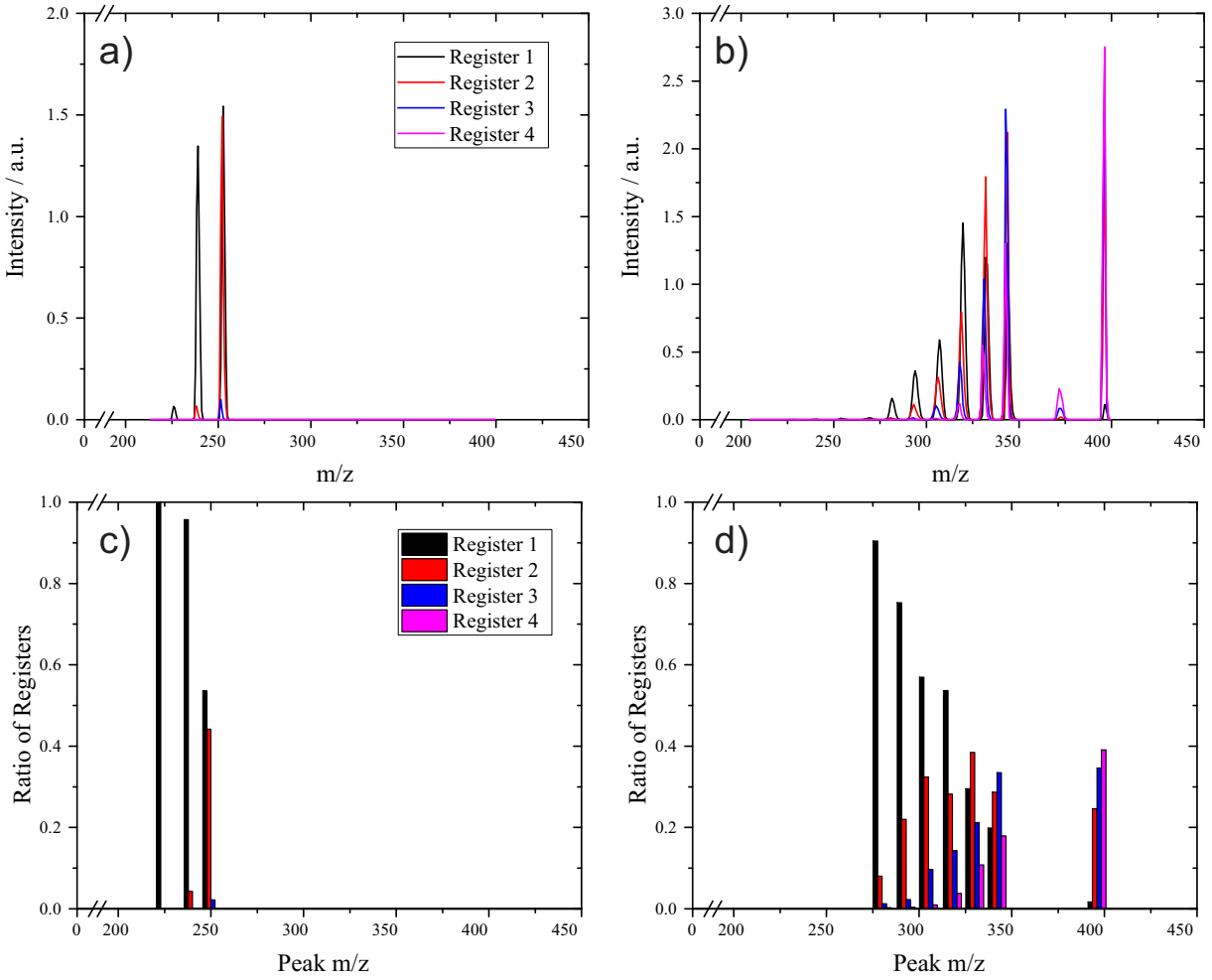

Figure 4.22: *Four plots detailing the relative contributions to the mass spectrum of data contained in the various memory registers in each pixel. The data were taken from the nine-pixel regions outlined in figure 4.20. Figures a) and b) show the register separated mass spectra, whilst figures c) and d) show the register ratio plots for their respective spectra. Across all four plots the data for the first, second, third, and fourth registers are marked in black, red, blue, and pink respectively.*

it drops as well. The contribution from the third register continually grows across all of the peaks, although even this contribution starts to plateau at the highest masses. Finally, there is a significant use of the fourth register which contributes the most to the final mass peak.

The use of the fourth register, observed in figure 4.22 d) indicates that there may be events that are missed by the PImMS1 camera that occur after the fourth register has already been filled. In applications where detection efficiency is key, this is not ideal; however, thanks to the multiple registers, this saturation point occurs at a much higher

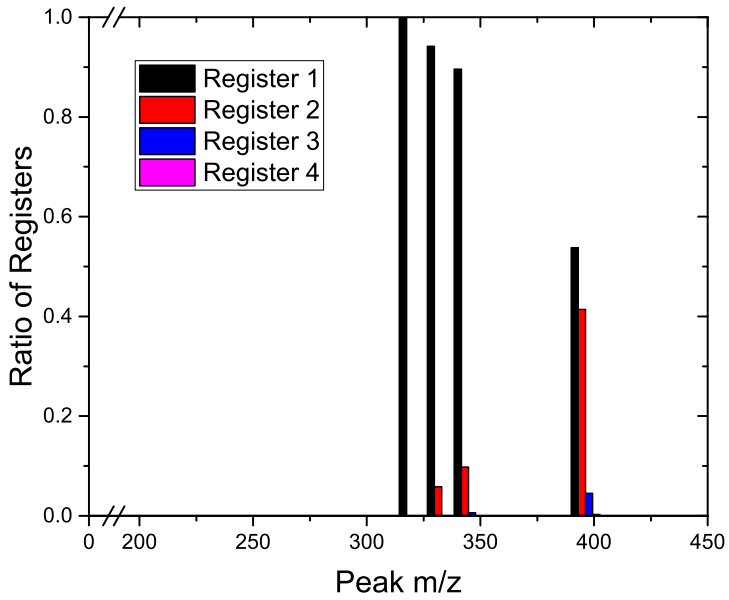

Figure 4.23: *A register ratio plot for a further nine-pixel region than those shown in figure 4.22. This region also correlates to one of the Rhodamine 590 stripes on that sample but the total ion count across these pixels was found to be half of that observed in figure 4.22 d).*

point with the PImMS1 camera than with other technologies.

It is worth noting the difference between the register separated, mass spectra shown in figures 4.21 a) and 4.22 b). There is an obvious disparity between the occupancy of later registers across these two plots with a much enhanced use of the later registers observed in figure 4.22 b) than in figures 4.21 a). This implies that although there was a high demand on those later registers in the specific nine-pixel region, this is not a trend that was true across the whole of the detector. As the occupancy of these later registers is related to the ion count, it follows that the ion incidence rate at those nine-pixel must have been much higher than that observed across the rest of the sensor.

Figure 4.23 shows a further register ratio plot for comparison with that shown in figure 4.22 d). In this plot the mass spectra were generated from a different nine-pixel region with an overall ion count of half that observed in the previous plot. Subsequently, the later registers are not filled to the same extent as was observed in figure 4.22 d). From this it can be seen that although the PImMS1 camera is much less likely to saturate across the

whole sensor, uneven illumination of the sensor may lead to localised saturation.

These data show that the extra registers do not completely overcome the issue of sensor saturation; however, they do allow for sensor saturation levels to be measured: a feature that is not otherwise possible. Furthermore, the extra registers in a pixel can only be used after that pixel has "recovered", a process which can take several hundred nanoseconds: the dead-time of the pixel. Although this would limit the use of the camera for absolutely quantitative applications, this is not a major concern as there are other limitations in MSI that hinder quantitative analysis [169].

4.5 Summary

In this chapter, the evolution of a velocity-map ion imaging instrument into a microscope-mode imaging mass spectrometer has been detailed. SIMION simulations of the instrument were presented and these were compared to experimental results obtained with a conventional arrangement of a CCD camera and PMT. The PImMS1 camera was next tested with a simple, single-species, sample to ascertain any limitations with its resolving power. The mass resolution was compared to that obtained with a PMT, and a measure of the spatial resolution was obtained. With both of these found to be satisfactory, the ability of the PImMS1 camera to image multiple masses simultaneously was tested with a direct comparison being made with a CCD camera and PMT.

Through these experiments the strengths and limitations of the PImMS1 camera have been presented. With conventional framing technologies a choice must be made between not selecting an exposure gate (and so giving up any correlation between position and time), and selecting out a specific exposure time (resulting in a loss of data). The PImMS1 camera is capable of acquiring all of the data from a sample whilst still retaining the position and time correlation of each event. Furthermore, with four memory registers an experiment may be run at a much higher count rate before the sensor reaches saturation which reduces the time needed to acquire the data considerably.

This first prototype version, the PImMS1 camera does suffer from a low pixel count

($72 \times 72 = 5184$) leading to lower quality ion images than might be obtained with higher resolution CCD cameras but by reducing the region of interest this limitation can be circumvented. The next generation sensor, PImMS2, which at the time of writing is in its testing phase, has a much higher pixel count of $324 \times 324 = 104976$. Likewise, the timing precision, which at the current maximum clock cycle setting is 12.5 ns, limits the maximum mass resolving power that can be achieved. This clock cycle can be improved by making adjustments to the hardware of the camera, and there are also certain data analysis methods that have shown promise in improving the quality of acquired data, some of which will be discussed in detail in chapter 6.

In the next chapter, the design and testing of a new microscope-mode instrument will be presented, building on the success of the experiments presented in this chapter. This new instrument will focus on improving the mass resolution over that described in this chapter so that it might be of more use to practical applications. To achieve this, modifications were be made to a commercially available linear TOFMS instrument.

Chapter 5

Increased Resolutions: PImMS and the LT2 Plus

In the previous chapter, a combination of a PImMS1 camera, and a modified velocity-map imaging instrument was presented. The marriage of these two technologies was capable of multi-mass chemical microscopy with, by virtue of the PImMS1 camera, a high saturation limit; however, the mass resolution of the instrument, obtained whilst spatially focussing the image, was found to be very low (no better than a resolving power of a few hundreds). The simple three-electrode ion optic assembly was capable of achieving a much higher mass resolution than this, but any spatial resolution is then lost. With only three electrodes, there are not enough degrees-of-freedom to align the ranges for the optimal mass resolutions and spatial resolutions (without adjusting the geometry of the ion optic assembly). Instead a more advanced design will be necessary in order to retain the spatial resolution whilst increasing the resolving power of the instrument.

To this end, an experiment was conducted in collaboration with a mass spectrometry instrument manufacturer, Scientific Analysis Instrument Ltd (SAI [149]). The aim was dually: to show that a commercial, mass spectrometer can be modified to acquire spatially resolved images in the microscope mode; and, that by using a more advanced ion optic design, better resolutions can be obtained. The instrument used was an LT2 Plus, a linear, time-of-flight instrument designed for bench-top, MALDI analysis. The LT2 Plus uses

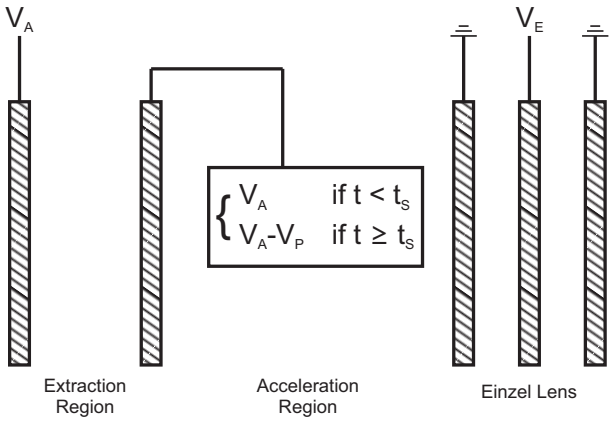

Figure 5.1: *A cartoon representation of the five-electrode ion optic assembly used in the LT2 Plus. The three voltage parameters are labelled: the acceleration voltage, V_A, applied to the repeller electrode; the pulse voltage, V_P, which is the potential difference applied to the extractor electrode from the repeller voltage after the switch time, t_S; and the einzel lens voltage, V_E, applied to the middle of the three electrodes that constitute the einzel lens.*

a five-electrode ion optic assembly with a delayed-extraction pulsing technique. These together offer more flexibility to adjust the compromise between the mass and spatial resolutions.

In this chapter, the results of combining the PImMS1 camera with a commercial mass spectrometer will be presented. First, the instrument will be simulated to see how it might be used as a microscope-mode imaging instrument. These results will then be compared to experimental time-of-flight results to evaluate the validity of the model. Next, modifications will be described that were made to the instrument enabling a spatial resolution to be measured with a CCD camera. After this, results obtained with the PImMS camera will be presented, and some further modifications to the ion optic regime will be described. Finally, a sample will be analysed that has two chemical species with different spatial distributions, the results of which can then be compared directly with the multi-mass imaging experiment in the previous chapter.

5.1 Simulations

The LT2 Plus has an ion optic assembly formed from five electrode plates, a schematic of which is shown in figure 5.1. The first two electrodes (the repeller and the extractor) form

the extraction region. The repeller electrode determines the acceleration voltage, V_A, of the ion optics. As the instrument is designed for the delayed extraction pulsing method, the extractor electrode is originally held at the same voltage as the repeller leaving the extraction region field-free. After a set amount of time, t_S, the voltage on the extractor is reduced by some extraction voltage, V_P, drawing the ions into the acceleration region. Once ions have passed the extractor electrode they are accelerated towards a grounded electrode plate which is the first of three plates that form a unipotential (or einzel) lens [170, 171]. This einzel lens is used to adjust the spatial focus without changing the kinetic energy of an incident analyte ion. Both the first and third electrode of the einzel lens are held at ground whilst the central electrode is held at a positive voltage — so called decel-accel mode, as the ions are first decelerated and the accelerated within the lens. In general the electric field generated by a lens of this type would therefore be symmetric along the time-of-flight axis, but in this assembly the field before the lens breaks this symmetry with the field-free region that comes after it.

Simulations were undertaken to predict the performance of the instrument at microscope-mode imaging. As before, the simulations were conducted using SIMION 8.1 as described in chapter 3.

5.1.1 Adapting the LT2 Plus for Imaging

For the simulations of the LT2 Plus, for a given acceleration voltage, three parameters were adjusted: the voltage applied to the einzel lens; the pulse voltage by which the extractor electrode is reduced from the acceleration voltage; and, the switch time at which the delayed extraction is applied.

The first simulations were employed to test how the mass and spatial resolutions of an ion are affected by adjusting the three parameters explained above. The results of these simulations are presented in figure 5.2. The simulations were conducted using an ion definition with a $m/z = 500$ and a velocity distribution assuming the a MALDI ablation process. Four ion sources were used in the simulation with the first placed directly at the centre of the ion optics, and the further three sources positioned at 100, 200, and 300 μm

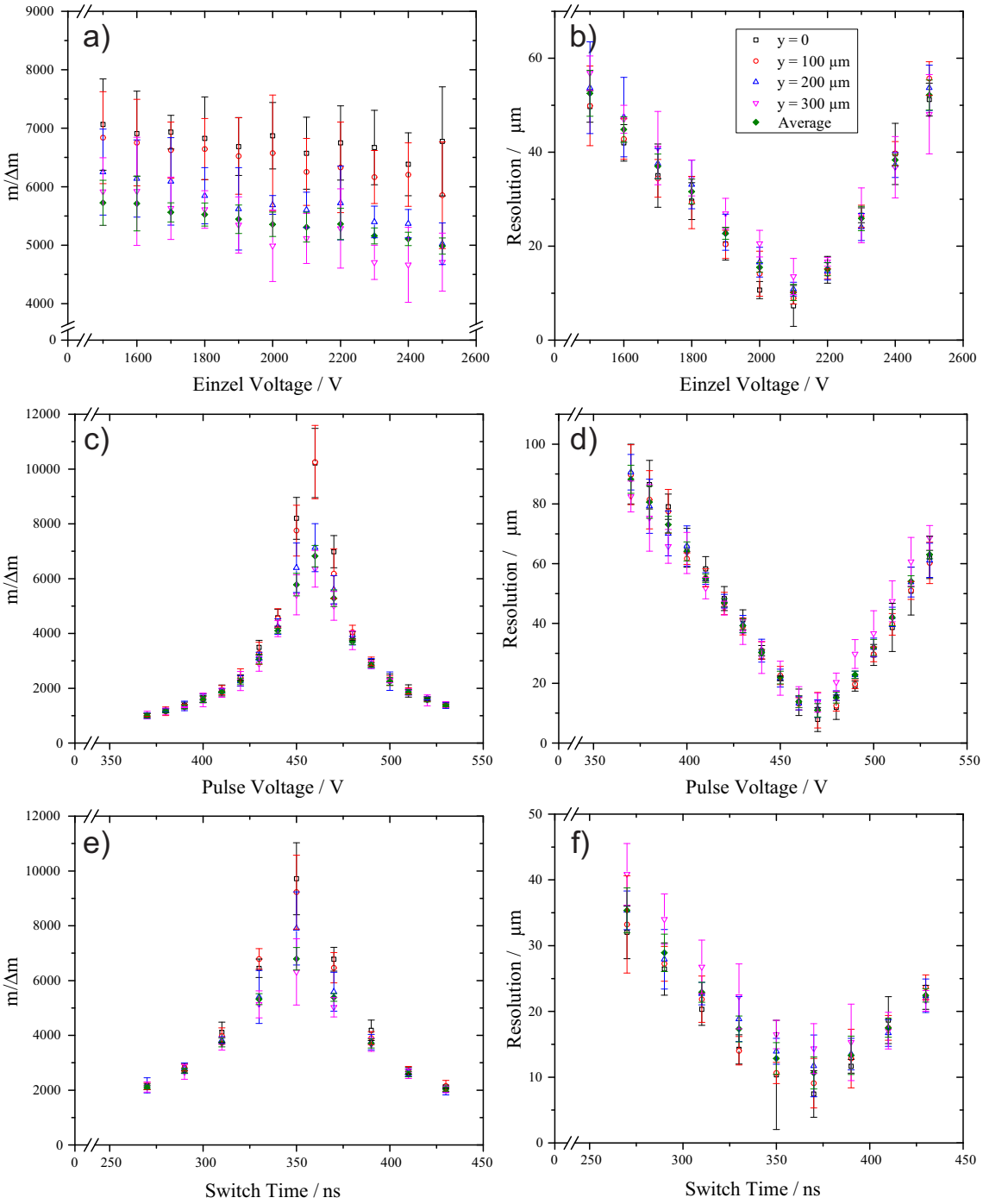

Figure 5.2: *Plots of simulations results showing the predicted dependence of the mass and spatial resolutions on the voltage applied to the einzel lens, the pulse voltage that generates the extraction field, and the delay time before the extraction field is switched. Each plot shows the relevant resolution for each individual ion source position (marked by open symbols) as well as the aggregate or average resolution (marked with a filled symbol). The legend located in sub-figure b) is applicable across the whole figure. Unless otherwise stated, the simulations were run with an einzel lens voltage of 2100 V, a pulse voltage of 470 V, and a switch time of 370 ns.*

from the time-of-flight axis. The plots in figure 5.2 are arranged so that those on the left depict the variation of the mass resolution and those on the right show the variation in the spatial resolution. For all of the plots, the open symbols represent the resolution of each individual spot, whilst the filled symbol represents the aggregate or average value (for the mass and spatial resolutions respectively).

The top two plots, figures 5.2 a) and b), show respectively the variation in the mass and spatial resolutions as a function of the voltage applied to the central electrode of the einzel lens. The mass resolutions, figure 5.2 a), show very little variation as the voltage is adjusted with an average average between $m/\Delta m$ =5000–6000. The mass resolutions found for each ion source position are quite close in value with the resolution of the central spot being the highest and the resolutions for the further spots decreasing slightly as the sources deviate from the time-of-flight axis. The value of the aggregated mass resolution is found to be somewhere between the third and fourth source position which implies that the resolution of each source is the limiting factor, rather than their deviation in arrival times. This is in contrast to the resolution of the modified velocity-map imaging instrument from the previous chapter.

Figure 5.2 b) shows the spatial focussing of the image as a function of the voltage applied to the einzel lens. As with the mass resolutions, these do not differ greatly between the different source positions implying that there is little contribution from spherical aberrations. However, the spatial resolution is strongly dependent on the einzel lens voltage. The optimal resolution is found to be approximately 11 μm, and although the resolution does deteriorate with any adjustment to the einzel lens voltage, it remains below 50 μm across the range 1700–2400 V.

The plots presented in figures 5.2 c) and d) show the variation of the mass and spatial resolutions as a function of the voltage by which the extractor electrode is reduced from the repeller electrode voltage (referred to as the pulse voltage). A larger pulse voltage means that the potential difference between the two plates is larger resulting in a stronger electric field in the extraction region. As with the extractor electrode in the three-electrode instrument, described in the previous chapter, this voltage also controls the ratio of the

electric fields in the extraction and acceleration regions.

The plot of mass resolution, shown in figure 5.2 c), shows a strong dependence on the pulse voltage. Over the range of voltage, 350–550 V, the resolving power increase by an order of magnitude. The mass resolution is found to be at a maximum when a pulse voltage is set to 460 V; here, the aggregate resolving power is found to be 6800, although the difference between the resolutions for each source position are greater than observed previously.

Figure 5.2 d) shows the dependence of the spatial resolution on the pulse voltage. The form of this plot is very similar to that shown in figure 5.2 b) except that the resolution here is more sensitive to a change in voltage. The optimal resolution of 11 μm is found at 470 V, which is close to the optimal voltage needed for the mass resolution.

Finally, the plots presented in figures 5.2 e) and f) show the mass and spatial resolutions as a function of the delay length before the extraction field is switched on. Both of these plots have a similar form to the previous figures where both the mass and spatial resolutions are affected by a change in the switch time.

Together, the plots presented in figure 5.2 give an overview of the effect that changing the three experimental parameters will have on the mass and spatial resolutions obtained. The most striking observation to be made is that voltage applied to the einzel lens can be used to adjust the spatial focus of the instrument without greatly affecting the mass resolving power. This partially removes the dependence of the two resolutions on one another.

There is a third consideration (after the mass and spatial resolutions) to take into account when simulating the experiment: the range of masses over which the mass and spatial resolutions are acceptable should overlap to as great an extent as possible. In order to investigate this, further simulations were run following the same methodology as was used to generate the data in figure 5.2 but with ions of various masses.

The plots in figure 5.3 show the behaviour of the mass and spatial resolutions across the mass range 100–1200 Da whilst the voltage applied to the einzel lens, the pulsed extraction voltage, and the time that the extraction voltage is switched are varied respectively. Across

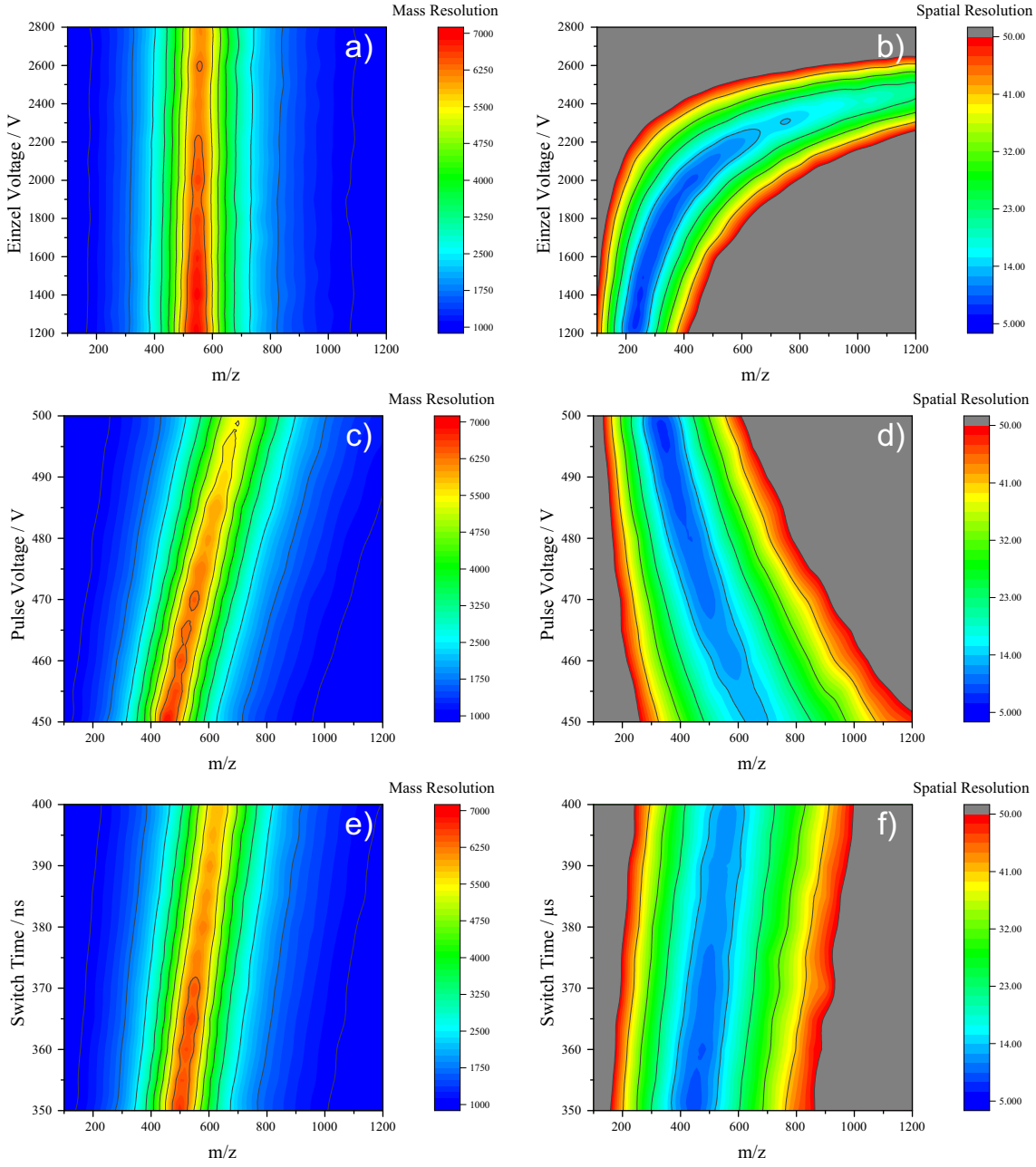

Figure 5.3: *Contour colour maps of the effect of changes to the three experimental parameters on the mass ranges for the mass and spatial resolutions predicted by simulation. The resolutions are represented by a colour referencing the accompanying colour charts with red denoting higher values and blue denoting lower values. The mass range, assuming unit charge, is shown on the horizontal axis of each graph, whilst the parameter being varied (einzel lens voltage, extraction pulse voltage, or extraction switch time) is shown on the vertical axis. All of the resolution values are given for the aggregate or average for the mass or spatial resolutions respectively. Unless otherwise stated, the simulations were run with an einzel lens voltage of 2100 V, a pulse voltage of 470 V, and a switch time of 370 ns.*

all of the plots, the mass of the ion (assuming a unit charge, z) is on the horizontal axis, whilst the parameter being varied is shown on the vertical axis, and the resolution obtained is depicted according to the accompanying colour bar. For the mass resolution plots, the colour map depicts the highest values, corresponding to the best resolutions, in red and the lowest values, corresponding to the worst resolutions, in blue. With the spatial resolution plots, the highest values are also depicted in red, but for the spatial resolution these correspond to the worst resolutions, and the lowest values, which are depicted in blue, correspond to the best resolutions. The grey area in the spatial resolution plots represents any spatial resolution worse than 50 μm which, although an arbitrary value, helps to visualise the region of "acceptable" resolution.

The first plot, figure 5.3 a), shows the mass range as a function of the voltage applied to the einzel lens. As was implied with the equivalent single mass plot in figure 5.2 a) there is very little variation in the position of the mass range with changing einzel lens voltage. However, the peak mass resolution does get lower as the voltage is increased.

The accompanying plot of the spatial resolution in figure 5.3 b) shows a far greater dependence on the einzel lens voltage. As the voltage is increased, the optimal spatial focus is shifted to higher masses. At the same time as this, the range of "well focussed" masses broadens; although, this also comes with a sacrifice in the peak spatial resolution. This can be interpreted as the spatial resolution being homogenised across a broader mass range eventually leading to the entire mass range being imaged with a resolution worse than 50 μm at voltages above 2600 V.

Figures 5.3 c) and d) show the variation of the mass and spatial resolution ranges as a function of the extraction voltage. Unlike in the previous plot, here the mass resolution range, shown in figure 5.3 c), is shifted with a change in the voltage: a higher voltage shifts the range to higher masses. The increasing voltage also reduces the peak mass resolution whilst also slightly increasing its range. The spatial resolution range, shown in figure 5.3 d), acts in almost the complete opposite manner: an increase in the pulse voltage results in the mass range shifting to lower masses; the optimal resolution is improved; and the range is reduced. The opposing trends in these two plots mean that it is possible to

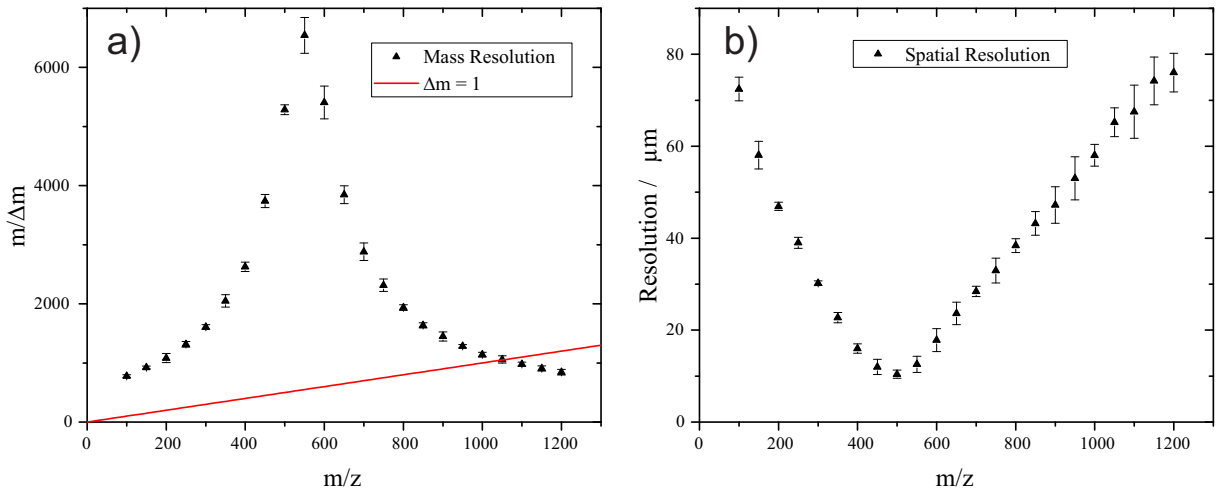

Figure 5.4: *Plots of the simulated mass resolutions, a), and spatial resolutions, b), obtained as a function of ion mass. The simulations were run with an acceleration voltage of 5000 V, a pulse voltage of 470 V, a switch time of 370 ns, and an einzel lens voltage of 2100 V. The red line in figure a) represents the isotopic resolution limit: any mass resolution above this line is sufficient to resolve two adjacent peaks separated by a single mass unit.*

further optimise their overlap.

The effect of the switch time on the mass and spatial resolution ranges is shown in figures 5.3 e) and f). Both graphs show very similar trends with increasing switch time shifting both of the ranges to higher m/z. This shift to higher m/z is also accompanied by a reduction in both resolutions. This means that with a set value for the einzel lens voltage and the pulse voltage, the switch time alone can be used to adjust the m/z range of the instrument.

The simulations presented in figure 5.3 demonstrate the flexibility of a more complex five-electrode system over the simpler three-electrode instrument used in the previous chapter. By adjusting the various parameters a compromise can be found that offers the optimum range for the mass and spatial resolutions: the Goldilocks zone [172].

Figure 5.4 shows the aggregate and average mass and spatial resolutions across the mass region of interest. The simulations were conducted with an acceleration voltage of 5000 V, a pulse voltage of 470 V, a switch time of 370 ns, and an einzel lens voltage of 2100 V. Figure 5.4 a) shows the mass resolution as a function of the ion mass. The plot has a peak mass resolution of $m/\Delta m = 6000$. The red line in the plot represents the mass

resolution limit $\Delta m = 1$: any mass resolution above this line is sufficient to resolve isotope peaks for a given species (i.e. to resolve two adjacent peaks separated by 1 Da). Here the instrument is expected to have isotopic resolution for species up to 1000 Da.

The spatial resolution of the instrument is shown in figure 5.4 b). The best resolution is found for ion with a mass of 500 Da and is around 11 μm. The spatial resolution can be seen to be better than 50 μm across the mass range of 200–800 Da.

The image magnification of the instrument was also found to have some dependence on mass: images of the positions of the smallest simulated molecules (100 Da) were magnified 27.5 times; whereas, the images of the positions of the largest molecules simulated (1200 Da) were only magnified by 24.5 times. However, across the majority of the range of interest (250–1000 Da) the magnification of the images only changed from 25.5–25.0. Whilst this magnification does affect the field-of-view of the instrument, it does not affect the quality of the images (although there can be instrumental difficulties); and any differences in the size of images between molecules of different mass can be simply accounted for by post-acquisition image processing.

5.2 A Comparison with Experiment

Having simulated the performance of the instrument an experiment was devised to compare some of these simulations against the instrument itself. These initial tests were conducted before the detector of the LT2 Plus was swapped with a spatially sensitive assembly; instead, the original electron multiplier was used. This detector, as was described in chapter 2, has a very short response time (better than 2 ns [173]), but only records time-of-flight information. This arrangement was therefore only capable of validating the accuracy of the simulated mass resolution.

Before the mass resolutions could be calculated, the instrument was calibrated. In order to do this several dye solutions were prepared all at a concentration of 1 mg/ml in 99% MeOH. These solutions were then applied, by the dried droplet method, to a standard sample plate (as shown in chapter 2). The dyes used were: Crystal Violet (372.24 Da);

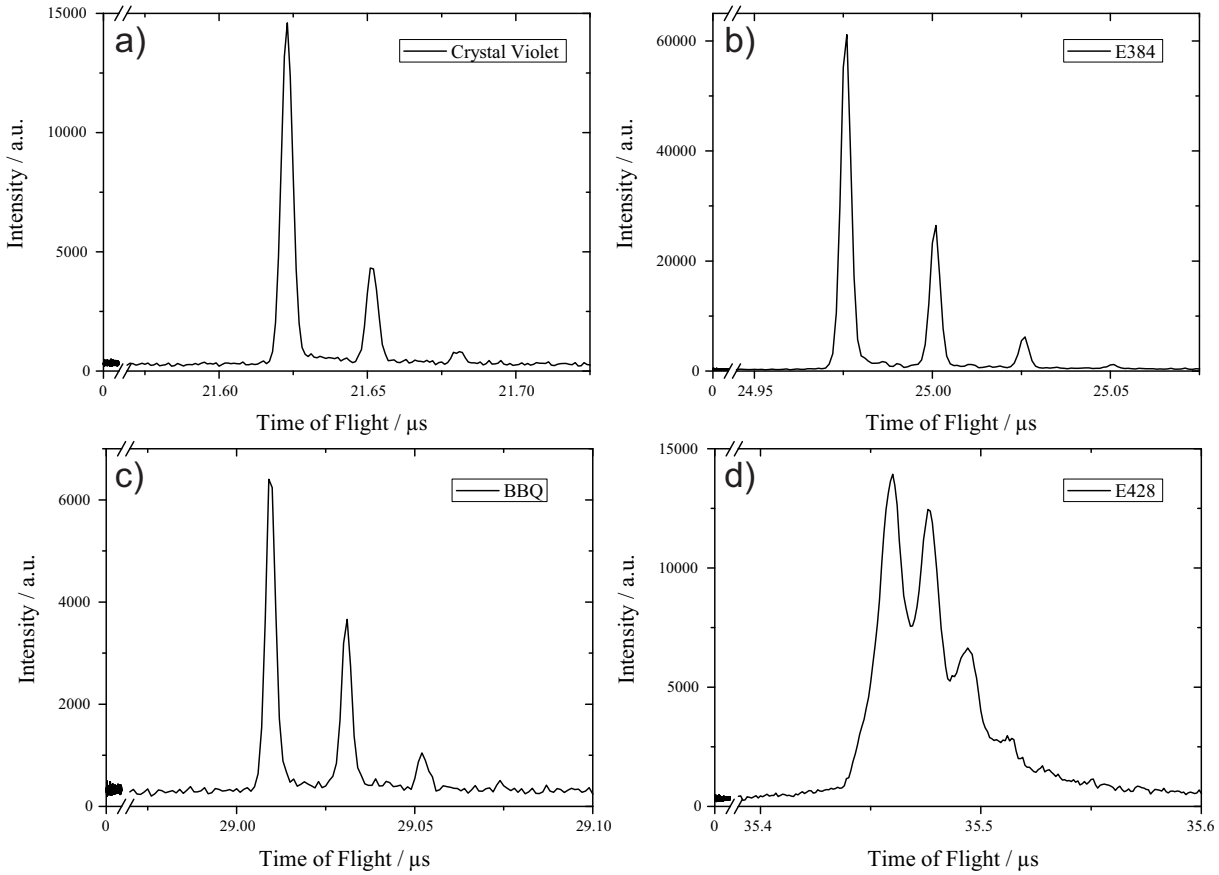

Figure 5.5: *Time-of-flight spectra for the four dye compounds a) Crystal Violet, b) Exalite 384, c) BBQ, and d) Exalite 428. All four of the spectra were obtained with the same experimental settings as those used to obtain the simulation results shown in figure 5.4: the acceleration voltage was set to 5000 V, the pulse voltage was 470 V, the switch time was set to 370 ns, and the einzel lens voltage was set to 2100 V.*

Exalite 384 (498.33 Da); BBQ (674.50 Da); Exalite 428 (1010.7 Da). The masses stated with each of these dyes are now their mono-isotopic masses (i.e. only the mass of the most abundant isotope rather than an average over all masses). This added precision is necessary when compared to the nominal masses used in the previous chapter, as the expected resolution of this new instrument was much improved over the former.

The instrument was run with the voltages and switch time used in the simulation: an acceleration voltage of 5000 V, a pulse voltage of 470 V, a switch time of 370 ns, and an einzel lens voltage of 2100 V. The power of the N_2 laser was increased to the minimum power necessary to acquire a reliable signal. The fluence required for this ranged from 5–25 mJ/cm^2.

The resulting time-of-flight spectra are presented in figure 5.5. In all four of the plots

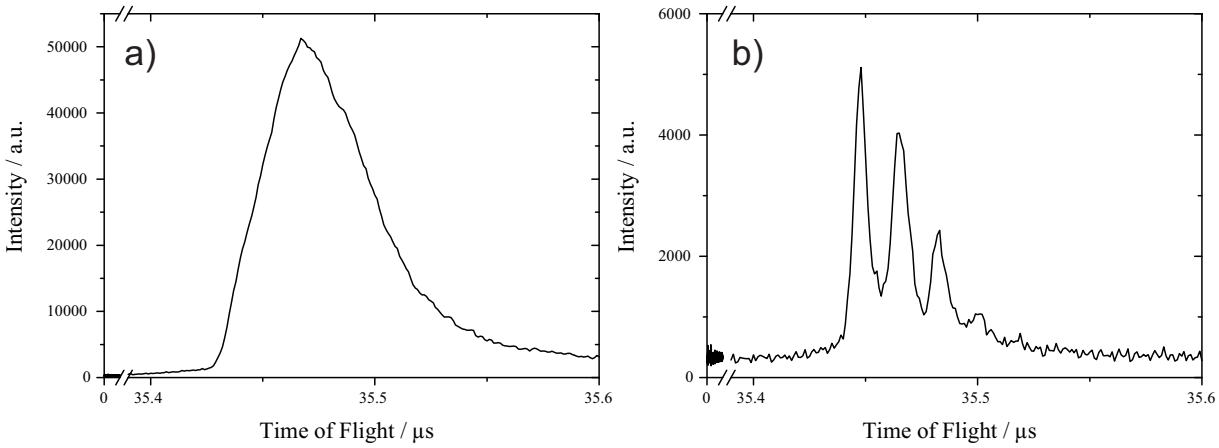

Figure 5.6: *Two plots showing time-of-flight spectra obtained with the LT2 Plus and the electron multiplier detector. Both plots were obtained from the same sample of Exalite 428 but they were recorded at different locations on the sample and with different laser fluences.*

there is a definitive resolution of the separate isotopes of each species. Figure 5.5 a) shows the time-of-flight spectrum of Crystal Violet. The most intense peak is observed at 21.62 μs and has a width (full width at half maximum) of 4.5 ns. These peaks have considerably more Gaussian form than those observed in the previous chapter when using the MCP-P47 detector. Whereas that previous detector had a long tail (more than 100 ns — much longer than the rise time of 1–2 ns) resulting from the exponential decay of the scintillating screen, the electron multiplier is specified to have a response time of less than 2 ns with a Gaussian shape (i.e. the rise time of the detector is comparable to its decay time).

The Exalite 384 peak, shown in figure 5.5 b), is observed at 24.98 μs and has a width of 3.3 ns; and the BBQ peak, shown in figure 5.5 c), is observed at 29.01 μs and has a width of 3.2 ns. The peaks presented in these two figures are very similar to those shown in the previous figure also having a predominantly Gaussian form.

The final plot in figure 5.5 d) shows the peaks of the Exalite 428 isotopes. This molecule has a mass greater than 1000 Da which, according to the simulated mass resolutions shown in figure 5.4 a), is at the extremity of the instruments range to resolve isotope peaks. This is reflected in the spectrum which shows four peaks that are far less well resolved. The most intense of these peaks occurs at 35.46 μs and has an estimated width of 14 ns, although fitting such poorly resolved peaks is far less reliable than fitting those that are completely separated from one another.

Figure 5.5 d) also highlights an additional complication that arises from the increased mass resolution obtainable with the new instrument: the velocity spread from the sample ablation is at this point comparable as a limiting factor in the mass resolution of the experiment. An excessive laser fluence can impart additional, unwanted, kinetic energy to the analyte ions ablated from the sample surface resulting in a broader distribution of velocities. This increases the chromatic blurring in the mass spectrum leading to less well resolved peaks. This will also be seen as blurring in the ion images.

Figure 5.6 shows two mass spectra of the Exalite 428 species. Both were obtained under the same experimental conditions as the spectra shown in figure 5.5 except that they were obtained from different areas of the sample, and were obtained with different laser powers. The resolution shown in figure 5.6 a) is below the limit for observing separate isotopes and so only a single peak is observed. The peaks appear to have a slow decay time which is observed due to the progression of isotopes each at a unit higher mass and with a lower abundance than the previous peaks[1]. Figure 5.6 b) shows a well resolved spectrum where each peak is easily identifiable.

5.2.1 Calibration

With time-of-flight spectra having been recorded for the four dyes, a calibration function was applied. This function relates the time-of-flight of an ion to its mass to charge ratio, m/z. For both the laser desorption ionisation method used for the dye molecules, as well as matrix assisted ablation, it can be assumed that only singly charged species are produced in any great abundance. This means that the m/z of an analyte ion can be cautiously assumed be equal to the mass number of the precursor molecule. This means that the calibration function now directly relates the time-of-flight of an ion to its mass, greatly simplifying chemical identification.

In its simplest, first order, form the arrival time of ions in a time-of-flight mass spectrometer can be assumed to be proportional to the square root of m/z, as was described

[1]It is worth noting that this isotope progression may have had some influence on the exponential decays calculated in the previous chapter; although, without the resolving power to corroborate this the two contributions cannot be separated.

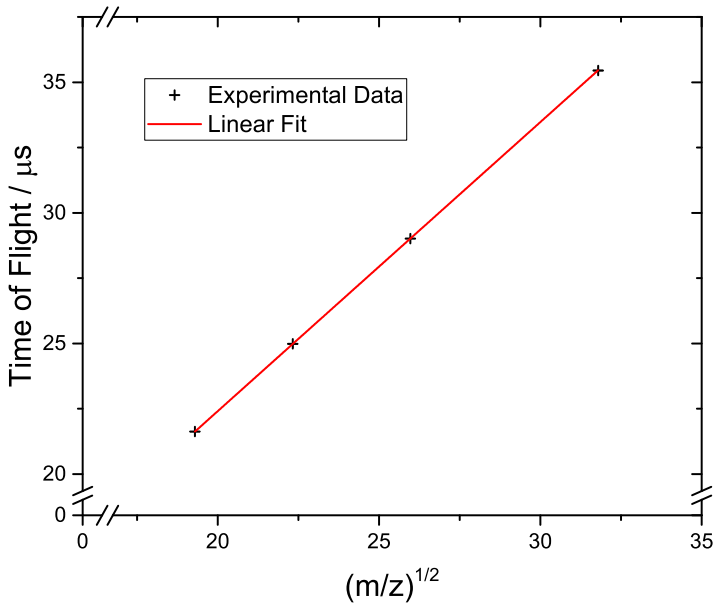

Figure 5.7: *A graph of the arrival times, obtained by experiment with the LT2 Plus and the original electron multiplier, for the four dye species plotted against the square root of their mass to charge ratios. A linear fit of the data is shown in red, and the result of this fit gives the calibration of the instrument.*

in chapter 1. With a delayed extraction pulsing technique such as the one used in the LT2 Plus, it can also be assumed that there will be some offset so that the time of flight is approximated to,

$$t_{\mathrm{ToF}} = A\sqrt{\frac{m}{z}} + C, \tag{5.1}$$

where A and C are parameters dependent on the design and use of the instrument. This equation assumes that ablated ions are accelerated fully to their final velocity in a negligibly short amount of time, so that the entire flight time can be approximated to the ions' transition through the field-free flight tube.

Figure 5.7 shows the first order calibration obtained from the time-of-flight data acquired with the dye species. The arrival time for each dye was measured several times and the averages are shown here. The values for the m/z were taken as the mono-isotopic masses of each species, assuming that they were each ablated into a singly charged state. The red line is a linear fit of their respective arrival times plotted against the square root of their mass to charge ratios and is found to have a slope of 1.11 μs and an intercept

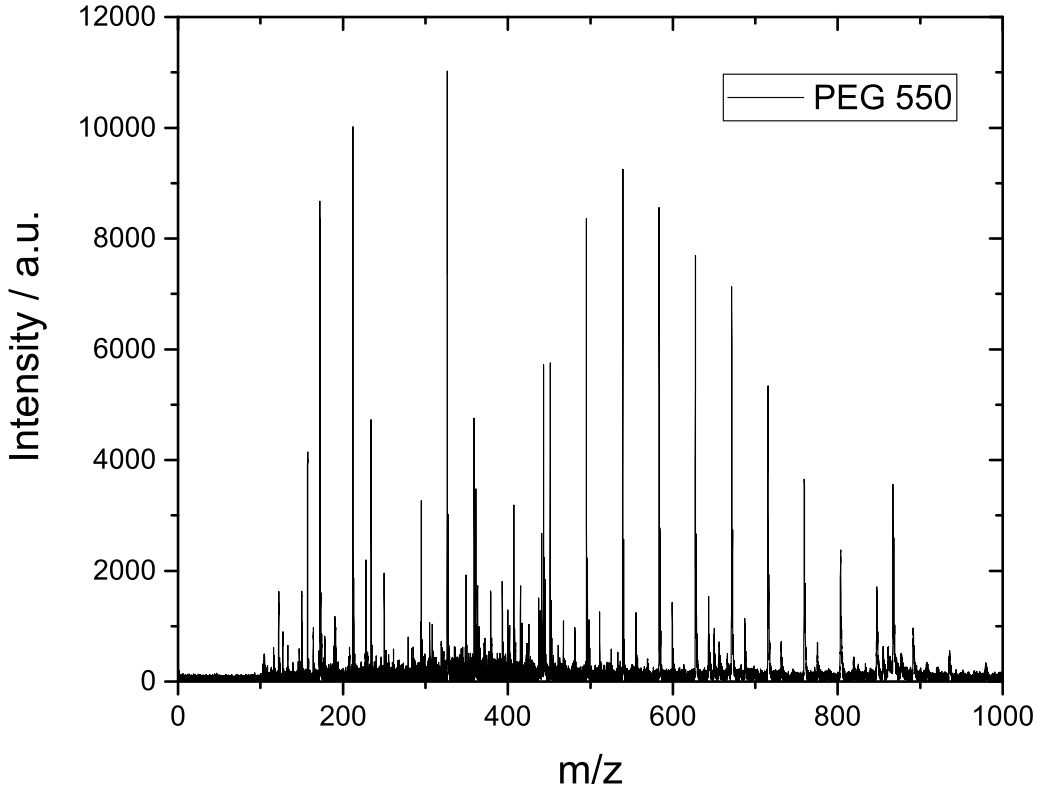

Figure 5.8: *A mass spectrum of the PEG polymer obtained experimentally using the LT2 Plus with its original electron multiplier detector. The acceleration voltage was set to 5000 V, the pulse voltage was 470 V, the switch time was 370 ns, and the einzel lens voltage was 2100 V.*

located at 0.269 μs.

This calibration is therefore valid for the experimental conditions that were used to acquire the time-of-flight data. Although the equation used assumes that only the final acceleration voltage and the total flight length are relevant in calculating the arrival time of an ion, the other parameters (pulse voltage, and einzel lens voltage) will have some effect on the calibration, so that it must be recalculated after any changes to these voltages. Similarly, the delayed switch time will have a direct effect on the intercept of the calibration.

n	m/z for mono-isotopic PEG species: $CH_3(OC_2H_4)_nOH$		
	$+H^+$	$+Na^+$	$+K^+$
8	385.46	407.44	423.55
11	517.62	539.60	555.71
14	649.77	671.75	687.86

Table 5.1: *A selection of calculated m/z values for various lengths of the mono-isotopic PEG molecule in their three expected adduct ion forms.*

5.2.2 MALDI Data

As the SIMION simulations in section 5.1 were conducted with an ion definition based on the MALDI ionisation mechanism, an experiment was performed to obtain a MALDI data set for fair comparison with those simulation. A polymer, poly(ethylene glycol) methyl ether (PEG — $CH_3(OC_2H_4)_nOH$), was chosen as the analyte. The polymer was chosen for its progression of masses, separated by 44.03 Da, centred around an average mass of 550 Da.

The MALDI matrix α-cyano-hydroxycinnaminic acid (CHCA) was used to facilitate the ionisation of the PEG. A solution of CHCA (8 mg/ml in 50% MeOH and 0.12% TFA) was produced, and 2 μl of PEG were added to 10 ml of this CHCA solution. This was then applied directly to a sample plate via the dried droplet method. Figure 5.8 shows a calibrated mass spectrum of the PEG sample analysed under the same conditions as were used above. The progression of the polymer peaks is immediately apparent with the most abundant peaks appearing close to the expected 550 Da. There are also a number of less intense peaks that accompany the progression of the polymer peaks. As expected, all of the peaks observed occur below $m/z = 1000$.

The MALDI process can produce adduct ions with either H^+, Na^+, or K^+ as the partner cation. Taking this into account, and with knowledge of the structure of the PEG polymer it is possible to calculate the different possible m/z ratios that should be observed in the mass spectrum. The polymer masses presented in table 5.1 all fall directly within the range of the observed polymer peak progression in figure 5.8.

Figure 5.9 shows four plots detailing expanded regions of the full mass spectrum presented in figure 5.8. The first three plots, figures 5.9 a), b), and c), focus on the isotope

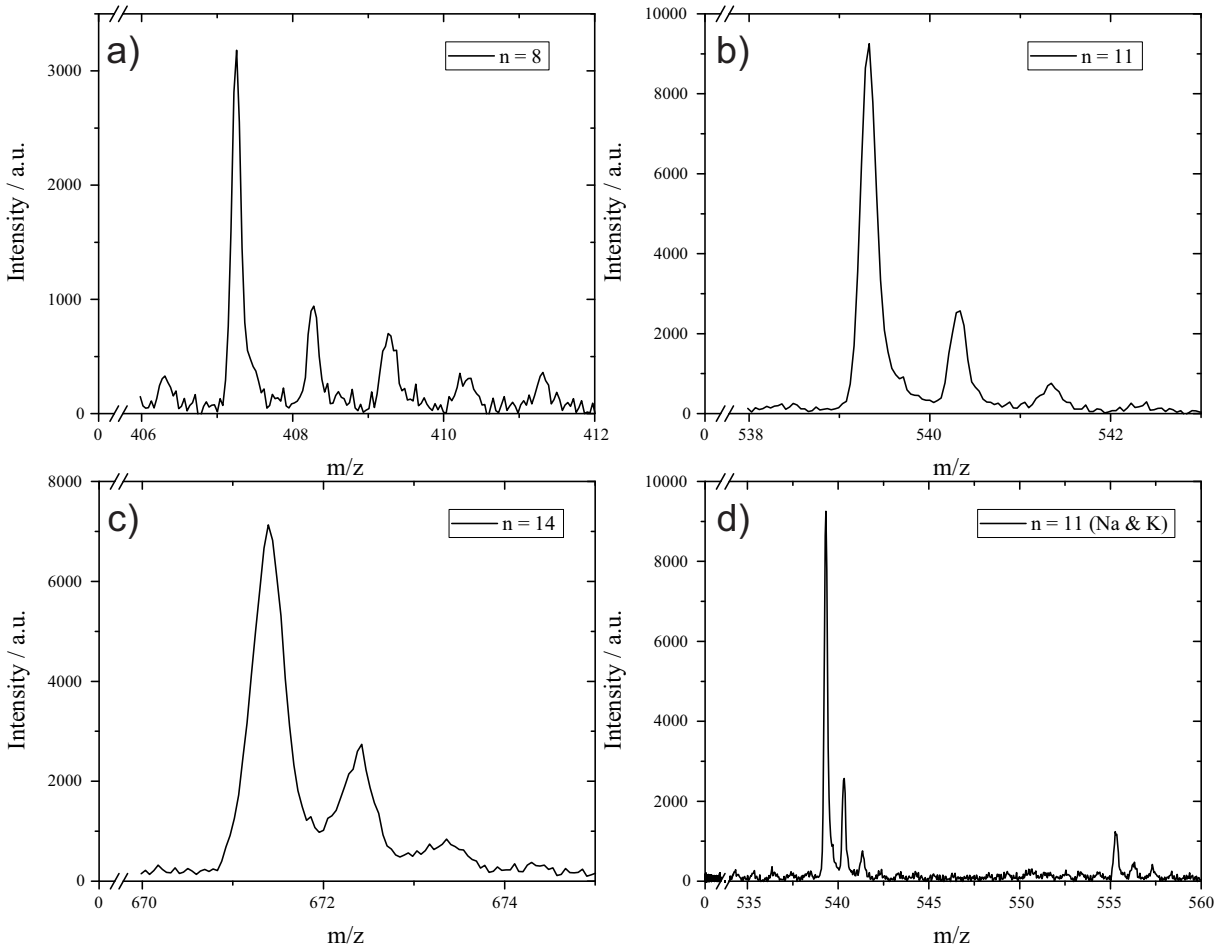

Figure 5.9: *Four plots showing expanded regions of the mass spectrum shown in figure 5.8, obtained experimentally with the LT2 Plus and the electron multiplier. The first three plots show the isotope peaks of the sodium adduct of the PEG polymer with chain lengths of a) 8, b) 11, and c) 14 units. Figure d) shows both the sodium and potassium adducts of the 11 unit long polymer.*

progressions of sequential polymer peaks. The final plot also shows one of the less intense regular peaks.

The major peak in figure 5.9 a) is observed at $m/z = 407.32$ with a peak width of 0.17. The m/z is very close to that expected for the sodium adduct of the eight unit long polymer $[CH_3(OC_2H_4)_8OH{+}Na]^+$ which, from table 5.1, has $m.z = 407.44$ (an accuracy of approximately 300 ppm). This implies that sodium adducts are the most abundant. The peak width can be used to arrive at a mass resolution for the species of $m/\Delta m \approx 2400$.

The next two plots, figures 5.9 b) and c), also appear to fit closely with the expected m/z values for sodium adduct ions formed with PEG molecules of eleven and fourteen units respectively. The most intense peak in figure 5.9 b) is found to have a $m/z = 539.55$

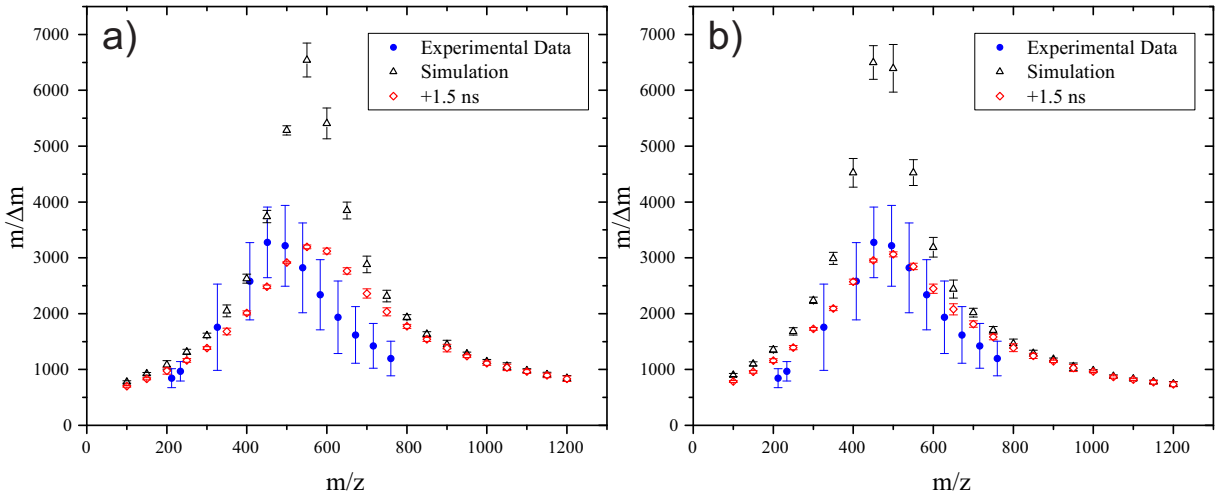

Figure 5.10: *Two comparisons between the mass resolutions obtained by experiment with the LT2 Plus and the electron multiplier, of the PEG polymer (blue points with error bars of one standard deviation), compared with mass resolutions found through SIMION simulation (black triangles). Figure a) shows the original simulations as presented previously in this chapter, whilst figure b) shows the result of new simulations obtained with a shorter switch time of 340 ns. Both plots also show (in red) the result of the convolution of the simulated mass resolutions with a Gaussian response function (1.5 ns — FWHM).*

(accurate to within 90 ppm) and a width of 0.23 leading to a mass resolution of $m/\Delta m \approx 2350$. The subsequent peak, shown in figure 5.9 c) is found to have a $m/z = 671.78$ (accurate to within 45 ppm) and a width of 0.48 leading to a rather lower resolution of $m/\Delta m = 1400$.

The final plot, shown in figure 5.9 d), again shows the peak corresponding to the sodium adduct ion with an eleven unit long PEG polymer. It also shows the subsequent progression of isotope peaks which appear at $m/z = 555.31$ (accurate to within 720 ppm). These peaks can therefore be attributed to the potassium adduct ion. This explains the observation of the regularly spaced, although less intense, peaks following each polymer peak in the mass spectrum.

The accuracy of the experimentally observed positions for each of the mass peaks in the mass spectrum, compared with literature values, validates the calibration of the instrument.

A plot of the experimentally obtained mass resolutions, as a function of mass, is shown in figure 5.10 a). The experimental data were recorded across a number of different samples,

and averaged. They are represented by the blue points with error bars that encompassing one standard deviation of the data from the mean. The simulation data, first presented in figure 5.4 a), is also plotted as the black triangles.

There is a marked disparity between the experimental and the raw simulated mass resolutions. As was the case in the previous chapter, there will be some response time affecting the experimentally obtained data which was not included in the simulation. Here, a fast electron multiplier was used, so the convolution of an exponential decay to the "true" ion signal is not valid. Instead, the response function can be assumed to have a more Gaussian form. This response function can be simply added to the results of the simulation by using the fact that the convolution of two Gaussian functions with standard deviations, σ_{a} and σ_{b}, is given by a third Gaussian function with a standard devation,

$$\sigma_{\mathrm{c}} = \sqrt{\sigma_{\mathrm{a}}^2 + \sigma_{\mathrm{b}}^2}. \tag{5.2}$$

By taking the width of the peak found by simulation, and applying a convolution of 1.5 ns (FWHM), the simulated data shown in red is obtained. This convolved simulation data fit the magnitudes of the experimental data far more closely, and the value of 1.5 ns is in keeping with the specification of the detector which states that the response time is $< 2\,ns$ (FWHM).

There is still an m/z offset between the peak in the mass resolutions obtained experimentally and those obtained through simulation. From the simulation results shown in figure 5.3 it is known that a change in either the pulse voltage, or the switch time, could produce a shift in the position of the peak mass resolution. Figure 5.10 b) shows a plot of the same experimental results plotted with new simulation data obtained after changing the switch time to 340 ns.

The match between the experiment and these new simulations can be seen to be much closer. The internal delay in the switch time pulsing of the LT2 Plus was specified as being 200 ns, although after testing it was found to be closer to 170 ns. This would support the hypothesis that the offset between the experiment and simulation was due to the switch

time of the ion optics, but it should be kept in mind that, as was discussed in chapter 3, absolute values obtained with SIMION should be regarded with caution.

5.3 Spatial Imaging

Having tested the mass resolution obtainable with the instrument, further modifications were made to enable spatial images to be acquired. The electron multiplier was removed, and replaced with an MCP detector and a scintillating screen with a diameter of 25 mm. The screen was composed of BC-408, a plastic scintillating material with a response time of around 4 ns [174]. With the image magnification factor of the instrument expected to be approximately 25, this would restrict the field-of-view of the detector to cover an area with a diameter of 1 mm on the sample plate.

The emission output intensity of BC-408 is estimated at being less than half of that of P47 so the intensified CCD camera was used for these initial spatial resolution experiments [46]. The CCD camera (Photonic Science [175]) was mounted above the detector and the BC-408 layer was brought into focus. A PMT (1P28, RCA [176]) was mounted alongside the camera so that the intensifier could be adjusted to overlap with the analyte mass peaks. The response time of the PMT is specified to be between 2–4 ns.

An Exalite 384 solution prepared to the same concentration as previously (1 mg/ml in 99% MeOH), was applied directly to a nickel mesh (33.5 μm wire diameter; 317.5 μm pitch) by the dried droplet method. This mesh was then attached, flush, to an ITO coated glass slide, and was secured using Kapton tape. The slide was then inserted into the modified sample holder (shown in chapter 2), and electrical connectivity between the ITO coating and the sample holder was ensured by bridging a short length of copper between the two.

The instrument was set to the same parameters as were used in the previous section, taking into account the shorter internal trigger delay of 170 ns. Although the field-of-view covered by the ion image was roughly 1 mm, the diameter of the laser spot was only 400 μm so in order to build up a full image of the sample surface the laser position was manually adjusted. This was achieved using two screws to alter the alignment of the fibre optic

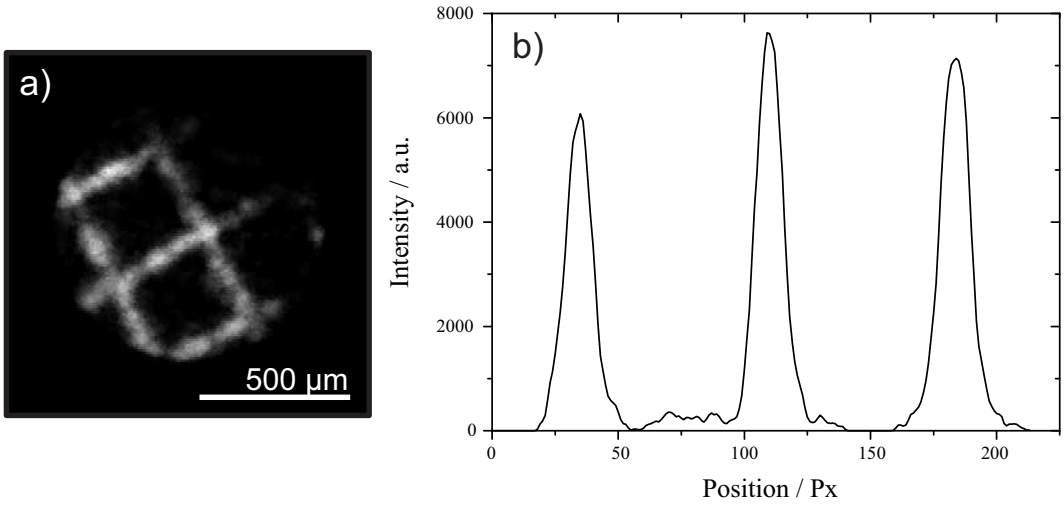

Figure 5.11: *An ion image of the Exalite 384 coated nickel mesh (33.5 µm wire diameter; 317.5 µm pitch), obtained with the LT2 Plus and a CCD camera, alongside a line profile taken from across the image. The data were obtained with an acceleration voltage of 5000 V, a pulse voltage of 570 V, a switch time of 370 ns, and an einzel lens voltage of 2100 V.*

where it was coupled to the instrument.

The voltages on the detector were increased up to a point where ion events could be observed. With 1.6 kV across the dual MCP stack (800 V across each plate), and 4.6 kV on the face of the scintillating screen (giving a potential difference of 3 kV from the back of the MCP stack) a strong signal was observed albeit without any resolvable image.

By adjusting the pulse voltage of the instrument a spatial focus was obtained. Figure 5.11 a) shows an example ion image obtained of the Exalite 384 coated nickel mesh obtained with a pulse voltage of 570 V. The rest of the instrument parameters were kept consistent with the previous experiments (acceleration voltage 5000 V, switch time 370 ns, and einzel lens voltage 2100 V). The magnification factor of the image is found to be 28 leading to a field-of-view of 900 µm across the sample. This factor is larger than the value of 25 found by simulation.

Figure 5.11 b) shows a line profile taken across the image. It shows a strong signal level compared with the background of the image. The pitch of the peaks is approximately 75 Px which, taking the 317.5 µm pitch of the nickel mesh, gives a ratio of 4.2 µm/Px. By measuring the rising edge of each peak between 20–80% a spatial resolution of 23 µm is found for the image.

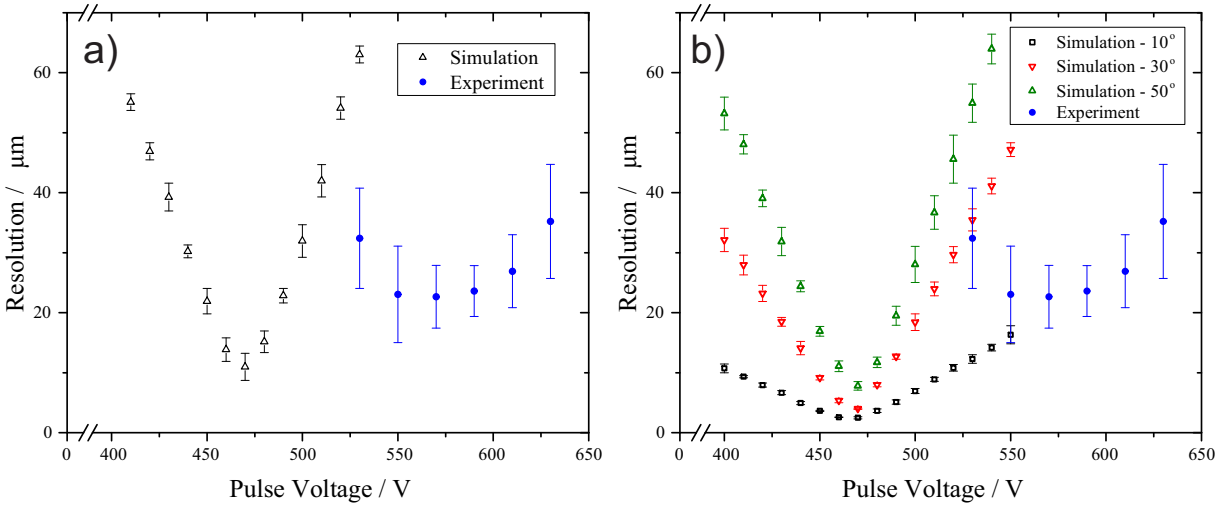

Figure 5.12: *Comparisons between the spatial resolutions obtained by experiment and simulation. Figure a) shows the results obtained by experiment (blue circles) and the simulated resolutions using the simulation definitions defined previously (shown by the open triangles). Each experimental data point was obtained over multiple acquisitions and the rising and falling edges, from 20–80%, were measured and averaged. The error bars represent two standard deviations from the mean value. Figure b) shows the same experimental data (again represented by the blue circles) this time compared to simulated spatial resolutions where the angular distribution of the ions' initial velocities has a FWHM of* 10°, 30°, *and* 50° *(marked by the open squares, red triangles, and green triangles respectively).*

The experiment was repeated several times with varying pulse voltages. For each experiment the ion image was analysed and the rising and falling edges of each image were measured to obtain the plot of spatial resolutions shown in blue in figure 5.12 a). The figure also includes the simulated spatial resolutions, marked by the black triangles, as a comparison. The most striking contrast between the experimental and simulated resolutions is the offset in the pulse voltage needed to obtain the optimum resolution: experimentally the optimum resolution is found with a pulse voltage of 570 V compared to the simulated value of 470 V. The best spatial resolution found by experiment was 23 μm where as the predicted optimum value was 11 μm. The form of these two curves is also different in as much as the spatial resolution increases far more rapidly, with a variation in the pulse voltage, in the simulation than is observed in the experiment.

Although the offset in the voltage needed for optimum spatial focussing differs by almost 100 V, this is not surprising. There are a couple of areas of uncertainty that may cause this to be the case. First and foremost amongst these is the fact that the voltage is

set through the internal software of the LT2 Plus, which then sends a 0–10 V level to the power supply. There is therefore a level of calibration needed which could be incorrect. Further to this, the spatial focussing in the simulation will be far more sensitive to small errors in the SIMION model of the ion optics than the mass resolution: to a first order approximation, the lensing of the ion optics does not affect the mass focussing of the experiment.

Even with these caveats, the trend observed in the spatial resolution obtained by experiment is different to that obtained by simulation. The simulation should, at the very least, be able to predict these trends, but it can be seen from figure 5.12 a) that the experimentally observed spatial resolution is far less affected by a variation in the pulse voltage than the simulated resolution. Figure 5.12 b) offers an explanation for this inconsistency by plotting the experimentally obtained spatial resolutions (marked by the blue circles) alongside resolutions obtained by simulation where the angular distribution of the ions' initial velocity distribution has been changed. The FWHM of the distributions is changed to 10°, 30°, and 50° in the data shown in black, red, and green respectively. It can be seen that with less angular spread the spatial resolution becomes less dependent on the pulse voltage. This does imply that the actual angular spread in the initial velocity distribution of the ions is much less than has been used in the simulation. As the values used in the simulation were chosen to represent an upper limit, taken from values found in the literature, it is unsurprising that this discrepancy has been found.

Although the definitions used in the simulation could be adjusted in an attempt to reflect this, it is known that the angular distribution of ion velocities does depend on the analyte being studied [129]. The precision of the simulation could also be brought into question with respect to, for example, modelling ion optic electrode apertures on a grid of square pixels. In the end it has to be accepted that although SIMION is a powerful tool for predicting the performance of ion optic assemblies, there are limitations to its direct comparison to experiment.

Despite the differences between the spatial resolutions obtained by experiment and simulation, there is a qualitative agreement between the two. A spatial focus is found by

altering the pulse voltage and the optimum spatial resolution is found at approximately 20 μm. Although this discrepancy highlights a need for a better understanding of the ablation dynamics it does not undermine the validity of the instrument. It has therefore been shown that a commercially built, linear, time-of-flight mass spectrometer, like the LT2 Plus, can be used for microscope-mode imaging.

5.4 Results with the PImMS1 Camera

With the instrument providing a spatially resolved image, the CCD camera was replaced by a PImMS1 camera. The lens used with the PImMS1 camera (Navitar, DO-5095 [177]) was designed for larger fields-of-view to be used in conjunction with 40 mm or 75 mm diameter detectors, and has a minimum focal distance of 60 mm. By inserting a 10 mm spacer between the lens and the PImMS sensor, the camera's field-of-view was reduced to 25 mm. This also resulted in a reduction in the minimum focal distance of the camera allowing it to be mounted 20–25 cm from the detector. This reduced distance allowed the lens to collect an increased fraction of the light produced by the scintillating screen.

As the PImMS1 camera does not have an image intensifier, it was necessary to increase the voltages applied to the detector in order to increase the detector gain. The voltage applied across the MCPs was kept at 1.6 kV but in order to observe signal the voltage applied to the scintillating layer had to be increased from 4.6 kV to 5.2 kV — a potential difference of 3.6 kV between the back face of the MCPs and the screen. A number of experiments were conducted with various voltages applied to the scintillating screen of the detector. A solution of Exalite 384 was applied to an ITO coated glass slide which was then inserted into a modified sample holder.

Figure 5.13 a) shows a plot of the cluster size frequency observed with the PImMS1 camera and the MCP detector. For each data set the voltage applied across the MCP was held at 1.6 kV but the voltage applied to the scintillating screen was altered from 5.2 kV to 5.4 kV, 5.5 kV, and 5.6 kV sequentially. As the PImMS1 camera converts analogue image data to a digital list of events, the cluster size frequency plot can be used as a surrogate

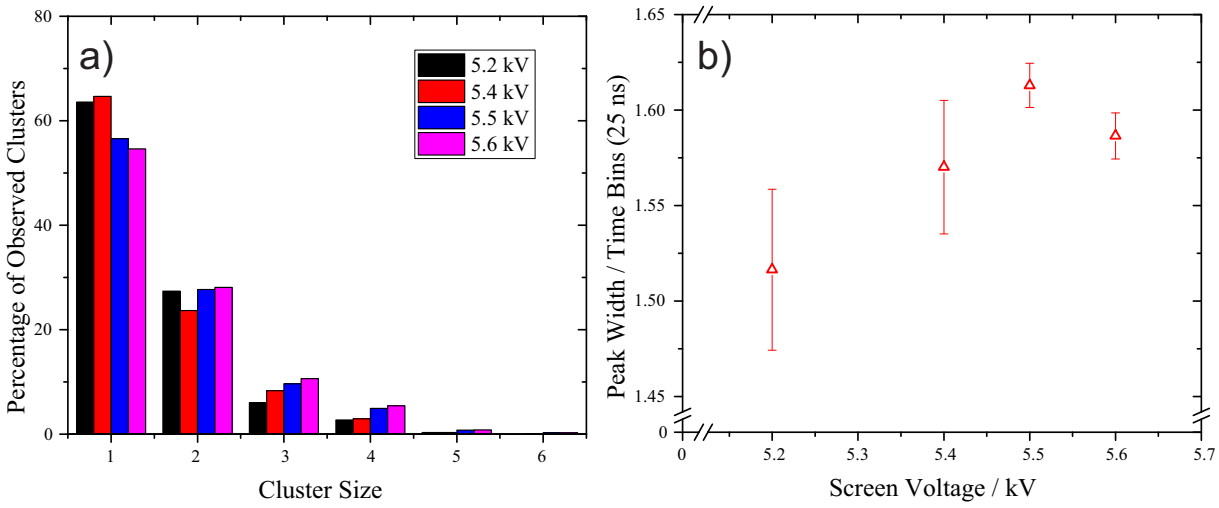

Figure 5.13: *Two plots showing the effect of increasing the voltage applied to the scintillating screen. Figure a) shows the cluster size frequency plots observed for data, obtained using the modified LT2 Plus and the PImMS1 camera, imaging a surface sample of Exalite 384. The data were acquired with scintillating voltages of 5.2 kV, 5.4 kV, 5.5 kV, and 5.6 kV (shown in black, red, blue, and pink respectively). Figure b) shows the variation in the width of the Exalite 384 mass peak (in time bins of 25 ns) as a function of the voltage. The error bars represent the standard error of the measurements.*

to understand the level of signal observed. The overall progression is the same for all four voltages with the majority of events occurring as clusters of only a single pixel, and the frequency of larger cluster sizes rapidly dropping off; however, as the detector voltage is increased, the proportion of larger cluster sizes also increases. As well as increasing the number of observed ion events, an increase in the frequency of larger cluster size events also improves the performance of the centroiding algorithm (as is explained in chapter 2). This allows for a better quality of PImMS data to be obtained.

Although, the quality of the data is improved, it is expected that an increase in the voltages applied to the detector should increase its response time leading to a worse resolving power. This is due to the increase in the charge repulsions in the expanding cloud of electrons that are accelerated from the back of the MCP stack to the scintillating screen. Figure 5.13 b) shows a plot of the Exalite 384 mass peak width as a function of the voltage applied to the scintillating screen of the detector, where the widths are measured in time bins (of 25 ns). This upward trend supports the idea that the increased detector gain has the unwanted effect of reducing the overall time resolution of the instrument.

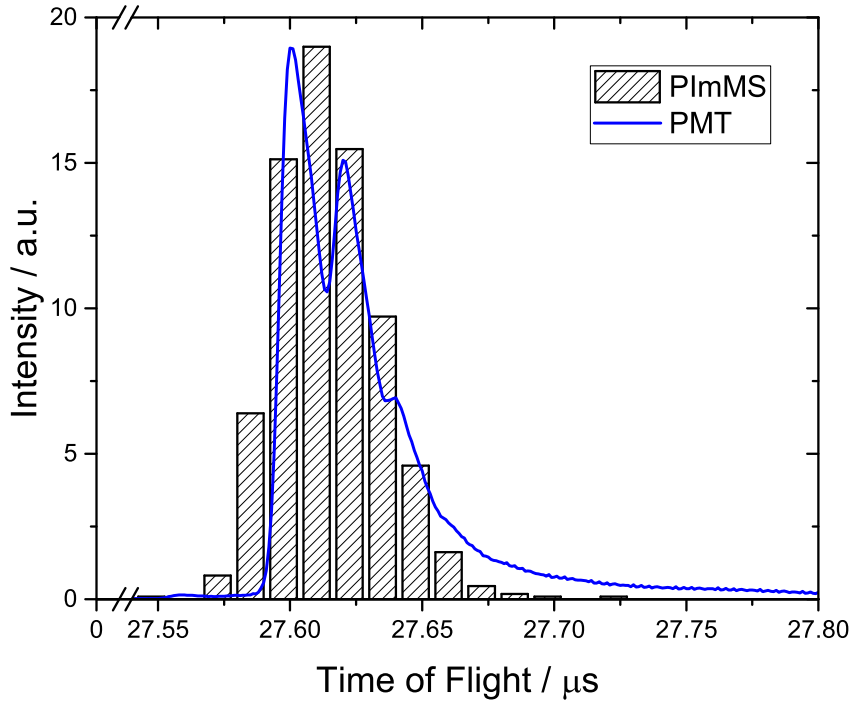

Figure 5.14: *A comparison of the time-of-flight spectra for the Exalite 384 parent ion peak, obtained using both the PImMS camera with a timing precision of 12.5 ns (represented by the columns), and the PMT (represented by the blue line). The data were obtained with an acceleration voltage of 5000 V, a pulse voltage of 500 V, a switch time of 370 ns, and an einzel lens voltage of 2100 V. The voltage applied across the dual MCP stack was set to 1.6 kV.*

Figure 5.14 shows the time-of-flight spectrum of the Exalite 384 parent ion obtained with both the PImMS camera (represented by the columns with widths of 12.5 ns) and the PMT (represented by the blue line). The data were acquired with an acceleration voltage of 5000 V, a pulse voltage of 500 V, a switch time of 370 ns, and an einzel lens voltage of 2100 V.

As would be expected, the data acquired with the PMT show a marked reduction in resolution when compared with that acquired with the electron multiplier. The combined response time of the BC-408 screen ($\approx$ 4 ns) and the PMT ($\approx$ 3 ns) can be estimated at 5 ns, which is considerably longer than the 1.5 ns observed for the electron multiplier. It is also comparable to the separation of the isotope peaks which, as can be observed in figure 5.14, is less than 25 ns.

Although the BC-408 scintillating material will have a decay lifetime similar in form to that observed with the P47 screen from the previous chapter, the decay time is now comparable to the rise time of the response function. This means that the convolution fitting method used in the previous chapter is no longer valid; however, the rise time and decay time of the scintillating material are also not equal so a simple Gaussian fit would not be valid either. Instead, a bi-Gaussian function[2] was used to fit the peaks. Using this, the peak width is found to be 16.9 ns leading to an approximate mass resolution of $m/\Delta m \approx 820$.

The peak observed in the PImMS spectrum does not show the presence of multiple isotope peaks. The time bin width (12.5 ns) is comparable to the peak separation so that resolving the separate peaks is not possible. This leaves the full peak width (containing all of the isotope peaks) at 45.6 ns, corresponding to a mass resolution of $m/\Delta m \approx 300$. This does not meet the target of isotope resolution ($\Delta m < 1$).

5.4.1 A Reduced Acceleration Regime

The experimental results that were presented in the previous section show that despite having optimised the ion optics of the LT2 Plus to achieve mass resolutions in excess of $m/\Delta m = 6000$, the resolving power of the modified instrument are found to be a far more modest 820 with the PMT, and only 300 with the PImMS camera. This is due to the response time of the detector and the method of acquiring the signal. In order to reduce the impact of this response time on the observed signal, the response time of the detection assembly must be reduced relative to the separation of the ion peaks. By increasing the time-of-flight for all ions, the time between subsequent peaks will also be increased, and so the response time of the detector will be reduced (in a relative sense).

To a first order, the arrival time of an ion in a time-of-flight mass spectrometer is proportional to the length of the field-free drift tube, L, and is inversely proportional to

[2] A bi-Gaussian function is similar to a Gaussian function except that the width of the peak differs either side of its centre. The fitting of these peaks was achieved using OriginPro 2015 [178]

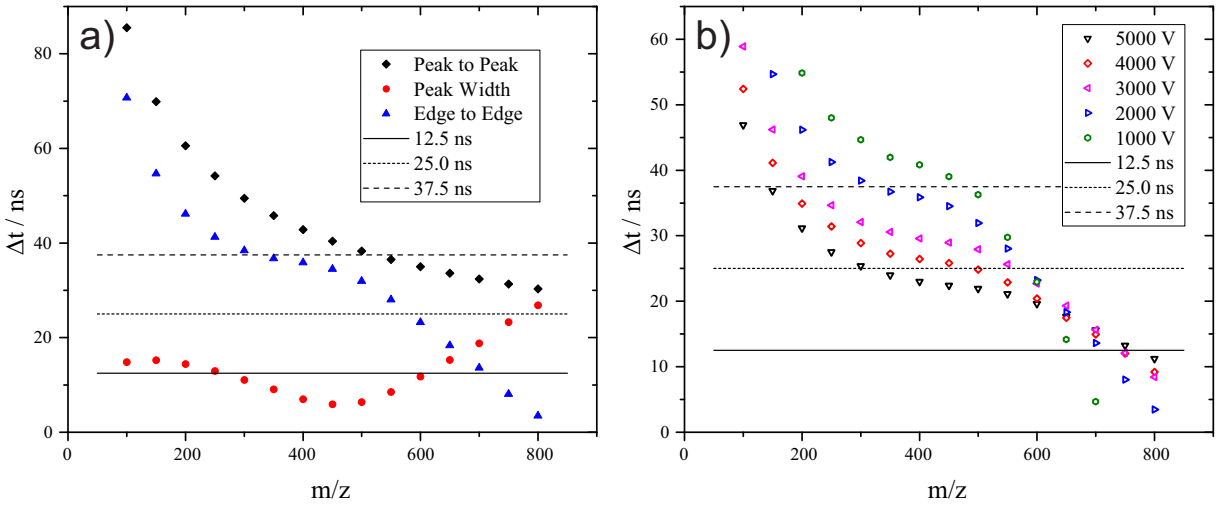

Figure 5.15: *Two plots of simulation data pertaining to the separation, in arrival time, of the different isotopes of species with $m/z < 800$. Figure a) shows the peak-to-peak separation (black diamonds), the peak width (red circles), and the edge-to-edge separation (blue triangles) of species with 1 Da mass difference. These simulations were run with an acceleration voltage of 2000 V. Figure b) shows the edge-to-edge separation at different acceleration voltages. Both figures also show the width of one, two, and three PImMS1 time bins for reference.*

the square root of the total accelerating voltage applied to the ion optics, V_A, such that:

$$t_{\mathrm{ToF}} \propto \frac{L}{\sqrt{V_A}}. \tag{5.3}$$

In an effort to minimise the modifications that must be made to the commercial instrument, and to avoid increasing the footprint of the instrument, simulations were performed to ascertain the improvement in the peak separation obtained from reducing the acceleration voltage of the instrument.

It is important to note that the detection efficiency of MCP detectors is known to reduce with a reduced acceleration voltage, but that this is most pronounced for larger molecules (hundreds of kDa) [179]. As the instrument was designed with small molecules (<1 kDa) as the target analyte, this was not considered a detrimental effect.

Figure 5.15 a) shows data obtained from simulations conducted of the LT2 Plus with an acceleration voltage of 2000 V. The pulse voltage was reduced to 230 V, the switch time was kept at 370 ns, and the einzel lens voltage was reduced to 1120 V. These parameters were chosen, as before, to optimise the spatial resolution, whilst also endeavouring to maintain

the best overlap between the mass ranges for the spatial and mass resolving powers. Three trends are presented as a function of the analyte ion mass: the peak-to-peak separation of species isotopes; the peak width; and the edge-to-edge displacement — that is, the time between 50% of the falling edge of the peak for one ion species, and 50% of the rising edge of a subsequent peak for an ion 1 Da larger. The edge-to-edge measurement is important as, for two peaks to be observed in a binned data set, there must, at the very least, be a whole time bin between them that is populated to a lesser extent than both of the peaks themselves.

The aforementioned trends are plotted alongside three horizontal lines which represent the width of one, two, and three PImMS1 time bins (assuming a 12.5 ns timing precision — 12.5, 25.0, and 37.5 ns respectively).

The peak-to-peak separation is marked by the black diamonds. It can be seen that the arrival time of ions within the mass spectrometer are bunched together as the m/z of those ions is increased. This would be expected as, using the simple calibration function in equation (5.1), the peak-to-peak separation, Δt_{P}, is given by,

$$\Delta t_{\mathrm{P}} = A\left(\sqrt{\frac{m}{z}+1} - \sqrt{\frac{m}{z}}\right). \tag{5.4}$$

The peak widths are shown in red, and can be seen to be comparable to the width of a single 12.5 ns time bin. The smallest peak width is observed for ions with a $m/z = 450$.

The edge-to-edge separation of the peaks, shown in blue, is calculated using the approximation that the widths of two adjacent peaks, with a difference of $\Delta(m/z) = 1$, are almost equivalent. It follows from this that the edge-to-edge separation can be found from the difference between the peak-to-peak separation and the peak width. The trend shows that, for an acceleration voltage of 2000 V, all species with $m/z < 700$ should arrive with at least a single time bin separating there constituent isotopes.

Figure 5.15 b) shows the simulated edge-to-edge separation of species for a range of acceleration voltages. Again, each parameter was chosen to optimise the spatial resolution, whilst also endeavouring to maintain the best overlap between the mass ranges for the

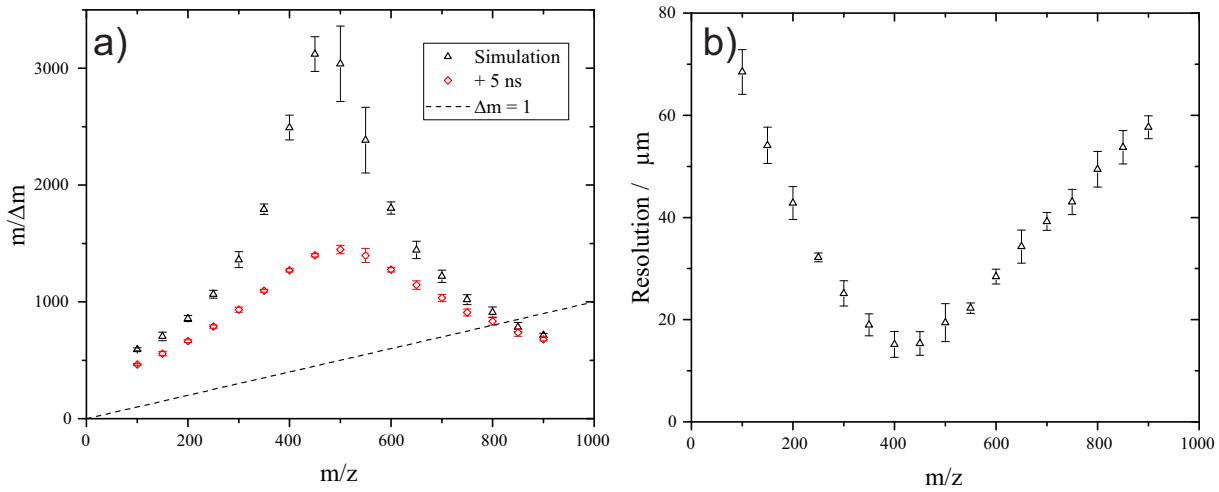

Figure 5.16: *Plots showing a) the mass resolutions, and b) the spatial resolutions obtained by simulation with the reduced acceleration regime: acceleration voltage of 2000 V, a pulse voltage of 230 V, a switch time of 370 ns, and an einzel lens voltage of 1120 V. In both figures the black triangles represent the simulated mass resolutions. In figure a) the red diamonds represent the mass resolution convolved with a 5 ns response time, and the dashed line represents the resolution needed to separate peaks with* $\Delta(m/z) = 1$.

spatial and mass resolving powers. None of these acceleration voltages are capable of separating sequential isotope peaks for species with $m/z > 800$ by more than a single time bin. This is because of the interplay between the peak-to-peak separation and the peak width: lowering the acceleration voltage increases the peak-to-peak separation; but it simultaneously increases the peak width as the chromatic blurring of the ions becomes more relevant.

The contributions of the peak-to-peak separation and the peak width can clearly be seen. With an acceleration voltage of 5000 V the range across which the edge-to-edge separation is greater than one time bin extends almost all the way to $m/z = 800$, but the majority of this range is separated by less than two time bins; whereas, with an acceleration voltage of 1000 V the range encompassed by an edge-to-edge separation of more than one time bin is reduced to almost $m/z < 650$, but the majority of this range has a separation greater than two time bins.

Between these two extremes there is a compromise. At an acceleration voltage of 2000 V a range of $m/z < 700$ is accessible over which species are separated from their isotopes by more than one time bin's width, and the majority are separated by more

than two time bins' width. Figure 5.16 shows the simulated mass and spatial resolutions predicted with an acceleration voltage of 2000 V, a pulse voltage of 230 V, a switch time of 370 ns, and an einzel voltage of 1120 V.

In figure 5.16 a) it can be seen that the mass resolutions are lower than was previously observed at the higher acceleration voltage. The mass range has been reduced from $m/z < 1000$ to $m/z < 800$; however, with the PImMS1 bin widths these higher masses could not be resolved anyway. Similarly, the spatial resolutions shown in figure 5.16 b) are not as good as before, with an optimum spatial resolution of approximately 15 μm. A spatial resolution of 50 μm or better is observed across the range $200 < m/z < 800$. The magnification factor for these parameters was found to have reduced, from that found at a higher acceleration voltage, to approximately 21. With the 25 mm detector diameter this corresponds to a field-of-view on the sample of approximately 1.2 mm.

5.4.2 Achieving a Higher Mass Resolution

In order to test this new reduced acceleration regime, an experiment was conducted to compare the spatial resolution of the instrument with that predicted by simulation. A sample of Crystal Violet (1 mg/ml in 99% MeOH) was sprayed onto an ITO coated glass slide through a nickel mesh (with a pitch of 317.5 μm, and a wire width of 33.5 μm). This was then inserted into the modified sample plate whilst a length of copper wire was used to ensure electrical connectivity with the glass slide.

The parameters of the LT2 Plus were set, according to the simulations, with an acceleration voltage of 2000 V, a pulse voltage of 230 V, and a switch time of 370 ns. The einzel lens voltage was then adjusted until a spatial image was observed. As before, the voltage predicted by the SIMION simulations did not sufficiently resolve the image. However, by reducing the einzel lens voltage, an image was obtained.

Figure 5.17 a) shows an image obtained with the einzel lens voltage set to 990 V. In order for the image to be observed the spatial resolution of the instrument must be better than 33.5 μm: the width of the nickel mesh. The PImMS1 data set was centroided although only clusters of one pixel were discarded so that there were enough events retained to produce

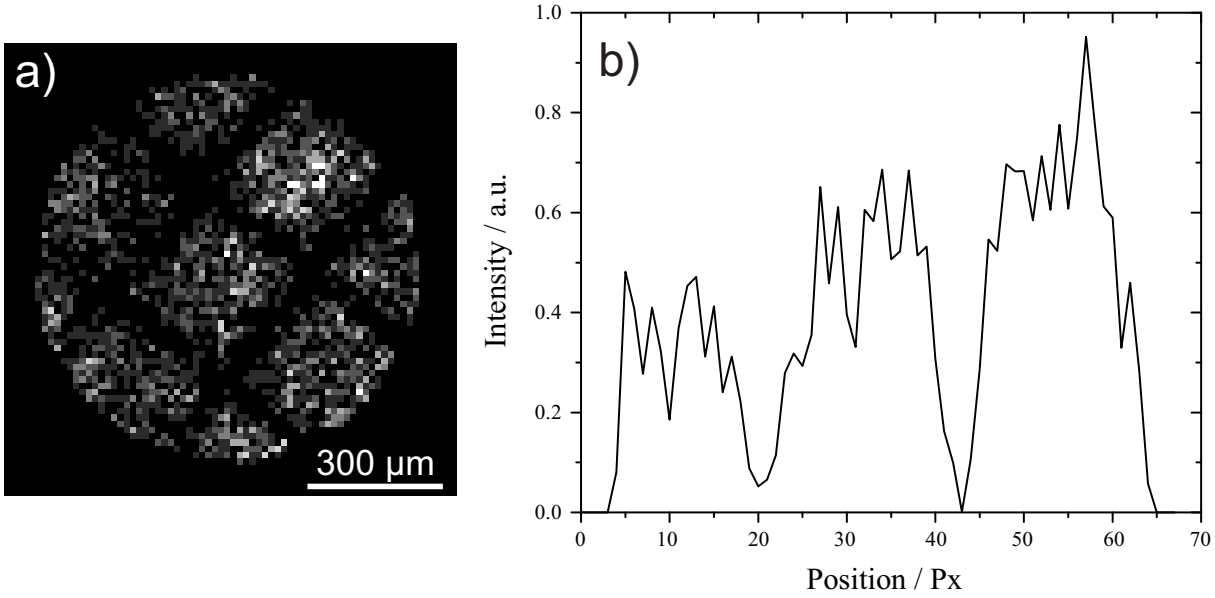

Figure 5.17: *Two figures relating to spatial resolution obtained with the LT2 Plus and the PImMS1 camera. Figure a) shows an experimental ion image, obtained with the PImMS1 camera, of a grid pattern of Crystal Violet. The image was obtained using the reduced acceleration voltages of 2000 V with a pulse voltage of 230 V, a switch time of 370 ns, and an einzel lens voltage of 990 V. Figure b) shows a plot of a line profile taken across the ion image.*

a smooth image. A resolution was obtained from the image by measuring the rising edge (from 20–80%) of features taken from line profiles taken across the image. One of these line profiles is shown in figure 5.17 b). It encompasses the width of three squares of the grid pattern produced by the nickel mesh. The pitch of the image, averaged across three different line profiles, was found to be 23 Px, corresponding to a pixel ratio of 13.8 μm/Px. This leads to a spatial resolution of approximately 27.2 μm.

Figure 5.18 shows the variation of the spatial resolution as a function of the voltage applied to the einzel lens. Images were only resolvable between the voltages of 960–1010 V. Outside of these voltages the resolution must be comparable, or worse, than the wire width of the nickel mesh so that it is not possible to obtain a spatial resolution. For the images that can be resolved there is a large variation in the calculated spatial resolutions so that there is no observable trend in the resolution; however, the absolute value of the spatial resolutions is found to be between 20–25 μm. This matches closely with the optimum simulated value of 19 μm. The magnification of the image is found to be

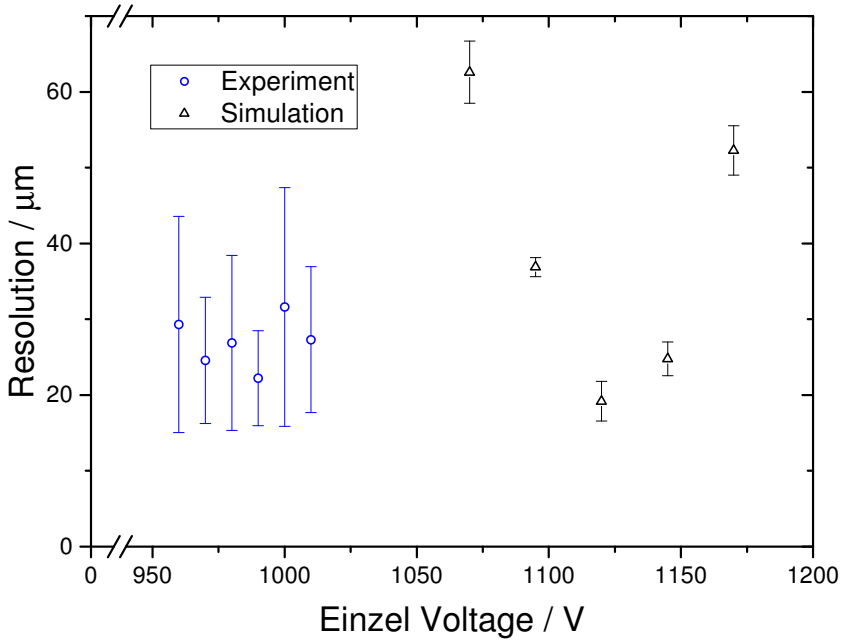

Figure 5.18: *A plot of spatial resolutions, obtained with the LT2 Plus and the PImMS1 camera, as a function of the voltage applied to the einzel lens (shown in blue with error bars of one standard deviation). Simulated data is presented alongside for comparison (represented by the open triangles).*

28.7 which is much larger than that predicted by simulation and results in a field-of-view of approximately 870 μm (in diameter).

A further experiment was conducted to investigate whether the mass resolutions, obtained with the reduced acceleration voltage, were improved over that observed previously. Four different dye samples (Auramine O, Crystal Violet, Exalite 384, and Exalite 404) were sprayed onto separate ITO coated glass slides and inserted into the spectrometer. The acceleration voltage was set to 2000 V, the pulse voltage was set to 230 V, the switch time was set to 370 ns, and the einzel lens voltage was set to 995 V.

Using the results obtained from analysing these dyes peaks, a calibration was found for these new instrument parameters. Two of the mass spectra, obtained with the PImMS1 camera, of these dyes are shown in figure 5.19. Figure 5.19 a) shows the ion peaks for the Crystal Violet sample, and figure 5.19 b) shows the ion peaks of the Exalite 384 sample. For both of these figures the PImMS1 data has been centroided discarding any data from

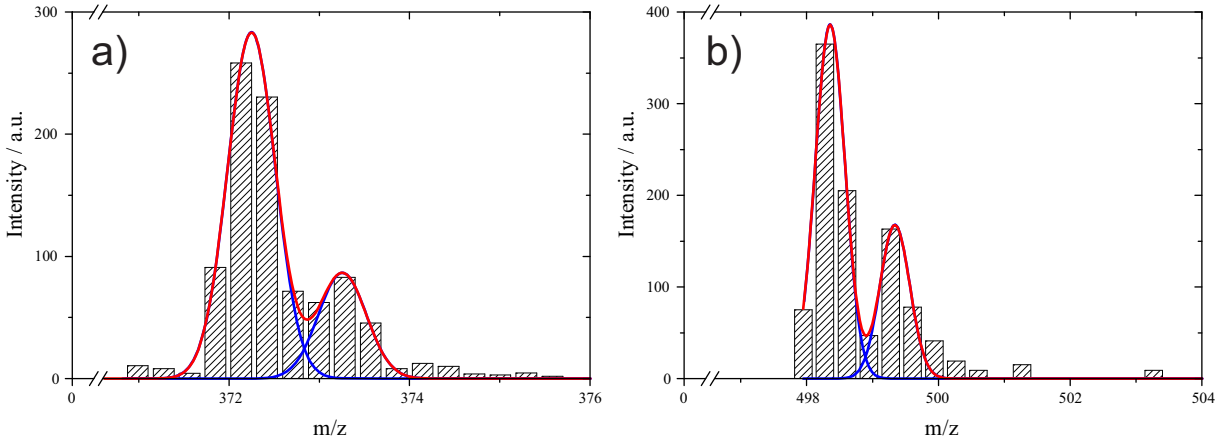

Figure 5.19: *Two plots of the mass spectra of a) Crystal Violet, and b) Exalite 384, obtained with the PImMS1 camera. The data were obtained using the reduced acceleration voltage of 2000 V, a pulse voltage of 230 V, a switch time of 370 ns and an einzel lens voltage of 995 V. A voltage of 1.8 kV was set across the MCP stack, and a voltage of 6.2 kV was applied to the scintillating screen. Both mass spectra have been fit with a Gaussian function across each peak for the various isotopes: the blue line represents the fit for each individual peak; and the red peak represents the sum of these individual fits.*

clusters of less than seven pixels. It can be seen from both of these plots that the separate peaks for the different isotopes of the species can be resolved. A Gaussian function was used to fit the mass peaks and this is shown in the plots as the blue lines. These individual fits are summed and shown in the plots as the red lines.

Figure 5.19 a), the peaks of the Crystal Violet sample, shows the major peak at $m/z = 372.25$ (compared to the literature value of $m/z = 372.24$). The width of the peak is 0.62 leading to a mass resolution of $m/\Delta m \approx 600$. It can be seen that there are at least two time bins between the peaks of the two isotopes which agrees with the predictions from the edge-to-edge separation simulations presented earlier in this section.

Figure 5.19 b) shows the ion peaks for the Exalite 384 sample. The major peak is observed at $m/z = 498.36$ (compared to the literature value of $m/z = 498.73$). The width of the peak is found to be 0.53 leading to a mass resolution of $m/\Delta m \approx 940$. The peaks in the data are more pronounced that those observed in figure 5.19 a). This is due to the alignment of the peaks in the time-of-flight spectrum with the PImMS1 time bins, as a better alignment will result in a more pronounced separation between the sequential peaks.

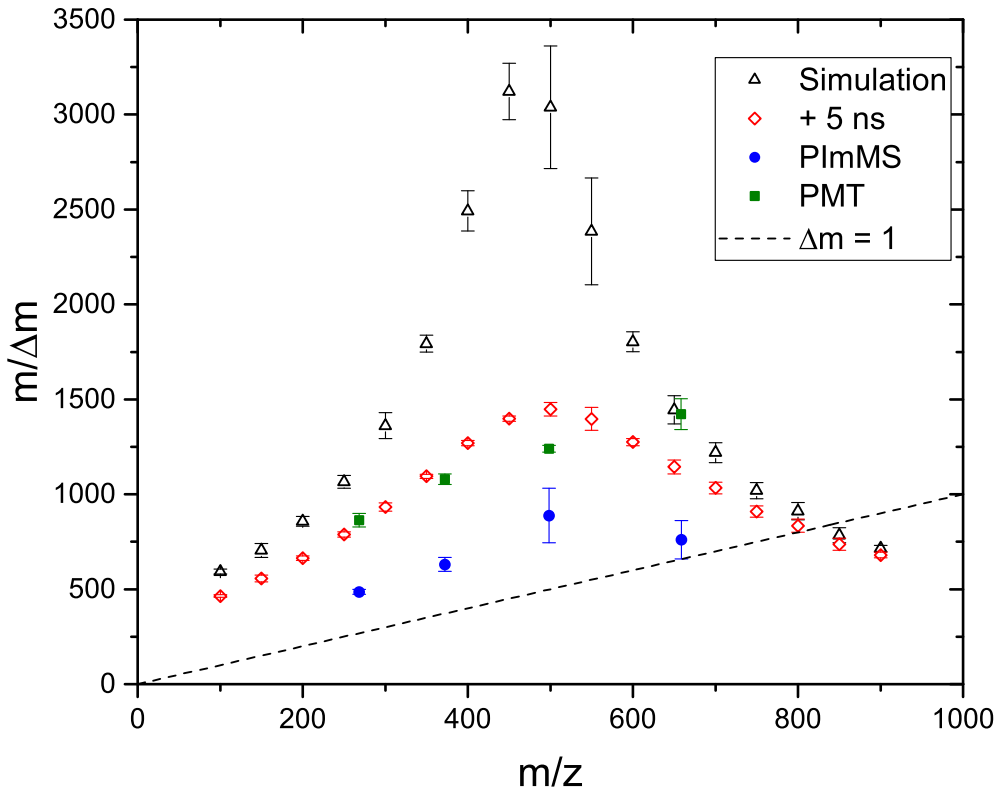

Figure 5.20: *A plot of the mass resolutions of the dye samples, obtained experimentally with both the PImMS1 camera (in blue) and the PMT (in green), as a function of the m/z of the species. The data are plotted alongside the mass resolutions predicted by simulation (represented by the black squares, and with a 5 ns convolution by the red diamonds). The limit for an isotopic mass resolution is shown by the dashed line.*

Figure 5.20 shows the mass resolutions observed for the dye peaks, obtained with both the PImMS1 camera (in blue) as well as the PMT (in green). The experimental data is plotted alongside those values predicted by simulation: the black triangles show the simulated values, and the red diamonds show the simulated values convolved with a 5 ns response function.

As would be expected the resolutions obtained with the PMT are better than those obtained with the PImMS1 camera. The 5 ns convolution to the simulated mass resolutions appears to be a good estimate as the PMT data fits closely to the simulated values. The PImMS1 mass resolutions are consistently above the limit for isotopic resolution although at higher m/z they come very close to this limit.

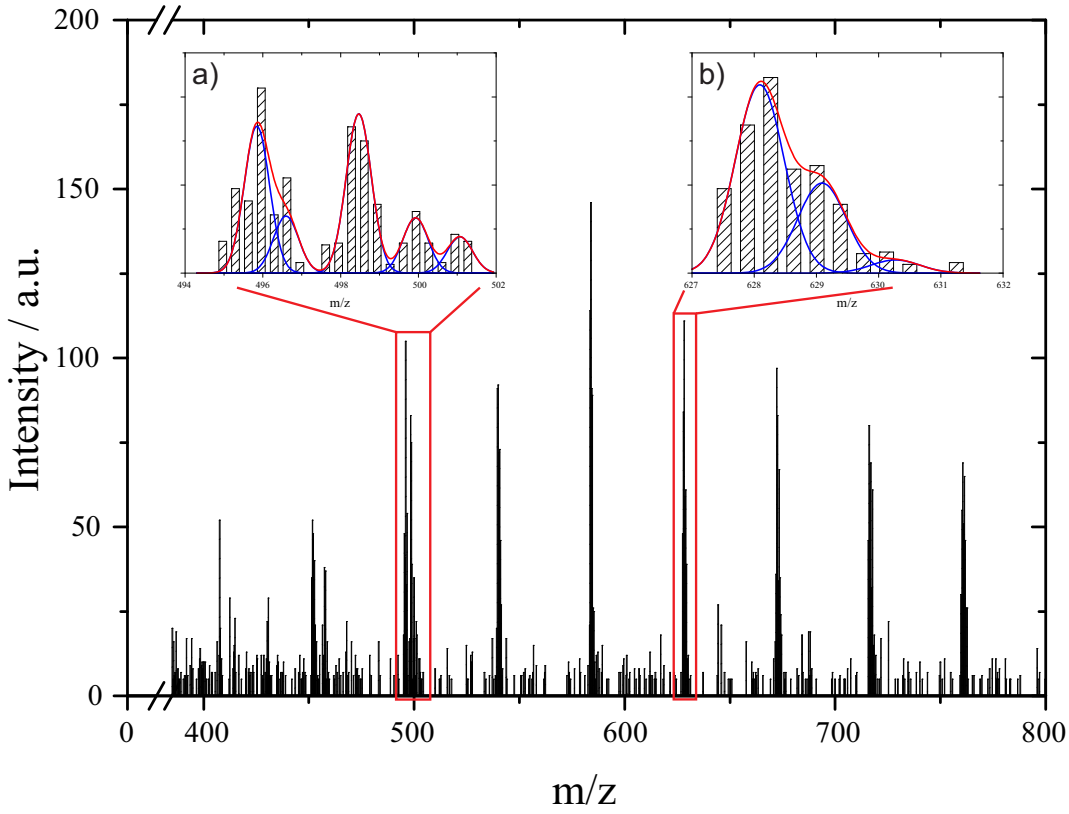

Figure 5.21: *A mass spectrum of the PEG polymer obtained using the PImMS1 camera. The polymer was ablated using a MALDI process and the reduced acceleration voltages optimised earlier in this section. Two regions of the mass spectrum have been enlarged and are shown in the two insets within the figure. The first inset shows the mass peaks of both the 10 unit long PEG polymer sodium adduct as well as peaks corresponding to Exalite 384 which had contaminated the sample. The second inset shows the peaks of corresponding to the 13 unit long PEG polymer sodium adduct. The blue fits to the peaks are Gaussian fits, and the red profile is the sum of these Gaussian fits.*

Although these data seem close to that which would be expected from the simulations, the ion definitions in the simulation assume that the analyte is ablated through a MALDI process.

A Comparison with MALDI Data

In order to compare the simulated mass resolutions with those obtained experimentally using the MALDI process a solution of PEG was prepared (100 μl in 5 ml of 2.65 mg/ml CHCA in 50% MeOH with 0.01% TFA). A few drops of this solution were applied to an ITO coated glass slide by the dried droplet method.

The parameters of the LT2 Plus were set to those used in the previous experiment

and a mass spectrum, shown in figure 5.21, was obtained with the PImMS1 camera, over 5000 shots. The data were centroided to the same level as was used previously (discarding clusters of fewer than seven pixels).

The characteristic progression of polymer peaks is immediately apparent in the mass spectrum. Two regions of the mass spectrum have been enlarged and are shown in the insets in the figure. Inset a) shows two sets of peaks: those at lower m/z correspond to the sodium adduct with the PEG polymer (10 units in length); whilst those at higher m/z correspond to a contamination of Exalite 384. The major peak of the polymer adduct is observed at $m/z = 495.84$ which can be compared with the literature value of $m/z = 495.55$ (a mass accuracy of 585 ppm). The peak width is found to be 0.77 leading to a mass resolution of $m/\Delta m \approx 645$.

Inset b) shows peaks belonging to the sodium adduct to the PEG polymer of 13 unit length. The peak is observed at $m/z = 628.09$ compared with the literature value of $m/z = 627.71$ (a mass accuracy of 605 ppm). The width of the peak is 0.92 which leads to a mass resolution of $m/\Delta m \approx 680$.

Figure 5.22 shows the mass resolutions from the analysis of the PEG sample, obtained with both the PImMS1 camera and with the PMT, alongside the resolutions predicted by simulation. The experimentally obtained data represent the sodium adduct ion of the polymer molecules between 8 and 10 units in length. As with the mass resolutions of the dye samples, those obtained with the PMT are better than those observed with the PImMS1 camera. The simulated resolutions are presented by the black triangles and resolutions obtained after convolution with a 5 ns response function are shown in red. These simulated results closely match those obtained with the PMT, with mass resolutions of $m/\Delta m$ =1000–1200. The PImMS1 data show mass resolutions of $m/\Delta m$ =500–800, which stays consistently above the limit for isotopic resolution (marked by the dashed line).

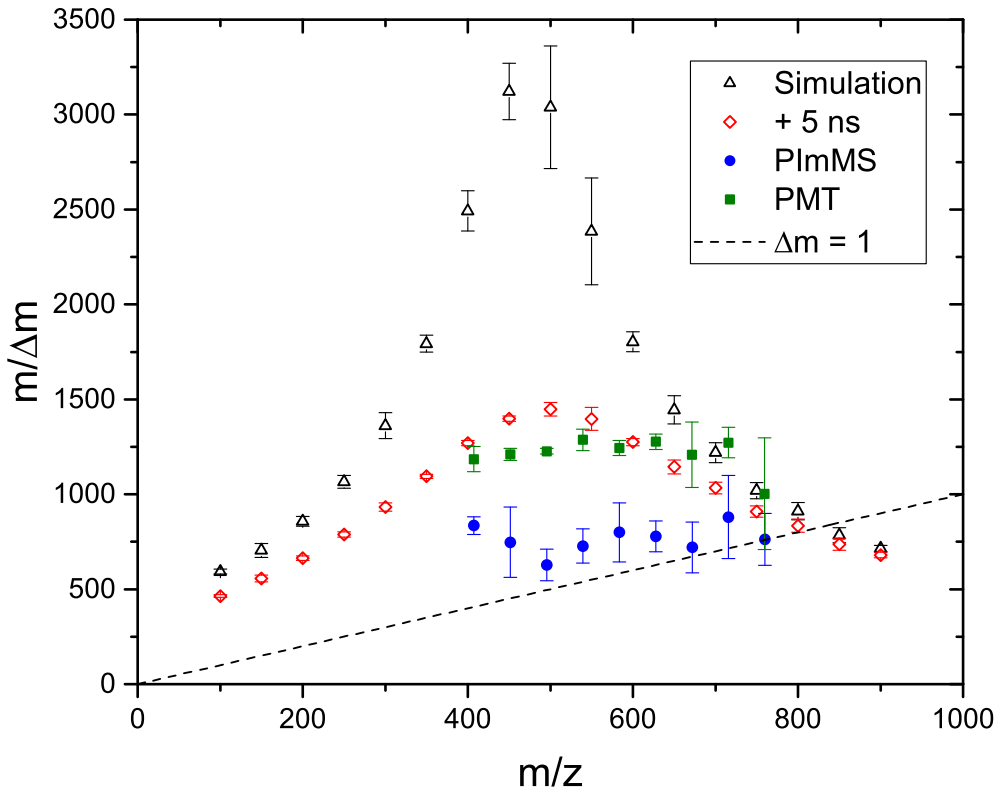

Figure 5.22: *A plot of the mass resolutions, obtained using the PImMS1 camera (in blue) and a PMT (in green), of the PEG polymer sodium adduct as a function of m/z of the species. The data are plotted alongside the mass resolutions predicted by simulation (represented by the black squares, and with a 5 ns convolution by the red diamonds). The limit for an isotopic mass resolution is shown by the dashed line.*

5.5 Multi-Mass Imaging

With the reduced acceleration voltage regime successfully allowing the PImMS1 camera to achieve isotopic resolution with a simultaneous spatial resolution of better than 50 μm across the range 200–700 Da, the final experiment conducted was to acquire data to compare with the multi-mass imaging proof-of-concept experiment that was presented in the previous chapter.

A final sample was prepared with both Auramine O, and Crystal Violet. The Crystal Violet solution (0.5 mg/ml in 99% MeOH) was sprayed first onto an ITO coated glass slide through a nickel mesh (with a pitch of 317.5 μm, and a wire width of 33.5 μm). This mesh

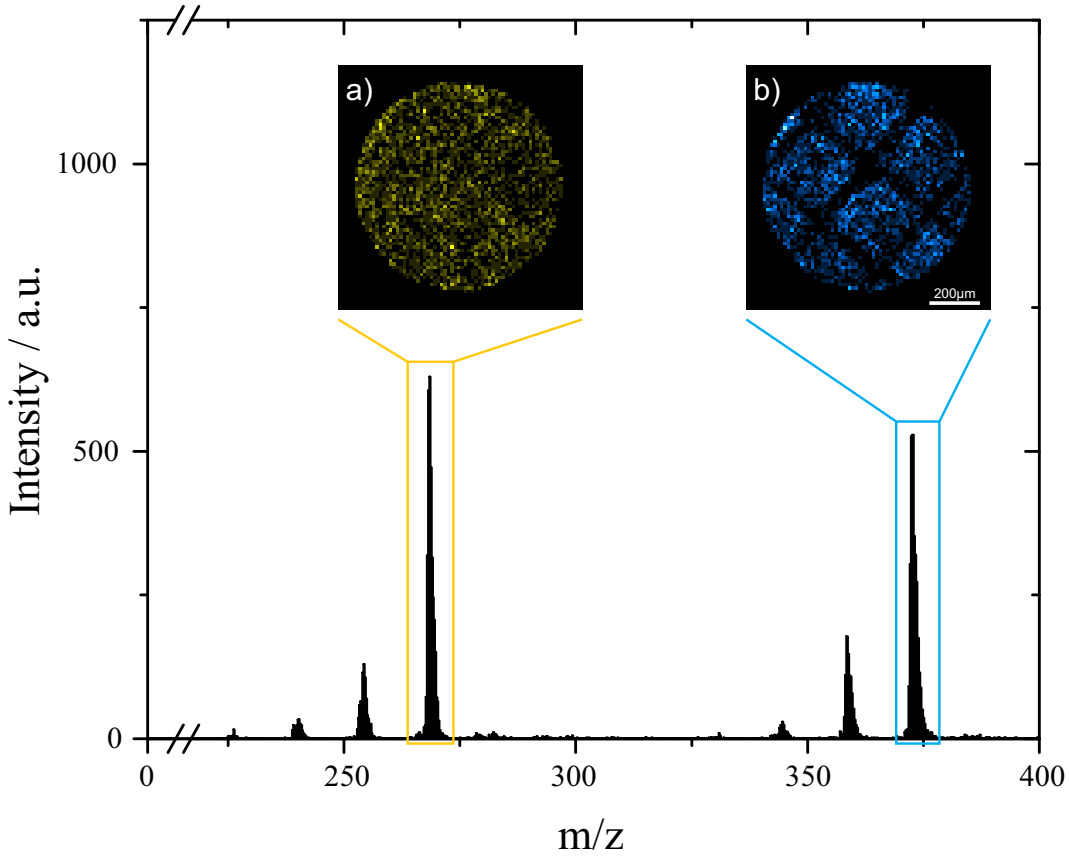

Figure 5.23: *A mass spectrum, obtained with the PImMS camera, of the dual dye sample. The data were obtained with the reduced acceleration voltage of 2000 V, a pulse voltage of 230 V, a switch time of 370 ns, and an einzel lens voltage of 995 V. The voltage applied across the MCP stack was 1.8 kV, whilst the voltage applied to the scintillating screen was 6.2 kV. The data were obtained over 5000 laser shots taking a total of 250 s. The inset images correspond to a) the homogeneous layer of Auramine O, and b) the grid patterned layer of Crystal Violet.*

was then carefully removed and an Auramine O solution (3.3 mg/ml in 99% MeOH) was sprayed uniformly across the surface of the same slide.

The instrument was set to the reduced acceleration voltage of 2000 V, with a pulse voltage of 230 V, a switch time of 370 ns, and an einzel lens voltage of 995 V. The voltage applied across the MCP was 1.8 kV, whilst the voltage applied to the scintillating screen was 6.2 kV. In order to get a full image filling the field-of-view (870 μm) the laser spot (diameter $\approx$ 400 μm) was swept across the image, as before.

Figure 5.23 shows the mass spectrum, obtained with the PImMS camera, of the dual dye sample. The data has been centroided but only clusters of one pixel were discarded so that there were enough events retained to produce smooth images. The data were

obtained over 5000 shots (over a duration of 250 s with the 20 Hz N_2 laser). The peaks at lower m/z correspond to the Auramine O dye with several species that are the products of demethylation of the precursor molecule present. Similarly, the peaks at higher m/z correspond to Crystal Violet with some peaks at lower m/z, again due to demethylation. Image a) shows an ion image of the homogeneous Auramine O layer obtained from the most intense ion peak. Image b) shows the grid structure of Crystal Violet obtained from the molecular ion peak at $m/z \approx 372$. The resolution of this image (taking the rising edge from 20–80%) is found to be approximately 25 μm with a magnification factor of approximately 29. This is in line with the spatial resolutions found earlier. After discarding any clusters of less than seven pixels, the mass resolutions of the Auramine O and Crystal Violet peaks are found to be $m/\Delta m \approx 540$ and 597 respectively.

Whilst this experiment shows the same ability for an instrument with the PImMS camera to acquire images of multiple species with different arrival times, the mass resolutions obtained from these data taken with the modified LT2 Plus are much improved over that obtained from the adapted velocity-map imaging instrument. This has also been achieved whilst maintaining a spatial resolution better than 50 μm and peaking at 20 μm.

5.6 Summary

In this chapter, a commercial, time-of-flight instrument has been modified so that it can acquire spatially resolved mass spectra using the microscope-mode. Early experiments showed that although the resolutions predicted by simulation were very impressive, the detection system of the instrument was the limiting factor. The voltage scheme for the instrument was then modified so that, although the ion optics resolution was decreased, the effect of the response time of the detector was reduced leading to an overall increase in the mass resolution.

This allowed for multi-mass imaging with an isotopic mass resolution, and a spatial resolution better than 50 μm, to be obtained with the PImMS1 camera, over the range $200 < m/z < 700$. These results are much improved over those obtained in the previous

chapter with the adapted velocity-map imaging experiment. The modifications necessary to the commercial instrument were also relatively minor, with the most extensive changes made to the detection system by replacing the electron multiplier with an MCP based detector.

Although the experiments meet the aims set out at the beginning of this chapter, it was the PImMS1 camera and the MCP-scintillator detector that limited the achievable resolutions. The timing precision of the PImMS1 camera at the time of writing was limited to a minimum of 12.5 ns, which for any linear time-of-flight mass spectrometer is comparable to the peak separation of species with $\Delta(m/z) \leq 1$. In order to obtain the best mass resolutions with the PImMS camera it was also necessary to discard a large number of the smaller clusters from the data which drastically reduces signal levels. In the next chapter, PImMS-data analysis methods will be presented which have shown promise in alleviating some of these limitations.

Chapter 6

Pixel Camera Data Analysis Techniques

In the preceding chapters, data obtained with the PImMS1 camera has been centroided using the recursive searching method outlined in chapter 2. It was noted that clusters appear to be made up of events that occur in spatially adjacent pixels, but can have a gap of up to seven time bins separating them temporally. It was also observed that the earliest time codes in a cluster are almost always found at the spatial centre of the cluster.

In this chapter, a model will be presented which attempts to explain these simple observations, whilst also making some predictions about the shape of clusters in (x, y, τ), and how this might be used to improve the methods used to process PImMS data.

6.1 The Shape of a Cluster

When an ion strikes the front face of an MCP stack it causes a cascade of electrons to be emitted. Over a dual MCP stack, operating with a gain voltage of 1.8–2.0 kV, a single incident ion can result in the emission of more than a million electrons from the back face of the back MCP [180] These electrons are then accelerated towards a scintillating screen. During their transit, the initial spread in the emission velocity of the electrons, and space-charge repulsions result in the electron cloud expanding to cover some area of the scintillating screen. Molecules within this area will then scintillate causing a flash of

photons which can be imaged by a camera. The dimensions of this flash will then be mapped onto the camera sensor covering a number of pixels. For a time-stamping camera, such as the PImMS1 camera, each of these pixels will record an event with a spatial coordinate, (x, y), and a time code, τ. This list of events all originate from a single ion event with a single set of coordinates, (x_0, y_0, τ_0).

6.1.1 The Spread in (x, y)

In acquiring the image from the scintillating screen, the camera will have a lens that focusses incident light onto the sensor. A first approximation for the distribution of this light across the sensor is that it can be described by a Gaussian function [160],

$$I(R) = I_0 . \exp\left[-\left(\frac{R^2}{2\sigma^2}\right)\right], \tag{6.1}$$

where the width of the distribution, σ, is identical in both the x-axis and the y-axis, and would be dependent (at the very least) on the gain applied to the detector and the focussing of the camera [180]. The variable, R, represents the distance (in pixels) from the original position of the incident ion such that $R = \sqrt{(x - x_0)^2 + (y - y_0)^2}$.

In order for an event to be triggered, the light incident on a pixel must exceed a predetermined threshold, I_{Th}. This assumes a number of things: that the intensity of incident light is directly proportional to the charge stored in the pixel; that the rise time of the charge increase has no impact on whether it crosses the threshold; that each pixel reacts identically given the same increase in charge and threshold value; and that the absolute intensity of the flash is the only parameter that differs between different events (for a given detector arrangement).

Accepting these assumptions and approximations, the distribution of light across a sensor surface will then follow the distributions shown in figure 6.1. The two curves represent distributions at different intensities, with that in red having a higher intensity than that in blue. These curves are plotted against the dashed line which represents the threshold level set on the camera. The implication is that any pixel for which the intensity distribution

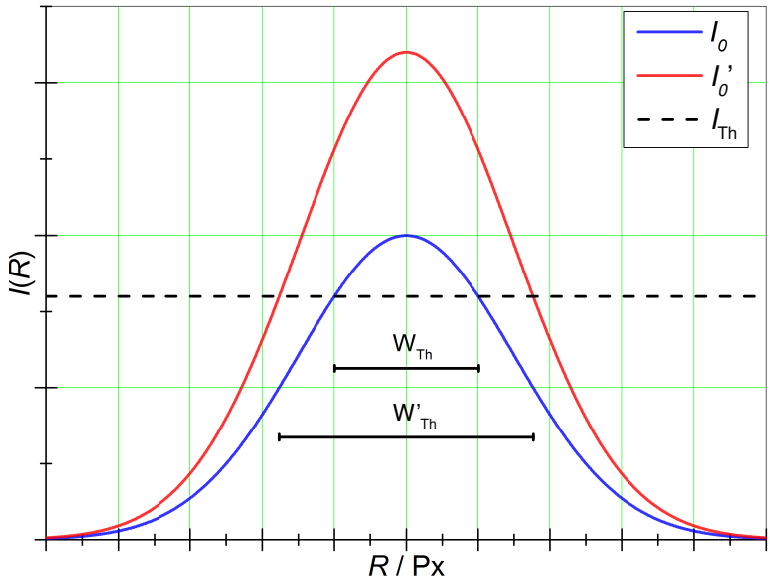

Figure 6.1: *Two Gaussian functions which represent the one dimensional distribution of charge across a sensor, resulting from the response of an MCP-scintillator detector to a single ion event. The two distributions differ in as much as the overall intensity of the red curve, I_0', is greater than that of the blue curve, I_0. The curves are plotted alongside a threshold level, I_{Th}, and the full widths of both curves above this threshold, W_{Th}' and W_{Th} respectively, are also marked as the black bars.*

is over the threshold level, will record an event. It can be seen that the number of pixels that will go over threshold for the less intense peak, W_{Th} (in blue), is less than the number that will go over threshold for the more intense peak, W_{Th}' (in red).

The position on the sensor, R_{Th}, where the intensity is equal to the threshold level, can be found by rearranging equation (6.1):

$$\begin{aligned} I_{\mathrm{Th}} &= I_0 . \exp\left[-\left(\frac{R_{\mathrm{Th}}^2}{2\sigma^2}\right)\right], \\ \ln\left(\frac{I_{\mathrm{Th}}}{I_0}\right) &= -\left(\frac{R_{\mathrm{Th}}^2}{2\sigma^2}\right), \\ R_{\mathrm{Th}}^2 &= 2\sigma^2 . \ln\left(\frac{I_0}{I_{\mathrm{Th}}}\right). \end{aligned} \tag{6.2}$$

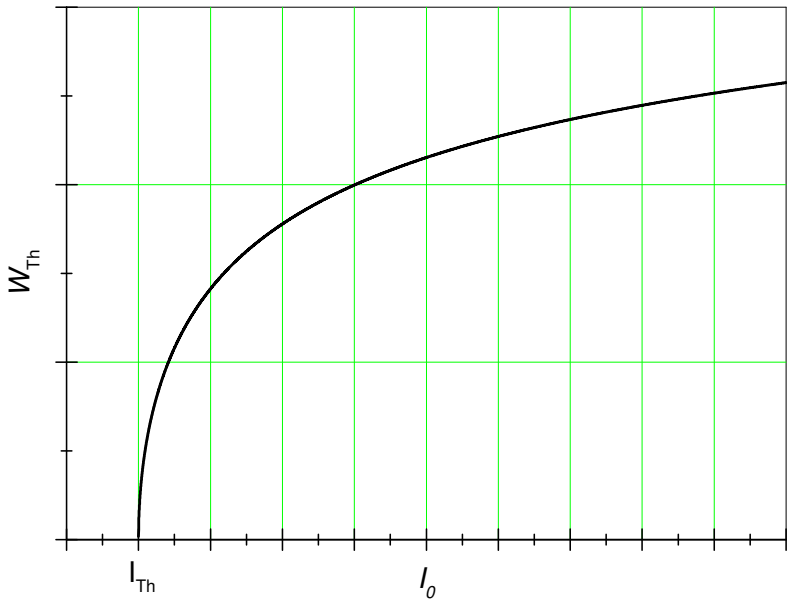

Figure 6.2: *A plot showing the relationship between number of pixels that will go over threshold and the amplitude of the illuminating source.*

The full width of the distribution above the threshold level is then given by:

$$\begin{aligned} W_{\mathrm{Th}} &= 2R_{\mathrm{Th}}, \\ &= 2\sigma\sqrt{2.\ln\left(\frac{I_0}{I_{\mathrm{Th}}}\right)}. \end{aligned} \tag{6.3}$$

Figure 6.2 shows this dependence of the width above threshold on the intensity. In practice, this offers a relationship between the number of pixels that are triggered and the amplitude of the illuminating light source. Below the threshold value no events are recorded, but once the threshold value is reached the number of pixels begins to increase although the gradient of this slope reduces with increasing brightness.

6.1.2 Response Times

Although it has been assumed that the rise time of the charge increase in a pixel has no impact on whether or not that pixel is triggered, it has not been considered how long

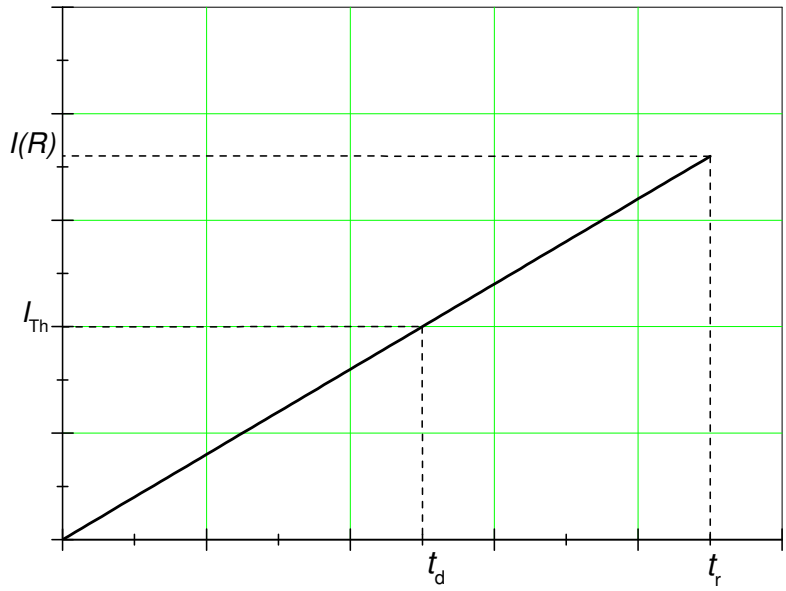

Figure 6.3: *A simple linear function which represents the increase in charge collected within a single pixel for a source that emits light with a rise time, τ_{r}, with an intensity, $I(R)$. The threshold level of the pixel, I_{Th}, is then reached at a time, τ_{d}.*

this process will take. Cartiglia et al. [181] explain that the time taken (here written as a fraction of the width of a PImMS time bin) for a pixel to go over threshold, τ_{d}, will be related to the rise time of the light source, τ_{r}, the amplitude of the light incident on the pixel, $I(R)$, and the threshold level, I_{Th}:

$$\tau_{\mathrm{d}} = \frac{\tau_{\mathrm{r}} I_{\mathrm{Th}}}{I(R)}. \tag{6.4}$$

The form of equation (6.4) is shown in figure 6.3. The slope of the line is defined by the rise time of the source and the intensity of the light emitted. For a given detector assembly, the rise time might be considered constant, but the intensity of the light emitted will differ[1]. This means that by increasing the intensity the slope of the graph will also increase, and as the threshold level is constant, this increase will result in a shorter delay time.

[1]For most MCP-scintillator detectors the response time of the MCPs will be much shorter (hundreds of picoseconds) than the response time of the scintillating screen (tens to hundreds of nanoseconds).

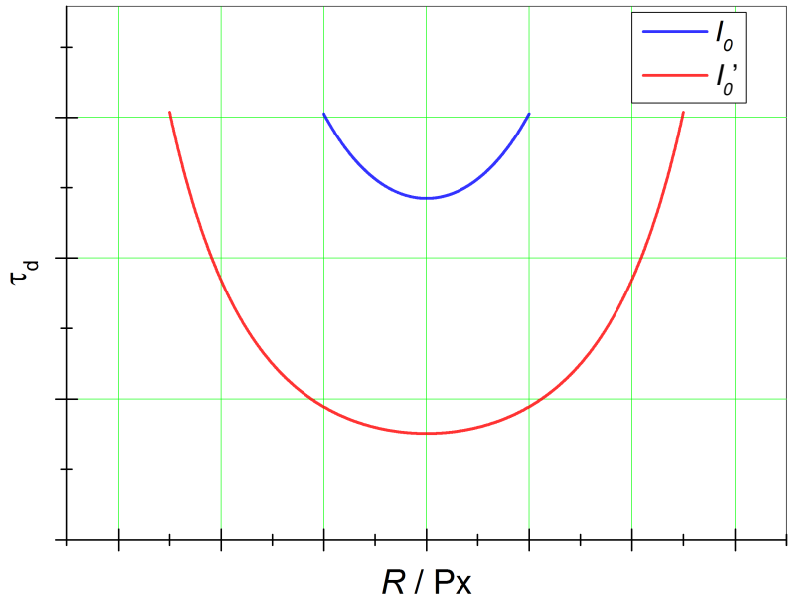

Figure 6.4: *A plot of the time delay observed for different pixels, as a function of their displacement from the centre of the original event. The two curves represent different intensities of the light source, where the red line is a more intense source, and the blue curve is less intense.*

As the delay time is dependent on the absolute intensity of light falling at a given point on the sensor, equation (6.1) can be substituted into equation (6.4) giving:

$$\tau_{\mathrm{d}} = \frac{\tau_{\mathrm{r}} I_{\mathrm{Th}}}{I_0 . \exp\left[-R^2/2\sigma^2\right]}. \tag{6.5}$$

Figure 6.4 shows two different plots of the delay time observed at different displacements from the centre of the original event. The two plots represent flashes of different brightness from the scintillator with the plot in red being more intense than the one in blue ($I_0' > I_0$). The plot shows the difference expected in the delay times for scintillator flashes of different intensities. The brighter flash has a much shorter minimum delay time and a broader overall shape leading to a larger number of pixels going over threshold.

The delay time is the difference between the original ion arrival time, τ_0, and the observed event time, τ. Using this, and resolving the distance, R, back to its relationship between the observed pixel coordinate, (x, y), and the original position of the incident ion,

(x_0, y_0) a full equation for the time delay within a pixel is found to be:

$$\tau = \tau_0 + \frac{\tau_{\rm r} I_{\rm Th}}{I_0 \exp\left[-\left(\frac{(x-x_0)^2+(y-y_0)^2}{2\sigma^2}\right)\right]}. \tag{6.6}$$

This equation describes the shape in, (x, y, τ), of a cluster given the original coordinate, (x_0, y_0, τ_0), some parameters dependent on the detector assembly, $(\tau_{\rm r}, I_{\rm Th}, \sigma)$, and the intensity of the light emitted from the scintillating screen for the event in question. The parameter $\tau_{\rm r}$ will depend on the scintillating material, and $I_{\rm Th}$ depends on the relative threshold level set on the camera. The final variable is the intensity of the light emitted from the scintillating screen which will vary for each event.

6.1.3 A Surrogate for the Intensity

Although the PImMS1 camera does not store the analogue information necessary to work out the intensity of light corresponding to each cluster, equation (6.3) gives an indirect measure of that intensity according to a measurement that is known: the number of pixels within the cluster, N.

The number of pixels in the cluster will be proportional to the square of the width:

$$\begin{aligned} N &= kW_{\rm Th}^2, \\ &= 8k\sigma^2 \ln\left(\frac{I_0}{I_{\rm Th}}\right), \end{aligned} \tag{6.7}$$

which can be rearranged to give the intensity of the flash relative to the threshold level of the camera,

$$\frac{I_0}{I_{\rm Th}} = \exp\left[\frac{N}{8k\sigma^2}\right]. \tag{6.8}$$

This equation for the intensity can then finally be substituted into equation (6.6) which is

then rearranged:

$$\begin{aligned}
\tau &= \tau_0 + \frac{\tau_\mathrm{r}}{\exp\left[\frac{N}{8k\sigma^2}\right].\exp\left[-\left(\frac{(x-x_0)^2+(y-y_0)^2}{2\sigma^2}\right)\right]}, \\
&= \tau_0 + \frac{\tau_\mathrm{r}}{\exp\left[-\left(\frac{(x-x_0)^2+(y-y_0)^2-N/4k}{2\sigma^2}\right)\right]}, \\
&= \tau_0 + \tau_\mathrm{r} \exp\left[\left(\frac{(x-x_0)^2+(y-y_0)^2-N/4k}{2\sigma^2}\right)\right]. \qquad (6.9)
\end{aligned}$$

Equation (6.9) should, within the breadth of the assumptions detailed earlier, describe the three dimensional shape of a PImMS1 cluster in (x, y, τ). It requires three parameters that depend on the detector: τ_r, the rise time of the signal level in time bins; σ, a measure of the spread of light over the sensor surface in pixels; and k, the geometric factor between the diameter of the spot of light spread across the sensor and the number of pixels that go over threshold. Finally, the equation needs the size of the cluster of events, N, which can easily be extracted from the data.

6.2 Attempts to Fit Clusters

The ideal case for the analysis of these event clusters, is where each cluster can be individually fit to the form of equation (6.9). This fitting, using the parameters τ_r and σ, would then yield the original coordinate of the ion event.

Figure 6.5 shows a surface fit to the coordinates of an eight pixel cluster obtained with the PImMS1 camera. The surface fit has a shape that is expected for the pixel response for an ion event; however, the parameters that are fit are highly dubious due to the fact that the three coordinates of the original ion event, and the three detector dependent parameters are all unknowns. With six unknown parameters $(x_0, y_0, \tau_0, \tau_\mathrm{r}, k, \sigma)$ and only eight data points there is no scope for a sensible or reliable fit. With such small cluster sizes, there is no opportunity to validate the pixel response model.

It is possible instead to attempt to take an average value for the relationship between the spatial and temporal displacement of events within clusters. Figure 6.5 b) shows a plot

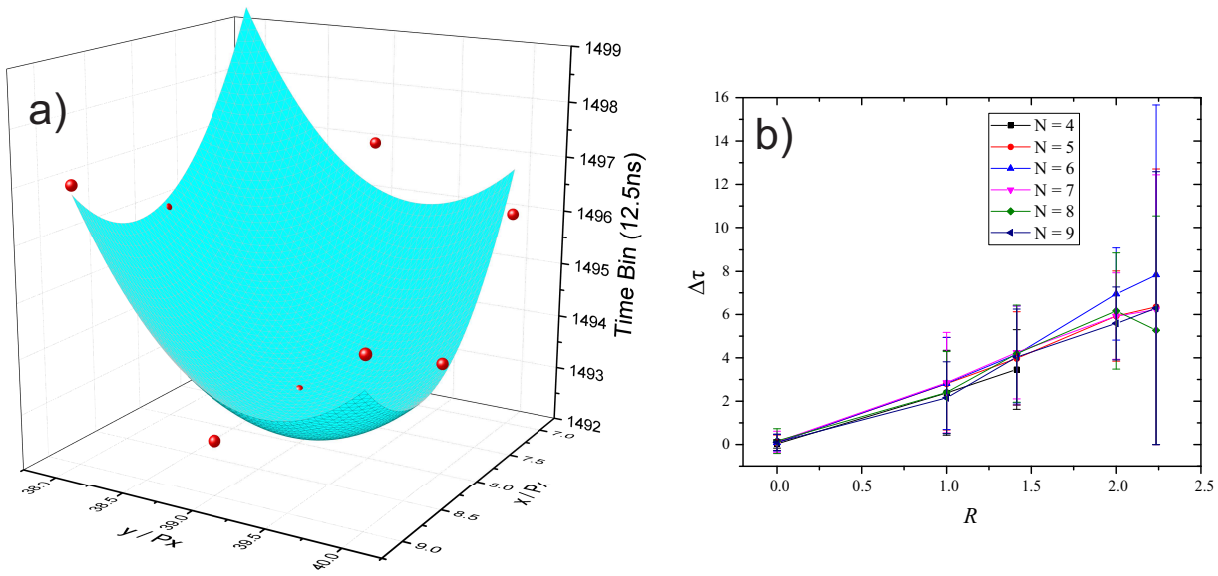

Figure 6.5: *Two plots showing attempts to fit clusters using the full cluster model (shown in equation* (6.9)*). Figure a) shows data taken from a single cluster of eight pixels which haven been identified as having all originated from the same ion event. The blue surface, is an example of a fit to this cluster. Figure b) is a plot of the displacement of an event in time bins from the first event in a cluster as a function of that event's spatial displacement from the centre of a cluster. The different sets of data represent different cluster sizes.*

of these values for different size clusters. Here the temporal displacement is $\Delta\tau = \tau[i] - \tau[0]$ and the spatial displacement has been reduced to $R[i] = \sqrt{(x[i] - x_0)^2 + (y[i] - y_0)^2}$, and the centre of the cluster is approximated by its weighted centre of mass [79, 159]:

$$x_0 = \frac{\sum_{i=1}^{N} \frac{x[i]}{\Delta\tau[i]+1}}{\sum_{i=1}^{N} \frac{1}{\Delta\tau[i]+1}}. \tag{6.10}$$

The subscript 0 represents the calculated, binned centre of the cluster; whereas the square brackets represent the index of one of the N events within that cluster. These events are sorted so that $\tau[0]$ is the first time code of that cluster.

As can be seen in figure 6.5 b) the variation standard deviation of that data in $\Delta\tau$ is much greater than the difference observed in their averages. This either implies that the intrinsic resolution of the sensor is not sufficient to show the trend, or that the precision and binning of the spatial displacements is too coarse to yield meaningful results.

At the time of writing, there is a second generation of PImMS camera, the PImMS2

camera, that will have a higher pixel count. There are also plans to increase the sensitivity of the camera with the addition of microlenses. Both of these developments should result in an increase in the size of observed clusters. These larger clusters should then, in turn, lend themselves to a more accurate and reliable fitting procedure where the validity of this model can be more thoroughly tested.

If this, or any similar, model can be found to fit the shapes of PImMS event clusters, the binning of data (both spatially and temporally) might be removed from the camera's influence on a data set. This will just leave the intrinsic resolution of the camera as the limiting factor. This intrinsic resolution is yet to be determined.

6.3 A Correction in τ

Although the clusters observed in PImMS1 data sets are not large enough to be reliably fit by the function, it is possible to make some simplifications that render the fitting more manageable with data sets obtained with the PImMS1 camera.

Rather than working with the full version of equation (6.9), it may be simplified to only relate to the central most pixel (i.e. $x = x_0$ and $y = y_0$) so that,

$$\tau = \tau_0 + \tau_\mathrm{r} \exp\left[-k'N\right], \tag{6.11}$$

where the geometric factor and the spread of the intensity of light across the sensor have been combined into $k' = \frac{1}{8k\sigma^2}$. As the central most pixel will have the earliest time code this simplification implies that the observed arrival time of a cluster will reduce exponentially with the size of the cluster. This trend was, to some extent, observed in chapter 2 where it was decided that larger clusters were found to arrive earlier than smaller ones and so the smallest clusters should be discarded. This model predicts a shape for this trend allowing a fit to be made.

Figure 6.6 shows a plot of the dependency of the position of the two most intense ion peaks (in time bins of 12.5 ns), observed in a mass spectrum of Crystal Violet, on the size of the clusters observed for each ion. The data were obtained using the PImMS camera

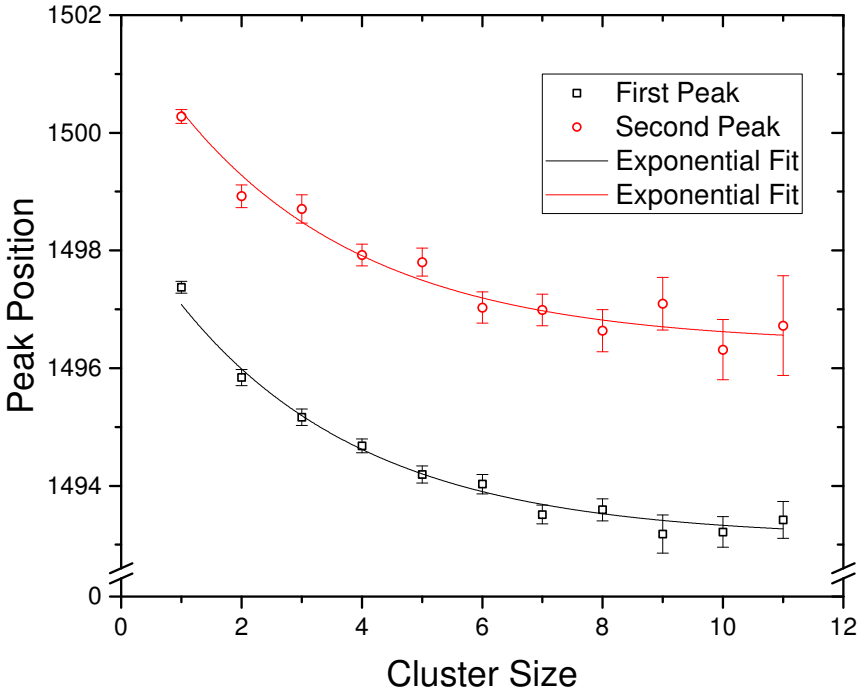

Figure 6.6: *Plots of the positions of the two most intense peaks in a mass spectrum of Crystal Violet as a function of the size of the clusters. The two trends a fit by the exponential function sharing the value of* τ_r *and* k'*.*

and the LT2 Plus, under the reduced acceleration voltage conditions outlined at the end of chapter 5. These two sets have been fit simultaneously with exponential decay functions according to equation (6.11), where the values of τ_r and k' were shared across both of the fits (i.e. only the offset, τ_0, differs between the fits).

Using this fitting method, it is possible to extrapolate back to an original arrival time for each of the peaks. Doing this, the first peak is found at 1493.1 time bins, and the second peak is found at 1496.4 time bins.

By using the values found for τ_r and k', a correction, τ_c, can be applied to the observed arrival time of any cluster, dependent on its size:

$$\tau_c = -\tau_r \exp\left[-k'N\right]. \tag{6.12}$$

Figure 6.7 shows the result of applying this correction shift to a centroided data set.

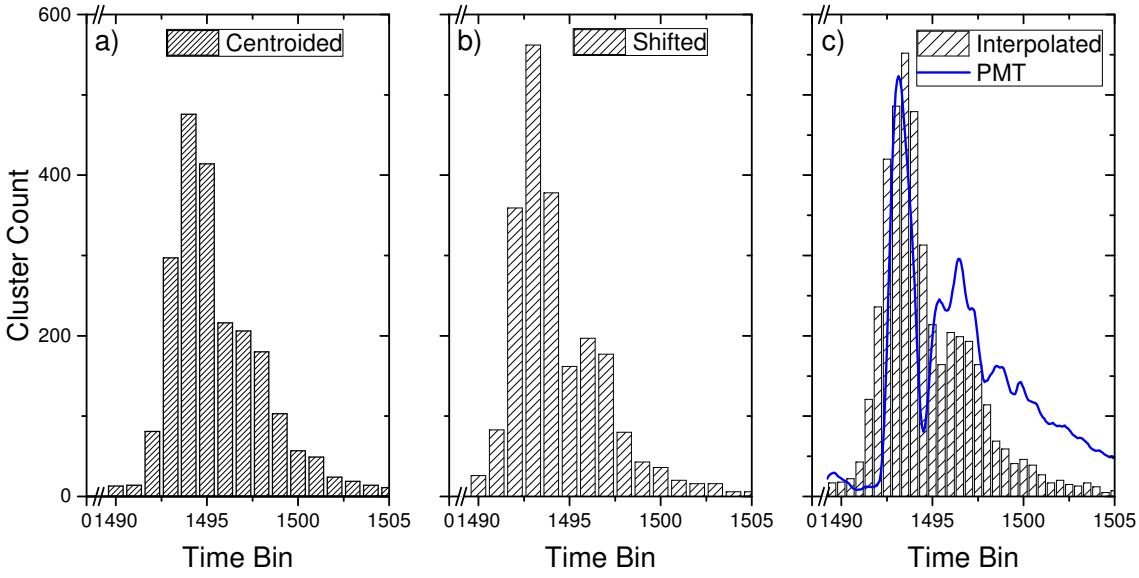

Figure 6.7: *A spectrum of Crystal Violet obtained with the PImMS1 camera. Plot a) shows the data after centroiding using the original method described in chapter 2; plot b) shows the data after the cluster size dependent correction, τ_c, has been applied; and c) shows the result of the correction once it has been extended to interpolate the spectrum.*

Figure 6.7 a) shows the Crystal Violet peak after the original centroiding method with all clusters of size three or larger included. The width of the most intense peak in the spectrum is found to be 34.5 ns.

Figure 6.7 b) shows the Crystal Violet peaks after the correction shift has been applied according to the size of the observed clusters. Again, all clusters of size three or larger have been included. The width of this peak is now 30.1 ns (a reduction of almost 13%). Qualitatively, it is also now possible to distinguish the second peak in the spectrum.

The correction applied to obtain the spectrum in figure 6.7 b) is limited as the data is re-binned after the correction has been applied; however, the precision of the correction is higher than the precision of the time bins so it is possible to interpolate the spectrum and shift an event by only a fraction of a time bin rather than by an integer value. If events are shifted in steps of half a time bin, the result is that the correction is extrapolating whether the even was more likely to have happened in the first half or the second half of a bin, using the intensity (cluster size) of the event as a discriminator.

Figure 6.7 c) shows the result of this interpolating event correction. As before, all

clusters of size three or larger have been included. The width of the most intense peak is again found to have been reduced to a value of 29.9 ns which is almost identical to the value found previously. This implies that the inherent resolution of the camera may not be sufficient to allow a timing precision better than 12.5 ns; although, with such a small sample size, this conclusion is far from definitive.

It is important to note that the peak width obtained using the original centroiding method, and removing all clusters of less than five pixels, is 30.3 ns. This means that by using the correction shift on a centroided data set, a resolution is obtained including all clusters of size three or more, that is comparable to (if not better than) the resolution obtained previously whilst only including clusters of size five or more. This allows far less data to be discarded whilst still achieving the same resolution.

6.4 Summary

In this chapter, a new method for analysing spectra obtained with the PImMS1 camera has been presented. The method stems from an attempt to model the shape of the clusters of events obtained with a PImMS camera in (x, y, τ). Although the data obtained with a PImMS1 camera does not have the sufficient statistics to validate the procedure, a simplified version of the model can be shown to correlate the size of PImMS1 data clusters to their centroided arrival time, using the size as a surrogate for the analogue intensity of an event. This leads to the use of a correction function which can be used to improve the resolution of a PImMS1 data set.

It has further been proposed that this method could be extended to interpolate a spectrum obtained with a PImMS camera by using the correction function to pinpoint an event with sub-time bin precision, although the data shown here is not conclusive in this respect. This interpolation will be limited by the inherent timing resolution of the PImMS camera which, at the time of writing, is not fully known.

At the very least, this analysis method allows less data to be discarded when analysing a PImMS data set. This is especially useful with the PImMS1 data set obtained with the

faster BC-408 scintillating screen, as this screen is less bright than a P47 screen, leading to much smaller clusters being observed. By retaining more of these small clusters, the statistics of an experiment can be greatly improved.

Chapter 7

Designs for a Primary Ion Source

In the previous sections of this thesis, the PImMS1 camera has been shown to ideally suit the needs of stigmatic imaging mass spectrometry. In chapter 4, the PImMS1 camera was used to test its ability to record spatially resolved mass spectra. This was followed, in chapter 5, where the limits of the PImMS1 camera were explored, particularly with regard to the limitation of the mass resolution by the 12.5 ns timing precision of the camera. Finally, methods were outlined to improve the resolutions achievable with the PImMS1 camera.

The work in these preceding chapters has given insight into the capabilities of a potential PImMS1-MSI instrument, which allow for a reassessment of the applications such an instrument should be targeting. So far, the ionisation mechanism used in the experiments presented in this thesis has been some combination of MALDI and simple LDI; however, there are benefits to branching out to other common ionisation sources, such as a primary ion source used for secondary ion mass spectrometry (SIMS).

One application that could be accessed with the implementation of a primary ion source is the use of mass tags. A mass tag is a species which can be added to a sample and binds to a specific target molecule. The tag is designed to be labile to the ion source used in the experiment so that the presence of the mass tag indicates the presence of the target molecule. An example of this would be the mass tags developed by the company BioSIMS [182]. These tags are especially labile when bombarded with Caesium ions.

In this chapter a design for a primary source of Caesium ions will be presented. First, a comparison of ion sources with laser sources will be discussed. This will be followed by an overview of the mechanical and electronic design considerations. SIMION simulations will then be presented leading up to a final design for use with an MSI experiment with the PImMS1 camera.

7.1 The Benefits of SIMS

As described in chapter 1, the SIMS ionisation mechanism uses a beam of primary ions to bombard a surface sample transferring kinetic energy to that surface resulting in the emission of secondary ions which are collected by the mass analyser. There is a plethora of primary ion species which are used in SIMS applications each of which produce secondary ions with different characteristics. This can be compared to MALDI which is considered a "universal" ionisation mechanism in as much as any analyte species should be ablated.

As a general rule, SIMS sources produce a large number of analyte ions with $m/z < 2000$. This range overlaps well with the accessible mass ranges studied earlier in this thesis. Different secondary ions will be produced dependent on the primary source, which can be tailored to a specific application, and likewise different fragmentation patterns will be produced. Whereas the MALDI mechanism promises a "universal" mechanism, the SIMS mechanism can be chosen to suit a given application.

Further to the selectivity, a primary ion source can also be more flexible than a laser source in terms of repetition rate, and fluence. Many laser systems have a restriction on the repetition rates that can be selected, either they can only be used at a number of discrete repetition rates, or are restricted by a maximum rate.

7.2 Simulating an Ion Source

A primary ion source was designed to fit the specifications of an instrument that might be used with the BioSIMS samples. Before accounting for the mechanical considerations it is easiest to conduct the electrode design *in silico*. The aims for the design were to create a

high fluence Caesium source with a short pulse width (i.e. comparable to the laser pulse width of 3–7 ns). It was also requested that the average beam energy should be in the range of 7 keV in order to most effectively cleave the mass tag from its target molecule in the analysis.

The *in silico* design was conducted using SIMION 8.1 and consisted of three parts. First, most simply but also most crucially, the parameters for the simulation had to be selected. This mainly concerned the definition for the ions' initial conditions. With the ions having been defined the design of the extraction optics surrounding the Caesium source was next. Here a low energy beam of ions travelling parallel to the time-of-flight axis was desired. This gives the best conditions for the next section: the ion buncher. The ion buncher was designed to compress down a packet of ions to a time focus (which can be overlapped with a sample). This has the rather obvious advantage of reducing the time spread in the creation of secondary ions but also results in an increase in the primary ion fluence.

7.2.1 Ion Distributions

The system was designed to be used with a 103060 Cs^+ source, produced by HeatWave Labs, Inc. [183]. These sources are similar to that described by Souzis et al. [184]. Ion generation is achieved through thermionic emission from a pellet of Cs-aluminosilicate in a Tungsten matrix which is heated, by Molybdenum heater wires, to a temperature of 1200 K [184–187]. This method results in a highly efficient production of Cs^+ [188–190].

Ions created in this manner can, to a first approximation, be deemed to exist in some thermal equilibrium in close proximity to the tip of the source pellet. In this case the magnitude of the velocities of these ions will be described by a Maxwell-Boltzmann distribution:

$$f(v) = \sqrt{\left(\frac{m}{2\pi kT}\right)^3} 4\pi v^2 \exp\left(-mv^2/2kT\right). \tag{7.1}$$

The SIMION software package does not include a method for initialising ions within a Maxwell-Boltzmann distribution but a Gaussian distribution can be used in its place.

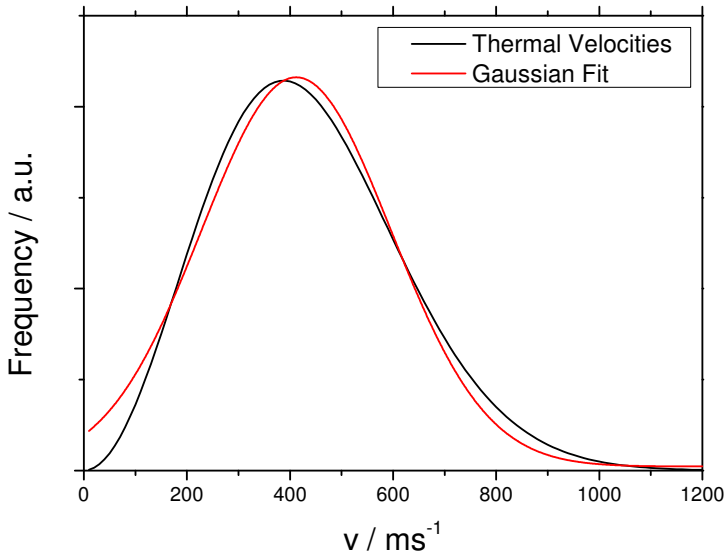

Figure 7.1: *A comparison between the Maxwell-Boltzmann distribution of speeds for Cs^+ ions at 1200 K, and the a Gaussian distribution of speeds which can be directly generated by SIMION. The Gaussian distribution has a mean value of 412 ms^{-1}, and a full width at half the maximum value of 433 ms^{-1}.*

Figure 7.1 shows a comparison between these two distributions. By fitting the Gaussian distribution to the distribution expected for Cs^+ ions at 1200 K a mean value of 412 ms^{-1} is obtained along with a full width at half the maximum value of 433 ms^{-1}.

Continuing with the above assumption, that the Cs^+ ions are in thermal equilibrium, the associated directional components of their velocities should be randomised within an arc facing away from the source pellet. This, in SIMION, is accomplished by setting the direction to a filled "cone direction distribution" with a half angle of 90°. The ions are generated within a cylinder positioned at the tip of the modelled source pellet (which is described later in section 7.2.2) matching the pellet with a radius of 2.6 mm. The extraction optics (also described later in section 7.2.2) will be continually drawing the ions away from the source so the cylindrical source position can be assumed to be shallow. A depth of 1 μm was chosen although this was chosen to give an upper limit to the achievable resolution of the system: Cs^+ ion generation occurs within the pellet where the source interacts with the Tungsten matrix, this means that ions will begin to feel the effects of the electrostatic extraction field very close to the surface of the pellet.

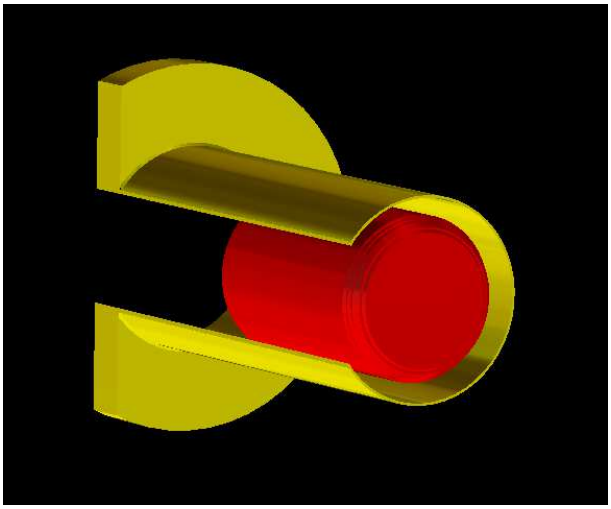

Figure 7.2: *The model of the Caesium source as created in SIMION. The source is defined as having cylindrical symmetry and only the externally facing parts are included. The red cylinder in the centre represents the tip of the aluminosilicate pellet, and the yellow surrounding represents the heat shield. The tip of the source has a diameter of 5.2 mm.*

The "time of birth" of the ions, and the number of ions created can be altered in order to calculate the fluence of the system. The source is capable of generating current densities of 1–10 $\mathrm{mAcm^{-2}}$ which translates to $\approx 1 \times 10^9$ ions in a microsecond [191]. These ions are set to the mass of Caesium (132.91 Da) and are assumed to solely be generated in a singly charged state.

7.2.2 Source Design

The source itself consists of two important parts: the tip, which is were the Cs-aluminosilicate resides in a porous Tungsten matrix; and the Molybdenum heater leads which connect to the tip and are used to heat the pellet to 1200 K. This assembly is then connected to a mounting base and surrounded by a Tantalum heat shield.

Figure 7.2 shows a model of the source as constructed in the SIMION software package. Only the pellet (in red) and the heat shield (in yellow) have been included as these are the only parts of the structure which will effect the electrostatic field of the extraction optics. The different colours have been added here for clarity and do not represent electrically separated sections (as is usual in SIMION): all parts of the source are electrically connected except for the heater element which is floated at the voltage of the source with an additional

bias current applied to generate the heating.

The ions generated from the source need to be collimated or focussed onto the part of the sample that is to be analysed. There is a great number of different designs for extraction and focussing optics used in conjunction with the various possible ion sources with the designs varying widely, depending on the application. The SIMS technique is often used for microprobe analysis where the smaller the primary beam focus can be obtained the better the spatial resolution of the image. These ion beams are generally space-charge limited: where the minimum beam waist is related to the current of the beam. As the beam current, I, is increased the coulomb repulsions of the ions within a beam exert an expansive force on the beam itself increasing the minimum focal spot size. This is somewhat quantified in the perveance, P, of a beam,

$$P = \frac{I}{V^{3/2}}, \tag{7.2}$$

where V is the accelerating voltage applied to the beam as it is extracted from its source.

With a beam intended for microscope-mode acquisition, there is no need to reduce the beam diameter as the size of the primary beam spot is completely decoupled from the obtained spatial resolution. Ideally, there should be some control over the diameter of the beam so that primary beam may be adapted for use with a variety of sample sizes but this can also be achieved through the use of an aperture (albeit the aperture approach will result in a reduction in the ion current).

Although the restrictions on the beam diameter are lifted, a microscope-mode, primary ion beam may need to have a uniform profile across the surface. This is especially true for static SIMS applications, where only the surface of the sample is being probed, and the relative ratios of the species on the surface need to be known. For applications where either the entirety of the sample is to be ablated and analysed, or where the relative abundances are not of interest, the beam profile is less important.

For the application of an array of mass-tagged samples, the demands of both the minimum beam size and the beam profile homogeneity are not great; rather, it is the

beam pulse duration which must be minimised. This will be dealt with separately from the ion extraction.

7.3 Forming a Beam Pulse

As the source continuously emits ions, the beam must be gated, chopped, or bunched in order to obtain a desirable short pulse width. Each of these mechanisms come with their own pros and cons, but as a general rule any attempt to produce a shorter ion pulse will either impose a restriction on the incoming ion beam, or will reduce the quality (fluence, or spatial focus) of the outgoing beam. Hence, the method of forming the pulse must be decided upon before continuing on with the design of the extraction optic as the former can (and will) effect the latter.

7.3.1 Gating

Gating the ion beam can be achieved by applying a retarding force to the ions, for instance by raising the voltage applied to the extraction electrode. The voltage can be lowered and then returned to its original voltage, using a fast "push-pull" switch (e.g. those produced by Behlke, originally for MS applications [72]), to form an ion packet. The switch time of the applied voltage depends on the resistance of the circuit and the capacitance of the electrode. The greater the range of voltages switched between the larger the resistance of the circuit needs to be, and so the slower the switching time becomes. In the majority of applications, switch times are on the order of tens of nanoseconds. This makes gating an ion pulse width down to 10 ns very troublesome.

7.3.2 Chopping

Another means for producing a pulsed ion beam from a continuous one is to chop the beam. This method is similar to the gating procedure in many ways in that it involves applying a retarding or deflecting force to the ion beam so that the ions do not reach their intended target apart from for a specified period of time. The difference here is that

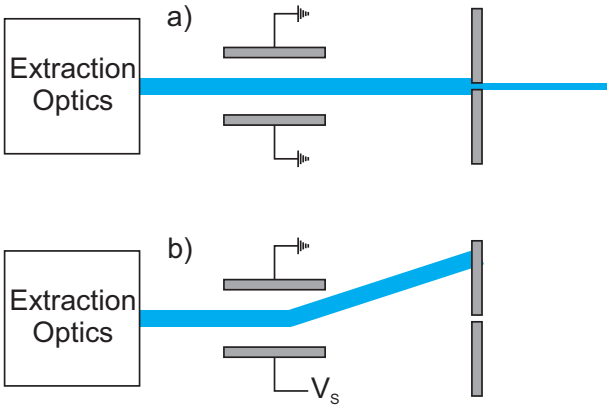

Figure 7.3: *A cartoon representation of a sweeping ion beam chopper. A beam of ions (represented in blue) is extracted from a source and sent between two parallel deflecting plates before reaching an aperture. When the deflecting plates are kept at ground, as in figure a), the beam continues through unperturbed. If a voltage is applied to one of the plates, shown in figure b), then the beam is deflected away from the aperture so that no ions make it through.*

rather than gating the source, the beam is chopped after it has been extracted [192].

Figure 7.3 shows a simple representation of an ion optic assembly that would achieve this. Ions are extracted from their source and are accelerated between two parallel deflecting plates. In figure 7.3 a) there are no voltages applied to the deflecting plates so the ion beam is not deflected and so continues on to an aperture with the majority of the beam passing through and reaching the target. In figure 7.3 b) a voltage, V_S, is applied to one of the deflecting plates so that the beam does not hit the aperture and so does not reach the target. The advantage gained from this procedure is that the pulsing time of the deflecting plate is not the defining factor in the pulse length; instead, the beam can be swept across the aperture, and it is then the duration of time that the beam overlaps with the aperture slit that defines the length of the pulse [193].

The drawback of this approach is that there is a direct trade off between the shortness of the pulse and the beam current. For a given ion source and extraction optic combination, a shorter pulse can only be obtained by sweeping the ion beam across the aperture faster which results in fewer ions passing through. For applications where only a small beam spot is required, this is not a concern, but for an ion microscope that probes a larger area of the surface a much higher beam intensity is needed to maintain the same fluence.

7.3.3 Bunching

One last method for creating an ion beam pulse is to bunch the ions [194, 195]. This is most simply achieved by producing an ion optic assembly that can apply an electric field along the TOF axis. The buncher is kept field free whilst it is filled with ions from the extraction optic. Once the buncher has been filled, the electric field is applied. Ions at the back of the buncher are accelerated to a higher final velocity than those at the front end so that all of the ions come to a time focus at the target.

This approach has the dual benefit of increasing the ion beam current as well as reducing the pulse length as a large "length" of ions are compressed down into a short pulse. The length of the pulse will depend on the quality of the design of the ion optics but also, crucially, on the spread in velocities of the ions that fill the buncher. The buncher compresses down ions of the same velocity but different positions along the TOF axis to a time focus; if the spread of velocities is too high, the resolution of the time focus will be reduced leading to a longer pulse.

7.4 Extraction Optics Design

In order to optimise the design of the ion optics assembly used to extract ions from the Cs^+ source, two different measurements are important: the transverse spatial spread of the extracted ions; and the angle between the ion velocity and the time-of-flight axis. Reducing these parameters for the extracted ion beam will improve the ability of any further optic to convert the continuous source into a pulsed beam.

Simulations were conducted in the SIMION particle trajectory software, using the ion definition outlined above. A grounded chamber, 600 mm in length, was modelled, with the ion source design included at one end so that the full flight distance from the tip of the source to the end of the chamber was 576 mm. The entire simulation was conducted with a scale factor of 0.1 mm/GU.

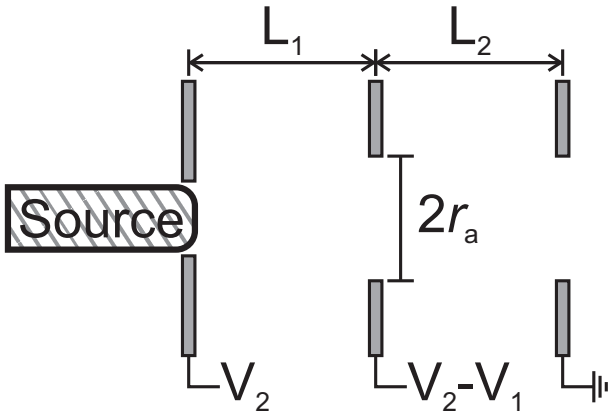

Figure 7.4: *A cartoon representation (not to scale) of the emission lens design for the extraction ion optics. The design consists of three electrode plates separated by distances $L_1 = L_2$. The Cs^+ source is inserted into the first electrode whilst the second and third electrodes both have apertures at their centres (both with a radius, r_a. The voltages applied to the plates are based on the scheme recommended by Liebl [163], except that they are shifted so that the drift tube following the extraction optic assembly is at ground.*

7.4.1 Emission Lens

The simplest method of extraction from a source is to construct an emission lens similar to the ion optic assembly described in section 2.1.2. The lens assembly transfers an image of the source surface to the target sample. The magnification of the system will determine the size of the beam spot, and the homogeneity of the beam profile should only depend on the emission from the source coupled with any aberrations arising from the lens arrangement.

In the work by Liebl [163], from which the derivations in chapter 3 are adapted, an emission lens assembly is described which achieves "telescopic" focussing (i.e. where the focal length of the assembly, $f = \infty$). The three electrodes are spaced equally, $L_1 = L_2$, and in the ideal case the ratio of the acceleration voltages relative to the repeller surface is found to be either, $V_1/V_2 = 0.34$, or $V_1/V_2 = 2.8$. The latter regime corresponds to an accel-decel arrangement where the ion extraction step is conducted by a strong field before the ions are then decelerated back down to their final velocity whilst they are focussed through the aperture of the final lens. This stronger extraction field is beneficial when working with a high current source as the perveance of the system will be lower. In the case presented by Liebl, the final electrode plate is held at some voltage, V_2, ; here, the voltages have been changed so that whilst the extraction optics work in the same way,

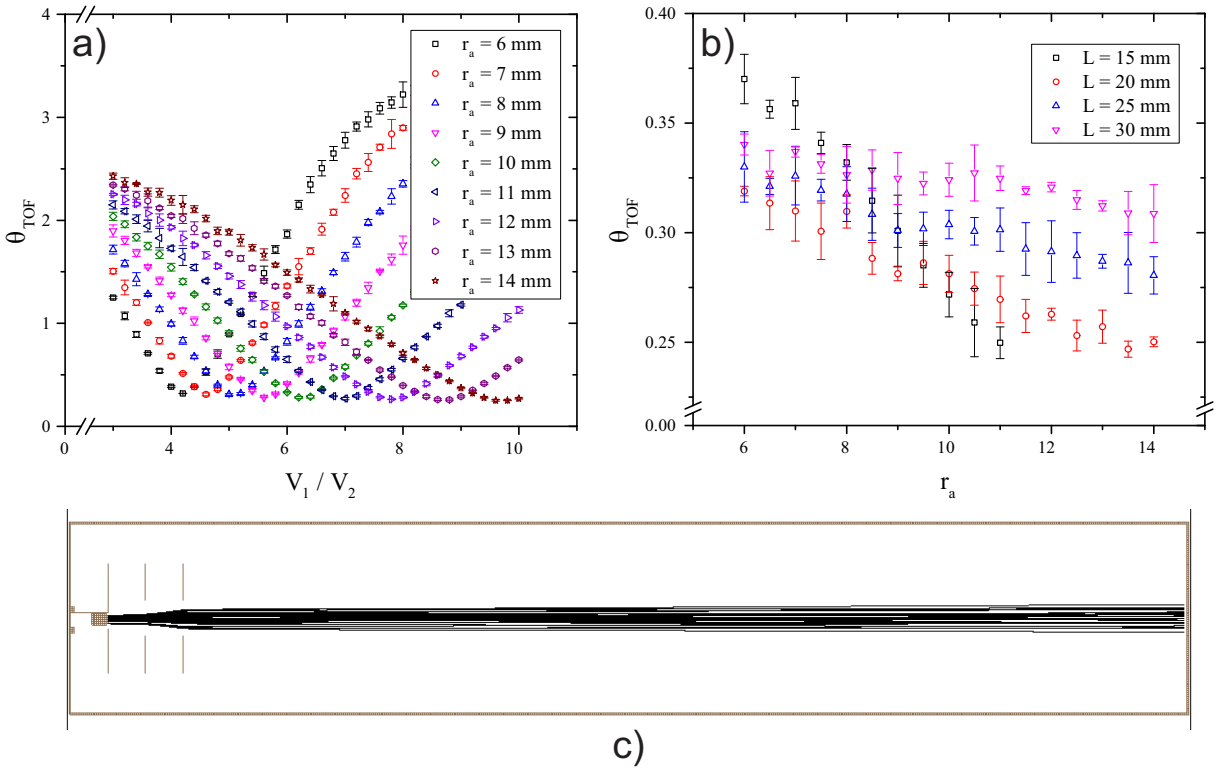

Figure 7.5: *Plots showing the results of simulations of the SIMS primary ion source with an emission lens extraction optic. Figures a) and b) show the dependence of the average angle, measured between the direction of motion of an ion reaching the end of the flight tube and the time-of-flight axis, on a) the electrode aperture radius, r_a, and the voltage ratio, V_1/V_2, and b) the distance between electrode plates, $L = L_1 = L_2$. Only values of $V_1 < 5000\,V$ are included. Figure c) shows an example simulation where the ions extracted from the source are collimated.*

the drift tube is grounded. In order to do this the first electrode is held at the positive voltage, V_2, and the second electrode is held at a voltage, $V_2 - V_1$. This therefore means that in the accel-decel regime, the second electrode is held at a negative voltage.

Figure 7.5 shows plots of results, obtained by simulation, of a primary ion source using an emission lens extraction optic. The first two plots, in figures 7.5 a) and b), show the variation of the average of the angle, θ_{TOF}, measured between the velocity vector of each ion as they reach the end of the flight tube and the time-of-flight axis. The lower the average value of θ_{TOF}, the closer to a collimated beam has been achieved. Figure 7.5 a) shows the variation of θ_{TOF} as a function of the ratio of voltages, V_1/V_2, for various different values of the radius of the aperture inside each of the electrode plates, r_a. It can be seen that the variation in θ_{TOF} is the same for different radii; except that for larger radii, the

optimum value is found at a higher voltage ratio. The actual optimum values do not vary widely for different radii.

Figure 7.5 b) shows the variation as a function of r_a for different distances between each of the electrode plates, $L = L_1 = L_2$. Each of the points has been tuned to the optimum voltage ratio for that geometry. These optimal voltages are found to be higher for both larger radii, and a smaller distance between the electrode plates. Although the angular spread can be reduced at higher radii this comes at the expense of needing a larger voltage ratio.

Figure 7.5 c) shows the production of a collimated beam using the emission lens extraction optic. The geometry of the optic is: L =20 mm, r_a =9 mm, and V_1/V_2 =5.6. The average value of θ_{TOF}, found for this geometry, is less than 0.28°, and the size of the spot produced is 13.2 mm. This spot size is approximately five times magnified from the face of the source.

7.4.2 Angled Electrodes

There are many more advanced forms of ion extraction optics that could be employed for a primary ion source [133, 196]. However, the majority of these are concerned with the reduction of the primary ion beam spot size for use with a microprobe-type experiment. As the aim here is to produce a larger beam spot with a high fluence and a short pulse length using a buncher, it is more important to consider the velocity distribution of the extracted ions.

Figure 7.6 shows two further designs for ion extraction optics. The first design, shown in figure 7.6 a) is based on the Pierce electrode design [197]. It consists of two electrode plates based on concentric spheres with radii r_1 and r_2. The ion source is mounted within the larger of the two electrodes and is held at the repeller voltage, V_R. The smaller electrode is held at ground. This design can produce a beam with a small angular divergence ($\approx 0.8°$) but this can only be achieved with a much larger beam spot than before (≈ 22 mm).

The Pierce electrode design was originally conceived to form a collimated beam of electrons, overcoming internal space-charge repulsions. For this application it is the focussing

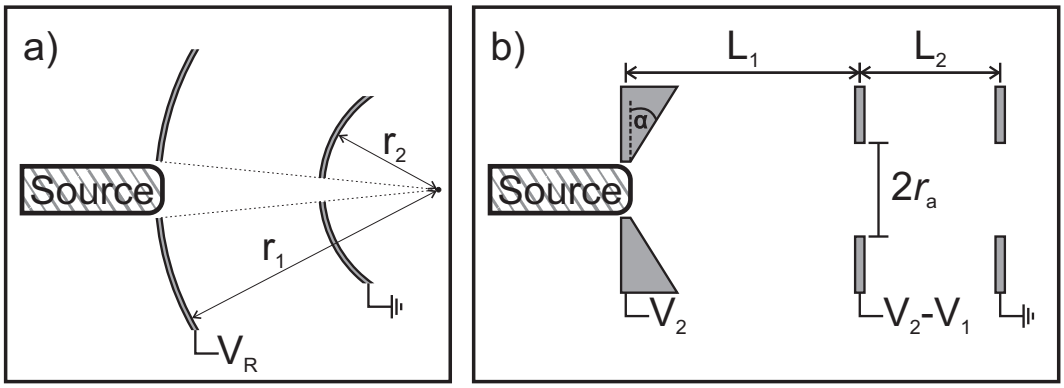

Figure 7.6: *Two designs for extraction optics. The first, shown in figure a), is based on theory by Pierce [197]. It consists of two electrodes based on concentric spheres, with radii r_1 and r_2, the smaller of which is held at ground. The design shown in figure b) uses an angled repeller electrode at the source to bring the beam down to a waist from which the other two electrodes then form an immersion lens.*

of ions from a large source area and with a spread of kinetic energies that must be focussed, so it is not surprising that a true Pierce design is not fit for purpose. However, the use of curved or angled electrodes to aid the focussing of particles is typically qualitative in many other electron and ion optic designs [198, 199].

Figure 7.6 b) shows a further design which incorporates an angled repeller electrode to form a beam waist at some point before a two electrode immersion lens. The beam waist acts as the object for the immersion lens which focusses the image onto the target.

This design does result in a modest reduction in the beam spot size, but only to 12.0 mm compared to the previous size of 13.2 mm. This reduction in the beam spot size comes at the cost of the angular distribution which is increased to an average of 0.62°.

The fact that the beam spot size is only improved with a increase in the angular spread is not surprising when considering the phase space inhabited by the ions. First it must be assumed that the ions can be completely described by their position in a two dimensional (y, v_y) phase space, where y is the perpendicular distance of an ion from the TOF axis and v_y is the component of an ions velocity perpendicular to the TOF axis. According to Liouville's theorem, the area occupied by a beam of ions must then be conserved through any lensing action. So in minimising the range of v_y, the spread in y is increased.

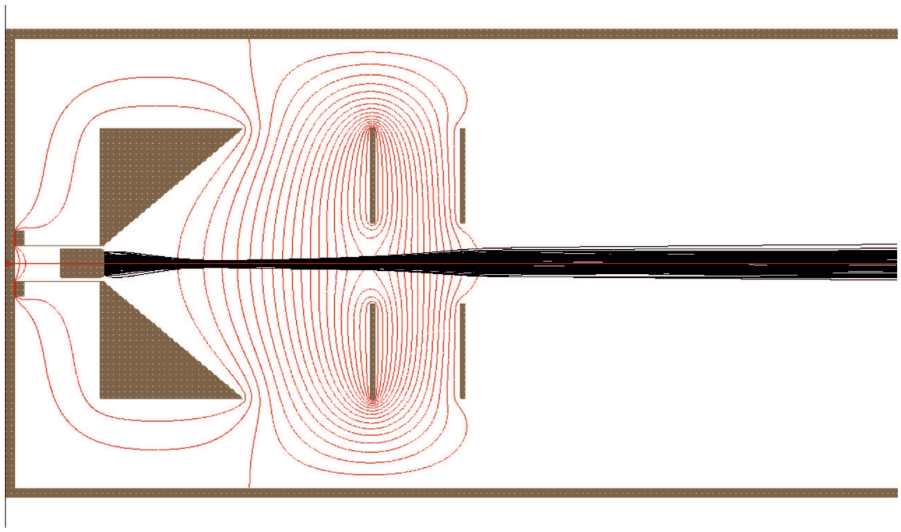

Figure 7.7: *An image showing the extraction optic with an angled repeller electrode followed by an immersion lens as simulated with the SIMION software package. A sample of ion trajectories are shown originating at the tip of the source, and each red line represents an equipotential for the voltage ratio* $V_1/V_2 = 7$.

7.5 Producing a Pulsed Beam

Despite an investigation into more "advanced" ion extraction optics the simple three electrode emission lens has been shown to produce the ion beam with the least angular divergence. The size of the spot produced by this beam is rather large but an aperture can be used to control this. The loss of ion current should not be an issue as the bunching of the ion beam will allow for a high fluence spot to be produced.

In designing the ion buncher, the longer it can be built, the more ions it can be filled with, and so the higher the beam spot fluence. A length of no more than 300 mm was decided on. For the simulation, 31 electrode plates were spaced apart by 8 mm cover a full distance of 250 mm. With an extraction voltage of 500 V this length takes 9 μs to fill. Each electrode within the buncher was modelled as being 1 mm thick, and was designed with an aperture at the centre of radius 8 mm.

Figure 7.8 shows the simulated buncher, b), combined with the emission lens, a), designed to the dimensions found earlier in section 7.4.1. Between the two is an aperture to control the beam spot size on its entry into the buncher, and an einzel lens is placed at the exit of the buncher, c), to focus the exiting beam pulse onto the target. The einzel

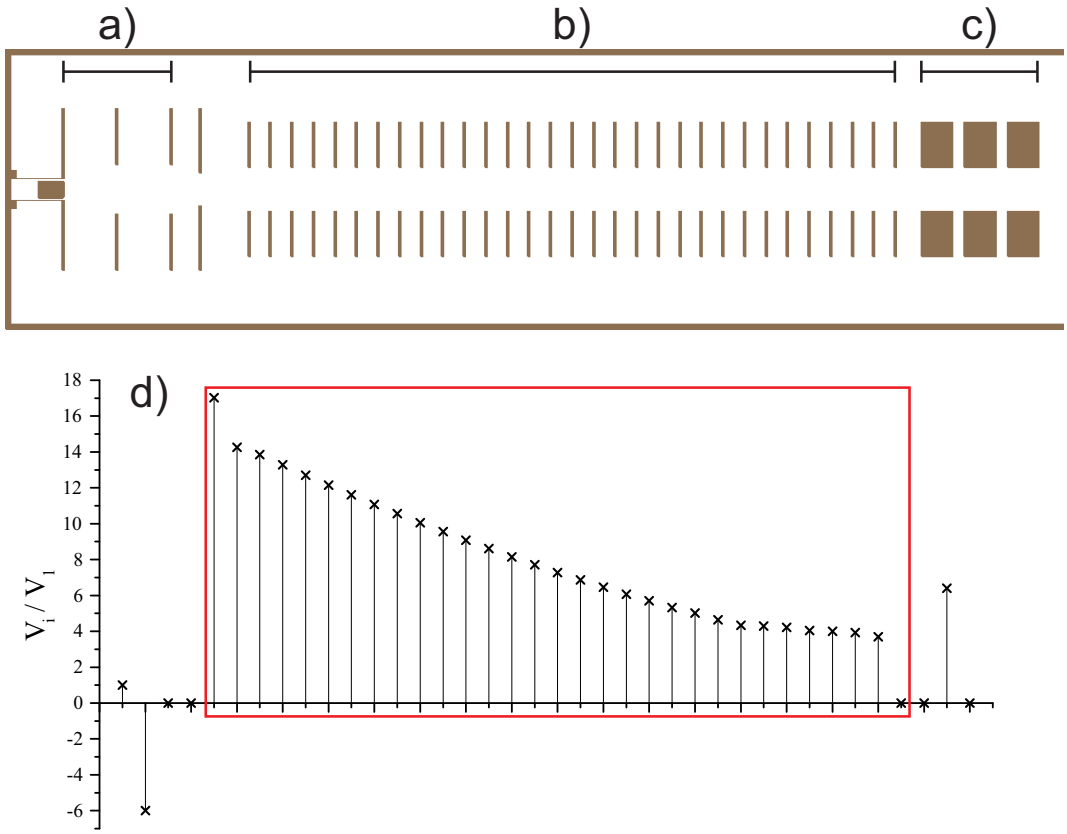

Figure 7.8: *An image showing the full ion gun simulation. The ion source is nested within the extraction optic, a). After the extraction optic there is an aperture which leads to the 31 plate ion buncher, b). Lastly, there is a three electrode ion lens, c), which allows the final pulse to be spatially focussed onto the target. Figure d) shows an example set of voltages that can be applied to each electrode in order to obtain a short beam pulse. The first three points refer to the extraction optics, the points within the red box correspond to the ion buncher, and the final three points are the voltages applied to the einzel lens.*

lens was composed of three identical electrodes. Each was 12 mm thick with an aperture of radius 8 mm. These electrodes were spaced with a 4 mm gap between them.

Figure 7.8 d) gives an example of the voltages that are applied to the various electrodes in the simulation in order to obtain a short beam pulse. These voltages are given relative to the acceleration voltage of the extraction optics, V_i/V_1. The first three points are the extraction optics followed by the aperture which is held at ground.

The 31 electrodes that are shown within the red box represent the voltages applied to the buncher. During the simulation, the buncher voltages are reduced to zero for 9 μs during which the buncher fills with ions. After this duration the voltages are returned to the values shown in figure 7.8 d) creating the short pulse.

The final three electrodes are those of the einzel lens which is used for a final level of control over the beam spot size.

Tuning the Buncher

In order to ascertain the voltages that should be applied to each electrode within the buncher an iterative tuning script was written to be used with the SIMION trajectory software. The script created 30 ions, each with a kinetic energy of 500 eV and a mass of 132.91 Da, and placed them between each pair of electrode plates in the ion buncher, directly on the TOF axis. The same voltage was applied to each plate so that the buncher was initially field free, and the simulation was run.

The arrival time of each ion was recorded and compared to a target value. The voltage of the electrode adjacent to each ion was then adjusted according to this comparison between recorded arrival time and target arrival time, the only caveat being that the voltage applied to a plate had to be lower than the voltage applied to the previous plate.

After each iteration, the new voltages were written to an output file, and the simulation was run again. The simulation was terminated either once all of the ions were found to arrive within 1 ns of the target time or until the voltages had converged. These voltage were then used for a full simulation using ions that were extracted from the ion source.

Figure 7.9 shows plots detailing some of the simulated characteristics of the ion beam, obtained from the full simulation of the extraction optic combined with the ion buncher. The simulations used the emission lens design found in section 7.4.1 followed by an aperture of radius 6 mm. The buncher was tuned to a target arrival time of 6 μs from its switch time. For these simulations the einzel lens was left at ground.

Figure 7.9 a) shows the arrival time spread of the ions. The peak is asymmetric with a tail towards longer arrival times. The peaks has a FWHM of 1.5 ns and a full width at one tenth the maximum (FWTM) of 4.4 ns. Although there is a tail to the peak, over 80% of the ions are contained within the 4.4 ns FWTM; and further, it can be seen that the majority of this peak is contained within the precision of the PImMS1 camera (12.5 ns) .

Figure 7.9 b) shows the arrival time of the ions separated out according to the kinetic

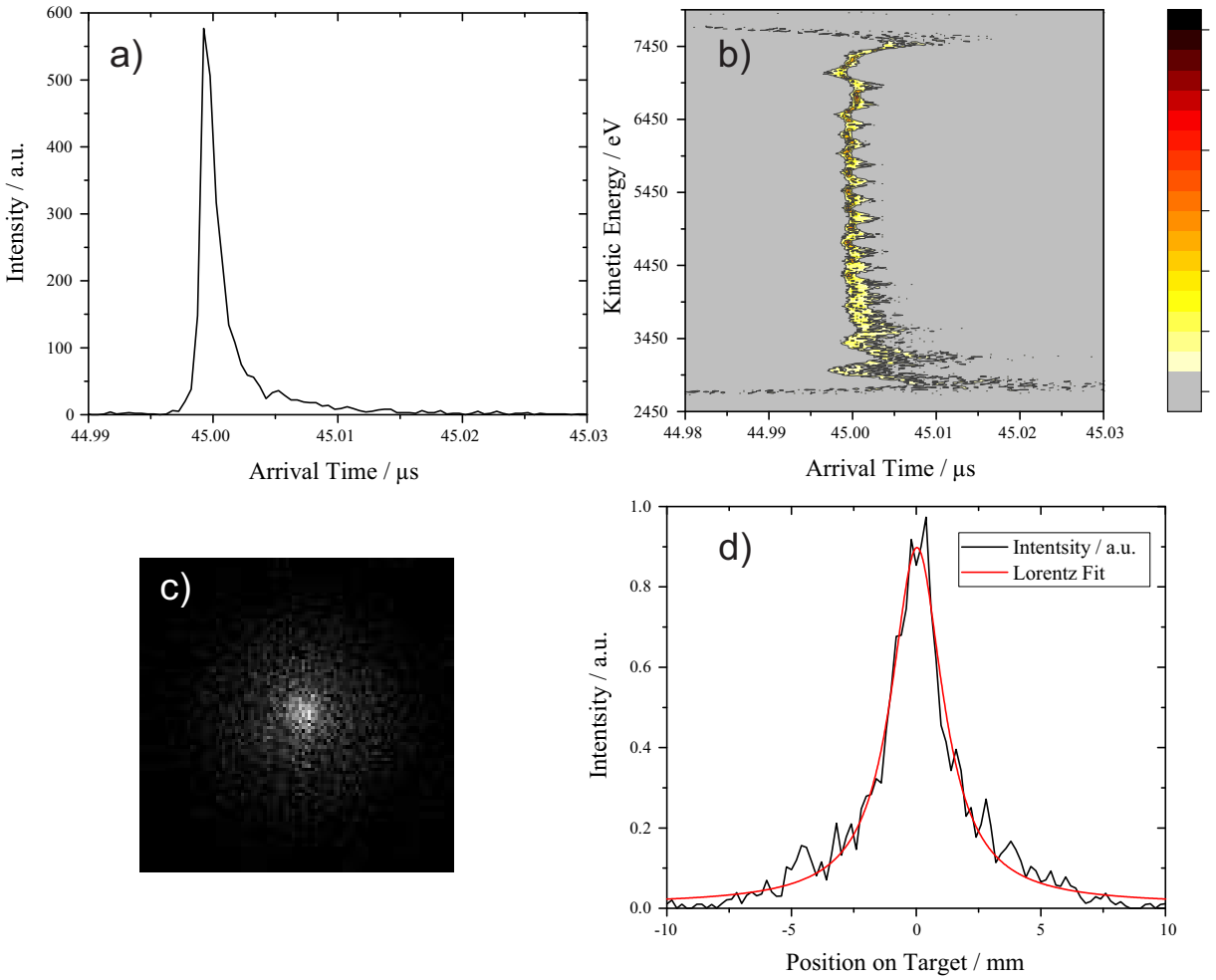

Figure 7.9: *Plots showing the simulated characteristics of the ion beam as it reaches the target. Figure a) shows the arrival time of the ions. Figure b) shows a frequency plot of the arrival time of ions against their kinetic energy on reaching the target. Figure c) shows an image of the beam spot on the surface of the target, and a line profile is taken from this image and shown in figure d) along with a Lorentz fit. The data were obtained using the emission lens and buncher combination whilst the einzel lens was left at ground.*

energy of each ion as it reaches the target. The kinetic energy of each ion gives information on its location in the buncher when the pulse was generated. The graph shows that it is the ions at the extremities of the kinetic energy distribution that contribute most to the spread in the arrival times. The periodic focussing of ions can also be seen where ions that were situated directly between two electrode plates are better focussed than those that were eccentric.

The image in figure 7.9 c) shows the spatial distribution of the ions at the target. Taking a profile across the image the plot in figure 7.9 d) is obtained. The peak can be fit

by a Lorentz function (which is shown in red), and a FWHM of 2.5 mm is found for the distribution. Although the spatial spread of the beam does continue further this can be simply curbed by the use of an aperture which could cut the beam spot size down to a diameter of 5 mm.

At an estimate, taking a source current density of 1 $\mathrm{mAcm^{-2}}$, an aperture acceptance of 88%, a fill time of 9 μs, a pulse length of 5 ns, and a target diameter of 5 mm, the current density on the target could be as great as 400 $\mathrm{mAcm^{-2}}$. This is a very high current density, well within the specifications of "dynamic" SIMS [133], which would allow, for example, the wells of a micro-array to be completely analysed. This current density could also be controlled by controlling either or both of the aperture size, limiting the number of ions entering the buncher, or by reducing the length of time that the buncher is filled for.

The Einzel Lens

Figure 7.10 shows a number of plots which show the effect of changing the voltage applied to the einzel lens, V_{E}, on the spatial and temporal distribution of the ion beam. Each row of plots represent a different voltage applied to the central electrode of the einzel lens: figures 7.10 a), b), and c) were obtained with $V_{\mathrm{E}} = 0$; figures 7.10 d), e), and f) were obtained with $V_{\mathrm{E}} = 1\,\mathrm{kV}$; figures 7.10 g), h), and i) were obtained with $V_{\mathrm{E}} = 2\,\mathrm{kV}$; and figures 7.10 j), k), and l) were obtained with $V_{\mathrm{E}} = 3\,\mathrm{kV}$.

The four plots in the left most column, figures 7.10 a), d), g), and j), show the distribution of ions in (y, z) — the plane of the target. As V_{E} is increased the distribution of ions concentrates towards the centre of the target. However, in figure 7.10 j) the voltage is high enough to stop some of the ions reaching the target. The plots in the central column, figures 7.10 b), e), h), and k), show the one-dimensional profiles taken across the images in the left column. It can be seen all of the spatial distributions follow the same peak shape with the best resolved spot obtained with $V_{\mathrm{E}} = 2\,\mathrm{kV}$.

Finally, the four plots in the right column, figures 7.10 c), f), i), and l), show the arrival time distributions for the different einzel lens voltages. They show that as soon as a voltage is applied to the einzel lens, the length of the beam pulse increases greatly. The

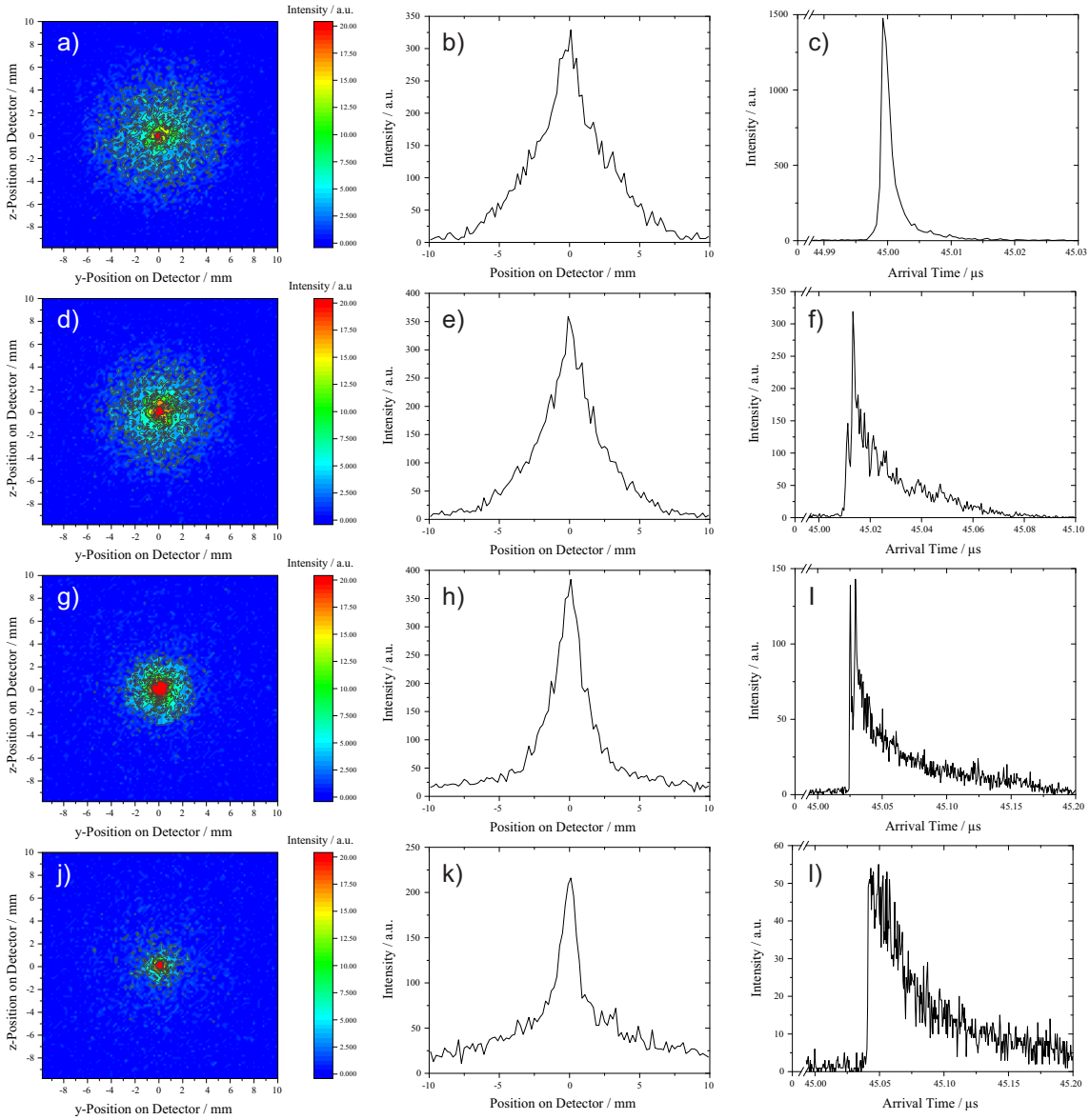

Figure 7.10: *A series of plots of simulations showing the effect of applying a voltage, V_E, to the central electrode of the einzel lens assembly. Each row of plots were obtained with a different value for V_E: figures 7.10 a), b), and c) were obtained with $V_E = 0$; figures 7.10 d), e), and f) were obtained with $V_E = 1\,kV$; figures 7.10 g), h), and i) were obtained with $V_E = 2\,kV$; and figures 7.10 j), k), and l) were obtained with $V_E = 3\,kV$. The plots on the left show the spatial distributions at the target, the central plots show a profile taken across these image, and the plots on the right show the arrival time distribution of the ions.*

time focussing of the buncher is ruined as ions with different kinetic energies take different amounts of time to pass through the lens.

7.6 Summary

In this chapter, a design for a primary ion source for SIMS was presented. The aim of this venture was to lay down the ground work for possible future developments into instrumentation that might be of use in in conjunction with the PImMS1 camera for MSI. In the simulations for the design, a Cs^+ source was chosen as a possible primary ion specifically for use with certain mass tags produced by the company BioSIMS. The source was designed to cover a large area (5 mm in diameter) with a high fluence on the target surface, and with a short pulse length.

A design was presented using a simple emission lens to extract ions from the source and to accelerate them into an ion buncher. The buncher then takes 9 μs of ions and compresses them down to a pulse of less than 5 ns. The beam spot at the target has a diameter of 2.5 mm (FWHM). It was also shown that an einzel lens can be used to control the shape of the beam spot but that this interferes (drastically) with the beam pulse length.

The design presented here does fulfil the criteria proposed at the beginning of the chapter. Although there will inevitably be further improvements that could be made to the design, it is now at a stage where more could be learnt from the production of a working model rather than further simulations. This would allow the assumptions that have been made in the simulations so far to be tested.

Chapter 8

Future Outlook

The work in this thesis has centred around the development of a time-of-flight stigmatic ion microscope for use with the PImMS camera. The product of this union is an instrument that can acquire spatially resolved ion images of various species, simultaneously.

Chapter 1 gave an overview of the theory and technology behind time-of-flight mass spectrometry and imaging techniques. This was followed by chapters 2 and 3 which outlined the methods used for the work in the main body of this thesis in terms of experiment and simulation respectively.

The first experimental data was presented in chapter 4, and covered the conversion of a conventional velocity-map ion imaging instrument for use with microscope-mode imaging mass spectrometry. This work was first simulated using the SIMION ion trajectory program and the results of these simulations were then compared to those obtained experimentally. With the PImMS camera a spatial resolution of 50 μm was observed with a mass resolution of $m/\Delta m \approx 200$ (for $m/z \approx 700$) — although this mass resolution was only obtainable by deconvolving the detector function from the mass spectrum. The experiment also allowed for the multi-mass imaging capability of the camera to be explored. A sample of Rhodamine 590 and Auramine O was imaged, and the resulting data set, obtained with the PImMS1 camera, was explored to investigate the strengths and limitations of such a multi-mass ion microscope. Issues were exposed limiting the use of such an instrument in complete quantitative analysis, the multiple registers of the PImMS camera allow for the

analysis of experiments with a much higher count rate compared to those accessible with other technologies.

Although there was success with the multi-mass imaging with the conventional velocity-map imaging instrument, this instrument was only capable of producing rather modest resolutions. Chapter 5 described modifications that were made to a commercial time-of-flight mass spectrometer so that it could perform microscope-mode imaging. Simulations were again performed, and compared with experimental results, culminating in another example of multi-mass imaging. The resolutions obtained with this instrument, and the PImMS1 camera, were far more impressive. A peak spatial resolution of $20\,\mu$m was obtained with this instrument along with a mass resolution of $m/\Delta m \approx 800$ across the range $200 < m/z < 800$. Crucially, this mass resolution was obtained without deconvolving the detector function from acquired spectrum, which means that no prior assumptions about the result are needed. This instrument is therefore capable of isotopic resolution, with a spatial resolution better than $50\,\mu$m, across the range $200 < m/z < 800$.

Chapter 6 presented a model for the shape of event clusters obtained with the PImMS in (x, y, τ). A full fit to the model was not obtained but through a simplification it was shown to successfully predict the variation in mass peak position as a function of cluster size. Using this, it was shown that a correction can be applied to PImMS1 data sets which allow fewer data to be discarded whilst still maintaining the same temporal resolution.

Finally, chapter 7 was concerned with the design for a possible new primary ion source to be used in microscope-mode SIMS analysis. A number of designs were presented with the final design consisting of a simple emission lens feeding ions into a buncher which compressed $9\,\mu$s of ions downs to a pulse 5 ns long.

Together, all of these developments trace the progression of a PImMS1 stigmatic imaging instrument from its proof-of-concept through to the creation of an instrument with specifications that are sufficient to accomplish "real-world" applications. However, rather than the culmination of a proof-of-concept, this work is setting the scene for further developments which should take such a system from being sufficient to being competitive.

8.1 Strengths and Weaknesses

In order to make multi-mass stigmatic mass microscopy a competitive technique, when compared to the myriad of mass spectrometry instrumentation available, it is very important to consider its limitations as much as its strengths. The greatest limitation is that the ion optic system of the instrument has to both focus spatially and temporally. In the majority of cases, techniques which are employed to increase one will limit the other. A prime example of this is delayed extraction: a technique that greatly increases the mass resolution of an instrument but at the same time reduces the spatial information. The PEDA technique overcomes this to some extent, but instead here the mass range of the instrument is limited and the system must be tuned for different mass ranges (made possible by VCPEDA).

There are also limitations with the technology. The PImMS1 camera does increase the throughput of an experiment by enabling all masses to be imaged simultaneously but it also imposes a limit on the temporal and spatial resolution. The PImMS1 sensor has a pixel count of 72×72 but this will be surpassed by the next generation of the sensor, aptly named PImMS2: this sensor has a pixel count of 324×324. The greater issue is the temporal precision, currently limited to 12.5 ns. This greatly limits the achievable mass resolution, as was shown in chapter 5 where an instrument capable of producing data with a resolution of several thousand was limited to resolutions of several hundred.

However, rather than viewing these technical limitations as a burden, they can be viewed as a liberation of certain requirements for the ion optic assembly. If the detector technology being used is limiting the resolution of the instrument to a resolving power of several hundred then there is no necessity to design ion optics that can produce resolving powers into the thousands. Instead the ion optics can be designed to focus on, for example, maximising the m/z range across which the lower resolving power is achievable. This focus on throughput, over absolute resolution, also aligns with the advantage that the PImMS1 camera can run at higher count rates.

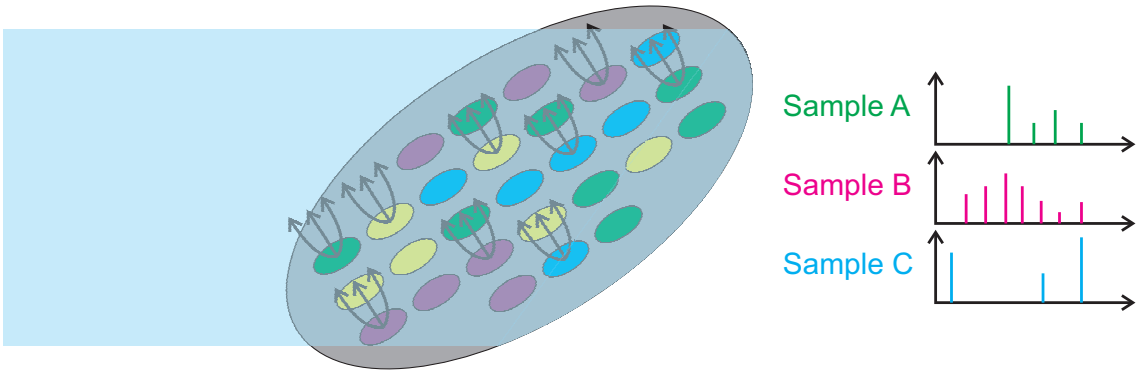

Figure 8.1: *A cartoon representation of the imaging of a micro-array of samples. The ionising beam simultaneously produces ions from a large number of sample wells. These ions are then imaged, and the spatial resolution of the image is used to differentiate between the different samples on the plate. In this way, the mass spectrum of each sample can then be extracted from the full data set.*

8.1.1 Goals for Future Development

The aim for the future development of a stigmatic ion microscope with the PImMS1 camera should focus on playing to the strengths of the union. When considering what the desired specifications of a future instrument might be there are a number that should be kept in mind: the spatial, and mass resolutions, the m/z range over which these resolutions should be obtained, the size of the sample which is to be analysed, and the efficiency of the system (that is the percentage of ions that are produced that are then detected).

One application area which might prove to be a fit with this technology is that of micro-array analysis (see figure 8.1). With a micro-array dozens (if not hundreds) of samples are applied to a sample plate with a micrometer level pitch ($\approx 50\,\mu$m). These samples are then screened either for the presence of some species of for the presence of a tag or marker which signals another species. This relieves the demands on the spatial, and to some extent the mass, resolving power of an instrument, and instead the efficiency and sample size are tested.

8.2 In Conclusion

The works in this thesis have shown the development of a viable multi-mass stigmatic imaging mass spectrometer from a proof-of-concept. The strengths and weaknesses of this system have been explored setting the stage for both turning the instrument to applications as well as developing further instrumental improvements. The PImMS1 camera has been shown to open up new avenues in instrumentation which, by playing to the strengths of the device, can produce powerful new tools for chemical analysis.

Bibliography

[1] J. J. Thomson, *Rays of Positive Electricity and their Application to Chemical Analysis*, Longmans, Green and Co., 1913.

[2] M. Careri, F. Bianchi, and C. Corradini, *J. Chromatogr. A*, **970**, 3–64 (2002).

[3] I. Horman, *Biomed. Mass Spectrom.*, **8**, 384–389 (2005).

[4] A. Belmonte Vega, A. Garrido Frenich, and J. L. Martinez Vidal, *Analytica Chimica Acta*, **538**, 117–127 (2005).

[5] J. Coumbaros, K. P. Kirkbride, G. Klass, and W. Skinner, *Forensic Sci. Int.*, **119**, 72–81 (2001).

[6] Z. Takats, I. Cotte-Rodriguez, N. Talaty, H. Chen, and R. G. Cooks, *Chem. Commun.*, pages 1950–1952 (2005).

[7] J. S. Knaack, Y. Zhou, M. Magnuson, E. Silvestri, and R. C. Johnson, *Anal. Chem.*, **85**, 2611–2616 (2013).

[8] Y. Hashimoto, H. Nagano, Y. Takada, H. Kashima, M. Sugaya, K. Terada, and M. Sakairi, *Rapid Commun. Mass Spectrom.*, **28**, 1376–1380 (2014).

[9] S. P. Gygi and R. Aebersold, *Curr. Opin. Biotech.*, **4**, 489–494 (2000).

[10] S. Khatib-Shahidi, M. Andersson, J. L. Herman, T. A. Gillespie, and R. M. Caprioli, *Anal. Chem.*, **78**, 6448–6456 (2006).

[11] Y. Hsieh, J. Chen, and W. A. Korfmacher, *J. Pharmacol. Toxicol. Methods*, **55**, 193–200 (2007).

[12] I. S. Parry, A. C. Hermes, A. Kartouzian, and S. R. Mackenzie, *Phys. Chem. Chem. Phys.*, **16**, 458 (2014).

[13] S. H. Gardiner, T. N. V. Karsili, M. L. Lipciuc, E. Wilman, M. N. R. Ashfold, and C. Vallance, *Phys. Chem. Chem. Phys.*, **16**, 2167 (2014).

[14] B. Nichols, H. Chadwick, S. D. S. Gordon, C. J. Eyles, B. Hornung, M. Brouard, M. H. Alexander, F. J. Aoiz, A. Gijsbertsen, and S. Stolte, *Chem. Sci.*, **6**, 2202 (2015).

[15] A. Kumar, S. Agarwal, J. A. Heyman, S. Matson, M. Heidtman, S. Piccirillo, L. Umansky, A. Drawid, R. Jansen, Y. Liu, K. Cheung, P. Miller, M. Gerstein, G. S. Roeder, and M. Snyder, *Genes Dev.*, **16**, 707–719 (2002).

[16] P. Chaurand, J. C. Latham, K. B. Lane, James A. Mobley, V. V. Polosukhin, P. S. Wirth, L. B. Nanney, and R. M. Caprioli, *J. Proteome Res.*, **7**, 3543–3555 (2008).

[17] D. Debois, E. Jourdan, N. Smargiasso, P. Thonart, E. De Pauw, and M. Ongena, *Anal. Chem.*, **86**, 4431–4438 (2014).

[18] A. F. M. Altelaar, S. L. Luxembourg, L. A. McDonnell, S. R. Piersma, and R. M. A. Heeren, *Nat. Protoc.*, **2**, 1185–1196 (2007).

[19] Z. Luo, J. He, Y. Chen, J. He, T. Gong, F. Tang, X. Wang, R. Zhang, L. Huang, L. Zhang, H. Lv, S. Ma, Z. Fu, X. Chen, S. Yu, and Z. Abliz, *Anal. Chem.*, **85**, 2977–2982 (2013).

[20] R. Bradshaw, R. Wolstenholme, R. D. Blackledge, M. R. Clench, L. S. Ferguson, and S. Francese, *Rapid Commun. Mass Spectrom.*, **25**, 415–422 (2011).

[21] L. F. Ferguson, R. Bradshaw, R. Wolstenholme, M. Clench, and S. Francese, *Anal. Chem.*, **83**, 5585–5591 (2013).

[22] E. de Hoffmann and V. Stroobant, *Mass Spectrometry: Principles and Applications*, John Wiley and Sons, 2007.

[23] A. E. Cameron and D. F. Eggers Jr., *Rev. Sci. Instrum.*, **19**, 605–607 (1948).

[24] F. Hillenkamp, E. Unsoeld, R. Kaufmann, and R. Nitsche, *Nature*, **256**, 119–120 (1975).

[25] R. B. Van Breemen, M. Snow, and R. J. Cotter, *Int. J. Mass Spectrom. Ion Pysics*, **49**, 35–50 (1983).

[26] R. N. S. Sodhi, *Analyst*, **129**, 483–487 (2004).

[27] Stanford Research Systems, *NL100 Nitrogen Laser Operation and Service Manual*.

[28] R. Knochenmuss and L. V. Zhigilei, *J. Mass Spectrom.*, **45**, 333–346 (2010).

[29] D. W. Koppenaal, C. J. Barinaga, M. B. Denton, R. P. Sperline, G. M. Hieftje, Schilling G. D., F. J. Andrade, and J. H. Barnes, *Anal. Chem.*, **77**, 418A–427A (2005).

[30] L. A. Klerk, A. F. M. Altelaar, M. Froesch, L. A. McDonnell, and R. M. A. Heeren, *Int. J. Mass Spectrom.*, **285**, 19–25 (2009).

[31] G. H. Morrison and G. Slodzian, *Anal. Chem.*, **47**, 932A–943A (1975).

[32] B. K. Furman and G. H. Morrison, *Anal. Chem.*, **52**, 2305–2310 (1980).

[33] A. J. Patkin and G. H. Morrison, *Anal. Chem.*, **54**, 2–5 (1982).

[34] G. Slodzian, *J. Microsc. Spectrosc. Electron.*, **3**, 447–449 (1978).

[35] C. J. Davisson and C. J. Calbick, *Phys. Rev.*, **38**, 585 (1931).

[36] C. J. Davisson and C. J. Calbick, *Phys. Rev.*, **42**, 580 (1932).

[37] D. W. O. Heddle, N. Papadovassilakis, and A. M. Yateem, *J. Phys. E:Sci. Instrum.*, **15**, 1210–1211 (1982).

[38] D. W. Chandler and P. L. Houston, *J. Chem. Phys.*, **87**, 1445–1447 (1987).

[39] A. T. J. B. Eppink and D. H. Parker, *Rev. Sci. Instrum.*, **68**, 3477–3484 (1997).

[40] M. T. Bernius, Y. C. Ling, and G. H. Morrison, *J. Appl. Phys.*, **59**, 3332–3338 (1986).

[41] W. C. Wiley, US 2685035 A, 1954.

[42] W. C. Wiley and I. H. McLaren, *Rev. Sci. Instrum.*, **26**, 1150–1157 (1955).

[43] M. L. Vestal, P. Juhasz, and S. A. Martin, *Rapid Comm. Mass Spectrom.*, **9**, 1044–1050 (1995).

[44] J. Aoki, H. Hazama, and M. Toyoda, *J. Mass Spectrom. Soc. Jpn.*, **59**, 57–61 (2011).

[45] B. Winter, E. Halford, and M. Brouard, *Int. J. Mass Spectrom.*, **356**, 14–23 (2013).

[46] B. Winter, *Novel Methods in Imaging Mass Spectrometry and Ion Time-of-Flight Detection*, DPhil Thesis, 2014.

[47] U. Boesl, J. Grotemeyer, K. Walter, and E. W. Schlag, *Anal. Instrum.*, **16**, 151–171 (1987).

[48] U. Boesl, R. Weinkauf, and E. W. Schlag, *Int. J. Mass Spectrom. Ion Processes*, **112**, 121–166 (1992).

[49] B. D. Leskiw, M. H. Kim, G. E. Hall, and A. G. Suits, *Rev. Sci. Instrum.*, **76**, 104101/1–104101/6 (2005).

[50] B. D. Leskiw, M. H. Kim, G. E. Hall, and A. G. Suits, *Rev. Sci. Instrum.*, **76**, 129901/1 (2005).

[51] M. H. Kim, B. D. Leskiw, L. Shen, and A. G. Suits, *Int. J. Mass Spectrom.*, **252**, 73–78 (2006).

[52] A. Bowdler, US 8212209 B2, 2012.

[53] J. H. Moon, D. W. Moon, T. G. Lee, S. Yoon, and J. H. Kim, US 20140183354 A1, 2014.

[54] A. A. Sysoev, *Eur. J. Mass Spectrom.*, **6**, 501–513 (2000).

[55] R. W. Odom, B. K. Furman, C. A. Evans, C. E. Bryson, W. A. Petersen, M. A. Kelly, and D. H. Wayne, *Anal. Chem.*, **55**, 574–578 (1983).

[56] FOM-AMOLF, Amsterdam, `http://www.amolf.nl/`.

[57] B. W. Schueler, *Micosc. Microanal. Microstruct.*, **3**, 119–139 (1992).

[58] S. L. Luxembourg, T. H. Mize, L. A. McDonnell, and R. M. A. Heeren, *Anal. Chem.*, **76**, 5339–5344 (2004).

[59] J. H. Jungmann, *Active Pixel Detectors for Mass Spectrometry Imaging*, PhD Thesis, 2012.

[60] D. Okumura, M. Toyoda, M. Ishihara, and I. Katakuse, *J. Mass Spectrom. Soc. Jpn.*, **51**, 349–353 (2003).

[61] H. Hazama, J. Aoki, H. Nagao, R. Suzuki, T. Tashima, K. Fukii, K. Masuda, K. Awazu, M. Toyoda, and Y. Naito, *Appl. Surf. Sci.*, **255**, 1257–1263 (2008).

[62] T. Satoh, US 20140166874 A1, 2014.

[63] C. Martin, P. Jelinsky, M. Lampton, R. F. Malina, and H. O. Anger, *Rev. Sci. Instrum.*, **52**, 1067–1074 (1981).

[64] M. Lamport, O. Siegmund, and R. Raffanti, *Rev. Sci. Instrum.*, **58**, 2298–2305 (1987).

[65] J. H. D. Eland and A. H. Pearson, *Meas. Sci. Technol.*, **1**, 36–40 (1990).

[66] J. H. D. Eland, *Meas. Sci. Technol.*, **5**, 1501–1504 (1994).

[67] H. Yoshimura, H. Hazama, J. Aoki, M. Toyoda, Y. Naito, and K. Awazu, *Jpn. J. Appl. Phys.*, **50**, 056701 (2011).

[68] O. Jagutzki, A. Cerezo, A. Czasch, R. Dorner, M. Hattass, M. Huang, V. Mergel, U. Spillmann, K. Ullmann-Pfleger, T. Weber, H. Schmidt-Bocking, and G. D. W. Smith, *IEEE T. Nucl. Sci.*, **49**, 2477–2483 (2002).

[69] M. Froesch, S. L. Luxembourg, D. Verheijde, and R. M. A. Heeren, *Eur. J. Mass Spectrom.*, **16**, 35–45 (2010).

[70] L. A. Klerk, N. P. Lockyer, A. Kharchenko, L. MacAleese, P. Y. W. Dankers, J. C. Vickerman, and R. M. A. Heeren, *Anal. Chem.*, **82**, 801–807 (2010).

[71] B. Winter, S. J. King, M. Brouard, and C. Vallance, *Rev. Sci. Instrum.*, **85**, 023306 (2014).

[72] Behlke, `http://www.behlke.com/`.

[73] M. Brouard, E. K. Campbell, A. J. Johnsen, C. Vallance, W. H. Yuen, and A. Nomerotski, *Rev. Sci. Instrum.*, **79**, 123115–1/8 (2008).

[74] M. Brouard, A. J. Johnsen, A. Nomerotski, C. S. Slater, C. Vallance, and W. H. Yuen, *JINST*, **6**, C01044 (2011).

[75] Teledyne DALSA, `http://www.dalsa.com/`.

[76] X. Llopart, R. Ballabriga, M. Campbell, L. Tlustos, and W. Wong, *Nucl. Instr. Meth. Phys. Res. A*, **581**, 485–494 (2007).

[77] M. Brouard, A. Nomerotski, and C. Vallance, PCT/GB2008/004085, 2007.

[78] A. Nomerotski, M. Brouard, E. Campbell, A. Clark, J. Crooks, J. Fopma, J. J. John, A. J. Johnsen, C. Slater, R. Turchetta, C. Vallance, E. Wilman, and W. H. Yuen, *J. Inst.*, **5**, C07007 (2010).

[79] J. H. Jungmann, A. Gijsbertsen, J. Visser, J. Visschers, R. M. A. Heeren, and M. J. J. Vrakking, *Rev. Sci. Instrum.*, **81**, 103112 (2010).

[80] J. H. Jungmann, L. MacAleese, R. Buijs, F. Giskes, A. de Snaijer, J. Visser, J. Visschers, M. J. J. Vrakking, and R. M. A. Heeren, *J. Am. Soc. Mass Spectrom.*, **21**, 2023–2030 (2010).

[81] J. H. Jungmann, D. F. Smith, A. Kiss, L. MacAleese, R. Buijs, and R. M. A. Heeren, *Int. J. Mass Spectrom.*, **341/342**, 34–44 (2013).

[82] S. R. Ellis, J. H. Jungmann, D. F. Smith, J. Soltwisch, and R. M. A. Heeren, *Angew. Chem. Int. Ed.*, **52**, 11261–11264 (2013).

[83] A. Kiss, J. H. Jungmann, D. F. Smith, and R. M. A. Heeren, *Rev. Sci. Instrum.*, **84**, 013704 (2013).

[84] A. Kiss, D. F. Smith, J. H. Jungmann, and R. M. A. Heeren, *Rapid Commun. Mass Spectrom.*, **27**, 2745–2750 (2013).

[85] J. Vallerga, J. McPhate, A. Tremsin, and O. Siegmund, *Nucl. Instrum. Meth. A*, **591**, 151–154 (2008).

[86] S. U. A. H. Syed, G. B. Eijkel, S. Maher, P. Kistemaker, S. Taylor, and R. M. A. Heeren, *Anal. Bioanal. Chem.*, **407**, 2055–2062 (2015).

[87] S. U. A. H. Syed, S. Maher, G. B. Eijkel, S. Ellis, F. Jjunju, S. Taylor, and R. M. A. Heeren, *Anal. Chem.*, **87**, 3714–3720 (2015).

[88] S. R. Ellis, J. Soltwisch, and R. M. A. Heeren, *J. Am. Soc. Mass Spectrom.*, **25**, 809–819 (2014).

[89] T. Poikela, J. Plosila, T. Westerlund, M. Campbell, M. De Gaspari, X. Llopart, V. Gromov, R. Kluit, M. van Beuzekom, F. Zappon, V. Zivkovic, C. Brezina, K. Desch, Y. Fu, and A. Kruth, *JINST*, **9**, C05013 (2014).

[90] R. A. D. Turchetta, G. E. Villani, and M. L. Prydderch, WO 2004099740 A2, 2004.

[91] J. A. Ballin, J. P. Crooks, P. D. Dauncey, A. M. Magnan, Y. Mikami, O. D. Miller, M. Noy, V. Rajovic, M. Stanitzki, K. Stefanov, R. Turchetta, M. Tyndel, E. G. Villani, N. K. Watson, and J. Allan. Wilson, *Sensors*, **8**, 5336–5351 (2008).

[92] A. T. Clark, J. P. Crooks, I. Sedgwick, R. Turchetta, J. W. L. Lee, J. J. John, E. S. Wilman, L. Hill, E. Halford, C. S. Slater, B. Winter, W. H. Yuen, S. H. Gardiner, M. L. Lipciuc, M. Brouard, A. Nomerotski, and C. Vallance, *J. Phys. Chem. A*, **116**, 10897–10903 (2012).

[93] J. J. John, M. Brouard, A. Clark, J. Crooks, E. Halford, L. Hill, J. W. L. Lee, A. Nomerotski, R. Pisarczyk, I. Sedgwick, C. S. Slater, R. Turchetta, C. Vallance, E. Wilman, B. Winter, and W. H. Yuen, *JINST*, **7**, C08001 (2012).

[94] B. M. Mazoyer, M. S. Roos, and R. H. Huesman, *Phys. Med. Biol.*, **30**, 385–399 (1985).

[95] S. Chick, R. Coath, R. Sellahewa, R. Turchetta, T. Leitner, and A. Fenigstein, *IEEE Trans. Electron Devices*, **61**, 2725–2731 (20014).

[96] J. J. Thomson, *Phil. Mag. S. 6*, **23**, 449–457 (1912).

[97] A. J. Dempster, *Phil. Mag. S. 6*, **31**, 438–443 (1916).

[98] W. Bleakney, *Phys. Rev.*, **34**, 157–160 (1929).

[99] M. S. B. Munson and F. H. Field, *J. Am. Chem. Soc.*, **88**, 2621–2630 (1966).

[100] F. H. Field, *Acc. Chem. Res.*, **1**, 42–49 (1968).

[101] R. Gomer and M. G. Inghram, *J. Am. Chem. Soc.*, **77**, 500–500 (1955).

[102] H. D. Beckey, *Int. J. Mass Spectrom. Ion Phys.*, **2**, 500–502 (1969).

[103] R. E. Honig and J. R. Woolston, *Appl. Phys. Lett.*, **2**, 138–139 (1963).

[104] F. J. Vastola, R. O. Mumma, and A. J. Pirone, *Org. Mass Spectrom.*, **3**, 101–104 (1970).

[105] M. A. Posthumus, P. G. Kistemaker, H. L. C. Meuzelaar, and M. C. Ten Noever de Brauw, *Anal. Chem.*, **50**, 985–991 (1978).

[106] M. B. Karas, D. Bachman, and F. Hillenkamp, *Anal. Chem.*, **57**, 2935–2939 (1985).

[107] J. Grotemeyer, U. Boesl, K. Walter, and E. W. Schlag, *Org. Mass Spectrom.*, **21**, 645–653 (1986).

[108] B. Spengler, J. W. Dolce, and R. J. Cotter, *Anal. Chem.*, **62**, 1731–1737 (1990).

[109] M. B. Karas, D. Bachman, U. Bahr, and F. Hillenkamp, *Int. J. Mass Spectrom. Ion Processes*, **78**, 53–68 (1987).

[110] M. Karas and F. Hillenkamp, *Anal. Chem.*, **60**, 2299–2301 (1988).

[111] R. C. Beavis and B. T. Chait, *Rapid Comm. Mass Spectrom.*, **3**, 432–435 (1989).

[112] V. Horneffer, K. Dreisewerd, H. C. Ludemann, F. Hillenkamp, M. Lage, and K. Strupat, *Int. J. Mass Spectrom.*, **185/186/187**, 859–870 (1999).

[113] P. Demirev, A. Westman, C. T. Reimann, P. Hakansson, D. Barofsky, and B. U. R. Sundqvist, *Rapid Comm. Mass Spectrom.*, **6**, 187–191 (1992).

[114] A. Ingendoh, M. Karas, F. Hillendkamp, and U. Giessman, *Int. J. Mass Spectrom. Ion Processes*, **131**, 345–354 (1994).

[115] K. Dreisewerd, M. Schurenberg, M. Karas, and F. Hillenkamp, *Int. J. Mass Spectrom. Ion Processes*, **141**, 127–148 (1995).

[116] G. Westmacott, W. Ens, F. Hillenkamp, K. Dreisewerd, and M. Schurenberg, *Int. J. Mass Spectrom.*, **221**, 67–81 (2002).

[117] K. Chan, P. Lanthier, X. Liu, J. K. Sandhu, D. Stanimirovic, and J. Li, *Anal. Chim. Acta*, **639**, 57–61 (2009).

[118] T. Porta, C. Grivet, R. Knochenmuss, E. Varesio, and G. Hopfgartner, *J. Mass Spectrom.*, **46**, 144–152 (2011).

[119] H. Ehring, M. Karas, and F. Hillenkamp, *Org. Mass Spectrom.*, **27**, 472–480 (1992).

[120] R. Zenobi and R. Knochenmuss, *Mass Spectrom. Rev.*, **17**, 337–366 (1999).

[121] R. Knochenmuss, *J. Mass Spectrom.*, **37**, 867–877 (2002).

[122] R. Knochenmuss, *Anal. Chem.*, **75**, 2199–2207 (2003).

[123] R. Knochenmuss, *Anal. Chem.*, **76**, 3179–3184 (2004).

[124] R. Knochenmuss, *J. Phys. Chem. B*, **109**, 22947–22957 (2005).

[125] M. Karas, M. Gluckmann, and J. Schafer, *J. Mass Spectrom.*, **35**, 1–12 (2000).

[126] T. W. Jaskolla and M. Karas, *American Society for Mass Spectrometry*, **22**, 976–988 (2011).

[127] A. Leisner, A. Rohlfing, U. Roehling, K. Dreisewerd, and F. Hillenkamp, *J. Phys. Chem. B*, **109**, 11661–11666 (2005).

[128] R. C. Beavis and B. T. Chait, *Chem. Phys. Lett.*, **181**, 479–484 (1991).

[129] W. Zhang and B. T. Chait, *Int. J. Mass Spectrom. Ion Processes*, **160**, 259–267 (1997).

[130] M. Gluckmann and M. Karas, *J. Mass Spectrom.*, **34**, 467–477 (1999).

[131] C. W. Liang, C. H. Lee, Y. T. Lee, and C. K. Ni, *Chem. Asian J.*, **6**, 2986–2991 (2011).

[132] A. Benninghoven, *Phys. Stat. Sol.*, **34**, K169 (1969).

[133] A. Benninghoven, F. G. Rudenauer, and H. W. Werner, *Secondary Ion Mass Spectrometry*, John Wiley and Sons, 1987.

[134] A. Benninghoven and W. K. Sichtermann, *Anal. Chem.*, **50**, 1180–1184 (1978).

[135] S. F. Belykh, V. V. Palitsin, I. V. Veryovkin, A. P. Kovarsky, R. J. H. Chang, A. Adriaens, M. Dowsett, and F. Adams, *Appl. Surf. Sci.*, **252**, 7321–7325 (2006).

[136] A. R. Bayly, A. R. Waugh, and K. Anderson, *Nucl. Instrum. Methods*, **218**, 375–382 (1983).

[137] A. E. Morgan and H. W. Werner, *J. Chem. Phys.*, **68**, 3900–3909 (1978).

[138] A. F. Maarten Altelaar, I. Klinkert, K. Jalink, R. P. J. de Lange, R. A. H. Adan, R. M. A. Heeren, and S. R. Piersma, *Anal. Chem.*, **78**, 734–742 (2006).

[139] D. Weibel, S. Wong, N. Lockyer, P. Blenkinsopp, R. Hill, and J. C. Vickerman, *Anal. Chem.*, **75**, 1754–1764 (2003).

[140] Z. Postawa, B. Czerwinski, M. Szewczyk, E. J. Smiley, N. Winograd, and B. J. Garrsion, *J. Phys. Chem. B*, **108**, 7831–7838 (2004).

[141] W. H. Yuen, *Ion Imaging Mass Spectrometry*, DPhil Thesis, 2012.

[142] A. Nomerotski, S. Adigun-Boaye, M. Brouard, E. Campbell, A. Clark, J. Crooks, J. J. John, A. J. Johnsen, C. Slater, R. Turchetta, C. Vallance, E. Wilman, and W. H. Yuen, *J. Inst.*, **5**, C07007 (2010).

[143] M. J. Bass, M. Brouard, A. P. Clark, and C. Vallance, *J. Chem. Phys.*, **117**, 8723–8735 (2002).

[144] M. Brouard, E. Halford, A. Lauer, C. S. Slater, B. Winter, W. H. Yuen, J. J. John, L. Hill, A. Nomerotski, A. Clark, J. Crooks, I. Sedgwick, R. Turchetta, J. W. L. Lee, C. Vallance, and E. Wilman, *Rev. Sci. Instrum.*, **83**, 114101 (2012).

[145] Pfeiffer Vacuum, GmbH, `https://www.pfeiffer-vacuum.com/en/`.

[146] Edwards, `https://www.edwardsvacuum.com/`.

[147] PHOTONIS USA, `http://www.photonis.com/`.

[148] BURLE INDUSTRIES, `http://www.burle.com/`.

[149] Scientific Analysis Instruments, Ltd, `http://www.saiman.co.uk/`.

[150] Schaefter and Kirchoff GmbH, `http://www.sukhamburg.com/produkte.html`.

[151] R. J. Wenzel and K. A. Prather, *Rapid Commun Mass Spectrom*, **18**, 1525–1533 (2004).

[152] S. W. Coles, *Development of a Microscope Mode Imaging Mass Spectrometer*, MChem Thesis, 2013.

[153] KD Scientific Inc., `http://www.kdscientific.com/`.

[154] M. S. Wilm and M. Mann, *Int. J. Mass Spectom. Ion Proc.*, **136**, 167–180 (1994).

[155] Goodfellow Cambridge Ltd, `http://www.goodfellow.com/`.

[156] B. Y. Chang, R. C. Hoetzlein, J. A. Mueller, J. D. Geiser, and P. L. Houston, *Rev. Sci. Instrum.*, **69**, 1665–1670 (1998).

[157] National Instruments Corporation (U.K.) Ltd, `http://www.ni.com/labview/`.

[158] C. S. Slater, S. B. Blake, M. Brouard, A. Lauer, C. Vallance, J. J. John, R. Turchetta, A. Nomerotski, L. Christensen, J. H. Nielsen, and H. Stapelfeldt, *Phys. Rev. A*, **89**, 011401–1–5 (2014).

[159] C. S. Slater, *Studies of Photoinduced Molecular Dynamics Using a Fast Imaging Sensor*, DPhil Thesis, 2014.

[160] Y. Ogi, H. Kohguchi, D. Niu, K. Ohshimo, and T. Suzuki, *J. Phys. Chem. A*, **113**, 14536–14544 (2009).

[161] A. Kharchenko, J. H. Jungmann, L. MacAleese, and R. M. A. Heeren, *Int. J. Mass Spectrom.*, **351**, 37–46 (2013).

[162] SIMION 8.1, `http://simion.com/`.

[163] H. Liebl, *Applied Charged Particle Optics*, Springer, 2008.

[164] T. L. Colliver, C. L. Brummel, M. L. Pacholski, F. D. Swanek, A. G. Ewing, and N. Winograd, *Anal. Chem.*, **69**, 2225–2231 (1997).

[165] D. M. Grim, J. Siegel, and J. Allison, *J. Forensic Sci.*, **47**, 1265–1273 (2002).

[166] El-Mul Technologies, Ltd, *ScintiMax Data Sheet*.

[167] J. L. Wiza, *Nucl. Instrum. Methods*, **162**, 587–601 (1979).

[168] J. A. Nelder and R. Mead, *Computer J.*, **7**, 308–313 (1965).

[169] S. R. Ellis, A. L. Bruinen, and R. M. A. Heeren, *Anal. Bioanal. Chem.*, **406**, 1275–1289 (2014).

[170] Liebmann1949, *Proc. Phys. Soc. LXII*, **62**, 213–228 (1949).

[171] H. L. Offerhaus, C. Nicole, F. Lepine, C. Bordas, F. Rosca-Pruna, and M. J. J. Vrakking, *Rev. Sci. Instrum.*, **72**, 3245–3248 (2001).

[172] R. Southey, *The Doctor*, Longman, Brown, Green, and Longmans, 1848.

[173] SGE International Pty Ltd, *Fast Discrete Dynode TOF Detectors from ETP*.

[174] Saint-Gobain Crystals, `http://www.detectors.saint-gobain.com/`.

[175] Photonic Science Ltd, `http://www.photonic-science.com/`.

[176] Radio Corporation of America, *Now defunct*.

[177] Navitar Inc., `http://www.navitar.com/`.

[178] OriginLab, Northampton, MA, `http://www.originlab.com/`.

[179] R. Liu, Q. Li, and L. M. Smith, *J. Am. Soc. Mass Spectrom.*, **25**, 1374–1383 (2014).

[180] A. S. Tremsin and O. H. W. Siegmund, *Rev. Sci. Instrum.*, **70**, 3282–3288 (1999).

[181] N. Cartiglia, M. Baselga, G. Dellacasa, S. Ely, V. Fadeyev, Z. Galloway, S. Garbolino, F. Marchetto, S. Martoiu, G. Mazza, J. Ngo, M. Obertino, C. Parker, A. Rivetti, D. Shumacher, H. F. W. Sadrozinski, A. Seiden, and A. Zatserklyaniy, *JINST*, **9**, C02001 (2014).

[182] BioSIMS Technologies, Rouen France, `http://www.biosims-technologies.com/`.

[183] HeatWave Labs, Inc., `http://www.heatwavelabs.com/`.

[184] A. E. Souzis, W. E. Carr, S. I. Kim, and M. Seidl, *Rev. Sci. Instrum.*, **61**, 788–792 (1990).

[185] J. P. Blewett and E. J. Jones, *Phys. Rev.*, **50**, 464–468 (1936).

[186] S. Datz and E. H. Taylor, *J. Chem. Phys.*, **25**, 389–394 (1956).

[187] R. E. Weber and L. F. Cordes, *Rev. Sci. Instrum.*, **37**, 112–113 (1966).

[188] O. W. Richardson, *Monographs on Physics*, New York Longmans, Green and Co., London, 1921.

[189] I. Langmuir and Kingdon K. H., *Proceedings of the Royal Society of London; Series A*, **107**, 61–79 (1925).

[190] M. J. Dresser, *J. Appl. Phys.*, **39**, 338–339 (1968).

[191] HeatWave Labs, Inc., *TB-118* (2002).

[192] B. T. Chait and Standing K. G., *Int. J. Mass Spectrom. Ion Phys.*, **40**, 185–193 (1981).

[193] T. K. Fowler and W. M. Good, *Nucl. Instrum. Methods*, **7**, 245–252 (1960).

[194] P. K. Dutt, *Nucl. Instrum. Methods*, **10**, 37–44 (1961).

[195] V. C. Parr, S. P. Thompson, and M. D. Mills, US 7045792 B2, 2006.

[196] I. G. Brown, *The Physics and Technology of Ion Sources*, John Wiley and Sons, 1989.

[197] J. R. Pierce, *Theory and Design of Electron Beams*, D. Van Nostrand Company, Inc., New Jersey, 1954.

[198] M. E. Haine and P. A. Einstein, *Br. J. Appl. Phys.*, **3**, 40–46 (1952).

[199] M. E. Haine, P. A. Einstein, and P. H. Borcherds, *Br. J. Appl. Phys.*, **9**, 482–486 (1958).

Chapter 9

Derivation of Transfer Matrices

The following derivations are adapted from those found in Liebl's "Applied Charged Particle Optics". Here the equations are derived whilst considering a positively charged particle with charge, q. This means that the kinetic energy gains of the particles have to be calculated relative to potential of the first (repeller) electrode, rather than from the local (circuit) ground,

$$\frac{mv_n^2}{2} = q\left(V_i + (V_0 - V_n)\right), \tag{9.1}$$

where m is the mass of the particle, v_n is the particles velocity at the n^{th} electrode, V_i is the initial of the particle after ablation (in electronvolts), V_0 the potential applied to the repeller electrode, and V_n the potential applied to the n^{th} electrode.

9.1 A Uniform Field

A particle passing from one electrode to another (electrodes $n-1$ to n) will experience a uniform electric field (assuming that any lens aperture in either of the electrodes produces a perturbation which can be dealt with later),

$$E_n = \frac{V_{n-1} - V_n}{L_n}, \tag{9.2}$$

such that a positively charged particle is accelerated towards the lower potential along the major axis leading from the first to the second plate,

$$\ddot{x}_n = \frac{qE_n}{m}. \tag{9.3}$$

The particles velocity at the first plate, v_n, can be split into two components,

$$\dot{r}_{n-1} = v_{n-1}\sin(\alpha_{n-1}), \tag{9.4}$$

$$\dot{x}_{n-1} = v_{n-1}\cos(\alpha_{n-1}), \tag{9.5}$$

where $\dot{r}$ is the radial component of the velocity, $\dot{x}$ is the axial (time-of-flight axis) component of the velocity, and α is the angle between the direction of motion and the major axis.

The axial position of the particle can be determined as a function of time,

$$x = x_{n-1} + \dot{x}_{n-1}t + \frac{\ddot{x}_n}{2}t^2, \tag{9.6}$$

and if rearranged and after substitution using equations (9.3) & (9.5),

$$\frac{qE_n}{2m}t^2 + v_{n-1}\cos(\alpha_{n-1})t - (x - x_{n-1}). \tag{9.7}$$

The solution for this equation can be found but it is prudent to bear in mind a few caveats: firstly, by solving this quadratic equation the solution assumes that weighting of the quadratic term is non-zero (i.e. the solution is not valid for a field-free drift tube); secondly, if the discriminant, $\left(v_{n-1}\cos(\alpha_{n-1})\right)^2 + \frac{2qE_n(x-x_n)}{m} < 0$, then there is no real solution to the equation (i.e. the particle does not reach x); and finally, it is the positive solution that we want so we will use the positive route of the discriminant.

So

$$\begin{aligned} t &= \frac{m}{qE_n}\left[-v_{n-1}\cos(\alpha_{n-1}) + \sqrt{v_{n-1}^2\cos^2(\alpha_{n-1}) + \frac{2qE_n(x-x_{n-1})}{m}}\right], \\ &= \frac{mv_{n-1}}{qE_n}\left[-\cos(\alpha_{n-1}) + \sqrt{\cos^2(\alpha_{n-1}) + \frac{2qE_n(x-x_{n-1})}{mv_{n-1}^2}}\right] \end{aligned} \tag{9.8}$$

which gives

$$t_n = \frac{mv_{n-1}}{qE_n}\left[-\cos(\alpha_{n-1}) + \sqrt{\cos^2(\alpha_{n-1}) + \frac{2qE_n(L_n)}{mv_{n-1}^2}}\right], \tag{9.9}$$

where t_n is the time that the particle reaches the n^{th} electrode, and L_n is the distance between electrode $n-1$ and n.

The radial position of the particle when it reaches the electrode is described by,

$$\begin{aligned} r_n &= r_{n-1} + \dot{r}_{n-1}t_n, \\ &= r_{n-1} + v_{n-1}\sin(\alpha_{n-1})t_n, \end{aligned} \tag{9.10}$$

and by substituting equation (9.9) the result is,

$$r_n = r_{n-1} + \sin(\alpha_{n-1})\frac{mv_{n-1}^2}{qE_n}\left[-\cos(\alpha_{n-1}) + \sqrt{\cos^2(\alpha_{n-1}) + \frac{2qE_nL_n}{mv_{n-1}^2}}\right]. \tag{9.11}$$

Finally, the particle energy can be expressed as a function of the electrode potentials (equation (9.1)):

$$r_n = r_{n-1} + \sin(\alpha_{n-1})\frac{2\left(V_i + (V_0 - V_{n-1})\right)}{E_n}\left[-\cos(\alpha_{n-1}) + \sqrt{\cos^2(\alpha_{n-1}) + \frac{E_nL_n}{(V_i + (V_0 - V_{n-1}))}}\right]. \tag{9.12}$$

9.2 The Initial Extraction Region

At this point there are two different scenarios to consider: an initial extraction region, and a generic field. First the initial extraction: here $n = 1$ so the initial kinetic energy is

equal only to the original energy from ablation,

$$r_1 = r_i + \sin(\alpha_i)\frac{2V_iL_1}{V_0 - V_1}\left[-\cos(\alpha_i) + \sqrt{\cos^2(\alpha_i) + \frac{(V_0 - V_1)}{V_i}}\right]. \tag{9.13}$$

Where the field, E_1, has also been expressed as in equation (9.2). The next assumption that can be made is that $(V_0 - V_1) >> V_i$, and this leads to both $\frac{V_0 - V_1}{V_i} >> \cos^2(\alpha_i)$ and $\sqrt{\frac{V_0 - V_1}{V_i}} >> cos(\alpha_i)$. Implementing these assumptions and tidying up the remaining terms yields

$$r_1 = r_i + \sin(\alpha_i)2L_1\sqrt{\frac{V_i}{V_0 - V_1}}. \tag{9.14}$$

This gives the radial position of the particle as a function of the initial angle of the direction of motion. It can be more suitable (as will be shown later) to use the "slope" of the particle motion, $\frac{\Delta r}{\Delta x}$. This is the tangent of the particle motion and so the angle of the direction of motion can be found by taking: $\arctan\left(\frac{\Delta r}{\Delta x}\right)$.

This slope can be calculated by taking the derivative of the position,

$$r_1' = \sin(\alpha_i)\sqrt{\frac{V_i}{V_0 - V_1}}. \tag{9.15}$$

9.3 A Generic Uniform Field

For the generic field it can be assumed that $V_i << (V_0 - V_n$,

$$r_n = r_{n-1} + \sin(\alpha_{n-1})\frac{2\,(V_0 - V_{n-1})}{E_n}\left[-\cos(\alpha_{n-1}) + \sqrt{\cos^2(\alpha_{n-1}) + \frac{E_nL_n}{(V_0 - V_{n-1})}}\right]. \tag{9.16}$$

The ratio of the electric field, E_n, to the acceleration voltage, $V_0 - V_{n-1}$, is equal to:

$$\begin{aligned}\frac{E_n}{V_0 - V_{n-1}} &= \frac{V_{n-1} - V_n}{L_n\,(V_0 - V_{n-1})}, \\ &= \frac{1}{L_n}\left[\frac{V_{n-1} - V_n}{V_0 - V_{n-1}}\right], \\ &= \frac{1}{L_n}\left[\frac{V_{n-1} - V_n + V_0 - V_0}{V_0 - V_{n-1}}\right], \\ &= \frac{1}{L_n}\left[-1 + \frac{V_0 - V_n}{V_0 - V_{n-1}}\right], \end{aligned} \tag{9.17}$$

which can be substituted into equation (9.16) yielding:

$$r_n = r_{n-1} + \sin(\alpha_{n-1})\frac{2L_n}{\frac{V_0 - V_n}{V_0 - V_{n-1}} - 1}\left[-\cos(\alpha_{n-1}) + \sqrt{\cos^2(\alpha_{n-1}) - 1 + \frac{V_0 - V_n}{V_0 - V_{n-1}}}\right]. \tag{9.18}$$

Substituting $\cos^2(\alpha) - 1 = -\sin^2(\alpha)$,

$$r_n = r_{n-1} + \sin(\alpha_{n-1})\frac{2L_n}{\frac{V_0 - V_n}{V_0 - V_{n-1}} - 1}\left[-\cos(\alpha_{n-1}) + \sqrt{-\sin^2(\alpha_{n-1}) + \frac{V_0 - V_n}{V_0 - V_{n-1}}}\right] \tag{9.19}$$

As the particle has already been accelerated such that $V_i << (V_0 - V_n$, it can also be assumed that the direction of motion is close to the major axis (paraxial approximation) so $\sin(\alpha) = \tan(\alpha) = r'$; $\cos(\alpha) = 1$,

$$r_n = r_{n-1} + r'_{n-1}\frac{2L_n}{\frac{V_0 - V_n}{V_0 - V_{n-1}} - 1}\left[-1 + \sqrt{\frac{V_0 - V_n}{V_0 - V_{n-1}} - r'^2_{n-1}}\right] \tag{9.20}$$

The paraxial approximation also implies that $\frac{V_0 - V_n}{V_0 - V_{n-1}} >> r'^2_{n-1}$.

$$\begin{aligned} r_n &= r_{n-1} + r'_{n-1}2L_n\frac{\sqrt{\frac{V_0 - V_n}{V_0 - V_{n-1}}} - 1}{\frac{V_0 - V_n}{V_0 - V_{n-1}} - 1} \\ &= r_{n-1} + r'_{n-1}\frac{2L_n}{\sqrt{\frac{V_0 - V_n}{V_0 - V_{n-1}}} + 1} \end{aligned} \tag{9.21}$$

As before the slope of the direction of motion can be found by taking the derivative

from equation (9.16):

$$\begin{aligned} r'_n &= \frac{d}{dx}\left(\sin(\alpha_{n-1})\frac{2\,(V_0 - V_{n-1})}{E_n}\left[-\cos(\alpha_{n-1}) + \sqrt{\cos^2(\alpha_{n-1}) + \frac{E_n L_n}{(V_0 - V_{n-1})}}\right]\right). \\ &= \sin(\alpha_{n-1})\frac{(V_0 - V_{n-1})}{E_n}\left[\cos^2(\alpha_{n-1}) + \frac{E_n L_n}{(V_0 - V_{n-1})}\right]^{-\frac{1}{2}}\frac{E_n}{(V_0 - V_{n-1})} \\ &= \sin(\alpha_{n-1})\left[\cos^2(\alpha_{n-1}) + \frac{E_n L_n}{(V_0 - V_{n-1})}\right]^{-\frac{1}{2}}. \end{aligned} \tag{9.22}$$

This, again, can be simplified using equation (9.17),

$$r'_n = \sin(\alpha_{n-1})\left[\frac{V_0 - V_n}{V_0 - V_{n-1}} - \sin^2(\alpha_{n-1})\right]^{-\frac{1}{2}}, \tag{9.23}$$

and again employing the paraxial approximation, $\sin(\alpha) \approx r'_n$, and assuming that $\frac{V_0 - V_n}{V_0 - V_{n-1}} >> r'^2_{n-1}$,

$$r'_n = \sqrt{\frac{V_0 - V_{n-1}}{V_0 - V_n}}\, r'_{n-1}. \tag{9.24}$$

9.4 Forming the Matrices

Now the matrices can be written down in the form:

$$\begin{pmatrix} r \\ r' \end{pmatrix}_n = M \begin{pmatrix} r \\ r' \end{pmatrix}_{n-1} \tag{9.25}$$

So, for the initial extraction region, equations (9.20)&(9.24) can be distilled into a transfer matrix,

$$M = \begin{pmatrix} 1 & \frac{2L_n}{\sqrt{\frac{V_0 - V_n}{V_0 - V_{n-1}}} + 1} \\ 0 & \sqrt{\frac{V_0 - V_{n-1}}{V_0 - V_n}} \end{pmatrix} \tag{9.26}$$

The initial extraction region is described by equations (9.14) & (9.15), which when com-

bined form the initial vector of an particles trajectory after extraction:

$$M_{\text{Extr}} = \begin{pmatrix} r_{p,i} + \sin(\alpha_i) 2L_1 \sqrt{\frac{V_i}{V_0 - V_1}} \\ \sin(\alpha_i) \sqrt{\frac{V_i}{V_0 - V_1}} \end{pmatrix} \tag{9.27}$$

These equations are not expressed as a function of the slope of the particle motion but rather as a function of the angle of the particle motion from the major axis. This is due to the fact that the paraxial approximation does not apply to particles ejected straight from the surface. If it were valid then a transfer matrix could be defined,

$$M_{\text{Extr}} \approx \begin{pmatrix} 1 & \frac{2L_n}{\sqrt{\frac{V_0 - V_n}{V_i}} + 1} \\ 0 & \sqrt{\frac{V_i}{V_0 - V_n}} \end{pmatrix}. \tag{9.28}$$